

Self-referencing Hybrid Plasmonic Nanostructures for Sensing

by

Reza Kohandani

A thesis

presented to the University of Waterloo

in fulfillment of the

thesis requirement for the degree of

Doctor of Philosophy

in

Electrical and Computer Engineering

Waterloo, Ontario, Canada, 2023

© Reza Kohandani 2023

Examining Committee Membership

The following served on the Examining Committee for this thesis. The decision of the Examining Committee is by majority vote.

External Examiner

Professor Mahi Singh
Department of Physics and Astronomy
Western University

Supervisor

Professor Simarjeet Saini
ECE Department
University of Waterloo

Internal Member

Professor William Wong
ECE Department
University of Waterloo

Internal Member

Professor Dayan Ban
ECE Department
University of Waterloo

Internal-external Member

Professor Vasudevan Lakshminarayanan
Department of Optometry
University of Waterloo

Author's Declaration

I hereby declare that I am the sole author of this thesis. This is a true copy of the thesis, including any required final revisions, as accepted by my examiners.

I understand that my thesis may be made electronically available to the public.

Abstract

The field of plasmonics has drawn a considerable amount of research interest for the past 20 years, and now, plasmonics is a vital part of nanophotonics. Numerous applications have been enabled by plasmonic structures in a wide range of areas, including engineering, medicine, biology, food science, and environmental science. Among all the applications, the field of plasmonic sensing has made remarkable progress, and it continues to grow quickly. Plasmonic sensors, empowered by cutting-edge nanofabrication techniques, are offering label-free and robust sensing performance. In order to apply the plasmonic sensor technology to even more areas and real-world problems, one needs to optimize and improve the sensor technology toward realizing low-cost, portable, and high-performance sensors that can operate in unstable environments.

In this thesis, we propose and fabricate several nanostructure-based plasmonic sensors to improve performance in variable environmental conditions and reduce the cost of characterizations. The first two sensors are based on metallic two-dimensional nanograting that can create high-quality factor resonance features in visible wavelengths. Both sensors have the ability of self-referencing, which makes them suitable for working in an unstable environment. Further, both sensors are highly sensitive to the small changes in the local refractive index and are also capable of detecting surface attachments. Last but not least, both sensors have simple structures resulting in ease of fabrication and operate in visible and near-infrared regions which makes them excellent candidates for low-cost applications. To demonstrate the sensors, we design and numerically evaluate the performance of the proposed structures using Rigorous coupled-wave analysis (RCWA) and Finite-difference time-domain (FDTD) methods. We also investigated the effect of geometrical parameters on the performance of the sensors and demonstrated that a photonic designer had many degrees of freedom to design for the proposed devices to optimize the sensors for diverse applications. Secondly, we fabricate the designed structures using nanofabrication techniques such as electron beam lithography (EBL) and lift-off, and we experimentally confirm the different plasmonic modes that are excited in the sensor. We also optimize the sensors to achieve desirable results. Finally, we characterize the fabricated sensors and experimentally evaluate them in terms of sensitivity. The experimental results agree with the simulations, and the sensors showed high performance as predicted during the design and simulations. Based on the experimental results, the sensors can generate several resonance features in the visible to near-infrared range, in which at least one of these resonance modes is very sensitive to the changes in

the surrounding refractive index and can be used as a sensitivity measurement point. On the other hand, at least one of the resonance features is isolated from the surrounding environment and can be used as a self-referencing point. We propose that using self-referencing, changes due to temperature can be extracted. For some designs, the sensitivity values achieved in the experiments are even higher than the values that were predicted in the simulations. The fabricated sensors showed lots of potential for realizing a low-cost platform for self-referenced plasmonic sensors.

The third proposed plasmonic sensor, designed and fabricated in this work, is a hybrid platform based on titanium dioxide (TiO_2) nanowire arrays integrated with plasmonic layers. The sensor can create a very sharp resonance feature in reflections in the visible range, resulting from the coupling of plasmonic modes and nanowire optical modes. While similar resonances have been demonstrated before in the transmission, e.g., with nano-hole plasmonic arrays, to our knowledge, this is the first demonstration of single peaked reflections. This results in the generation of very vivid structural colors. After designing and evaluating the proposed design using FDTD and RCWA simulations, we fabricate the nanowire arrays using the dry etching technique and achieve highly ordered nanowire arrays. Further, the structure is sensitive to the changes in the surrounding refractive index, which makes it suitable for realizing low-cost colorimetric sensors requiring only a camera and image processing instead of a spectrometer. This will appreciably reduce the cost of a sensing system.

Acknowledgements

I would like to express my deepest gratitude to Professor Simarjeet Saini, my PhD supervisor, for his unwavering support, exceptional mentorship, and passionate dedication throughout my PhD journey. Professor Saini has been an invaluable source of guidance, continuously pushing the boundaries of my knowledge and understanding and inspiring me to reach new heights in my research.

I would like to extend my appreciation to my Ph.D. committee members, Professor Dayan Ban, Professor William Wong, Professor Vasudevan Lakshminarayanan, and Professor Mahi Singh. Their collective wisdom, guidance, and insightful comments have been instrumental in shaping the trajectory of my research and the quality of my work.

I am deeply grateful to the dedicated staff members of the Quantum Nano Fabrication and Characterization Facility at the University of Waterloo for their exceptional training, guidance, and invaluable discussions. Additionally, I extend my warm appreciation to all my fellow PhD students and colleagues, who have been an essential source of support and camaraderie throughout this challenging journey.

I want to thank my wonderful wife, Sahar Kalani, for always being there with her love and belief in me right from the start. She's encouraged me to step out of my comfort zone and has been my constant support and help throughout this journey. Her selflessness and dedication to my academic pursuits have made this journey more fulfilling and enriched my life in countless ways. I am blessed to have her by my side, and I am forever grateful for her love and unwavering faith in me.

I want to express my heartfelt thanks to my parents, my family, and my wife's family for their help and support throughout my academic journey. Their love, encouragement, and sacrifices have been the driving force behind my success. I also extend my appreciation to all of my former teachers and mentors for their continuous guidance and belief in my potential. Their encouragement and valuable lessons have played a pivotal role in helping me reach this significant milestone.

Table of Contents

Author’s Declaration	iii
Abstract	iv
Acknowledgements	vi
List of Figures	xi
List of Tables.....	xix
Chapter 1 Introduction.....	1
1.1 Bulk Plasmons.....	1
1.2 Surface Plasmon Polaritons (SPPs).....	3
1.3 Surface Plasmon Resonance (SPR).....	4
1.4 Localized Surface Plasmon Resonance (LSPR).....	5
1.5 Plasmonic Sensing.....	7
1.6 Plasmonic Structural Colors and Colorimetric Sensors	7
1.7 Nanowires Integration with Plasmonics.....	8
1.7.1 Optical Modes in Nanowire Arrays.....	9
1.8 Current Issues with Plasmonic Sensors.....	11
1.8.1 Inaccuracy in Unstable Environments.....	11
1.8.2 Expensive and Bulky Readout Technology.....	12
1.8.3 The High Cost Associated with Complicated Geometry.....	12
1.9 Motivations and Structure of the Thesis.....	13
Chapter 2 Self-Referencing Plasmonic Array Sensors.....	15
2.1 Introduction	15
2.2 Proposed Design.....	18
2.3 Effect of Geometrical Parameters	24

2.4 Bulk Sensing.....	25
2.5 Surface Sensing	26
2.6 Lessons from Simulations and Fabrication Tolerances	29
2.6.1 Gold Film	29
2.6.2 Dielectric Layer	29
2.6.3 Lithography	30
2.6.4 Grating Layer.....	31
2.7 Limitations of the Simulations	31
2.8 Conclusions	32
Chapter 3 Fabrication of the Self-Referencing Plasmonic Sensors Based on Gold Nano-grating Arrays	33
3.1 Glass Substrate	34
3.2 Electron Beam Physical Vapor Deposition (EB-PVD) of the Gold Film	35
3.3 Deposition of the Dielectric Spacer Layer Using PECVD	36
3.4 Deposition of the E-beam Resist	40
3.5 Electron Beam Lithography and Lift-off.....	41
3.6 Summary and Conclusion.....	48
Chapter 4 Characterization of the Self-Referencing Plasmonic Array Sensors	49
4.1 Reflection Measurement.....	49
4.2 Refractive Index Liquids	50
4.3 Effect of the Dielectric Spacer Layer	50
4.4 Effect of Pitch Variations	53
4.5 Effect of Cube Side Length and Cylinder Diameter.....	54
4.6 Performance of the Triangular Arrays.....	57

4.7 Bulk Sensitivity	58
4.7.1 Cubic Nano-gratings, SiON Spacer Layer, Pitch 400 nm	58
4.7.2 Cubic Nano-gratings, SiON Spacer Layer, Pitch 450 nm	64
4.7.3 Cubic Nano-gratings, SiON Spacer Layer, Pitch 500 nm	68
4.7.4 Cylindrical Nano-gratings, SiON Spacer Layer, Pitch 400 nm.....	71
4.7.5 Cylindrical Nano-gratings, SiON Spacer Layer, Pitch 450 nm.....	75
4.7.6 Cubic Nano-gratings, SiN Spacer Layer, Pitch 400 nm	78
4.7.7 Cubic Nano-gratings, SiN Spacer Layer, Pitch 450 nm	82
4.7.8 Cubic Nano-gratings, SiN Spacer Layer, Pitch 500 nm	86
4.7.9 Cylindrical Nano-gratings, SiN Spacer Layer, Pitch 400 nm.....	87
4.7.10 Cylindrical Nano-gratings, SiN Spacer Layer, Pitch 450 nm.....	90
4.8 Advantage of Self- Referencing	98
4.9 Summary and Conclusion.....	100
Chapter 5 High Quality-Factor Hybrid Plasmonic-Nanowire Structural Color Generation	101
5.1 Introduction	101
5.2 Proposed Design.....	103
5.3 Effect of NW Diameter	106
5.4 Gold Layer Thickness.....	109
5.5 Total TiO ₂ Thickness Variations	111
5.6 Conclusion.....	114
Chapter 6 Fabrication and Characterization of the Plasmonic-Nanowire Hybrid Structure	116
6.1 Fabrication of the TiO ₂ Nanowires Capped with Gold	116
6.1.1 Lithography and Mask Definition	116
6.1.2 Dry Etching	117

6.1.3 Al Mask Removal.....	120
6.1.4 Fabricated Structure.....	120
6.2 Characterization of the TiO ₂ Nanowires	121
6.3 Color Generation and Sensitivity	124
6.4 Summary and Conclusion.....	135
Chapter 7 Summary and Future Works	136
References	139

List of Figures

Figure 2.1. Schematic diagram of the proposed structure, (a) the longitudinal cut view of the structure, (b) three-dimensional view of the nano-grating structure with cubic geometry and (c) three-dimensional view of the nano-grating structure with cylindrical geometry **19**

Figure 2.2. (a) Absorption and reflection spectra of the optimized nano-grating structure with cubic geometry, (b-d) distribution of H_y for three resonance frequencies of the nano-grating structure with cubic geometry **21**

Figure 2.3. (a) Absorption and reflection spectra of the optimized structure with cylinders as nano-gratings, (b-e) distribution of H_y for four resonance features of the optimized structure with cylinders as nano gratings **23**

Figure 2.4. Reflection spectra of the nano-grating structure with cubic geometry where (a) nano-grating height is changing from 20 nm to 90 nm, (b) dielectric height is changing from 20 nm to 90 nm, and (c) thickness of the gold film is changing from 20 nm to 90 nm. **25**

Figure 2.5. (a) Reflection spectra of the nano-grating structure with cubic geometry when refractive index of surrounding materials varies from 1.33 to 1.4, (b) variations of the resonance wavelength of the cubic nano-gratings as the refractive index of surroundings changes, (c) Reflection spectra of the nano-grating structure with cylindrical geometry when refractive index of surrounding materials varies from 1.33 to 1.4 and (d) variations of the resonance wavelength of the cylindrical nano-gratings as the refractive index of surroundings changes. **27**

Figure 2.6. (a) Reflection spectra of the nano-grating structure with cubic geometry when thickness of surface layer varies from 1 nm to 10 nm, (b) variations of the resonance wavelength of the cubic nano-gratings as the thickness of the surface layer changes, (c) Reflection spectra of the nano-grating structure with cylindrical geometry when thickness of surface layer varies from 1 nm to 10 nm, and (d) variations of resonance wavelength of the cylindrical nano-gratings as the thickness of the surface layer changes. **28**

Figure 3.1. Fabrication steps of the proposed self-referencing sensors based on cubic and cylindrical nano-gratings. **33**

Figure 3.2. SiON optical model fitted to the measured data with ellipsometer. A decent fit has been achieved with an MSE of 4.7. **38**

Figure 3.3. Refractive index of the deposited SiON using PECVD, extracted using ellipsometer. **39**

Figure 3.4. Refractive index of the deposited SiN using PECVD, extracted using ellipsometer.	40
Figure 3.5. SEM images of nano-cube arrays with different e-beam doses of (a) 200 $\mu\text{C}/\text{cm}^2$, (b) 220 $\mu\text{C}/\text{cm}^2$, (c) 240 $\mu\text{C}/\text{cm}^2$, (d) 260 $\mu\text{C}/\text{cm}^2$ and (e) 280 $\mu\text{C}/\text{cm}^2$	43
Figure 3.6. SEM images of Some of the representative cubic arrays with (a) 170 nm side length and 400 nm pitch, (b) 180 nm side length and 450 nm pitch, (c) 220 nm side length and 400 nm pitch, and (d) 250 nm side length and 400 nm pitch.	44
Figure 3.7. A microscopic image of the cubic arrays taken by an optical microscope.	45
Figure 3.8. SEM images of two nano-cylinder arrays with diameters of (a) 200 and (b) 250 nm, respectively. The pitch is 400 nm for both arrays.	46
Figure 3.9. A microscopic image of the cylindrical arrays taken by an optical microscope.	46
Figure 3.10. SEM images of equilateral triangles with side length of (a) 180 nm and 450 nm pitch, (b) 200 nm and 400 nm pitch, (c) 220 nm and 400 nm pitch and (d) 250 nm and 400 nm pitch.....	47
Figure 4.1. Reflection spectra measured from nano-grating arrays with two different dielectric spacer layers of SiON and SiN for (a) cubes with 200 nm side length and 400 nm pitch, and (b) cylinders with 200 nm diameter and 400 nm pitch.	51
Figure 4.2. Reflection spectra measured from nano-grating arrays with different lattice spacing for the sample with SiON spacer layer for (a) cubes with 200 nm side length, and (b) cylinders with 200 nm diameter.	53
Figure 4.3. Reflection spectra for the sample with SiON spacer layer for (a) cubic arrays with 400 nm pitch and different side length, (b) cubic arrays with 450 nm pitch and different side length, (c) cylindrical arrays with 400 nm pitch and different diameters, and (d) cylindrical array with 450 nm pitch and different diameters.	55
Figure 4.4. Reflection spectra for the sample with SiN spacer layer for (a) cubic arrays with 400 nm pitch and different side length, (b) cubic arrays with 450 nm pitch and different side length, (c) cylindrical arrays with 400 nm pitch and different diameters, and (d) cylindrical array with 450 nm pitch and different diameters.	56
Figure 4.5. Reflection spectra of the sample with SiON spacer layer with equilateral triangular arrays with side lengths of (a) 220 nm and (b) 250 nm, for different lattice spacings.	57
Figure 4.6. Reflection spectra of the cubic arrays with different surrounding refractive index and side lengths of (a) 170 nm, (b)180 nm, (c) 200 nm, (d) 220 nm, and (e) 250 nm, respectively. for the sample with SiON spacer layer and 400 nm pitch.....	60

Figure 4.7. (a, c, e) First derivatives of the reflection spectra of the cubic arrays with 200, 220 and 250 nm side length respectively, for different surrounding indices and, (b, e, f) changes in the resonance wavelengths of mode 1 and 2 corresponding to Figure 4.7a, c, e respectively.	62
Figure 4.8a-c. Resonance wavelengths of the local maximum for different surrounding refractive indices, for the cubic arrays with 200, 220 and 250 nm, respectively.....	64
Figure 4.9. Reflected colors from the cubic arrays with SiON spacer layer and 400 nm pitch. Moving from top to bottom, the cube side length increases, and from left to right, the surrounding refractive index increases.....	65
Figure 4.10a-e. Reflection spectra of the cubic arrays with different surrounding refractive index and side lengths of 170, 180, 200, 220 and 250 nm, respectively. The dielectric spacer layer is SiON and the lattice spacing is 450 nm.....	66
Figure 4.11. (a, c, e) First derivatives of the reflection spectra of the cubic arrays with 200, 220 and 250 nm side length respectively, for different surrounding indices and, (b, e, f) changes in the resonance wavelengths of mode 1 and 2 and the local maximum, corresponding to Figure 11, a, c, e respectively. The dielectric spacer layer is SiON and the lattice spacing is 450 nm.	67
Figure 4.12. Reflected colors from the cubic arrays with SiON spacer layer and 450 nm pitch. Moving from top to bottom, the cube side length increases, and from left to right, the surrounding refractive index increases.....	68
Figure 4.13. Reflection spectra with different surrounding indices, first derivatives of the reflection spectra and changes in the resonance wavelengths of the modes, for the cubic arrays with 250 nm side length and 500 nm pitch, respectively. The spacer layer is SiON.	69
Figure 4.14. Reflected colors from the cubic array with 250 nm side length and 500 nm pitch, for different surrounding refractive indices. The spacer layer is SiON.	70
Figure 4.15a-e. Reflection spectra of the cylindrical arrays with different surrounding refractive indices and diameters of 170, 180, 200, 220 and 250 nm, respectively. The dielectric spacer layer is SiON and the lattice spacing is 400 nm.....	72
Figure 4.16. (a, c, e) First derivatives of the reflection spectra of the cylindrical arrays with 200, 220 and 250 nm diameter respectively, for different surrounding indices and, (b, e, f) changes in the resonance wavelengths of the modes, corresponding to Figure 4.16 a, c, e respectively. The dielectric spacer layer is SiON and the lattice spacing is 400 nm.	73

Figure 4.17. Reflected colors from the cylindrical arrays with SiON spacer layer and 400 nm pitch. Moving from top to bottom, the cylinder diameter increases, and from left to right, the surrounding refractive index increases.	74
Figure 4.18a-e. Reflection spectra of the cylindrical arrays with different surrounding refractive indices and diameters of 170, 180, 200, 220 and 250 nm, respectively. The dielectric spacer layer is SiON and the lattice spacing is 450 nm.....	76
Figure 4.19. (a, c, e) First derivatives of the reflection spectra of the cylindrical arrays with 200, 220 and 250 nm diameter respectively, for different surrounding indices and, (b, e, f) changes in the resonance wavelengths of the modes, corresponding to Figure 4.19a, c, e respectively. The dielectric spacer layer is SiON and the lattice spacing is 450 nm.	77
Figure 4.20. Reflected colors from the cylindrical arrays with SiON spacer layer and 450 nm pitch. Moving from top to bottom, the cylinder diameter increases, and from left to right, the surrounding refractive index increases.	78
Figure 4.21a-e. Reflection spectra of the cubic arrays with different surrounding refractive index and side lengths of 170, 180, 200, 220 and 250 nm, respectively. The dielectric spacer layer is SiN and the lattice spacing is 400 nm.	79
Figure 4.22. (a, c, e) - First derivatives of the reflection spectra of the cubic arrays with 200, 220 and 250 nm side length respectively, for different surrounding indices and, (b, e, f) changes in the resonance wavelengths of mode 1 and 2 and the local maximum, corresponding to Figure 4.22a, c, e respectively. The dielectric spacer layer is SiN and the lattice spacing is 400 nm.	81
Figure 4.23. Reflected colors from the cubic arrays with SiN spacer layer and 400 nm pitch. Moving from top to the bottom, the cube side length increases, and from left to right, the surrounding refractive index increases.	82
Figure 4.24a-e. Reflection spectra of the cubic arrays with different surrounding refractive index and side lengths of 170, 180, 200, 220 and 250 nm, respectively. The dielectric spacer layer is SiN and the lattice spacing is 450 nm.	83
Figure 4.25. (a, c, e) - First derivatives of the reflection spectra of the cubic arrays with 200, 220 and 250 nm side length respectively, for different surrounding indices and, (b, e, f) changes in the resonance wavelengths of mode 1 and 2 and the local maximum, corresponding to Figure 25a, c, e respectively. The dielectric spacer layer is SiN and the lattice spacing is 450 nm.....	84

Figure 4.26. Reflected colors from the cubic arrays with SiN spacer layer and 450 nm pitch. Moving from top to the bottom, the cube side length increases, and from left to right, the surrounding refractive index increases.	85
Figure 4.27. Reflection spectra with different surrounding indices, first derivatives of the reflection spectra and changes in the resonance wavelengths of the modes, for the cubic arrays with 250 nm side length and 500 nm pitch, respectively. The spacer layer is SiN.	86
Figure 4.28. Reflected colors from the cubic array with 250 nm side length and 500 nm pitch, for different surrounding refractive indices. The spacer layer is SiN.	87
Figure 4.29a-e. Reflection spectra of the cylindrical arrays with different surrounding refractive indices and diameters of 170, 180, 200, 220 and 250 nm, respectively. The dielectric spacer layer is SiN and the lattice spacing is 400 nm.....	88
Figure 4.30. (a, c, e) First derivatives of the reflection spectra of the cylindrical arrays with 200, 220 and 250 nm diameter respectively, for different surrounding indices and, (b, e, f) changes in the resonance wavelengths of the modes, corresponding to Figure 4.30a, c, e respectively. The dielectric spacer layer is SiN and the lattice spacing is 400 nm.	89
Figure 4.31. Reflected colors from the cylindrical arrays with SiN spacer layer and 400 nm pitch. Moving from top to the bottom, the cylinder diameter increases, and from left to right, the surrounding refractive index increases.	90
Figure 4.32a-e. Reflection spectra of the cylindrical arrays with different surrounding refractive indices and diameters of 170, 180, 200, 220 and 250 nm, respectively. The dielectric spacer layer is SiN and the lattice spacing is 450 nm.....	91
Figure 4.33. (a, c, e) First derivatives of the reflection spectra of the cylindrical arrays with 200, 220 and 250 nm diameter respectively, for different surrounding indices and, (b, e, f) changes in the resonance wavelengths of the modes, corresponding to Figure 4.33a, c, e respectively. The dielectric spacer layer is SiN and the lattice spacing is 450 nm.	93
Figure 4.34. Reflected colors from the cylindrical arrays with SiN spacer layer and 450 nm pitch. Moving from top to bottom, the cylinder diameter increases, and from left to right, the surrounding refractive index increases.	94
Figure 4.35. (a) and (b), The sensitivity results of the sample with the SiON spacer layer for the cubic and cylindrical arrays, respectively. (c) and (d), the sensitivity results of the sample with SiN spacer layer for the cubic arrays and cylindrical arrays, respectively.	95

Figure 4.36 Reflection spectra of the cubic array with 250 nm side length and 400 nm pitch from the sample with SiN spacer layer for two different days.....	99
Figure 5.1. Schematic diagram of the proposed nanowires array.....	104
Figure 5.2. (a) Absorption, reflection, and transmission spectra of the proposed nanowire array, (b) and (c) distribution of H_y for two resonance features of optimized structure.....	105
Figure 5.3. Reflection spectrum of the optimized structure and magnetic field distributions of corresponding resonance features.....	107
Figure 5.4. (a) Reflection spectra of the proposed design with different NW diameter and the reflected color from each spectrum, (b) a three-dimensional view of the reflection spectra as functions of NW diameter and wavelength, and (c) magnetic field distributions of SLR and LSPR resonance features with a unit of $A/m \times 10^3$	108
Figure 5.5. Reflected colors from 18 samples with different NW diameters. The dashed line with arrow shows the evolution trend of colors when the size of NW diameters is increased.	109
Figure 5.6. (a) Reflection spectra of the proposed design with different thicknesses of the top gold layer and the reflected color from each spectrum, (b) a three-dimensional view of the reflection spectra as functions of gold thickness and wavelength, and (c) magnetic field distributions of SLR and LSPR resonance features with a unit of $A/m \times 10^3$	110
Figure 5.7. Reflected colors from 15 samples with different gold thicknesses. The dashed line with arrow shows the evolution trend of colors when the gold thickness is increased.	111
Figure 5.8. Reflection spectra of proposed nanowire structure for different etch values, (a) total TiO_2 thickness of 130 nm and NW diameter of 100 nm, (b) total TiO_2 thickness of 160 nm and NW diameter of 150 nm, (c) total TiO_2 thickness of 200 nm and NW diameter of 100 nm, and (d) total TiO_2 thickness of 250 nm and NW diameter of 100 nm.	112
Figure 5.9. Reflected colors from the proposed nanostructure with total TiO_2 thicknesses of (a) 130 nm, (b) 160 nm, (c) 200 nm, and (d) 250 nm. The black dashed line shows the color evolution as etch increases.	113
Figure 6.1. Summary of the fabrication steps for the TiO_2 nanowires capped with a layer of gold..	117
Figure 6.2. Fit result from the ellipsometer for Tauc-Lorentz model for TiO_2 film.	119
Figure 6.3. Refractive index of the deposited TiO_2 extracted using the ellipsometer.	120

Figure 6.4. SEM images of the fabricated nanowires with (a) 400 nm pitch and 130 nm diameter, (b) 400 nm pitch and 150 nm diameter, (c) 450 nm pitch and 170 nm diameter and (d) 450 nm pitch and 230 nm diameter.	121
Figure 6.5a, b. Reflection spectra collected from the nanowire arrays with different diameters, for lattice spacings of 400 nm and 450 nm, respectively.	122
Figure 6.6a, b. The reflection spectra of the nanowire arrays with different diameters, for 400 nm and 450 nm lattice spacing, respectively. The spot size is 62.5 μm	123
Figure 6.7. Reflected colors from the nanowire arrays.	123
Figure 6.8. Reflected colors from the metallic nano-discs including Ti, gold and Al. Nanowires were not etched, yet. Each array is 100 μm \times 100 μm and there is a 300 nm TiO_2 film underneath.	124
Figure 6.9. Reflected colors from the TiO_2 arrays with a 100 nm length capped with 50 nm gold and 100 nm Al with (a) air surrounding, (b) surrounding index of 1.33 and (c) surrounding index of 1.39.	125
Figure 6.10. Reflected colors from the TiO_2 arrays with a 260 nm length capped with 50 nm gold and 100 nm Al with the air surrounding.	126
Figure 6.11a-c. Reflection spectra of the nanowire arrays with 350, 400 and 450 nm lattice spacings, respectively. The TiO_2 film is 40 nm, the nanowire length is 260 nm and nanowires are capped with 50 nm gold and 100 nm Al, with air as the surrounding.	127
Figure 6.12a-c. Reflection spectra of the nanowire arrays with 350, 400 and 450 nm lattice spacings, respectively. The TiO_2 film is 40 nm, the nanowire length is 260 nm and nanowires are capped with 50 nm gold and 100 nm Al, with 1.33 as the surrounding refractive index.	128
Figure 6.13a-d. Reflection spectra of the nanowire arrays with 350 nm pitch, for nanowire diameters of 170, 190, 210 and 230 nm, respectively. The surrounding refractive index was changing from 1.33 to 1.39. Further, the changes in the resonance wavelength versus the surrounding refractive index and the calculated sensitivity is shown within each figure.	130
Figure 6.14a-c. Reflection spectra of the nanowire arrays with 400 nm pitch, for nanowire diameters of 210, 230 and 250 nm, respectively. The surrounding refractive index was changing from 1.33 to 1.39. Further, the changes in the resonance wavelength versus the surrounding refractive index and the calculated sensitivity is shown within each figure.	131

Figure 6.15. Reflection spectra of the nanowire array with 450 nm pitch and 250 nm diameter, with different surrounding indices. Changes in the resonance wavelengths versus the refractive index is also shown. **132**

Figure 6.16a-c. Reflected colors from the nanowire arrays under an optical microscope with surrounding refractive indices of 1.33, 1.36 and 1.39, respectively. **133**

Figure 6.17a-d. Reflected colors from the nanowire arrays without the Al mask, under an optical microscope with surrounding refractive indices of 1 (air), 1.33, 1.36 and 1.39, respectively.... **134**

List of Tables

Table 3.1. Summary of the sensor’s variations studied in this experiment.	34
Table 3.2. Refractive index of the glass substrate at different optical wavelengths [80].	35
Table 3.3. Process Parameter Range for deposition of SiON using PECVD system.	37
Table 3.4. Process Parameters for deposition of SiN using PECVD system.	40
Table 4.1. Summary of the highest sensitivity values achieved for different designs	97
Table 4.2 Comparison of the previously fabricated self-referenced plasmonic sensors with this work.	98
Table 4.3 Resonance wavelengths of SPR, LSPR and local maximum for day 1 and 2.....	99
Table 5.1. Quantitative information of SLR resonance feature.....	109
Table 5.2. Simulated colors from different designs.	114
Table 6.1. Details of the recipe for the dry etching process of TiO ₂	118

Chapter 1

Introduction

Plasmonic was unknowingly used hundreds of years ago by Roman glassmakers for making colorful glass cups through the incorporation of nanometallic particles in between two glass planes [1]. Stained glass windows in European Cathedrals employed the same technique. Scientifically, the phenomena of surface plasmon polaritons (SPPs) were first observed by R. W. Wood [2] in 1902 while he was monitoring the spectrum of reflected light from a metallic grating. Almost a century after Wood's discovery, plasmonics has drawn a great deal of interest and has now become a vital part of nanophotonics with a wide range of applications, including chemical and environmental sensing, structural color generation, and bio-detection [3,4]. Plasmonic sensors provide a robust and label-free sensing platform that has immense potential to be used in a variety of fields, such as cancer detection, food safety, homeland security, etc., and has been recently used for rapid screening of COVID-19 [3]. Recent advancements in micro and nano fabrication techniques, which resulted in the precise fabrication of thin film and nanostructures, have led to remarkable progress in producing and utilizing plasmonic sensors for a variety of applications. Nowadays, plasmonic sensors exploiting both propagating and localized surface plasmons are capable of detecting analytes as small as a single molecule. Although plasmonic sensing technology now seems to be quite mature, there are several critical issues that current plasmonic sensors are suffering from and need to be addressed. In this chapter, we discuss the history of surface plasmons and will try to elaborate on how plasmonics can be helpful in building high-performance sensor technologies and artificial structural colors. Then, we will summarize some of the critical issues that current plasmonic sensors are facing and will try to provide a brief solution for them. At the end of the chapter, we explain our motivations and briefly discuss the structure of this thesis.

1.1 Bulk Plasmons

The optical properties of metals can be explained by the plasma model for a wide range of frequencies. In the plasma model, it is assumed that a gas of free electrons with n number of electrons per unit volume moves against a fixed background containing positive ion cores. One can write the simple motion equation of the plasma electrons in the presence of a time dependence electric field and derive the complex dielectric function of free electron gas as follows [4-8]:

$$\varepsilon(\omega) = 1 - \frac{\omega_p^2}{\omega^2 + i\gamma\omega} \quad (1.1)$$

$$\omega_p^2 = \frac{ne^2}{\varepsilon_0 m} \quad (1.2)$$

where ω_p is called the plasma frequency and γ is the collision frequency, which is, in fact, the inverse of electron relaxation time. Further, ε_0 is the vacuum permittivity, and m is the effective optical mass of electrons. It should be mentioned that in the plasma model, the effect of lattice potential and electron-electron interactions are not considered, and only some aspects of band structure are incorporated into the effective electron mass. In the loss-free limit, in which damping is negligible, γ is equal to zero, and equation (1.1) is simplified as follows [4-8]:

$$\varepsilon(\omega) = 1 - \frac{\omega_p^2}{\omega^2} \quad (1.3)$$

The equation (1.3) is the dielectric function of undamped free electron plasma. For plasma frequency, equation (1.3) yields to $\varepsilon(\omega) = 0$. Maxwell's equations can be employed to further understand the meaning of this. Maxwell's equations can be effectively used to understand the interactions of metals with electromagnetic fields. For the case of a plane wave in the form of $e^{i(K \cdot r - \omega t)}$ when there is no external source present, the Maxwell's Gauss Law equation $\nabla \cdot D = 0$ yields to [4-8]:

$$\varepsilon(\omega) K \cdot E = 0 \quad (1.4)$$

Where K is the wavenumber, and E is the electric field. There are two solutions for equation (1.4) as follows:

$$K \cdot E = 0 \quad (1.5)$$

$$\varepsilon(\omega) = 0 \quad (1.6)$$

The first solution corresponds to a transverse wave, while the second solution corresponds to a purely longitudinal mode. Thus, according to equation (1.3), at plasma frequency, a pure longitudinal mode exists in metals that corresponds to longitudinal collective oscillations of the electrons. The plasma

frequency can be assumed as the natural frequency of a free oscillation of the metal electrons. The quanta of this charge oscillation are called bulk plasmons or volume plasmons [4-8].

In conclusion, based on equation (1.3), for frequencies lower than plasma frequency, the real part of the dielectric function of metal would be negative. In this situation, electrons will oscillate 180 degrees out of phase with the incident wave. This causes a strong reflection. If the light has a frequency higher than the plasma frequency, which would normally be in the ultraviolet range for noble metals, the real part of the dielectric constant of metals would be positive. In this situation, electrons cannot respond quickly to the driving force of the incident field. Thus, the electrons will not oscillate with the incident light, and light will be absorbed or transmitted in the interband transitions [4-8].

The effect of bulk plasmon was first observed by Ruthemann [9] while he was bombarding thin metal films with fast electrons. By monitoring the energies of un-deflected electrons, unexpected peaks at 16 eV intervals were observed. This phenomenon was explained later by realizing that long-range Coulomb interactions of valence electrons in the metal films lead to longitudinal oscillations of the collective excitations of the electron density. Due to the similarity of the phenomenon with the electronic plasma oscillation in discharged gas, the word plasmon was used for the excitations [4-8].

At the end of this section, we should mention that the simple plasma model for describing plasmonic phenomena has limitations, especially in the case of noble metals such as gold and silver. For noble metals, an extension to the plasma model is needed, especially for regions with frequencies higher than plasma frequency where interband transitions cause an enhancement in absorption. To mitigate this limitation, the classical Drude model for the AC conductivity of metals can be linked to the simple plasma model [4-8]. A huge advantage of the Drude model is that it can be easily incorporated into time-domain-based numerical solvers for Maxwell's equations. To further improve the model, the effect of restoring forces is taken into account, and a new model is developed, which is referred to as the Drude-Lorentz model [4-8].

1.2 Surface Plasmon Polaritons (SPPs)

Surface electromagnetic waves (SEWs) are a specific type of electromagnetic waves that are bound to the interface of two dissimilar media and contain evanescent electric fields such that their magnitude decays away from the interface. By solving Maxwell's equations for such interfaces, it can be seen that for non-magnetic media, only a p-polarized surface wave can exist. Further, for the mode to be bound to the surface, the normal component of the wavevector needs to be imaginary, which requires the two

media to have real permittivity values with opposite signs. Noble metals such as gold and silver have negative permittivity in frequencies below the plasma frequency. Thus, an interface containing noble metals and a dielectric can support a specific form of surface electromagnetic waves called surface plasmon polaritons (SPPs). An electromagnetic wave that propagates along the planar interface of a dielectric and a metal is the simplest form of SPPs. Such a wave decays exponentially into each media when the distance increases from the interface. By solving Maxwell's equations with corresponding boundary conditions, one can see that only a transverse magnetic (TM) wave can excite surface plasmons on the interface between the metallic and dielectric material. This means that the electric field must have a normal component to the surface [4-8].

As discussed earlier, volume plasmons are the longitudinal oscillations of the collective excitations of the charge density at the plasma frequency of the metal. Surface plasmons are another type of collective excitation of the electron density at a reduced frequency $\omega_p/\sqrt{2}$, which only exists at the surface of two media. Polaritons are referred to quasi-particles formed from the coupling of the electromagnetic fields with a fundamental excitation of the system. Here, the fundamental excitation of the system is surface plasmon, and thus the related quasi-particle is called surface plasmon polaritons (SPPs) [4-8].

1.3 Surface Plasmon Resonance (SPR)

The general charge density oscillations induced by photons in the interface of two media with opposite permittivity signs is called surface plasmon resonance (SPR). Basically, SPR is the resonances caused by propagating types of SPPs. By solving Maxwell's equations for a metal-dielectric interface and applying the boundary conditions, the wave number of SPP propagating in the x direction can be obtained as follows [4-8]:

$$k_x = \frac{\omega}{c} \cdot \sqrt{\frac{\epsilon_1 \cdot \epsilon_2}{\epsilon_1 + \epsilon_2}} \quad (1.7)$$

In the above equation, ω is the angular frequency of the incident light, c is the speed of light, and ϵ_1 ϵ_2 are the real permittivity of metal and dielectric, respectively. We can also write down the SPP wave vector, normal to the interface in the i^{th} medium ($i = 1, 2$), as follows [4-8]:

$$\begin{aligned}
k_{zi} &= \left[\varepsilon_i \frac{\omega^2}{c^2} - k_x^2 \right]^{\frac{1}{2}} \\
&= \frac{\omega}{c} \left[\frac{\varepsilon_i^2}{\varepsilon_1 + \varepsilon_2} \right]^{\frac{1}{2}}
\end{aligned} \tag{1.8}$$

If the k_{zi} is purely imaginary and positive, then the amplitude of the SPP wave will have a form of $\exp(-k_{zi}|z|)$, and the wave will decay exponentially by increasing the distance from the interface. This condition can be met if $\varepsilon_1 + \varepsilon_2$ it becomes a negative number. This can happen at the interface of a noble metal and dielectric around the plasma frequency. However, the dielectric constant of a real metal is a complex number, and thus both k_x and k_{zi} will be complex. As a result, the SPP wave will also decay along the direction of the propagation (which is x here). Further, the imaginary part of k_{zi} needs to be positive to insure the confinement of the wave in the z direction [4-8].

One can understand from the wave number of SPP in equation (1.7) that SPRs cannot be excited directly by the incident light as the free space wave number $k_0 = \frac{\omega}{c} \varepsilon_1^{\frac{1}{2}}$ is smaller than that of SPPs. This momentum mismatch can be solved by using prism coupling, diffractive grating coupling, or wave coupling through optical waveguides or fiber. When a grating is employed, both TM and TE modes can excite the SPPs [4-8].

1.4 Localized Surface Plasmon Resonance (LSPR)

Localizing SPPs in the nanoparticles or nanostructures with sub-wavelength feature sizes can lead to another type of collective excitation called Localized Surface Plasmon Resonance (LSPR). Since the geometry of the nanostructure supports the additional momentum, LSPR can be excited directly by the incident light, simplifying the set up for exciting the surface plasmons. Further, confining the collective oscillations of electrons in nanostructures can intensify the local electromagnetic field and make it several orders of magnitude stronger than the primary incident field. The shape, location, and intensity of the LSPR mode depend on the geometry and dimension of the nanostructures and surrounding refractive index.

Understanding the optical properties of these nanoparticles and nanostructures is crucial for designing devices and materials. Mie theory can be used to predict LSPR modes in metallic nanoparticles. Mie theory, often referred to as Mie scattering theory, is a mathematical framework used to describe the scattering of electromagnetic waves by spherical particles. Mie theory provides a mathematical framework for understanding how plasmonic nanoparticles interact with incident light, leading to the calculation of scattering and absorption properties. It provides an intuitive understanding of the design and optimization of plasmonic nanoparticles for various applications in nanotechnology and photonics. Let us consider a spherical nanoparticle with a radius a embedded in a surrounding medium with refractive index n_1 . The nanoparticle itself has a refractive index n_2 . When light of wavelength λ is incident upon this particle, according to the Mie theory, the scattering cross-section can be calculated as follows [4-8]:

$$\sigma_S = \frac{2\pi}{k^2} \sum_{n=1}^{\infty} (2n+1) [|a_n|^2 + |b_n|^2] \quad (1.9)$$

Where $k = \frac{2\pi}{\lambda} n_1$ is the wavenumber in the surrounding medium and, a_n and b_n are the Mie coefficients that depend on the size of the particle, the refractive indices, and the polarization of the incident light. The scattering cross-section represents the fraction of incident power that is scattered in all directions. Further, the absorption cross-section, which represents the fraction of incident power that is absorbed by the nanoparticle, can be calculated as follows [4-8]:

$$\sigma_a = \frac{2\pi}{k^2} \sum_{n=1}^{\infty} (2n+1) |a_n|^2 \quad (1.10)$$

The absorption cross-section is particularly important in plasmonics because it quantifies the energy absorbed by the nanoparticle's plasmonic resonances. The Mie coefficients can be computed by solving a system of recursive equations based on the size parameter (x) and the refractive indices. The size parameter is defined as [4-8]:

$$x = \frac{2\pi}{\lambda} n_2 a \quad (1.11)$$

Solving for a_n and b_n involves a series of equations known as the Mie coefficients equations, which depend on the type of polarization (e.g., transverse electric (TE) or transverse magnetic (TM)). Mie's theory reveals that when the particle size is on the order of the wavelength of the incident light, resonance effects can occur where the light gets guided along the surface due to the excitation of whispering gallery modes. These are called Mie resonances. Further, Particles with higher refractive

indices generally scatter more light than those with lower refractive indices. A change in refractive index can shift the Mie resonance peaks and affect the scattering and absorption spectra.

In summary, Mie's theory provides a mathematical framework for understanding how plasmonic nanoparticles interact with incident light, leading to the calculation of scattering and absorption properties. It plays a critical role in the design and optimization of plasmonic nanoparticles for various applications in nanotechnology and photonics.

1.5 Plasmonic Sensing

Resonance conditions of both SPR and LSPR modes depend on the dielectric medium surrounding the metal. Once the surrounding medium is changed or a target analyte is bound onto the metal, the resonance conditions of both SPR and LSPR modes change. This property is the fundamentals of plasmonic sensing. In refractive index sensors, sensitivity is defined as [4-8]:

$$S = \frac{\Delta\lambda}{\Delta n} \quad (1.11)$$

in which λ is the wavelength of SPP excitation, and n is the refractive index. Once the local refractive index is changed, the resonance wavelength of SPPs will change based on the Drude model, and thus, the sensitivity can be measured. To better evaluate the performance of SPP-based sensors, figure of merit (FOM) can be employed to express both the sensitivity and linewidth of the resonance peak as follows:

$$FOM = \frac{S}{FWHM} \quad (1.12)$$

FWHM is the full width at half maximum linewidth. Thus, the sharper the resonance peak, the higher the FOM. Improving both sensitivity and FOM is the main goal in designing plasmonic sensors.

1.6 Plasmonic Structural Colors and Colorimetric Sensors

Artificial structural colors, made from nanostructures, have drawn a considerable amount of interest due to their potential applications in color filters, imaging, and high-resolution display technology [10]. Among all the diverse types of nanostructures, sub-wavelength plasmonic arrays attracted even more interest due to their ability to produce high-resolution colors and tunability in color generation [11]. As discussed, the location and shape of the LSPR and SPR modes are highly dependent on the shape,

composite materials, and geometrical parameters of the nanostructures. Accordingly, absorption peaks due to LSPR and SPR modes can happen in the ultraviolet-visible-near infrared range. One can design the metallic nanostructure in a way that absorption enhancement happens in the visible range. Thus, vivid colors can be generated using the plasmonic nanostructures. Since the shape and location of the SPR and LSPR modes are dependent on the geometrical dimensions of the nanostructure, by tuning the dimensions of the nanostructures, a wide range of colors can be generated.

There is a considerable need for portable sensor technologies which are low-cost, lightweight, and simple to use. Plasmonic structural colors can be effectively used to make low-cost colorimetric sensors [12]. In plasmonic structural color generators, SPR and LSPR modes are in the visible range. Any change in the surrounding refractive index will change the excitation properties of surface plasmons and thus alter the location and shape of SPR and LSPR resonance features. As a result, reflected and transmitted colors from the nanostructure will change due to the change in the surrounding medium. If the changes in the colors are big enough, it can be detected by the naked eye and thus make the readout of the sensor very simple and low-cost. In the previous works, the color generation has been done by removing some wavelengths from the reflected spectra. These are the wavelengths where LSPR modes are excited and are thus absorbed within the plasmonic structure. As such, color changes are not very predictable or linear. Alternatively, it was also shown through diffraction in nanowire arrays that if we can have single-peaked reflections, the color changes become linear with refractive index changes [13]. So, a question naturally arises whether we can achieve single-peaked plasmonic structures since plasmonic peaks have the highest sensitivity to both bulk and surface sensing.

1.7 Nanowires Integration with Plasmonics

Nanowires (NWs) are one-dimensional nanostructures with typical lengths on the order of microns and diameters on the order of tens to several hundred nanometers. By introducing a new class of materials, NWs can overcome the limitations of conventional bulk or thin film devices. Based on their chemical composition and electronic properties, nanowires can be divided into metallic, dielectric and semiconductor nanowires. Although each type of nanowire has various applications, metallic and metallic - dielectric nanowires, through exploiting surface plasmon polariton, have shown great potential for realizing plasmonic-photonic waveguides. Metallic nanowires can confine the light at the surface in a few nanometers and propagate the light with surface plasmon polaritons and thus overcome the diffraction limits that dielectric nanowires face. However, high surface loss of plasmonic

transmission limits the performance of subwavelength optical waveguides made of metallic NW arrays. Accordingly, by optical coupling between metallic and dielectric nanowires, photonic-plasmonic hybrid waveguides have shown high performance with a relatively lower transmission loss [14, 15].

Integration of NW arrays with plasmonics resulted in high-performance hybrid photonic-plasmonic waveguides. However, there are few works discussing the sensitivity properties of such hybrid structures, and the recent works are rather associated with complicated structures [16] that are not suitable for low-cost sensing applications. There are numerous benefits while integrating NW arrays with plasmonics for sensing applications. Firstly, the fabrication techniques of NW arrays are now quite mature, and thus, precise, flexible, and tunable fabrication is possible, which ensures the desirable optical properties. Further, the highly sensitive nature of plasmonic nanostructures can improve the performance of current NW-based sensors. Last but not least, coupling the optical modes of NW arrays with plasmonic modes can lead to Fano resonances and, thus, sharp resonance features, which is essential for high-quality sensors.

1.7.1 Optical Modes in Nanowire Arrays

When nanowire arrays are placed in a periodic lattice, several types of optical modes can get excited within a nanowire array. Further, a single nanowire in an array can interact with neighboring nanowires through near-field coupling. This creates wavelength-dependent funneling of light into the nanowire. Also, for larger diameters, Fabry-Perot (F-P) modes can get excited in nanowire arrays where nanowires act like a cavity. Moreover, nanowires can confine the light in wavelengths comparable to their diameters, which leads to the excitation of the bound modes or leaky modes, depending on the cut-off conditions. To integrate nanowires with plasmonic, it is crucial to understand and predict the optical modes in nanowire arrays. Understanding these modes is possible through analyzing the nanowire arrays using Maxwell's equations and mathematical tools. In this section, we will briefly discuss each mode, which will help us later in understanding the excited modes within our proposed structures [17].

1.7.1.1 Hybrid Modes

Modal excitation within cylindrical waveguides is primarily driven by the phenomenon of total internal reflections along the cylinder's periphery, following a helical path. Consequently, in cylindrical waveguides, it's challenging to completely eliminate the z-component of the electric and magnetic fields. As a result, radial modes are denoted as hybrid HE and EH modes. This characteristic is

particularly prominent in semiconductor nanowires, where there exists a substantial refractive index difference. Moreover, due to the small dimensions of nanowires, the resonant modes within them tend to exhibit leakage and more effective interactions with the external environment, sometimes even coupling with one another [17].

Solving Helmholtz's wave equation in cylindrical coordinates for nanowires gives the electric and magnetic field relations in z direction. Then, r and ϕ components can be derived from Maxwell's equations using z component. The modified Bessel function of the second kind (K_p) describes the guided modes outside the nanowires, and the expression for the electric field is [17]:

$$E_z(r, t) = C_{core} K_p(mr) e^{j(\omega t + q\phi - \beta z)} \quad (1.13)$$

$$E_z(r, t) = C_{air} K_p(lr) e^{j(\omega t + q\phi - \beta z)} \quad (1.14)$$

Where C_{core} and C_{air} are constants and can be eliminated using the boundary conditions. q is the azimuthal component, and $m^2 = n_{core}^2 k_0^2 - \beta^2$, in which n_{core} is the refractive index of the material. On the other hand, Hankel function (H_p) physically describes the leaky modes [17]:

$$E_z(r, t) = C_{air} H_p(lr) e^{j(\omega t + q\phi - \beta z)} \quad (1.15)$$

Magnetic field expressions can be derived similarly.

1.7.1.2 Photonic Crystal Modes

Because of the well-organized arrangement of nanowires, alterations in their absorption properties can occur as a result of the presence of photonic crystal modes. These modes arise from the excitation of Bloch modes, a consequence of the periodic symmetry of the nanowires. They can be considered analogous to the perturbation of energy levels of atoms in crystals compared to the energy levels of individual atoms. Photonic crystal modes can enhance the absorption in nanowire arrays and further increase the quality factor of the resonance features [18].

1.7.1.3 Fabry-Perot Modes

Fabry-Perot modes in nanowire arrays represent an optical phenomenon that occurs within periodic arrays of nanoscale cylindrical structures. These arrays act as a collective Fabry-Perot resonator, where longitudinal interfaces of the nanowires act as high-quality mirrors, reflecting and transmitting light. The resonance conditions are defined by the array's periodicity, the nanowire diameter, and the

surrounding medium's refractive index. These modes lead to unique optical properties, such as spectral filtering and enhancement, making nanowire arrays valuable in applications like photonic crystals, optical sensors, and metamaterials. Harnessing these Fabry-Perot modes allows for precise control over light-matter interactions at the nanoscale, paving the way for innovative devices and systems in nanophotonics and beyond.

1.8 Current Issues with Plasmonic Sensors

Recent advancements in nano and micro fabrication techniques have enabled the possibility of the production of high-performance, highly sensitive, and high-efficient plasmonic sensors. These sensors have been employed in a wide range of applications and are showing promising potential to be the solution to many challenges in the future. Although the technology of plasmonic sensors seems to be mature enough, there are several issues that plasmonic sensors are facing now, which have limited their practical applications. The next generation of plasmonic sensors needs to be able to provide satisfactory sensing performance while mitigating these problems. In this section, we will name some of the important issues with the current plasmonic sensors and will try to provide a solution for each issue.

1.8.1 Inaccuracy in Unstable Environments

Plasmonic and structural color sensors are highly desirable for detecting the analyte concentrations in gas and liquid, and they play a significant role in the areas of food safety, healthcare, biomedical diagnosis, and environmental monitoring [19-22]. Further, the high sensitivity and decent figure of merit of the current plasmonic sensors make them unique in the area of sensing. However, in practice, they are often vulnerable to changes in the local environmental factors due to their high sensitivity. For instance, variations in the temperature, humidity, and vibration of the environment can influence the shape and location of SPR and LSPR modes and cause errors in the measurements. Further, in practical applications, light intensity fluctuations can manipulate the optical response of the surface plasmons and significantly reduce the accuracy of the measurements. Thus, current plasmonic sensors are only limited to those applications that are less involved with environmental variations. The next generation of plasmonic and structural color sensors need to be immune to environmental variations and should be able to provide accurate results under complicated and unstable environments. Such a sensor should have the ability of multi-parameter sensing and self-correcting. In one word, the sensor should be “self-referenced”.

1.8.2 Expensive and Bulky Readout Technology

Another issue with the current plasmonic sensors is the bulky and expensive spectroscopic laboratory instrumentation required for the sensor readout. As discussed earlier, depending on the shape, size, composite materials, and local refractive index of the nanostructure, absorption enhancement due to the surface plasmon resonance can happen in the UV to NIR range. Any changes in the local refractive index lead to a shift in the resonance wavelength of the surface plasmons. Monitoring the shift in the wavelength of the plasmon resonance can be done using spectroscopic instrumentations. In fact, in many biological, chemical, and medical sensing applications in which plasmonic sensors are being used, sensor readout is being done using spectroscopic equipment, which usually consists of a broadband light source, bulky lenses, and photodetectors. Although spectroscopic readout is quite accurate, it makes the sensor bulky and expensive and thus limits the applications of plasmonic sensors. Future plasmonic sensors need to be robust, low-cost, and lightweight. To this end, one can design the nanostructure and its composite materials in a way that the plasmonic absorption enhancement happens in the visible spectrum. This condition is normally met in the nanostructures containing gold and silver. In this situation, any change in the local refractive index will change the resonance conditions of surface plasmons and, thus, the location and shape of SPR and LSPR modes in the visible spectrum. Accordingly, reflected and transmitted color from the nanostructure is expected to change once the local refractive index is changed. This feature of plasmonic sensors has enabled a new platform for developing plasmonic colorimetric sensors. These types of sensors are promising candidates for the future low-cost and lightweight sensors. If the color changing due to the binding analyte is large enough, the sensor can be read out by the eye. However, to further extend the applications of the sensor, a smartphone camera can be employed for image acquisition and analysis. Even if the changes in the color are not big enough for a simple readout by the eye, the entire sensing and readout setup would be much less complicated when working in the visible spectrum.

1.8.3 The High Cost Associated with Complicated Geometry

The geometry and material composition of the nanostructure can greatly influence the excitation conditions and sensitivity of the plasmonic sensors. To achieve extremely sensitive plasmonic sensors with narrow resonance features (high FOM), various types of nanostructures with complicated geometries have been developed. Although, in many reports, extremely high sensitivity (10^5 nm/RIU) and figure of merit (10^5 /RIU) have been achieved [23, 24], there are high fabrication costs due to the

complicated geometries of these nanostructures. Thus, high fabrication costs can be another limiting factor for future plasmonic sensors. To minimize the fabrication costs of plasmonic sensors, easy-to-fabricate geometries need to be proposed while the performance remains satisfactory.

1.9 Motivations and Structure of the Thesis

Although plasmonics has shown enormous potential for providing low-cost, portable, high-performance, and accurate sensing technology, it is still suffering from several important issues that need to be mitigated in the next generation of plasmonic sensors. In this thesis, we design, fabricate, and characterize several easy-to-fabricate plasmonic sensors and structural colors that have the ability of self-referencing and, at the same time, can provide satisfactory performance in case of sensing and figure of merit. Self-referencing of a sensor is defined as the ability of that sensor to correct the errors generated by changes in environmental factors or experimental issues by measuring a reference within the same measurement. A good example of self-referencing sensors is pulse oximeters, which measure the transmission in the presence of pulse and not of blood pulse and in its absence. This way, it is able to correct skin color, different sizes of fingers, and different muscle properties among different human beings. Thus, self-referencing provides one of the most accurate ways of measuring an unknown. We propose and demonstrate such a self-referencing sensor. We believe that the fabricated sensors are cost-effective and can provide a platform for high-performance plasmonic sensing under unstable environmental conditions.

In chapter two, we will propose and evaluate two simple-to-fabricate plasmonic sensors based on gold nanostructures with self-referencing capability that can show high-performance properties for biochemical sensing. The structures are numerically simulated using finite difference time domain (FDTD) and rigorous coupled wave analysis (RCWA) methods, the effects of possible variations in the structures during the fabrication are discussed, and the performance of the sensors is predicted. In chapter three, we will discuss the fabrication details of the self-referencing plasmonic sensors based on the gold nanostructures. During the fabrication process, different structural variations were considered to achieve the optimal design, which provides high-performance sensing and self-referencing capabilities. In Chapter 4, we will characterize the fabricated self-referencing sensors and experimentally evaluate their sensing performance. In addition, we will compare the performance of the different structures and further investigate the color-sensing performance of the sensors. In Chapter 5, we will propose and evaluate a hybrid plasmonic-nanowire structure that is able to produce high

quality-factor resonance features and has potential application in structural color generation and sensing. The structure is based on titanium dioxide nanowires capped with a layer of gold, which is able to match the plasmonic modes with the optical modes in nanowires and thus generate high quality factor resonance features. The structure will be evaluated by FDTD and RCWA simulations, and different variations of the design will be simulated in order to understand the performance of the structure. In chapter six we will provide the fabrication and characterization details of the hybrid nanowire-plasmonic structure and will evaluate the performance of the nanowires in terms of different color generations. Further, the sensing performance of the structure will be experimentally evaluated. In Chapter 7, a summary and conclusion of this work will be presented, along with suggestions and recommendations for future works.

Chapter 2

Self-Referencing Plasmonic Array Sensors

As discussed in the previous chapter, next generation of plasmonic sensors need to be immune to the environmental variations and they should provide accurate results under unstable conditions. In addition, the design of the sensors must be simple, so the fabrication costs are minimized. Further, sensor must operate in the visible range and also provide high Q resonance features, so the high performance and low-cost readout is ensured. Accordingly, in this chapter a new self-referencing plasmonic platform is proposed and analyzed. By introducing a thin gold layer below a periodic two-dimensional nano-grating, the structure supports multiple modes including localized surface plasmon resonance (LSPR), surface plasmon resonance (SPR), and Fabry-Perot resonances. These modes get coupled to each other creating multiple Fano resonances. A coupled mode between the LSPR and SPR responses is spatially separated from the sensor surface and is not sensitive to refractive index changes in the surrounding materials or surface attachments. This mode can be used for self-referencing the measurements. In contrast, the LSPR dominant mode shifts in wavelength when the refractive index of the surrounding medium is changed. The proposed structure is easy to fabricate using conventional lithography and electron beam deposition methods. A bulk sensitivity of 429 nm/RIU is achieved. The sensor also has the ability to detect nanometer thick surface attachments on the top of the grating. We demonstrate that the sensor can also detect nanometer thick surface attachments on the top of the grating.

2.1 Introduction

Over the last decade, surface plasmonic sensors have been demonstrated in the area of biochemical sensing [25], medical diagnostics [26], environmental monitoring [27], food safety [28], water testing [29], and homeland security [30]. In recent years, periodic metallic structures have been used to generate Fano resonances resulting from the interference between the plasmonic mode and broad optical modes [31–34]. This results in narrowing of the resonance, increasing the quality factor (Q), and increasing the wavelength shift due to refractive index change, thereby increasing the sensitivity of the sensors [34–36]. Periodic nanostructures like split-ring resonators [37], ring nanocavities [38], disc nanocavities [39], nanoclusters [40], and crescents [41] allow for the excitation of localized surface plasmons. Sensitivities of up to 725 nm/ RIU have been realized in these structures [42], and surface

attachment of nanometer-scale layers can be detected making these sensors very promising in sensing-related applications [43]. A figure of merit (FOM) defined as sensitivity (S) divided by the spectral linewidth ($\Delta\lambda$) has been used to compare different structures [44]. Using Fano resonances, the FOM of 72/RIU has been demonstrated [39]. In a previous work, a plasmonic sensor was demonstrated which also created vivid structural colors [45]. The colors changed as the refractive index of the surrounding medium changed, and detection could be achieved by using a simple camera. The structure employed a two-dimensional periodic structure on top of a conducting layer creating a Fano resonance between the localized surface plasmon resonance (LSPR) and Fabry Perot modes. Similar structural color sensors were also demonstrated using nano-cups fabricated on a plastic substrate [46]. Such sensors provide a promise of bringing low-cost applications to the fore.

However, an issue with surface plasmon sensors is their sensitivity to environmental changes like temperature, fluid fluctuations, humidity, and fluctuations in the intensity of the incident light. In many applications, the sensing chip has to be placed far away from the light source and the detection system [47, 48], and due to the long distance required for light propagation, the light intensity fluctuates as a result of thermal variations along the path. Thus, the detection accuracy which is done through measurement of wavelength, angle, or intensity of light suffers. Highly successful commercial optical sensors like oximeters use a self-referencing measurement [49]. If one can add another resonance peak in the surface plasmonic sensor which does not change in the presence of the detectants, then that peak can be used to self-reference the detection. Such self-referencing has been demonstrated in optical fiber sensors [50, 51] and photonic bandgap sensors [52].

However, there are only a few reports for self-referenced plasmonic sensors [34, 53–57]. Zhang et al. demonstrated a structure by placing a one-dimensional plasmonic grating on top of a thin metallic layer [53]. While they only investigated the structure numerically for high Q nature due to excitation of Fano resonances, two resonance peaks were observed, and the structure can in principle be used for self-referencing. However, both the resonances shifted with changing the refractive index of the surrounding medium but at different rates. Chen [58] proposed and simulated a double Fano resonance structure using different cavity modes in a metallic waveguide resonator. The structure is difficult to fabricate and couple light into and thus is not appropriate for low-cost applications. A similar structure was demonstrated in [55] where self-referencing was achieved using extraordinary transmission from metallic one-dimensional gratings operating at longer wavelengths. Further, the quality factor of the peaks was not high, partly due to the fabrication variations in the one-dimensional slits. In another

recent work, the first experimental demonstration of a self-referenced plasmonic sensor was done using a one-dimensional metallic grating which guides multiple transverse modes [34]. This resulted in two surface plasmon resonances (SPR) being supported in the structure, one at the top of the grating surface and the other at the bottom of the surface. Since the bottom SPR is not coupled to the detectant, its wavelength shifts minimally when the refractive index of the surrounding material changes. The sensitivity of 470 nm/RIU and FOM of 31/RIU was achieved using the top SPR. While easier to fabricate than previous structures, the self-referencing peak is not very well defined and difficult to isolate in the spectrum which will limit the accuracy of the self-referencing measurement. In another work [56], dielectric grating on top of a silver thin film was proposed and numerically analyzed. The structure supported an LSPR peak at ~ 1550 nm and long-range plasmonic peak at ~ 1464 nm. In bulk sensing, the peak at 1550 nm changed at a rate of 490 nm/RIU, and the peak at 1464 nm shifted at a rate of 20 nm/RIU. However, light sources and spectrometers in this wavelength band are expensive making the sensor not suitable for low-cost applications.

In this chapter, we propose and numerically evaluate a structure consisting of a periodic nano-plasmonic grating on top of a metallic plasmonic thin-film sandwiched in between a dielectric. The proposed structure is very easy to fabricate with the smallest feature sizes larger than 200 nm while creating very well-defined high Q peaks. The structure supports LSPR modes within the grating, Fabry-Perot modes within the dielectric layer and LSPR-SPR coupled modes within the thin film. This allows a designer to control many parameters allowing optimization of the structure for different applications very easily. We optimize the structure for sensing in water like mediums and achieve a sensitivity of 429 nm/RIU and FOM of 8 /RIU using the LSPR mode resonances. LSPR-SPR coupled mode resonance does not shift at all as the refractive index of the surrounding medium changes and thus, this resonance can be used for self-referencing. Further, The LSPR-SPR coupled-mode has a very high Q of 143 making it very suitable for a self-referencing peak. To our knowledge, this is the first report of high Q mode which is isolated from the top of the sensor and hence, its resonance does not change when the analyte changes. We also show that the sensor is sensitive enough to detect a 1 nm layer of surface attachment on the top surface of the detector. The chapter is organized as follows. In the next section, we discuss the proposed design and analyze the different optical modes supported in the structure. We then discuss how the resonance peaks are excited when different geometrical parameters are changed. Finally, the sensitivity of the sensor for both bulk and surface sensing applications is analyzed.

2.2 Proposed Design

The proposed self-referenced Plasmonic sensor is schematically shown in **Figure 2.1**. The device consists of a two-dimensional periodic grating structure placed on a dielectric spacer layer. Further, both these layers are placed on a thin metallic film that can support an SPR mode. For the design in this paper, gold is being considered as a metallic film due to strong polaritons which can be excited [59,60] in it, its stable nature over time [61], and its ease of deposition through electron beam evaporators. The structure is designed on a low-cost glass substrate. This provides enough refractive index contrast for exciting the SPR modes in the gold layer. **Figure 2.1.b, c** shows the three-dimensional view of the sensor. A primary design criterion considered was the ability to easily fabricate the device and thus, a cube nanostructure and a cylinder nanostructure geometry were considered. Both these shapes can be very easily fabricated with projection lithography [62], ultra-violet lithography [63], and electron beam lithography [64]. The two-dimensional grating is also easier to fabricate than one-dimensional grating because of the difficulty to make long narrow lines as straight as possible. The two-dimensional grating will also be polarization independent. Of the two shapes studied, the cylindrical shape is the easiest to fabricate because of the lack of sharp corners. The proposed structure allows the excitation of LSPR in the top dimensional grating, LSPR in the interface between the gold nano-grating and the dielectric spacer, SPR in the thin film surrounded by the spacer layer and the substrate, and Fabry-Perot modes between the two gold layers in the spacer layer. In the composite structure, these modes may couple with each other and hence, create multiple Fano resonances.

The various parameters which are important in the design include the nanostructure width and height; dielectric refractive index and height, and thin-film thickness. By changing these parameters, the excitation and coupling of the modes can be controlled based on the application. Thus, the structure gives many degrees of freedom to the designer to optimize the performance. The structure can be designed to have at least two peaks in the absorption spectra and correspondingly two anti-peaks in the reflection spectra. These resonances should happen in the resonance frequencies of LSPR's and SPR's modes. A design is developed where one resonance frequency is extremely sensitive to the variations of the surrounding material and another resonance frequency is completely insensitive to the changes in the surrounding material. Thus, the structure can allow for self-referencing the measurements.

Similar structures have been proposed to increase the sensitivity and Q of the resonance mode. For example, in [57], gold nano-discs were placed on a gold film with a silicon dioxide spacer between

them. The structure excited various modes including propagating surface plasmon, localized surface plasmon, and cavity modes. However, the resonances at all these wavelengths shifted with bulk refractive index change and hence, the structure is not suitable for self-referencing. The goal of the work was to increase the sensitivity of the structure without any self-referencing considerations.

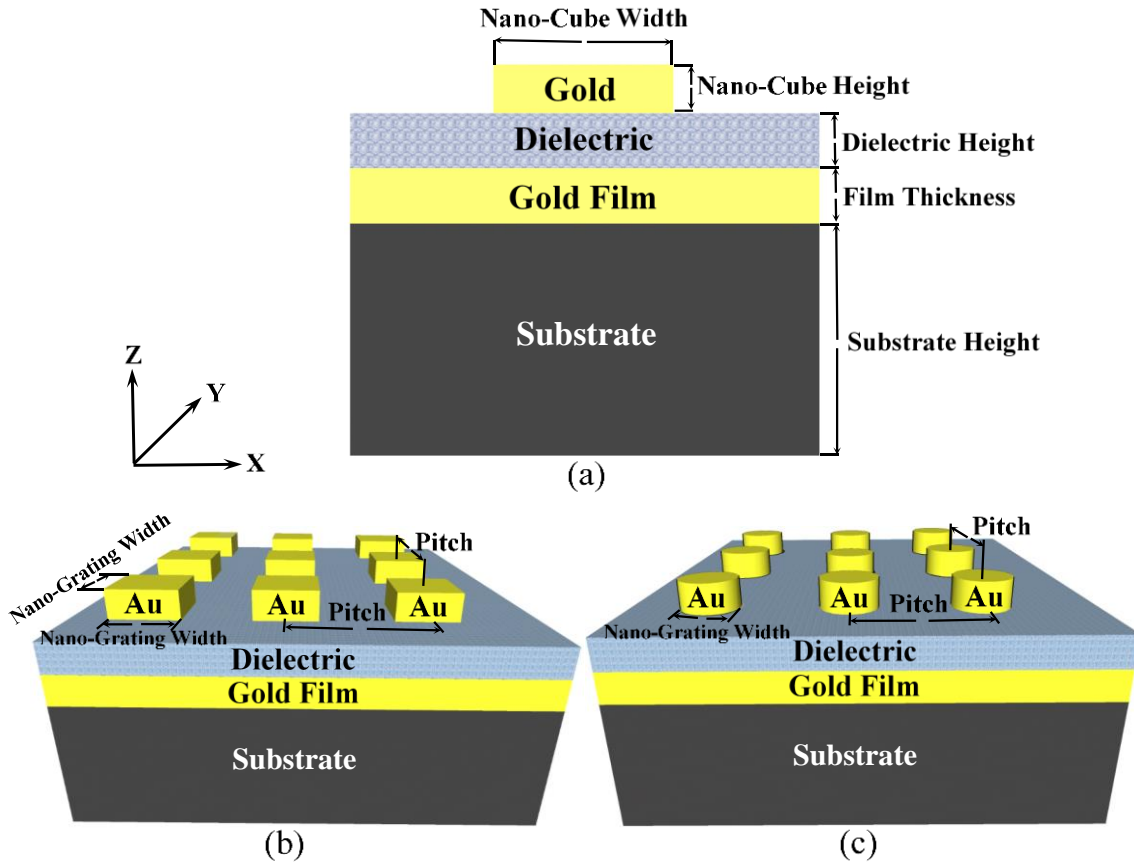


Figure 2.1. Schematic diagram of the proposed structure, (a) the longitudinal cut view of the structure, (b) three-dimensional view of the nano-grating structure with cubic geometry and (c) three-dimensional view of the nano-grating structure with cylindrical geometry

To understand the various optical modes which are excited and the resonances which are created, the structure was simulated using Rigorous Coupled Wave Analysis [65] method using commercial software [66]. Dielectric properties of gold were extracted from the experimental data in [67]. The structure was simulated in three dimensions and to account for its periodic nature, periodic boundary conditions were used in the transverse plane to create a cell containing one gold nanostructure. The incident light on the gold nano-grating is assumed to be a plane wave incident on the structure normally.

Convergence studies were done on the number of harmonics used in the simulation and 12 harmonics were chosen. Further, some of the sample results were verified using simulations with finite difference time domain method to ensure accuracy.

The structure was optimized to sense changes in the refractive index when the surrounding medium is water. Design criteria was to create well defined resonance peaks with high Q. Once optimized, it was observed that this design criterion also had the highest sensitivity. Such a sensor would have applications in biochemical sensing because the surrounding refractive index is nearly that of water [25]. Given these design considerations, for the cube nano-grating, the optimized design has a nano-grating height, dielectric height, and gold film thickness all equal to 40 nm. Nano-grating width and pitch are set to 200 nm and 400 nm, respectively. Furthermore, the refractive index of the dielectric layer is 1.8 (at 630 nm wavelength) and water is considered as the surrounding material ($n=1.33$ at 630 nm wavelength). The refractive index of the spacer layer played a very important role in isolating the self-referencing peak of the sensor from the surface. Silicon oxy-nitride (SiON) as a dielectric material can achieve a refractive index of 1.8 (while having very low loss) by changing the concentration of oxygen and nitride during the deposition and have been used for photonic circuits previously [68-70]. SiON is very easy to grow with plasma-enhanced chemical vapor deposition (PECVD). Absorption and reflection spectra of the optimized structure with cubes as nano gratings are shown in **Figure 2.2a**. There are three peaks in the absorption spectra of the structure at wavelengths of 637 nm, 757 nm, and 945 nm. In order to analyze and understand the reason for absorption enhancement of light in these wavelengths, the distributions of the magnetic field, $|H|$, were calculated and are shown in **Figure 2.2b-d**, respectively. As seen in **Figure 2.2b**, at a wavelength of 637 nm, the majority of the light field is concentrated in the center of the dielectric layer. This peak results from a Fabry-Perot mode in the structure where the top and bottom gold layers are acting as two mirrors. The Fabry-Perot mode also creates a cavity-enhanced LSPR on the bottom part of the nano-grating and an SPR mode on the top part of the thin film. Most of the field is concentrated within the structure, and thus, high sensitivity is not expected when the refractive index of the surrounding medium changes.

At a wavelength of 757 nm, as seen in **Figure 2.2c**, strong LSPR mode is excited on top of the gold nano-grating and has some coupling to the SPR modes at the interface of the dielectric layer with gold film. This creates a Fano resonance where most of the field is localized in the surrounding medium and hence, this wavelength peak should be sensitive to changes in the surrounding refractive index. For discussion purposes, the mode is referred to as LSPR dominant mode. Compared to the previous work

where a metallic mirror was used just below the nano-grating, the sensitivity is expected to be slightly lower because there is coupling to the SPR mode [45]. The quality factor, Q , for the resonance is 14. Finally, the field distribution at a third resonance peak at a wavelength of 945 nm is demonstrated in **Figure 2.2d**. As seen in the distribution, very strong SPR modes are excited in the interface of gold film and substrate resulting in a narrow dip in reflection spectra of the structure with a high quality factor of 143. Further, there is hardly any field in the surrounding medium indicating that the resonance should be insensitive to the surrounding medium. The high Q of the peak makes it ideal for self-referencing measurements as the location of the peak will be easily determined experimentally. The mode is referred to as SPR dominant mode in the discussions.

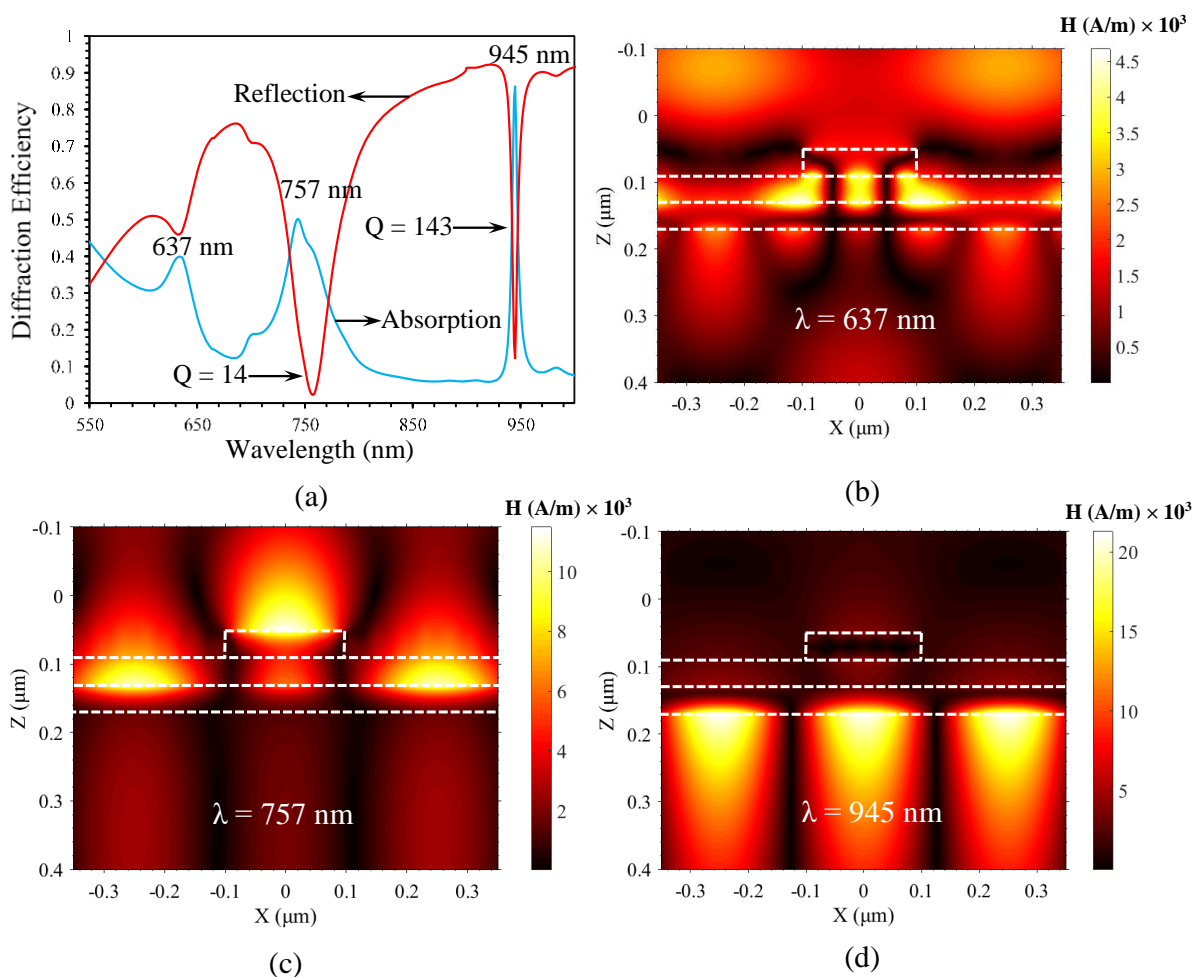


Figure 2.2. (a) Absorption and reflection spectra of the optimized nano-grating structure with cubic geometry, (b-d) distribution of H_y for three resonance frequencies of the nano-grating structure with cubic geometry

Figure 2.3a demonstrates the absorption and reflection spectra of the optimized structure with cylinders as nano-gratings instead of cubes. In this structure, four resonance features can be seen in the reflection spectra at wavelengths of 637 nm, between 733 nm, 750 nm, and 944 nm. To understand this behavior, the distribution of the magnetic field, $|H|$, at these resonance wavelengths were calculated and are shown in **Figure 2.3b-e**. As in the cube, the absorption enhancement of the light field at a wavelength of 637 nm is mostly due to Fabry-Perot interferences. In **Figure 2.3c** at the wavelength of 733 nm, strong LSPR and SPR modes are excited on top of the gold nano-grating and interfaces of the gold film with dielectric layer and substrate layer, respectively.

This excitation was not observed in the nano-cube geometry. At the wavelength of 750 nm, LSPR mode is excited on top of the nano-grating and SPR mode is excited in the interface between the gold and dielectric layer. There is some excitation of the SPR mode in the interface between the gold spacer layer and the substrate. This feature looks like the resonance feature at the wavelength of 757 nm for the cube. On the other hand, in the absorption characteristics, the highest absorption is observed at 733 nm and a single peak is observed. This is because of the strong localization of the field both in the cylinder and the thin film resulting in the incident light being absorbed in both layers. For the 750 nm resonance, the transmission is larger than at 733 nm. Further, the SPR mode for the cylindrical structure is stronger than the nano-cube geometry. Looking at the field distributions, we expect the sensitivity of 750 nm optical mode to be significantly larger than that of the resonance at 733 nm.

However, we also expect the sensitivity of the cylindrical structure to be smaller than that of the nano-cube structure because of the lightning rod effect. At the wavelength of 944 nm, again very strong SPR modes are excited on the interface of the gold film with the substrate layer and caused a considerable increment in the light absorption at wavelength of 944 nm. Moreover, a very narrow dip is created in the reflection spectra with a high-quality factor of 118. Thus, self-referencing should be achieved even with the simple cylindrical geometry.

The field distributions in both the structures demonstrate that LSPR, SPR and Fabry-Perot modes are excited in the structure and further, they couple with each other to create Fano resonances. This allows the structure to support multiple anti-peaks in reflection spectra and each is expected to have a different sensitivity to the variation of the surrounding material. Hence, a self-referenced sensor should be realizable with the structure.

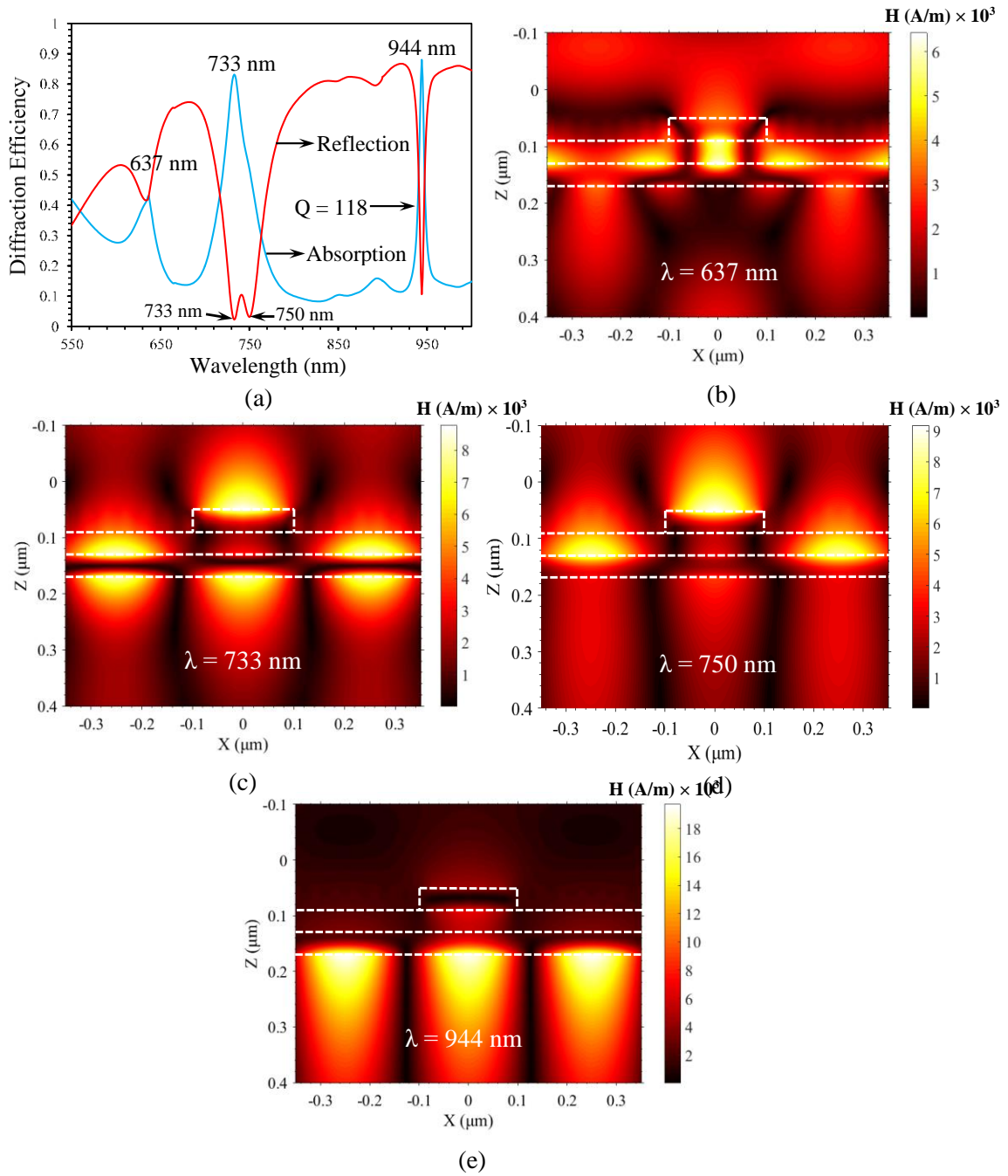


Figure 2.3. (a) Absorption and reflection spectra of the optimized structure with cylinders as nano-gratings, (b-e) distribution of H_y for four resonance features of the optimized structure with cylinders as nano gratings

While the proposed structure is simple to conceptualize, as seen above there are complex interactions between the different optical modes and the various parameters need to be carefully optimized to

achieve a self-referencing peak which is optically isolated from the analyte. For example, the refractive index of the dielectric layer plays an important layer. If the refractive index of the dielectric layer is 1.5 (e.g. the dielectric layer is silicon dioxide instead of SiON), then the self-referencing peak is observed when the surrounding medium is air but not observed when the surrounding medium is water. Achieving a self-referenced peak which does not shift with wavelength is unique to the proposed structure and has been achieved by careful optimization. The effect of geometrical parameters is described in detail in the next section.

2.3 Effect of Geometrical Parameters

It is instructive to understand how the wavelength, strength, and Q of the resonance peaks depend on the various geometrical parameters. Simulations were done for the nano-cube geometry by changing the height of the nano-grating, dielectric height, and the thickness of the gold thin film. The reflection spectra for these different cases are shown in **Figure 2.4a-c**. As seen in **Figure 2.4a** when the nano-grating height is increased, there is not much effect for the Fabry-Perot resonance until a thickness of 60 nm, above which the resonance becomes very weak. The Q of the LSPR-SPR coupled-mode becomes higher when the nano-grating height is decreased. However, the coupling to SPR mode becomes stronger as the nano-grating height is decreased, thereby, the expected sensitivity should decrease. Thus, for this work, we chose 40 nm as the optimal thickness for the grating where the Q is high and LSPR mode is stronger than SPR mode. One can increase the sensitivity by increasing the nano-grating height to 60 nm at the cost of lower Q. The resonance wavelength doesn't shift till a thickness of 40 nm but increases 0.7 nm per 1 nm increase in the thickness after that. The self-referencing peak doesn't change significantly due to changing the height of the nano-grating. The peak is very well defined above a height of 30 nm and maintains high Q over the wavelength range simulated.

As seen in **Figure 2.4b**, when we change the thickness of the dielectric spacer, LSPR-SPR coupled mode is strongest between 30 nm – 50 nm. It also shifts to longer wavelengths with increasing thickness. When the dielectric spacing layer is thicker than 60 nm, the resonance is separated into two components, similar to what was observed in the cylindrical geometry. The self-referencing peak again is well defined over the range simulated and doesn't shift with varying thickness.

As seen in **Figure 2.4c**, the gold film thickness plays a particularly important role in the definition of a self-referencing peak. The self-peak referencing is well defined for gold film thickness ranging between 25 nm and 45 nm. This peak becomes very weak as the thickness increases further. The Fabry-

Perot peak centered in the dielectric layer does not have much effect above a gold thickness of 35 nm which is expected as the gold layer is mainly acting as a mirror there. For the LSPR-SPR coupled resonance, the SPR excitation is stronger for film thickness between 20 nm – 50 nm. Above 50 nm, the SPR effect becomes constant and LSPR part plays an important part. This is again expected as the bottom layer starts to act more like a mirror with increasing thickness. However, with this thickness, the self-referencing peak is not well defined, and while the sensitivity of the sensor may increase, self-referencing is not achieved.

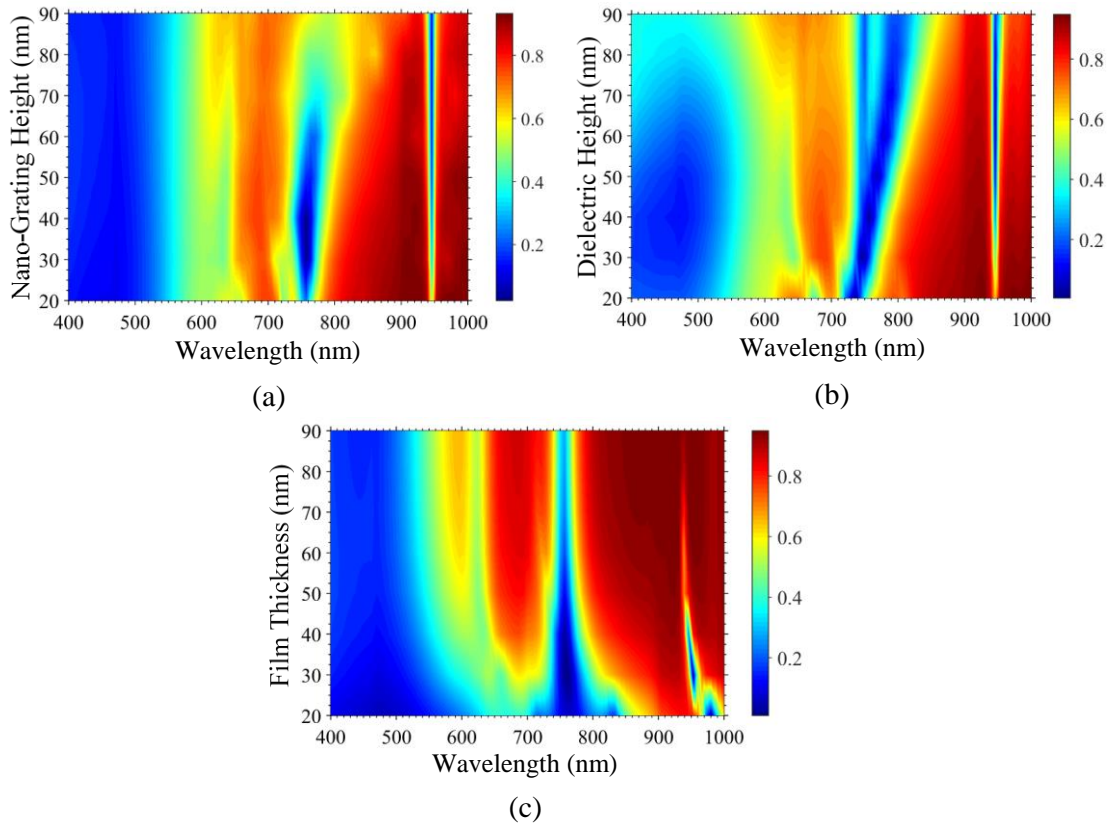


Figure 2.4. Reflection spectra of the nano-grating structure with cubic geometry where (a) nano-grating height is changing from 20 nm to 90 nm, (b) dielectric height is changing from 20 nm to 90 nm, and (c) thickness of the gold film is changing from 20 nm to 90 nm.

2.4 Bulk Sensing

The first sensing application that was considered was when the refractive index of the surrounding medium changed. The device was simulated for refractive index varying in the range from 1.33 to 1.40.

Figure 2.5a shows the reflected spectra from the nano-cube geometry as the refractive index changes

and **Figure 2.5b** plots the change of resonance wavelength as the refractive index of the medium changes. A nearly linear shift in the wavelength is observed for the LSPR dominant mode and a sensitivity of 429 nm/RIU is achieved. The FOM for the resonance is 8 /RIU. The sensitivity is only slightly lower than nano-cubes on a metal where the LSPR dominant mode was designed to be on the top surface [45]. The SPR dominant resonance at 945 nm does not shift at all with changes in the refractive index. The stability of the SPR dominant resonance with changes in the surrounding index makes it useful for self-referencing purposes. For example, if the temperature changes, it is expected that both Plasmonic peaks will shift because of the changes in the refractive index of the gold layer and the dielectric. Thus, by monitoring the shift of wavelength in the 945 nm resonance, one can correct for any temperature changes.

Figure 2.5c plots the reflected spectra for the cylinder geometry as the refractive index changes. Again, the resonance at 944 nm does not shift. The longer wavelength LSPR dominant dip shifts linearly with a change of refractive index and has a sensitivity of 400 nm/RIU. The field distributions had predicted the reduced sensitivity because of the stronger SPR coupling in the mode as compared to the nano-cube geometry. The shorter wavelength LSPR dominant dip shifts very little and only has a sensitivity of ~ 100 nm/RIU. For this asymmetric Fano resonance, the resonance frequency can be defined as the midpoint between the longer wavelength dip (750 nm) and the peak (741 nm) [71-73]. The linewidth is defined as the difference between the dip and peak (9 nm in this case). Using this method, Q was estimated to be 82. Simulations indicate that even the cylindrical geometry has enough sensitivity for practical applications for bulk sensing while being very easy to photolithograph. One can increase the sensitivity by using other shapes but at the cost of complex fabrication.

2.5 Surface Sensing

Plasmonic sensors are used for detecting monolayer attachment to the surface [43, 74, 75]. The sensitivity of the sensor to the attachment of nanometer layers was also investigated. Layers with thickness ranging from 1 to 10 nm and with a refractive index of 1.5 were placed only on top of the grating layer (as would be the case for surface attachments) and the reflection spectra simulated. The surrounding refractive index was that of water as is normally the case in most biochemical sensing. The refractive index of the surface attached layer of 1.5 was chosen because most biological materials have a refractive index close to it [76].

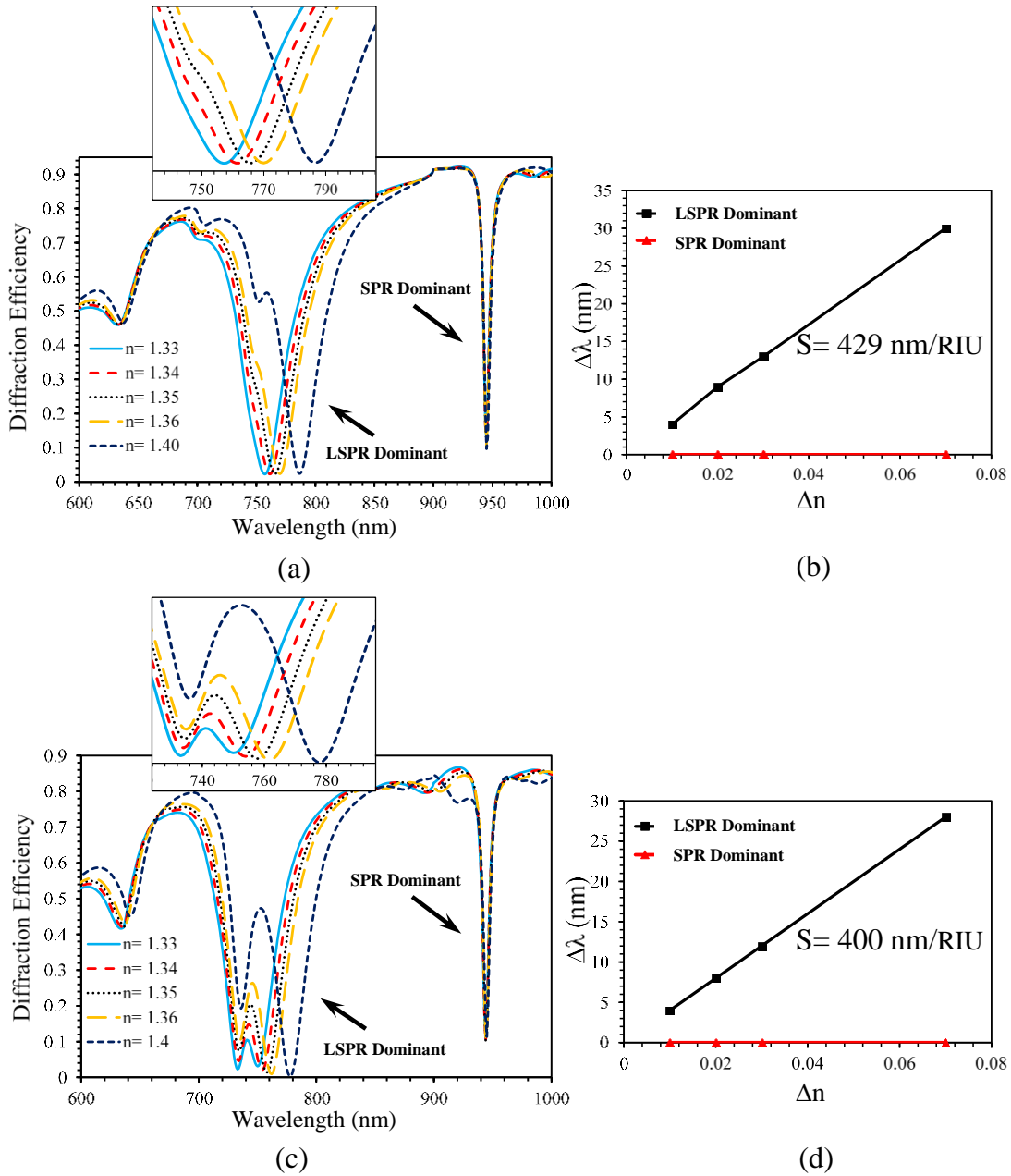


Figure 2.5. (a) Reflection spectra of the nano-grating structure with cubic geometry when refractive index of surrounding materials varies from 1.33 to 1.4, (b) variations of the resonance wavelength of the cubic nano-gratings as the refractive index of surroundings changes, (c) Reflection spectra of the nano-grating structure with cylindrical geometry when refractive index of surrounding materials varies from 1.33 to 1.4 and (d) variations of the resonance wavelength of the cylindrical nano-gratings as the refractive index of surroundings changes.

A typical DNA has a layer thickness between 3-4 nm. Thus, if the sensor can detect shifts in this range, it would be suitable for DNA hybridization experiments. **Figures 2.6a, b** plot the change in the

reflection spectra and the change in the resonance wavelength, respectively for different thickness layers for the nano-cube geometry. For 1 nm layer thickness, a 0.5 nm shift in resonance wavelength for the LSPR dominant mode is observed. For 10 nm layer thickness, the shift is 4 nm. The sensitivity matches well with other Plasmonic sensors [43] and is suitable for monolayer attachments of biomaterials. Corresponding results for the cylindrical geometry are shown in **Figures 2.6c, d**.

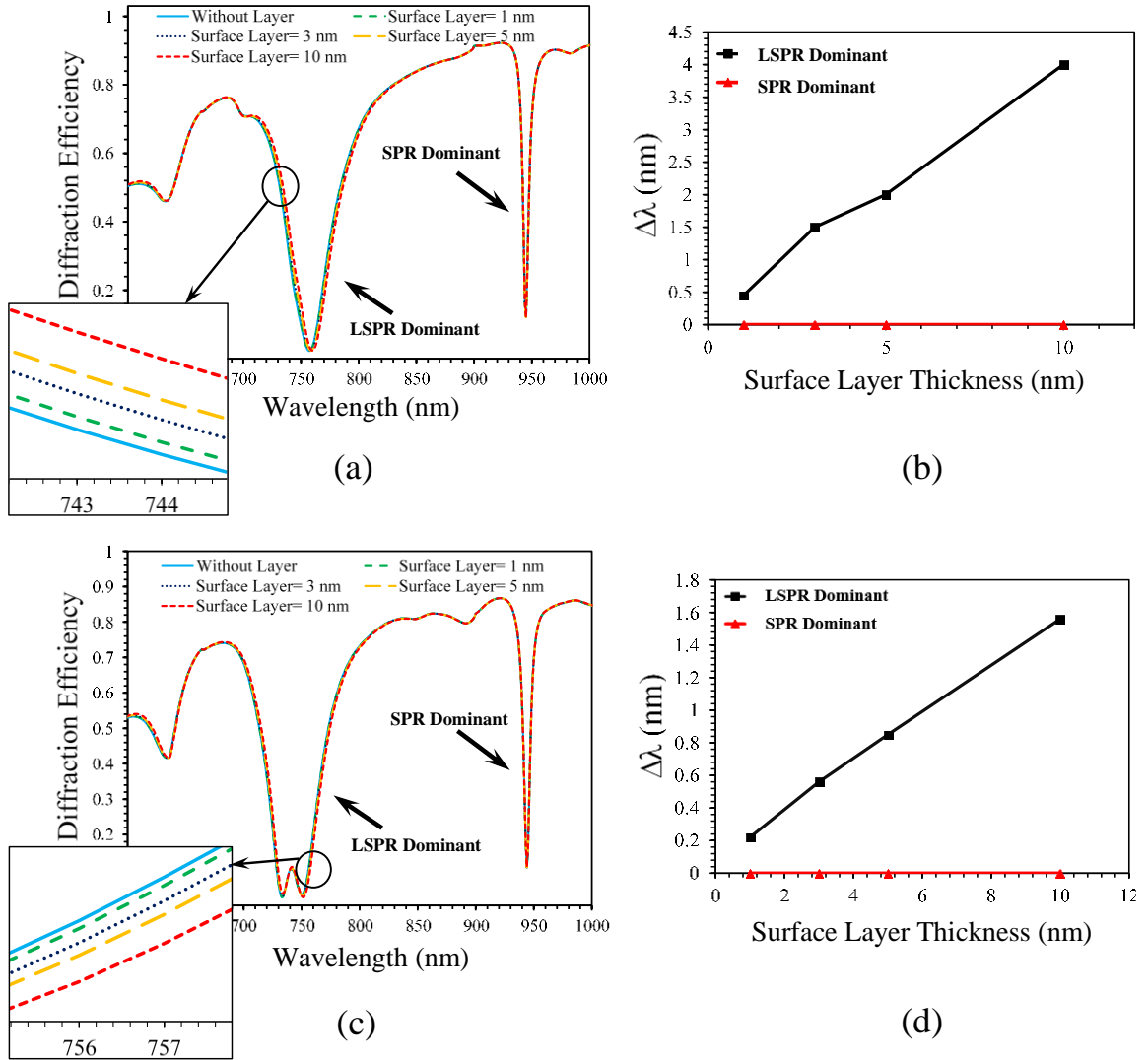


Figure 2.6. (a) Reflection spectra of the nano-grating structure with cubic geometry when thickness of surface layer varies from 1 nm to 10 nm, (b) variations of the resonance wavelength of the cubic nano-gratings as the thickness of the surface layer changes, (c) Reflection spectra of the nano-grating structure with cylindrical geometry when thickness of surface layer varies from 1 nm to 10 nm, and (d) variations of resonance wavelength of the cylindrical nano-gratings as the thickness of the surface layer changes.

The sensitivity for the cylindrical geometry is nearly 2.5 times lower than that of the cube structure. This was expected because of the weaker LSPR in the cylindrical geometry for the resonant mode. While for bulk sensing, the cylinder was still good, and had only slightly lower sensitivity compared to the nano-cube; its sensing is much lower for thin films.

2.6 Lessons from Simulations and Fabrication Tolerances

2.6.1 Gold Film

As mentioned, 40 nm thick gold layer would be deposited on the glass substrate using e-beam evaporator. E-beam evaporation has ± 2 nm resolution [77], so the gold film thickness can vary from 38 – 42 nm. The effect of gold film variations was investigated and was summarized earlier in **Figure 2.4c**. It was observed in that figure that when the gold film has a thickness of 25 nm to 45 nm, the self-referencing peak is very well defined. Thus, the fabrication error of 2 nm will not have much effect in the self-referencing peak. On the other hand, LSPR dominant peak will have a higher Q if the fabrication error leads to a thicker gold film as shown in **Figure 2.4c**. However, if the gold film is less than 40 nm, the Q will slightly decrease. In conclusion, small variations in gold film thickness will not have a considerable effect on the output of the sensor and control of this layer beyond what is already available is not critical to the success of the project.

2.6.2 Dielectric Layer

Plasma-Enhanced Chemical Vapor Deposition (PECVD) will be used to deposit 40 nm thick SiON layer on top of the gold film. PECVD also have 1 nm resolution and thus again we can have a variation from 39 nm – 41 nm in the thickness of the dielectric layer. The dependency of the resonance features on the dielectric layer thickness was summarized in **Figure 2.4b**. As seen in this figure, when the dielectric layer thickness is between 30 nm to 50 nm, the LSPR dominant peak is very strong, and the Q of the peak remains almost constant. Only the resonance wavelength will slightly shift when the thickness is changing from 30 nm to 50 nm. Also, the SPR dominant peak is very well defined for dielectric thickness higher than 30 nm. As a result, the small fabrication errors in thickness of dielectric layer is not going to change the resonance features of the sensor.

Another parameter that is critical is the refractive index of the dielectric layer. As mentioned, the dielectric layer should have a refractive index of 1.8. SiON can have a refractive index in the range of 1.46 to 2.1 by changing the concentration of oxygen and nitride. However, there can be error in

achieving the exact refractive index of 1.8. For the sensor to work as designed for water as a solvent, the refractive index needs to be controlled from (1.75) to (1.85), as observed during the simulations. This requires a control of approximately 10% in the ratio of the oxygen to nitrogen in the dielectric [78]. While this is a large error and we should be able to control the ratio better, we don't have control of refractive index while the layer is being grown in the cleanroom, as the PECVD is not equipped with an in-situ ellipsometer. So this could be a major issue while fabricating the devices.

This risk can be mitigated by tuning the refracting index of surrounding medium, at least for the demonstration purposes. As mentioned, the sensor was optimized when the surrounding medium is water with a refractive index of 1.33 to target biochemical processes. We will be using Cargille refractive index fluids for characterizing the sensor for bulk sensing. Cargille fluids have been designed for refractive index matching and we can get refractive indices varying from 1.0 to 2.1 in steps of 0.01. Further, these fluids are highly stable. Thus, if we cannot achieve the exact refractive index of 1.8 for the SiON, we are able to tune the surrounding refractive index in a way that the refractive index difference between the dielectric and surrounding medium remains constant and we should still be able to measure the self-referencing peak.

2.6.3 Lithography

Lithography of the last layer which is the grating structure can have some issues. As electron beam lithography will be used to generate the cubic and cylindrical nano gratings on top of the dielectric layer, negative charges may gather in the dielectric and cause beam distortion and thus leads to pattern distortion. Also, creating sharp edges for the cubic structure may be hard because of the proximately effect due to this build up charge. We can use anti-charging techniques to eliminate the charging effect in the dielectric layer. For example, a thin layer of aluminum or a conductive polymer can be coated on top of the resist and then removed after the lithography step. Another method will be to use different pattern exposures which has been shown to reduce charge buildup [79]. Also, achieving ideal sharp edges in the cubic structure would be hard in presence of charge buildup and we will get fewer sharp edges. This will lead to a reduction in the concentration of localized plasmons on the edges and thus a reduction in Q of the LSPR mode. Further, due to the surface roughness the Q will be decrease compared to the simulations. Since there are no sharp edges in the cylindrical structure, we expect to achieve decent cylindrical patterns. However, again surface roughness can cause a reduction in Q. Thus,

we have proposed the two structures to fabricate and test. Between them we can understand the optical interactions and the effect of shape in the plasmon resonances.

Since we would try to achieve a decent cubic pattern with sharp features, we might have to enhance the electron beam dose to a certain amount. We will run a dose test and will try different electron beam doses to find the right dose for our structure. Once the electron beam dose is higher than a threshold value, we should be able to achieve highly ordered patterns. However, our purpose would be to find the minimum electron beam dose that give us highly order patterns along with sharp features. Condition of achieving sharp features might force us to enhance the dose to a higher amount than the threshold amount, which is required for an ordered pattern. This will cause the cubic patters to be larger than the targeted patterns. We can mitigate this problem by fabricating cubes with smaller size and then achieve cubes with 200 nm side length.

2.6.4 Grating Layer

For both structures, the thickness of the grating layer would be 40 nm. For cubic structure, the width of the cube would be 200 nm and for cylindrical structure, the diameter would be 200 nm. Again, we expect to see almost ± 2 nm error in the thickness of the nano gratings. The effect of nano grating thickness on the resonance features was already investigated in **Figure 2.4a**. As seen in this figure, the self-referencing peak is very well defined for grating thickness above 30 nm and does not change significantly when the grating thickness changes. However, decreasing the grating thickness less than 40 nm will increase the Q of LSPR dominant mode and will decrease the sensitivity and vice versa. Small changes in the thickness is not going to significantly change the LSPR mode resonance conditions. Also as mentioned, the width of nano grating is 200 nm, and it is big compared to the fabrication error of ± 2 nm. Thus, small variations in width of nano grating during the fabrication, is not going to change the resonance conditions of the sensor. Further, we will be testing different widths as part of design variations.

2.7 Limitations of the Simulations

We have used simulations to develop the understanding of the proposed self-referencing plasmonic sensor. However, there are some limitations which these simulations do not completely account for. First, the refractive index of the dielectric spacer layer is a constant value of 1.8 in the complete wavelength range. However, there will be chromatic dispersion in the dielectric which will change the

performance of the device. The chromatic dispersion of the grown dielectric was measured and will be considered in Chapter 4 when the experimental results are discussed. Second, the simulations do not account for any adhesion metals that may be required in between gold and the layers below it. The adhesion metals have optical losses which can affect the Q of the modes. These will again be considered in Chapter 4. Finally, the simulations also neglect the surface roughness in different layers which should also reduce the Q of the structure. Nevertheless, the simulation results presented in this chapter do provide a guidance to design experiments and study the proposed structure.

2.8 Conclusions

In this chapter, we proposed a new structure for a self-referenced Plasmonic sensor. By introducing a thin gold film that can support an SPR mode, various coupled modes are excited in the structure. The LSPR dominant mode shifts when the surrounding index or surrounding material is changed while the SPR dominant mode remains insensitive to the surrounding medium. Two simple-to-fabricate geometries were analyzed. Bulk sensitivity of 429 nm/RIU and the ability to detect surface attachment of 1 nm monolayers was achieved with a cubic geometry. The structure was analyzed for different geometrical parameters and thickness of the gold thin film played the main role in excitation of the self-referencing resonance peak. The parametric analysis also shows that the design is fabrication tolerant and promises a good practical platform for realizing self-referenced Plasmonic sensors.

Chapter 3

Fabrication of the Self-Referencing Plasmonic Sensors Based on Gold Nano-grating Arrays

In this chapter, the experimental details about the fabrication of the self-referencing sensors proposed in Chapter 2 are described. These sensors are based on gold nano-grating arrays containing nano-cubes and nano-cylinders that can support multiple plasmonic and Fabry-Perot modes. **Figure 3.1** shows the fabrication steps for the proposed plasmonic sensors and consists of e-beam metal deposition and e-beam lithography followed by lift-off process. The fabrication steps for both sensor arrays are similar, with only the e-beam lithography pattern being different. Both sensor structures are fabricated at the same time on one sample, and during the lithography, different masks are designed to create different patterns of nano-cubes and nano-cylinders. The next sections discuss these fabrication steps in detail.

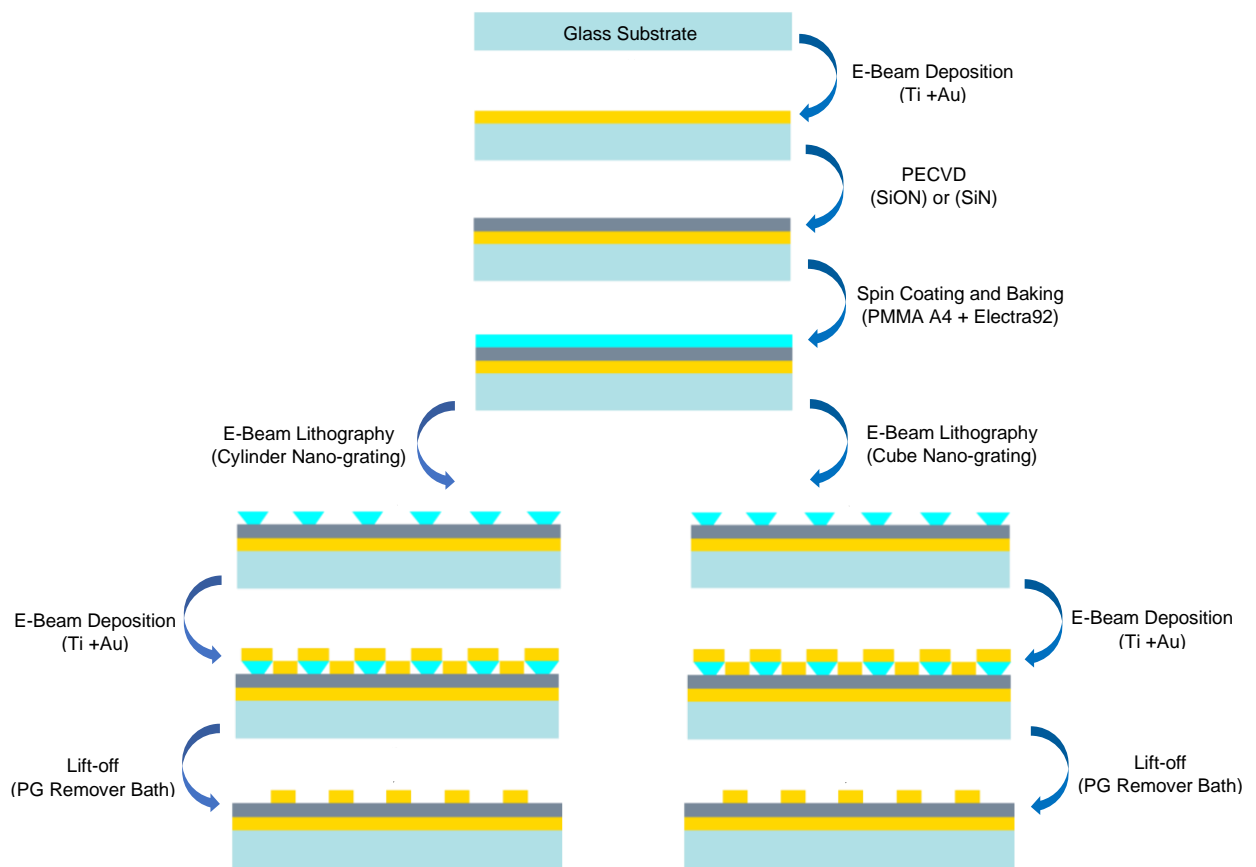


Figure 3.1. Fabrication steps of the proposed self-referencing sensors based on cubic and cylindrical nano-gratings.

To understand the important physical parameters and their effect on the performance of the proposed sensors, we have studied different variations related to the structure of the sensors. These variations include two different dielectrics for the spacer layer, three different shapes for the nano-gratings, and various physical dimensions related to the gratings and the lattice. **Table 3.1** summarizes the variations we studied during this experiment. In total, 150 different designs were fabricated and studied.

Table 3.1. Summary of the sensor’s variations studied in this experiment.

Parameter	Variation
Dielectric Spacer Layer	<i>SiON, SiN</i>
Grating shape	<i>Cube, Cylinder, Equilateral Triangle</i>
Lattice spacing	<i>400 – 600 nm in steps of 50 nm</i>
Cube Side Length/Cylinder Diameter/Triangle Side Length	<i>170 nm, 180 nm, 200 nm, 220 nm, 250 nm</i>

To study these variations, different arrays were fabricated on a single sample. Array sizes of $100\ \mu\text{m} \times 100\ \mu\text{m}$ with a particular design were fabricated with a spacing of $100\ \mu\text{m}$ between the arrays. This allows for minimal variation of other parameters like the refractive index of the substrate or the refractive index of the dielectric spacer layer between different arrays, allowing us to confirm and improve the theoretical models developed in Chapter 2.

3.1 Glass Substrate

Since an SPR mode needs to be excited in the thin metallic film, the refractive index and the absorption of the substrate need to be low. The two options available were either first growing a thick silicon dioxide layer on a silicon substrate or using a glass substrate. Corning EAGLE GX glass substrate with a dimension of $25\ \text{mm} \times 25\ \text{mm} \times 0.7\ \text{mm}$ was chosen as the substrate. The Corning EAGLE GX glass has low loss in the visible spectrum, excellent environmental durability, and high chemical resistance [80]. **Table 3.2** shows the refractive index of the glass substrate measured at different wavelengths provided by the manufacturer [80]. As discussed in Chapter 2, a refractive index of ~ 1.5 is needed to support the SPR mode, and thus, Corning EAGLE GX is ideal as the substrate. It is also a low-cost substrate, costing \$10 per wafer, even in small volumes. Only a small part of the substrate at the center

($\sim 1 \text{ mm} \times 3 \text{ mm}$) was used. The size was chosen for ease of handling during the fabrication and also to ensure uniformity of the processes within the small central area of the wafer.

Table 3.2. The refractive index of the glass substrate at different optical wavelengths [80].

Optical Wavelength	Refractive Index
<i>435.8 nm</i>	<i>1.5198</i>
<i>467.8 nm</i>	<i>1.5169</i>
<i>480 nm</i>	<i>1.5160</i>
<i>508.6 nm</i>	<i>1.5141</i>
<i>546.1 nm</i>	<i>1.5119</i>
<i>589.3 nm</i>	<i>1.5099</i>
<i>643.8 nm</i>	<i>1.5078</i>

3.2 Electron Beam Physical Vapor Deposition (EB-PVD) of the Gold Film

Electron Beam Physical Vapor Deposition (EB-PVD) is a thin film deposition technique used in the manufacturing of advanced coatings for various industrial applications. In this process, a material source is heated to a high temperature in a vacuum chamber, and an electron beam is directed onto the source, causing it to evaporate and form a vapor plume. The vaporized material then condenses on the substrate surface, resulting in a thin film with precise microstructural control. The EB-PVD technique offers advantages over conventional physical vapor deposition methods due to its ability to create columnar microstructures, low thermal stress, and improved adherence to complex geometries [81].

EB-PVD was used to deposit 40 nm gold film on the glass substrate. The samples were installed in an upside-down rotating stage inside an Intlvac e-beam deposition chamber [82]. To improve the adhesion of the gold layer on the glass substrate, a 3 nm thick Titanium (Ti) layer, with a deposition rate of 0.5 \AA per second, was first deposited on the substrate before depositing the gold layer. Noble metals such as gold adhere poorly to the substrate due to their low chemical reactivity [83]. This leads to some phenomena, such as peeling and time-dependent device performance deterioration. However, Ti is known to be more chemically reactive compared to noble metals, and thus, it chemically binds to the substrate and improves the adhesion [83]. It should be noted that the optical properties of Ti were not considered in Chapter 2 and may affect the excitation of the plasmonic peaks, especially the Q of the resonances, due to its high optical loss. These properties will be considered in the next chapter when

we discuss the experimental results. The 40 nm thick gold film was deposited with a deposition rate of 1 Å per second. A tape test was done to test for the adhesion of the film to the substrate. Scotch 3M tape was applied to the film and peeled off. There was no peeling of the metal with the removal of the tape, demonstrating that the adhesion of the film was adequate.

During the e-beam deposition, the final gold layer thickness given by the crystal monitor in the Intlvac system was 40.2 nm. Further, from the latest recommissioning report of the equipment, there was a 5% error between the targeted value and the actual deposited value. This measurement was from the center of a 100 mm silicon wafer. Our samples were always installed in the center of the stage in the chamber, and considering the dimension of the samples (25 mm × 25 mm), we can conclude that there was -5% error from the targeted value. Thus, the film thickness lies in the range of 38-40 nm. As seen in Chapter 2 in **Figure 2.4a**, when the gold film has a thickness of 25 nm to 45 nm, the self-referencing peak is very well defined. Thus, the fabrication error of 2 nm will not have much effect on the self-referencing peak. On the other hand, the LSPR dominant peak will have a higher Q if the fabrication error leads to a thicker gold film.

3.3 Deposition of the Dielectric Spacer Layer Using PECVD

Plasma Enhanced Chemical Vapor Deposition (PECVD) is a thin-film deposition technique used to deposit thin layers of different materials on substrates. In PECVD, a plasma is generated from a precursor gas mixture in a low-pressure environment, typically in a vacuum chamber. The plasma provides energy to break down the precursor molecules, leading to the formation of reactive species, such as ions, electrons, and radicals. These reactive species then react with each other or with the substrate surface to deposit a thin film with desired properties [84-86]. PECVD has the advantage over thermal CVD in that it can operate at lower temperatures, reducing the risk of damaging temperature-sensitive substrates and enabling the deposition of materials with high melting points. PECVD can also produce films with improved conformality due to the directional nature of plasma species [84-86]. Low-pressure CVD (LPCVD) operates at low pressure and moderate temperatures, allowing for higher purity films. However, it may not be suitable for depositing certain materials, especially those with complex chemistries. PECVD, on the other hand, offers a broader range of material deposition options, including silicon-based films and dielectrics [84-86].

For our sensor, PECVD was used to deposit a dielectric layer on top of the gold film using Oxford PlasmaLab System 100. As mentioned in Chapter 2, the refractive index of the dielectric spacer layer

plays a significant role in separating the LSPR and SPR modes. By setting the refractive index to 1.8 in FDTD simulations, two separate modes were observed in visible and near IR regions. We also mentioned that silicon oxynitride (SiON) can achieve a refractive index of 1.8 in the visible region and can be a potential candidate for the spacer layer.

In order to deposit SiON, we needed to develop our own recipe in Oxford Plasma Lab System 100, as no recipe existed for SiON in this instrument, in the Quantum Nano Fabrication and Characterization Facility (QNFCF) of the University of Waterloo. The optimized recipe uses a mixture of 5% silane (SiH₄) diluted in nitrogen (N₂) as the silicon source, nitrous oxide (N₂O) as the oxygen source, and ammonia (NH₃) as the nitrogen source. This combination provides high process performance while maximizing the operational safety of the system by reducing the explosion risk associated with silane. **Table 3.3** shows the optimized process parameter range for the PECVD deposition of SiON.

Table 3.3. Process Parameter Range for deposition of SiON using PECVD system.

Process Parameter Range	
(5% SiH ₄ /95% N ₂)	→ flow 400 sccm
NH ₃	→ flow 20 sccm
N ₂ O	→ flow 60 sccm
N ₂	→ flow 600 sccm
Pressure	→ 650 mTorr
R.F. power	→ 10 Watts @ 13.56 MHz
Temperature	→ 300 – 4000 °C

The temperature was set to 330 °C, and the SiON was deposited using PECVD on a 100 mm silicon wafer. In order to acquire the deposition rate and the refractive index of the SiON, the sample was examined using a Woollam M-2000 ellipsometer.

The Woollam M-2000 ellipsometer probes the sample with S and P-polarized light and measures the relative change in phase and intensity between these two reflected components of the light. The ellipsometer compares the measured data with a model that describes the optical properties and thickness of the thin film. The ellipsometer uses advanced mathematical models, such as the Cauchy, Tauc-Lorentz, or Cody-Lorentz models [87], to describe the optical behavior of the materials being analyzed. By fitting the experimental data to the model, the ellipsometer extracts information about the

film's thickness, refractive index, and extinction coefficient. All three models, for most of the materials and substrates, are included in the ellipsometer software. The user can choose any available mathematical model for the test. Each model provides several parameters that the user has the freedom to activate. For example, the user has the freedom to include the surface roughness parameters when doing a measurement. A decent model with appropriate parameters will give a nice fit to the experimental data with a very low Mean Square Error (MSE).

Through examining the deposited SiON film with the ellipsometer, the deposition rate of SiON was found to be approximately 53 nm/min with a standard deviation uniformity of $\pm 0.48\%$ on a 100 mm silicon wafer. The only model available for the SiON in the ellipsometer was the Cody-Lorentz model. **Figure 3.2** shows the SiON optical model and fitted curves using the measurement extracted from the ellipsometer. As can be seen, a very fine fit from the measurements (green and red lines) is achieved for the optical model (black lines). The MSE for this fit was found to be 4.7. In general, an MSE of 10 or less provides reliable information regarding the thin film. Thus, the modified optical model for the SiON was a decent model, and we could trust the data extracted from this model.

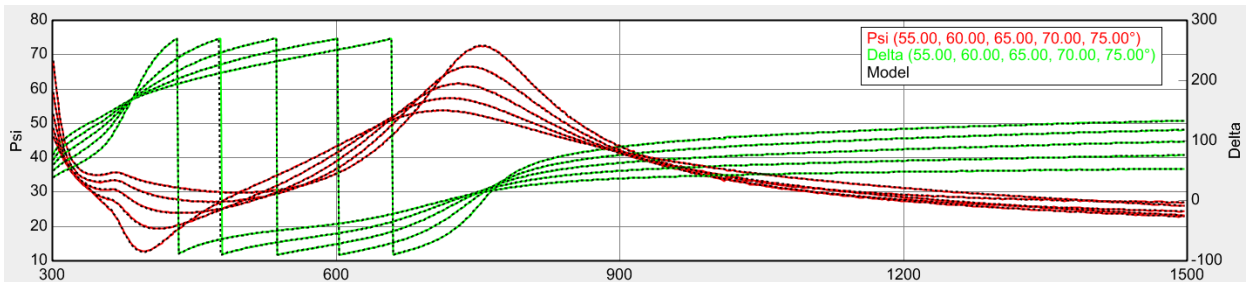


Figure 3.2. The SiON optical model was fitted to the measured data with an ellipsometer. A decent fit has been achieved with an MSE of 4.7.

The refractive index curve of the deposited SiON, extracted using the Cody-Lorentz model in the ellipsometer, is shown in **Figure 3.3**. As seen in this figure, in the range of 400 nm to 1000 nm wavelength, the refractive index value changes between 1.83 to 1.74. In developing the understanding of the proposed structure through simulations, a refractive index of 1.8 was used for the spacer layer. In the simulations, the chromatic dispersion seen experimentally was not considered. This may again affect the performance of the resonances, especially in the Q of the LSPR mode. The effect of the chromatic dispersion of the SiON will be considered in Chapter 4 when the experimental results are discussed.

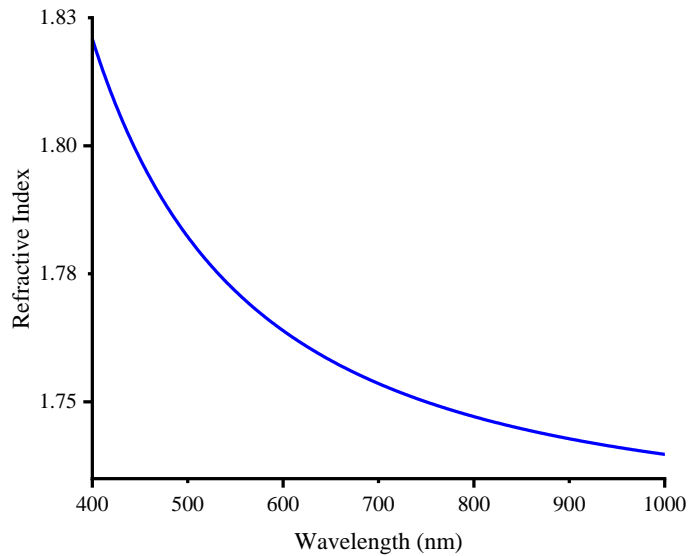


Figure 3.3. The refractive index of the deposited SiON using PECVD extracted using an ellipsometer.

Based on **Figure 3.3**, approximately after 440 nm wavelength, the value of the refractive index drops below 1.8. Although the range of the measured refractive index provides the necessary conditions for the excitement of two modes, in order to make sure that modes are separated, and both have adequate quality factors, we also decided to deposit a different dielectric layer with a higher refractive index on a separate sample. One option was tuning the process parameters of the current recipe for the SiON in the PECVD system. It is possible to increase the refractive index of the SiON by enhancing the flow of NH_3 and also controlling the ratio of SiH_4/N_2 [88, 89]. However, this option was going to be time-consuming. Another option was to use a recipe for silicon nitride (SiN) that existed in QNFCF. This was tried first. According to this recipe, SiN can be deposited using PECVD at a temperature of 300 °C with a deposition rate of 19.8 nm/min. **Table 3.4** shows the process parameters of the PECVD system during the deposition of SiN. Further, the refractive index of SiN extracted using an ellipsometer is shown in **Figure 3.4**. The refractive index ranges from 1.89 to 1.83, which is close to the value we used in simulations and yet higher than that of SiON. Thus, by using two different spacer layers on two different samples, there is a higher chance for exciting two separate modes, and further, it allows us to study experimentally the importance of the refractive index of the spacer layer and its effect on the resonance excitations.

Table 3.4. Process Parameters for deposition of SiN using PECVD system.

Process Parameters During Deposition	
(SiH ₄ / N ₂)	→ flow (900/30) sccm
Pressure	→ 600 mTorr
R.F. power	→ 40 Watts
Temperature	→ 300 °C

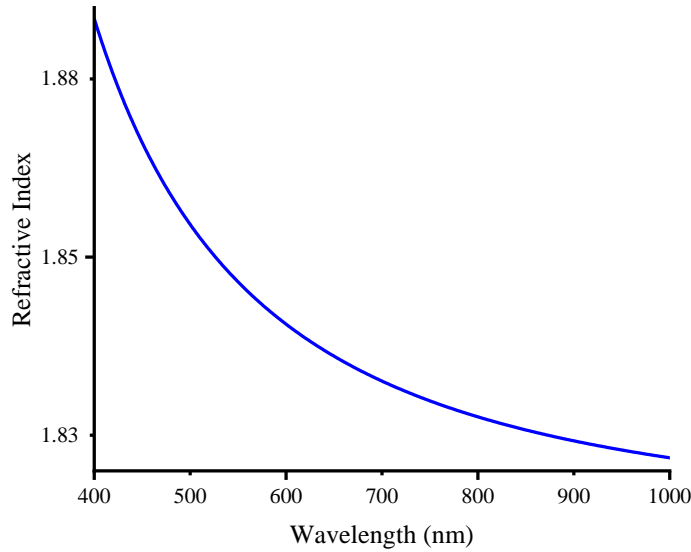


Figure 3.4. The refractive index of the deposited SiN using PECVD extracted using an ellipsometer.

3.4 Deposition of the E-beam Resist

The samples were spin-coated with 950 K poly (methyl methacrylate) (PMMA) A4 resist at a speed of 4000 rpm. Subsequently, the samples were baked on a hot plate for 3 minutes at 180 °C, resulting in a final film thickness of approximately 250 nm.

Due to the presence of the dielectric layer underneath the e-beam resist, there was a significant chance of building up charges in the dielectric. During Electron Beam Lithography (EBL), a charge build-up issue can arise due to the interaction of the electron beam with the insulating or semi-insulating materials used as substrates. When the electron beam strikes the surface of these materials, it can deposit charges, causing an accumulation of electric potential. This charge build-up can significantly affect the accuracy and precision of the lithography process. It leads to undesired deflection of subsequent electron beam shots, resulting in distorted patterns and misalignment of features. To mitigate this issue,

various techniques are employed, such as using conducting substrates or implementing charge dissipation layers, which help to dissipate the accumulated charges and maintain better control over the electron beam trajectory. To avoid the charge build-up problem, PMMA Electra92 was spin-coated at a speed of 6000 rpm on top of the photoresist. Electra92 is a conductive protective coating that is used for dissipation of e-beam charges on insulating substrates. Electra92 can be easily removed after lithography by DI water.

3.5 Electron Beam Lithography and Lift-off

Electron Beam Lithography (EBL) was used to pattern the gold nano-gratings of the final layer. Using EBL allows us to have precise control over the size and spacing between the grating structures. EBL is a high-resolution lithographic technique used in micro and nanofabrication processes to create precise patterns and structures. EBL uses a focused beam of electrons to write patterns directly onto the substrate with extremely high resolution. It offers sub-nanometer precision, making it ideal for cutting-edge research and development in nanotechnology. The unparalleled nature of the EBL, where patterns are created sequentially rather than in parallel, holds significant advantages. This approach enables the easy incorporation of multiple unique designs on a single sample, making it exceptionally useful during the experimental design phase. Although optical lithography is a highly parallel process and can achieve high throughput at relatively low cost, as the feature sizes decrease, diffraction limits the resolution of optical lithography, and it faces challenges in achieving sub-10 nm resolution. On the other hand, nanoimprint lithography can achieve high resolution, comparable to EBL, but in a more parallel manner. However, challenges remain in terms of mold fabrication, defect control, and material selection for large-scale commercial implementation.

EBL was done at 20 kV using RAITH150^{two} lithography system. Periodically arranged patterns containing nano-cubes and nano-cylinders were designed using RAITH150^{two} Computer Aided Design (CAD) software. We also designed nano-gratings arrays with triangular cross-sections, to see if the sharper corners in triangle patterns can help to excite stronger plasmonic fields. The step size of the e-beam was set to 10 nm, and the aperture size was 20 μm . Each array was designed to have a 100 μm \times 100 μm dimension to fit within the 100 μm write field. Also, arrays were separated by 100 μm distance to make sure each array can be measured independently during the characterization. Five different values of 400, 450, 500, 550, and 600 nm were chosen for the pitch. For nano-cubes, nano-cylinders, and triangles, five different values of 170, 180, 200, 220, and 250 nm were chosen for the width,

diameter, and side length, respectively. The patterned samples were soaked in DI water for 2 minutes to remove the Electra92 PMMA and dried with nitrogen. Then, the samples were developed in Methyl-isobutyl-ketone (MIBK) and isopropyl alcohol (IPA) solution in 1:3 proportions respectively for 30 seconds and then IPA as a stopper for 30 seconds and then dried with nitrogen. Then, the samples were installed in the Intlvac e-beam deposition chamber. Again, a 3 nm thick Ti layer was deposited as the adhesion layer, along with a 40 nm thick gold layer. Finally, lift-off was done by soaking the samples in a PG remover bath overnight.

During the lithography, we had to experimentally determine the exact amount of e-beam dose required for our patterns. E-beam dose is a critical exposure variable and controls the number of electrons per unit area of exposure. Based on the existing recipe in the QNFCF, the required e-beam dose for developing PMMA on a silicon substrate was $200 \mu\text{C}/\text{cm}^2$. The e-beam dose needed to be changed around this number to determine the right dose for our structure. We started from $100 \mu\text{C}/\text{cm}^2$ for the e-beam dose and each time increased the dose by $20 \mu\text{C}/\text{cm}^2$. Cubic nano-gratings, with a SiON spacer layer with a side length of 200 nm and lattice spacing of 400 nm, were examined during the dose test. A matrix containing ten identical nano-cube arrays was designed in CAD software in which the first array had an e-beam dose of $100 \mu\text{C}/\text{cm}^2$ and the last array had an e-beam dose of $280 \mu\text{C}/\text{cm}^2$. We changed the e-beam dose around the optimized amount to see which dose works best for our structure. We limited the first experiment to 10 different e-beam doses to have a reasonable exposure time. In case a satisfactory structure was not achieved, a second experiment could be designed with higher e-beam doses to find the right dose. We were interested in the minimum amount of e-beam dose that can give us cubic gratings that are highly ordered and, at the same time, have very sharp features. Minimizing the e-beam dose ensures the minimum difference between the targeted cube sizes and fabricated ones. Further, it minimizes the exposure time, which leads to cost reduction. After development in MIBK and IPA and depositing the final gold layer, the lift-off was done. Finally, the sample was examined using a Scanning Electron Microscopy (SEM) system. For the e-beam doses less than $200 \mu\text{C}/\text{cm}^2$, no pattern was observed in SEM. **Figure 3.5a-e** shows the SEM of the fabricated nano-cube arrays with 200, 220, 240, 260, and $280 \mu\text{C}/\text{cm}^2$ e-beam doses, respectively. As seen in **Figure 3.5a**, for an e-beam dose of $200 \mu\text{C}/\text{cm}^2$, only a few cubes are observed, and no periodic arrangements can be seen. As the e-beam dose was increased to $220 \mu\text{C}/\text{cm}^2$, as seen in **Figure 3.5b**, an array of cubes was observed. However, the cubes were not completely formed. As the dose was increased to 240 and $260 \mu\text{C}/\text{cm}^2$, as shown in **Figure 3.5c** and **d**, respectively, the shape of the cubes

was improved; however, still some defects can be seen. By enhancing the e-beam dose to $280 \mu\text{C}/\text{cm}^2$, as seen in **Figure 3.5e**, highly ordered cubic arrays are achieved.

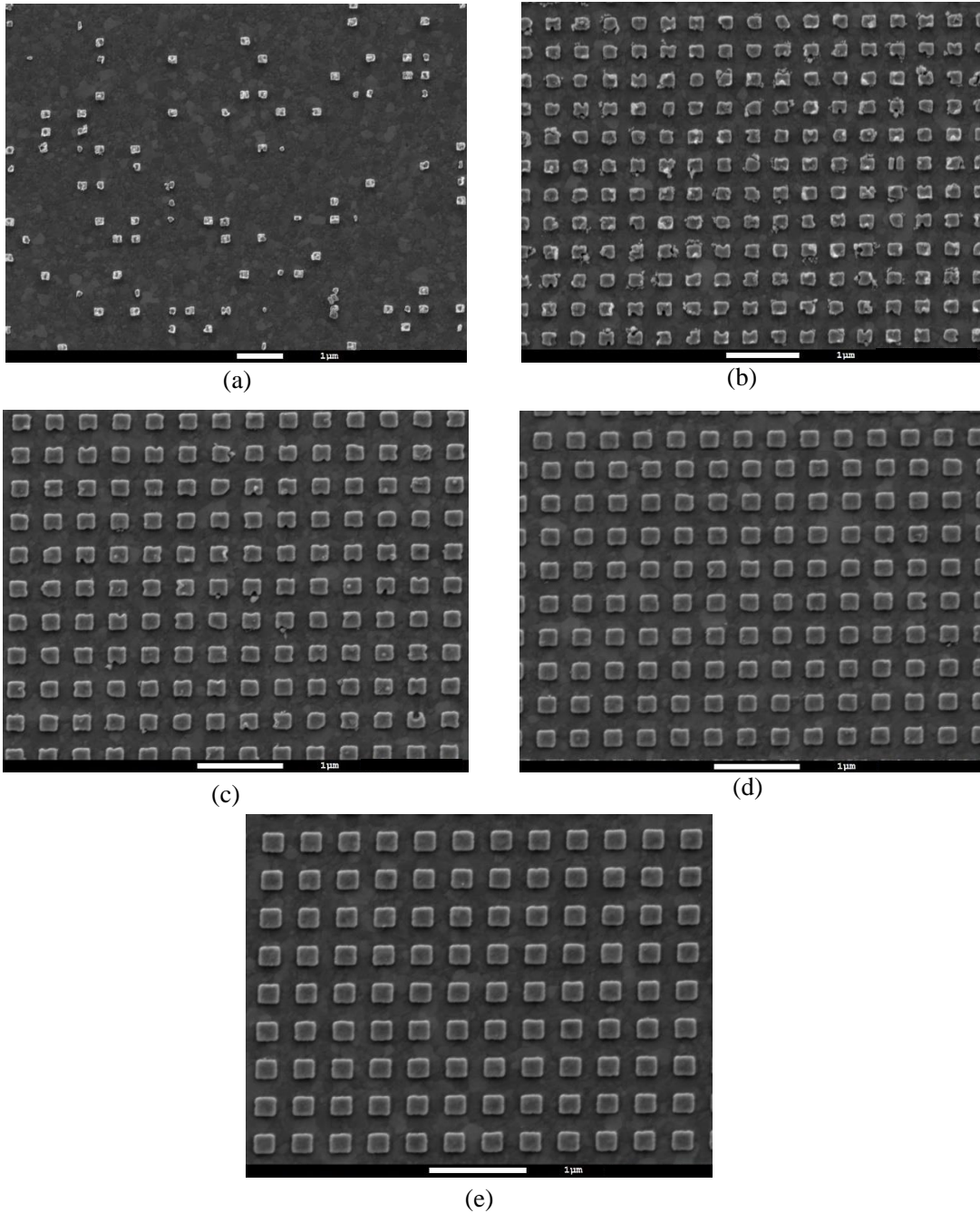


Figure 3.5. SEM images of nano-cube arrays with different e-beam doses of (a) $200 \mu\text{C}/\text{cm}^2$, (b) $220 \mu\text{C}/\text{cm}^2$, (c) $240 \mu\text{C}/\text{cm}^2$, (d) $260 \mu\text{C}/\text{cm}^2$ and (e) $280 \mu\text{C}/\text{cm}^2$

As a result, an e-beam dose of $280 \mu\text{C}/\text{cm}^2$ was chosen to pattern the nano-cube arrays. As the pitch was increased to 550 nm and 600 nm, the e-beam dose needed to be enhanced to $300 \mu\text{C}/\text{cm}^2$, in order to form a highly ordered cubic array. For smaller pitch sizes, there is proximity effect where exposure in one nano-cube affects the exposure of the neighboring ones. Thus, a lower dose is required. This effect becomes smaller as the pitch is increased. The same e-beam dose values were used for both samples with SiON and SiN spacer layers. Some of the representative cubic arrays with SiON spacer layer are shown in **Figure 3.6a-d**, with 170 nm side length and 400 nm pitch, 180 nm side length and 450 nm pitch, 220 nm side length and 400 nm pitch, and 250 nm side length and 400 nm pitch, respectively.

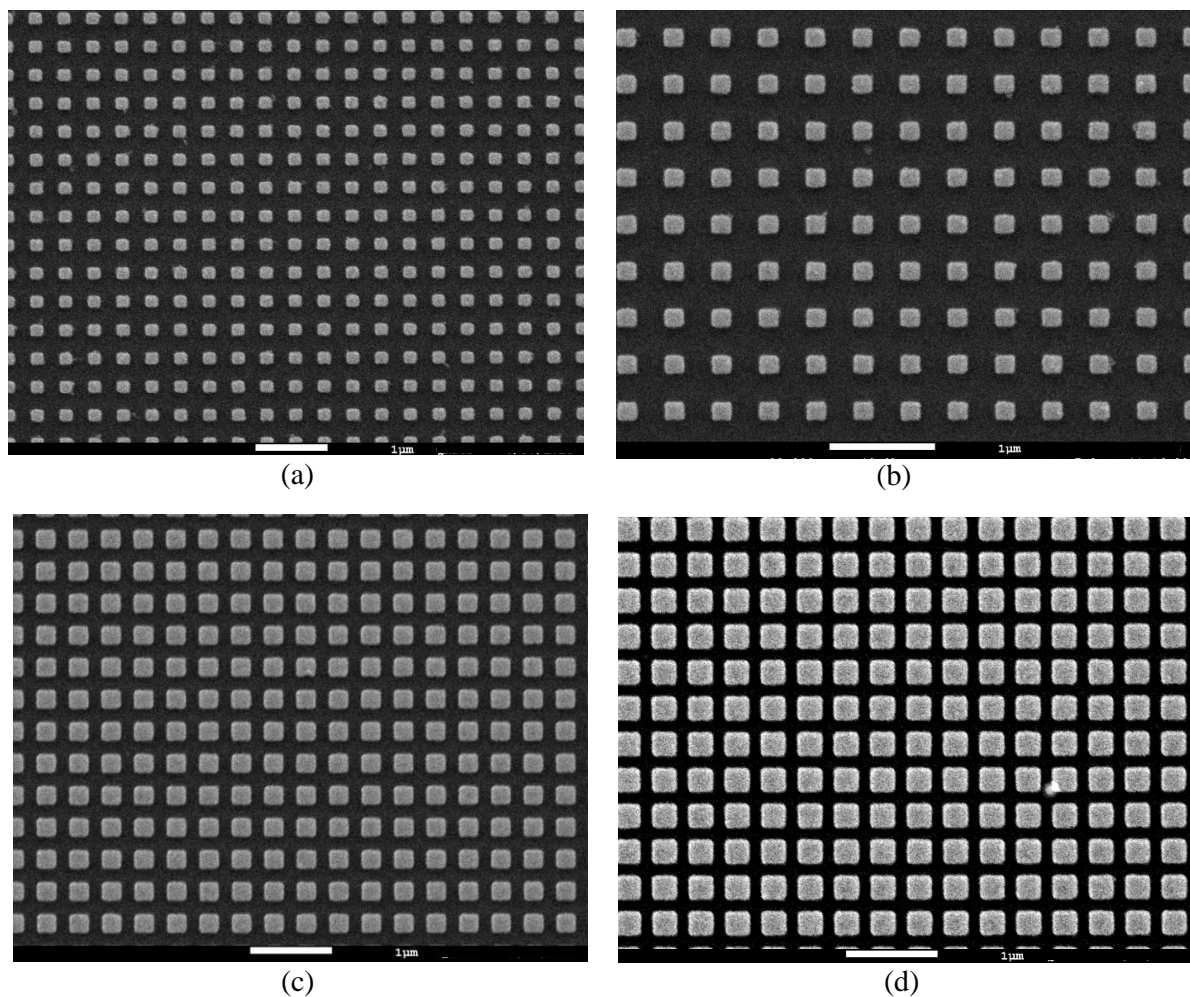


Figure 3.6. SEM images of Some of the representative cubic arrays with (a) 170 nm side length and 400 nm pitch, (b) 180 nm side length and 450 nm pitch, (c) 220 nm side length and 400 nm pitch, and (d) 250 nm side length and 400 nm pitch.

Figure 3.7 shows a microscopic image of the cubic arrays taken by an optical microscope. Each array has a dimension of $100\ \mu\text{m} \times 100\ \mu\text{m}$, and it is separated from the other arrays by a $100\ \mu\text{m}$ distance. The top left array is for the nano-cubes with $170\ \text{nm}$ side length and $400\ \text{nm}$ pitch. As we go to the right side, the pitch values increase to $450, 500, 550,$ and $600\ \text{nm}$. As we go to the bottom, the side lengths of the nano-cubes change to $180, 200, 220,$ and $250\ \text{nm}$. As seen in **Figure 3.7**, each array reflects a different structural color, showing that the reflection spectra are being manipulated due to the excitation of different plasmonic modes within each array.

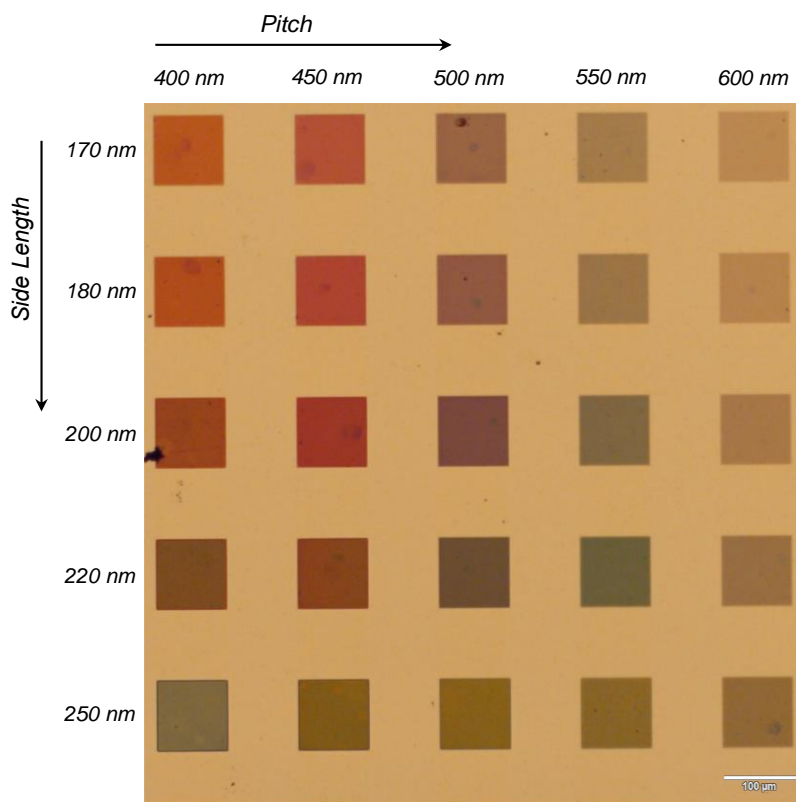


Figure 3.7. A microscopic image of the cubic arrays taken by an optical microscope.

Similar values of e-beam doses were used for patterning the gratings with circular and triangular shapes. **Figure 3.8a, b** shows SEM images of two nano-cylinder arrays with diameters of 200 and $250\ \text{nm}$, respectively. The pitch is $400\ \text{nm}$ for both arrays. As seen in **Figure 3.8**, highly ordered gold nano-cylinders are achieved. A microscopic image of the nano-cylinder arrays with different diameters and pitch is shown in **Figure 3.9**. As can be seen, every array is reflecting a different color, showing that different surface plasmon modes are being excited within the arrays.

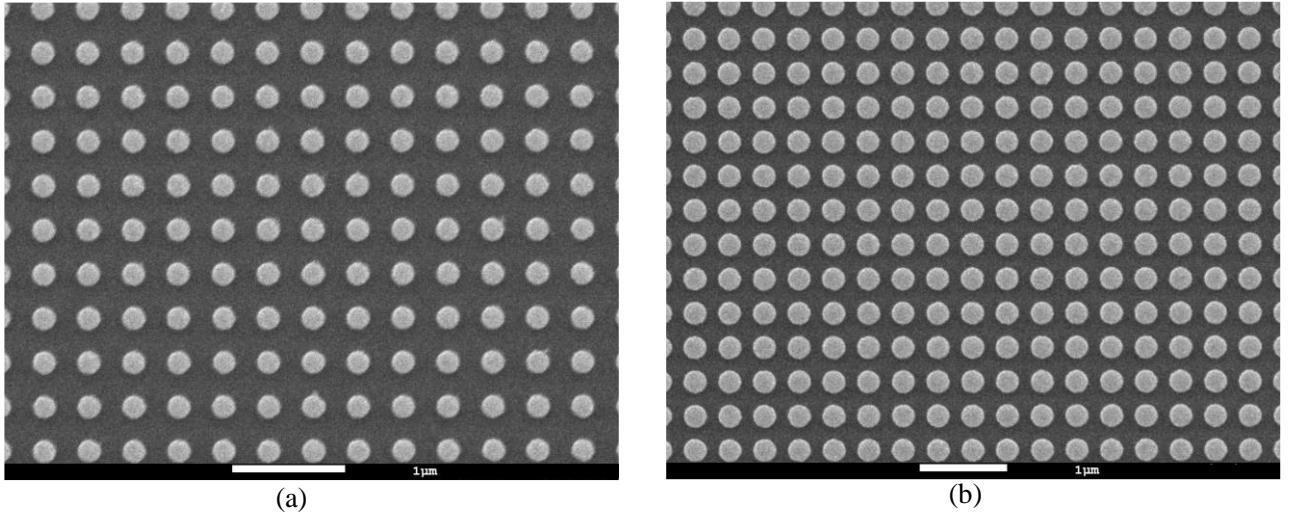


Figure 3.8. SEM images of two nano-cylinder arrays with diameters of (a) 200 and (b) 250 nm, respectively. The pitch is 400 nm for both arrays.

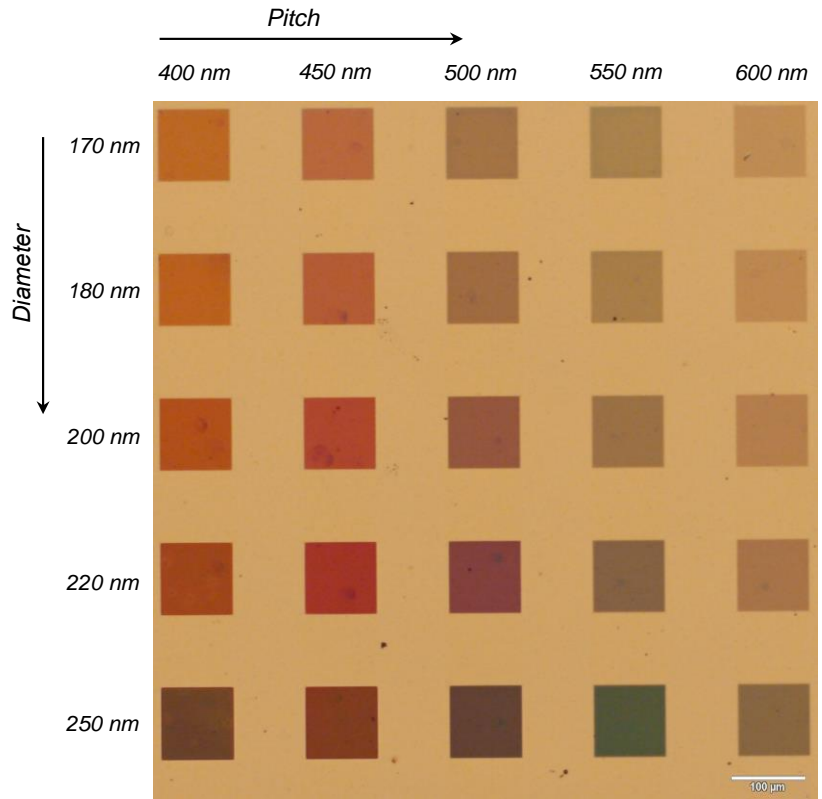


Figure 3.9. A microscopic image of the cylindrical arrays taken by an optical microscope.

Figure 3.10a-d shows the nano-gratings with triangular cross-sections. **Figure 3.10a** is for equilateral triangles with side lengths of 180 nm and 450 nm pitch. In **Figure 3.10b-d**, the pitch is 400 nm, and the side lengths are 200, 220, and 250 nm, respectively. As seen in **Figure 3.10a**, the triangular array is not completely formed.

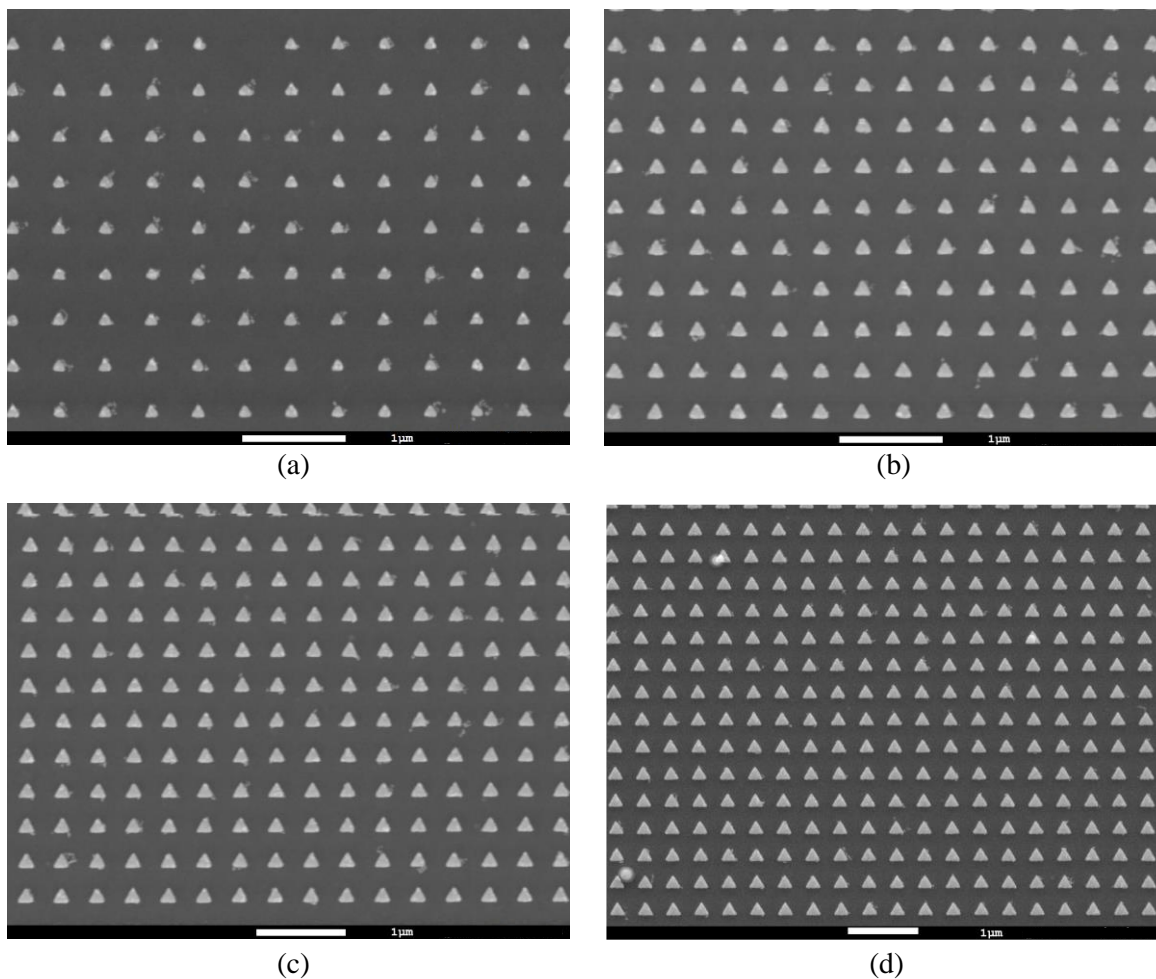


Figure 3.10. SEM images of equilateral triangles with side lengths of (a) 180 nm and 450 nm pitch, (b) 200 nm and 400 nm pitch, (c) 220 nm and 400 nm pitch, and (d) 250 nm and 400 nm pitch

A similar issue was seen with SEM for triangular arrays with 170 nm side lengths. One way to solve this problem was to try higher values of e-beam doses and find the right dose for these two lengths. However, as we will see in the next chapter, even for triangular arrays with 250 nm side length, the plasmonic effect is very weak, and thus, we were sure that for 170 nm and 180 nm side lengths, we would not get strong plasmonic resonances and thus we decided to not try higher doses for the triangular

arrays with 170 and 180 nm side lengths. As seen in **Figures 3.10b** and **c**, for the side lengths of 200 and 220 nm, the triangular arrays are formed, and the shape of the triangles is also acceptable. Further, as the side length is increased to 250 nm in **Figure 3.10c**, a highly ordered triangular array with sharp corners is achieved.

3.6 Summary and Conclusion

In this chapter, a detailed description of the fabrication steps of the self-referencing plasmonic sensors was provided. Two different dielectric spacer layers were deposited on two different samples using PECVD to make sure at least two separate plasmonic modes were achieved. A recipe was developed for SiON in the PECVD system, and an acceptable range for the refractive index of the deposited SiON, compared to the one we used in simulations, was achieved. Further, SiN was deposited on another sample, which provides a higher range of refractive index compared to SiON. Then, a series of e-beam dose tests were done to find the appropriate dose for different nano-gratings with various sizes and lattice spacing. Finally, several arrays with different cross-sections and pitch values were patterned using EBL, and highly ordered nano-grating arrays with circular, cubic, and triangular cross-sections were achieved through the lift-off process.

Chapter 4

Characterization of the Self-Referencing Plasmonic Array Sensors

In this chapter, we discuss the experimental optimization and characterization of the fabricated plasmonic sensors for excitation of different plasmonic modes and for the bulk sensitivity. As mentioned in the chapter 3, cubic and cylindrical arrays with different variations were fabricated on two different samples with the SiON and SiN dielectric spacer layer. The sensors are designed to excite at least two resonance features in the visible to near IR wavelengths range. Further, the thickness of each layer and the size and spacing of the grating layers are optimized to achieve Fano resonances, resulting from the coupling of LSPR, SPR and Fabry-Perot modes. It is expected that at least one of the modes shifts with the change of the surrounding refractive index and another mode becomes isolated from the surrounding environment. It is noted that at first, we ran experiments to understand and confirm the theoretical predictions of mode excitations. Using that understanding, we then then optimized the sensor to achieve the highest performance in terms of bulk sensitivity.

4.1 Reflection Measurement

The measurements of the reflection spectra were done using benchtop F40-UV thin film measurement system [90]. F40-UV excites a sample with a broadband light source spanning ultra-violet, visible and near-infrared wavelengths from 190 nm – 1100 nm, and then measures the reflection in a confocal setting. It uses these reflected spectra to determine the thickness of thin films. In our experiments, we use this capability to measure the reflection spectra and see how it changes as different refractive index fluids are used. F40-UV uses a confocal setting and the exact spot to be measured is seen through a microscope camera. The lens and thus, the beam spot can be changed all the way from 1000 μm to 10 μm using 5X to 100X microscope objectives. Since we want to measure many different designs, it makes it experimentally efficient and economical to put them in closely spaced arrays requiring only a single fabrication run. However, since periodic nature of the structure is also important for its operation, the spot size has to be large enough to excite multiple nanogratings. We used a 15X microscope objective to create a beam spot larger than 16 microns. This choice was confirmed by measuring the reflectance spectra with different microscope objectives and making sure the spectra was similar to larger beam spots. Further, at this low magnification, the presence of longitudinal fields is still low [91],

and the beam can be approximated as linearly polarized. This should allow experimental results to match simulations where plane wave approximation is used.

4.2 Refractive Index Liquids

To evaluate the sensing performance of the array, a series of Cargille index liquids [92] were employed, each having a known refractive index. These refractive indices ranged from 1.3 to 1.39, with increments of 0.01. This range was chosen as the refractive index of water lies within the range. We had designed the sensors to work optimally with water as the surrounding medium. Cargille fluids are oil-based liquids which are very stable, with no polarity and thus, the constituents do not electromigrate near gold surfaces. As such, the experiments exhibit high measurement repeatability when compared to conventional solutions used for sensor characterization like sodium chloride or glucose [93].

4.3 Effect of the Dielectric Spacer Layer

As mentioned in chapter 3, SiON and SiN were deposited as spacer layers on two different samples, in order to make sure that sufficient refractive index difference is created for exciting at least two modes in the visible to near IR range. To see the effect of dielectric spacer layers, both samples were tested using F40-UV while the surrounding refractive index was 1.33. **Figure 4.1a** shows the reflection spectra measured from nano-cube arrays with 200 nm side length and 400 nm pitch, with different dielectric spacer layers. **Figure 4.1b** also shows the reflection spectra measured from the nano-cylinder arrays with 200 nm diameter and 400 nm pitch with different dielectric spacer layers. These two geometries are the optimized arrays we designed in chapter 2. As seen in **Figure 4.1a**, two plasmonic resonance features are excited for both cubic arrays with different spacer layers. The resonance features of the cubic array with SiN spacer layer are slightly red shifted compared to the cubic array with the SiON spacer layer. This is due to the higher refractive index of the SiN spacer layer and follows the trend we had observed in simulations. At this wavelength range, the real permittivity of the gold is negative and decreases (the absolute value increases) as the wavelength increases. When the refractive index of the dielectric layer is higher, at resonance the real permittivity of the gold must decrease, in order to satisfy the resonance conditions of the surface plasmons at the interfaces of dielectric layer with gold layers. Therefore, the resonances will happen at a higher wavelength to match the gold permittivity with the dielectric permittivity. As seen in **Figure 4.1a**, a very weak resonance dip is also happening around 600 nm wavelength. This resonance was also observed during the simulations in chapter 2 as seen in **Figure 2.2a**, at 637 nm wavelength and is a Fabry-Perot (FP) mode, coupled with

the LSPR mode. Compared to the simulations, the mode is blue shifted and also weakened, due to several reasons. Firstly, the FP mode is happening at a different wavelength due to the presence of the Ti adhesion layers. Further, chromatic dispersion of all the layers especially the dielectric layer as compared to the simulations and the small thickness variations of the deposited layers also change the results. In the simulations, we had just used a single value of refractive index for the spacer layer for all wavelengths. That was an approximation. There are also experimental reports [94, 95] regarding the effect of adhesion layers on the variations of resonance wavelength of plasmonic modes which match the blue shift we observe. With regards to the mode being weakened with a reduction of Q , a few reasons include the surface roughness, variations in the thickness and refractive index of different layers and also not achieving perfectly sharp corners in the nano-cubes.

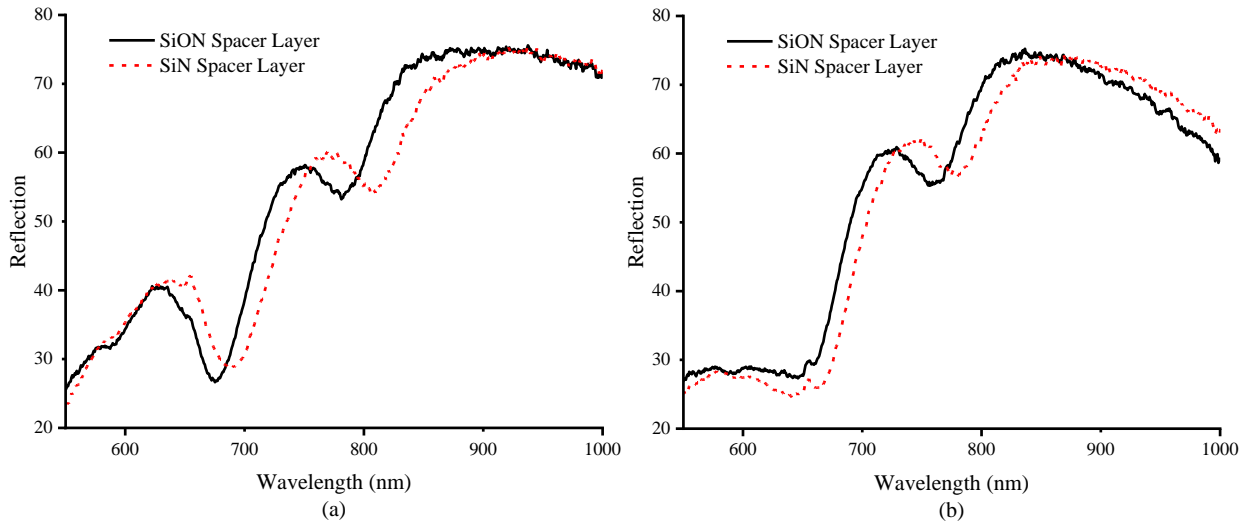


Figure 4.1. Reflection spectra measured from nano-grating arrays with two different dielectric spacer layers of SiON and SiN for (a) cubes with 200 nm side length and 400 nm pitch, and (b) cylinders with 200 nm diameter and 400 nm pitch.

Another mode is being observed around the 700 nm wavelength. As discussed in chapter 2, this mode is an LSPR dominant mode in which is coupled with the SPR modes of the underneath layers. This mode was observed on 757 nm wavelength during the simulations. However, like the FP mode, the LSPR dominant mode is also blue shifted and weakened due to the same reasons mentioned above. A third mode is excited around the 800 nm wavelength. This mode is the SPR dominant mode which is due to the strong plasmonic modes getting excited in between the gold film and glass substrate, coupled with the SPR and LSPR modes happening on the top layers. During the simulations this mode was observed in NIR region at 945 nm wavelength. The mode is also blue, shifted to the visible region and

weakened (qualitative reduction in Q). These results show that indeed, all the predicted modes in the simulations are being excited. However, all the modes are blue shifted and have a lower quality factor as compared to the simulations. The structure was designed to completely isolate the SPR dominant mode from the surroundings. However, the chromatic dispersion happening for the dielectric spacer layer changes this situation and the structure may not be optimized for achieving our goals. Thus, it becomes important to experimentally study the variations to find the optimal solutions.

For the nano-cylinders, as seen in **Figure 4.1b**, again two major plasmonic modes are excited for both arrays with SiON and SiN spacer layers. A very weak mode is happening just below 600 nm wavelength which is an FP mode coupled with the LSPR modes, as observed during the simulations. The LSPR dominant mode, happening between 600 nm and 700 nm wavelength, is divided into two modes, suggesting that full Fano resonance is not achieved. This was also predicted during the simulations in chapter 2 for non-optimized structures, (see **Figure 2.3a**). The mode excited in the lower wavelength is coupled with an SPR mode in the substrate, while the mode in the higher wavelength is not coupling with the substrate. This will cause the lower wavelength mode to move slower when the surrounding index changes, compared to the mode in the higher wavelength when the refractive index of the surrounding medium is changed. For the LSPR dominant mode, the arrays with the SiN spacer layer have a stronger resonance compared to the SiON array. Also, the mode is slightly red shifted when the spacer layer is changed from SiON to SiN. Finally, the SPR dominant mode is happening around 800 nm wavelength which is blue shifted as well compared to the simulations.

Comparing **Figure 4.1a** and **b** together, the cubic arrays are able to excite a stronger LSPR dominant mode compared to the cylindrical arrays. This was observed in simulations, and it is due to stronger plasmonic effect happening in the sharp corners. However, the SPR dominant mode is not very different for the cubic and cylindrical arrays, since this mode is highly dependent on the SPR mode happening in thin gold layer and less dependent on the LSPR modes happening in the grating layer.

In conclusion, both SiON and SiN spacer layers provide sufficient refractive index for exciting two separate plasmonic modes in the visible range. Further, the expected modes are being observed in the spectra. Comparing the experimental results with the simulations, the modes are blue shifted and weakened. These results gave us confidence to experimentally optimize the structures. Experiments were designed to study the effect of lattice separation, size and shape of the nanostructures and are described next.

4.4 Effect of Pitch Variations

Nano-grating arrays were fabricated with different lattice spacings of 400, 450, 500, 550 and 600 nm. To see the effect of pitch variations, nano-cube and nano-cylinder arrays with side length and diameter of 200 nm respectively, were tested for the sample with the SiON spacer layer. The surrounding refractive index was set to 1.33. **Figure 4.2a, b** shows the reflection spectra for different pitch values for nano-cubes and nano-cylinders, respectively. The reflection spectra for the underneath layers, off the arrays is also shown. As seen in **Figure 4.2**, for both shapes, as the pitch increases, the resonance wavelengths shift to longer wavelengths. This was predicted by the simulations. Further, both modes get weaker as the pitch increases. This is due to the reduced near-field coupling between neighboring nanostructures and the reduction in the surface area of the grating layers. This leads to a reduction of absorption in surface plasmons in the top layers. For both shapes, after 500 nm pitch, more than two plasmonic modes can be observed which is due to the separation of the modes that were previously creating Fano resonances. As a result, these separated modes are weaker and have lower quality factors. Also, for pitch values above 550 nm, a mode is getting excited between the 600 nm and 700 nm wavelengths which is very similar to the mode in the off-the-pad reflection spectra. This shows that the near field coupling is negligible for these pitches and the arrays are allowing the light to transmit without absorption for shorter wavelength. For the purpose of sensitivity, we are mainly interested in those arrays that can produce Fano resonances with higher Q. Thus, a pitch below 500 nm is needed.

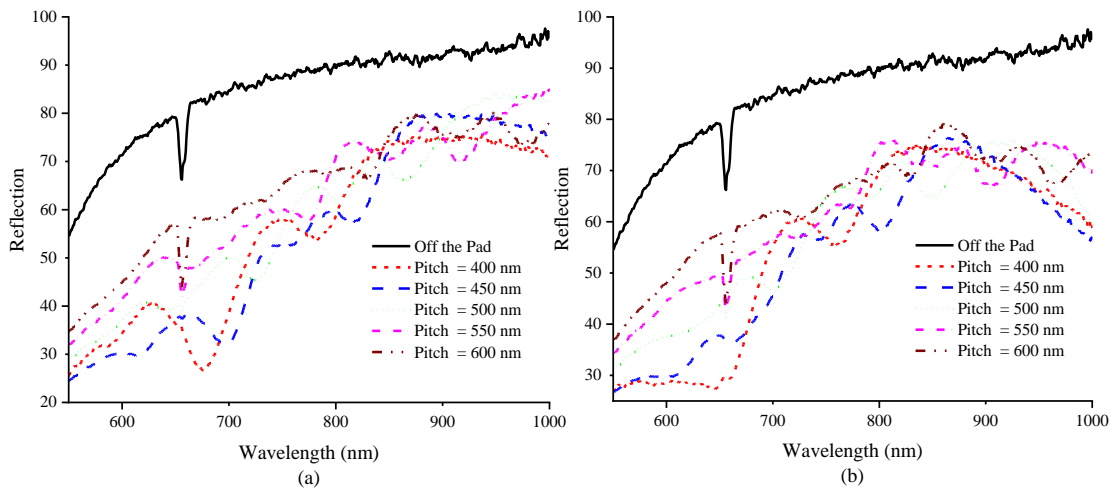


Figure 4.2. Reflection spectra measured from nano-grating arrays with different lattice spacing for the sample with SiON spacer layer for (a) cubes with 200 nm side length, and (b) cylinders with 200 nm diameter.

4.5 Effect of Cube Side Length and Cylinder Diameter

Cubic and cylindrical arrays were fabricated with five different side lengths and five different diameters of 170, 180, 200, 220 and 250 nm, respectively. **Figure 4.3a, b** shows the reflection spectra for the nano-cube arrays with SiON spacer layer and different side lengths. In **Figure 4.3a, b** the pitch is 400 nm and 450 nm, respectively. The surrounding index was also 1.33. As seen in **Figure 4.3a**, by increasing the cube side length, the LSPR dominant mode gets stronger, and its resonance wavelengths shifts to longer wavelengths. The reason for the modes getting stronger is increased near-field coupling, increased surface area of the cubes and excitation of more surface plasmons. However, the SPR dominant mode is qualitatively stronger for 220 nm side length as compared to the 250 nm side length. The SPR dominant mode is a Fano resonance, and the constituent resonances seems to be getting separated in wavelength as the side length increases to 250 nm and thus the Q decreases. In chapter 2, the optimized cubic structure with 200 nm side length, has the highest Q for both plasmonic modes. However, as can be seen in **Figure 4.3a**, the cubic array with 220 nm side length is generating two plasmonic modes with the highest Q compared to the other arrays with similar pitch and different side length. The reason for this is the small changes in the thickness of different layers, the Ti adhesion layers and also the chromatic dispersion of the dielectric layer, which changed the resonance conditions and led to the reduction of Q for the cubic array with 200 nm side length. For the cubic arrays when the pitch is increased to 450 nm pitch, as seen in **Figure 4.3b**, when the cube side length is less than 220 nm, more than two dips is observed in the reflection spectra for the LSPR dominant mode. This means that the arrays need further optimization in order to create Fano resonances from these modes. Once the side length reaches 220 nm, two strong plasmonic modes are being generated from the Fano resonances of LSPR and SPR modes. As the side length increases to 250 nm, both modes get stronger and also shift to longer wavelengths. Comparing **Figure 4.3a** and **b**, arrays with 400 nm pitch are creating stronger plasmonic modes and thus the cubic array with 220 nm side length while for 450 nm pitch, the optimal design moves to 250 nm side length. Qualitatively, it appears that the 400 nm pitch design provides the highest Q for both LSPR dominant and SPR dominant modes and should be optimal for self-referencing sensor. Nevertheless, we will also study the sensitivity of both the pitches. .

Figure 4.3c, d shows the reflection spectra for the cylindrical shapes with 400 nm and 450 nm pitch, respectively. The spacer layer is SiON, and the surrounding refractive index is 1.33. For nano-cylinder arrays with 400 nm pitch, as seen in **Figure 4.3c**, the strength of the LSPR dominant mode increases as the diameter increases, a behavior similar to the cubic arrays. Further, the resonance wavelengths of

the modes are red shifted. For the 200 nm and 250 nm diameter arrays, the LSPR dominant mode consists of two modes, which was discussed in the previous section. However, as the diameter increases to 250 nm, these modes combine together completely and thus generate a Fano resonance with higher Q. For the SPR dominant mode, the highest Q is obtained for the cylindrical array with 200 nm diameter. As the pitch increases to 450 nm, as shown in **Figure 4.3d**, for each cylindrical array, several dips are created in the visible range. Although by increasing the diameter of the nano-cylinders, some of the modes combine together and create Fano resonances, even for the highest diameter, modes are still not fully combined, and the structure needs further optimizations.

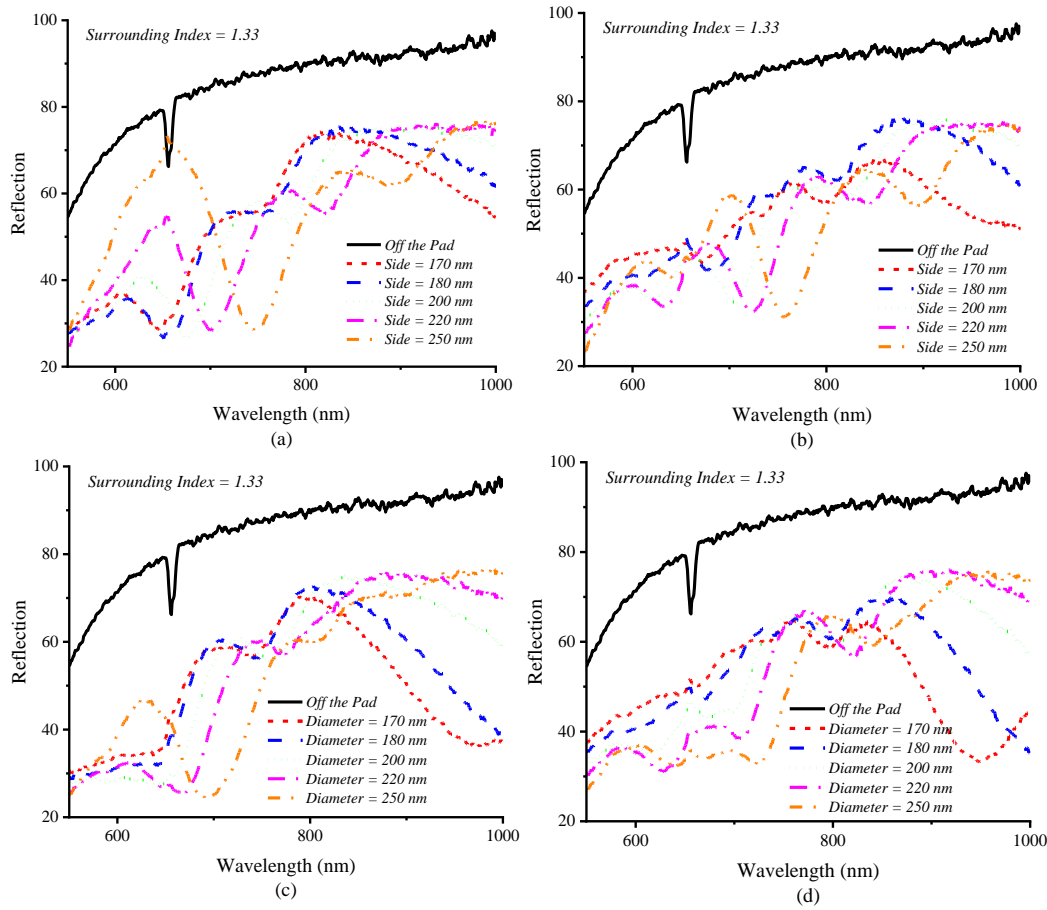


Figure 4.3. Reflection spectra for the sample with SiON spacer layer for (a) cubic arrays with 400 nm pitch and different side length, (b) cubic arrays with 450 nm pitch and different side length, (c) cylindrical arrays with 400 nm pitch and different diameters, and (d) cylindrical array with 450 nm pitch and different diameters.

Figure 4.4a-d shows the reflection spectra of the sample with the SiN dielectric spacer layer. **Figures 4.4a, b** belong to the cubic arrays with different side length and 400 nm and 450 nm pitch, respectively.

Further, **Figures 4.4c, d** are for cylindrical arrays with different diameters and 400 nm and 450 nm pitch, respectively. As the side lengths and diameters change, the reflection spectra vary similar to the sample with the SiON spacer layer. However, it seems that the cubic array with 400 nm pitch and 200 nm side length is showing a higher Q for the SPR dominant mode compared to the other cubic arrays. The LSPR dominant mode is still stronger for the cubic array with 220 nm and 250 nm side lengths. For the cylindrical arrays, the array with diameters of 200 nm with 400 nm pitch, is performing better than other arrays in exciting the SPR dominant mode. The LSPR dominant mode turns into a fine Fano resonance once the diameter reaches 250 nm, as seen in **Figure 4.4c**. However, the self-referencing SPR dominant mode weakens. For cylindrical arrays with 450 nm pitch in **Figure 4.4d**, several modes are excited separately and thus the structure is not suitable for achieving Fano resonances.

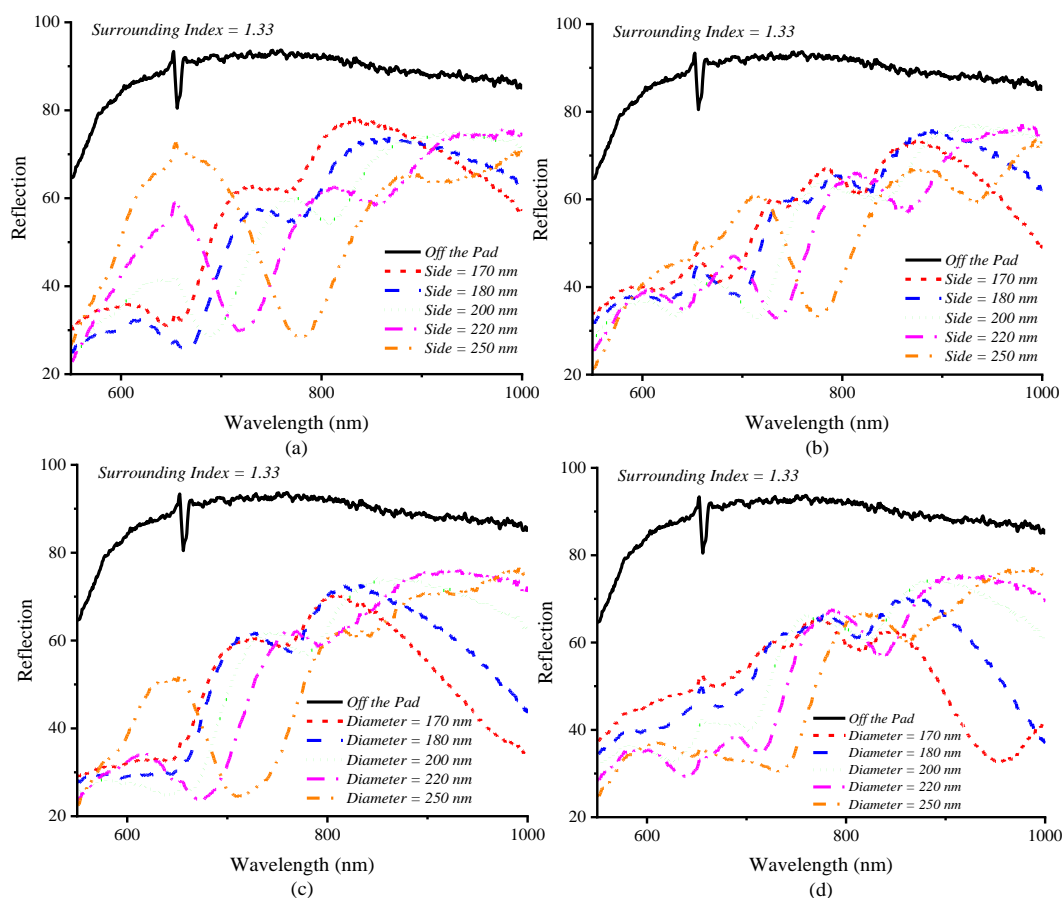


Figure 4.4. Reflection spectra for the sample with SiN spacer layer for (a) cubic arrays with 400 nm pitch and different side length, (b) cubic arrays with 450 nm pitch and different side length, (c) cylindrical arrays with 400 nm pitch and different diameters, and (d) cylindrical array with 450 nm pitch and different diameters.

4.6 Performance of the Triangular Arrays

As discussed in chapter 3, equilateral triangular arrays were also fabricated with different side lengths and lattice spacings, in an effort to achieve stronger plasmonic resonances due to the presence of sharp corners in triangles. **Figure 4.5a, b** shows the reflection spectra of the sample with SiON spacer layer with equilateral triangular arrays with side lengths of 220 nm and 250 nm, respectively. The arrays were tested for different pitches and the surrounding index was set to 1.33. As seen in **Figure 4.5**, for shorter wavelengths, triangular arrays allow the light to pass through them, and the reflection spectra has a minor resonance similar to the reflection from the off the pads. This resonance belongs to the surface plasmons excited in the gold film underneath. For longer wavelengths, some weak modes are observed, however, compared to the cylindrical and cubic arrays, these modes have much lower Q, and the triangular arrays are not showing any advantage over the cubic and cylindrical arrays. The reason for this poor performance in regard to the mode excitation, despite the sharper corners, is the smaller surface area of the triangles compared to the cubes and cylinders. One can achieve stronger plasmonic modes by either increasing the side length of the triangles or decreasing the lattice spacing. Both actions will require further experiments during the lithography for finding the right e-beam dose. Thus, we gave priority to the cubic and cylindrical arrays that were already working and did not go forward with the triangular shapes.

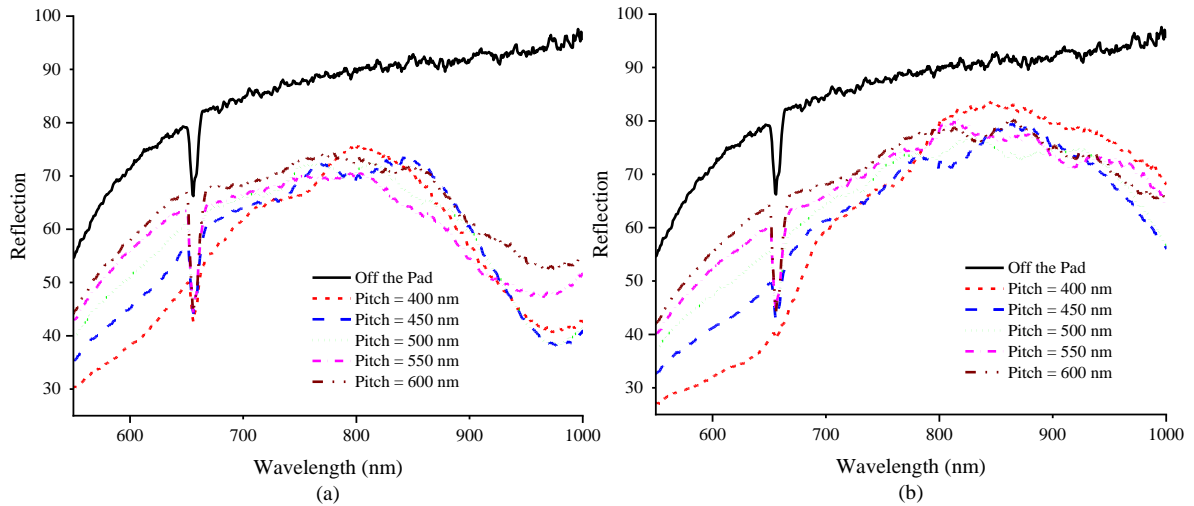


Figure 4.5. Reflection spectra of the sample with SiON spacer layer with equilateral triangular arrays with side lengths of (a) 220 nm and (b) 250 nm, for different lattice spacings.

4.7 Bulk Sensitivity

To further optimize the structures, nano-grating arrays were tested for the bulk sensitivity when the surrounding refractive index was subjected to change. Cargille refractive index liquid were used with different values from 1.33 to 1.39 and the reflection spectrum of each array was measured using the F40-UV. After applying the Cargille oil to the sample, appropriate time (~2 minutes) was given to the oil to spread over the sample. After each test, samples were cleaned with IPA and Acetone, multiple times, and dried with nitrogen, and then the next oil was applied.

4.7.1 Cubic Nano-gratings, SiON Spacer Layer, Pitch 400 nm

Figure 4.6a-e shows the reflection spectra of the cubic arrays with different surrounding refractive index and side lengths of 170, 180, 200, 220 and 250 nm, respectively. **Figure 4.6** is for the sample with SiON spacer layer and 400 nm pitch. For comparison, when the surrounding was air, the reflection from each array and off the arrays were also measured. For cubic array with 170 nm side length in **Figure 4.6a**, two major modes are excited and are labelled on the figure. The modes are expected to red shift by increasing the surrounding refractive index, unless a mode is strongly coupled with SPR modes of the underneath layers and the Fano conditions change. By changing the surrounding index from $n=1.33$ to $n=1.34$, the resonance wavelengths of the modes are blue shifted. This means increasing the surrounding index, changes the dominance of the LSPR and SPR modes. In this situation, the resonance wavelengths are not going to simply red shift as the mode coupling conditions are being changed. In simple terms, the Fano resonances are still being created and the constituent modes shift differently with changing refractive index. Once the surrounding index is increased above 1.34, mode 1 starts to red shift in resonance wavelength and thus the LSPR-dominant Fano resonance is achieved. Mode 2 also starts to shift red in wavelength, but the shift is slower than mode 1.

Another weak mode is also observed between modes 1 and 2, and as the side lengths of the cubes increased to 180 nm and 200 nm, as seen in **Figure 4.6b, c** respectively. With increasing refractive index of the surrounding medium, this weak mode moves toward mode 2 and eventually create a Fano resonance. For the cubic array with 180 nm side length in **Figure 4.6b**, similar to the 170 nm side length cubes, the resonance wavelengths start to red shift for both modes when the surrounding refractive index goes above 1.34. Compared to the 170 nm side length cubes, the quality factor of mode 1 is increased and mode 2 seems to be shifting slower, suggesting that the mode is getting isolated from the top region. For the cubic array with 200 nm side length in **Figure 4.6c**, the quality factors of both modes

are increased compared to the smaller size cubic arrays. Further, it seems that the Fano resonance of mode 1 is almost created and the LSPR mode is becoming the dominant mode, and thus the resonance wavelength of mode 1 is red shifting when the refractive index increases from $n=1.33$. However, in mode 2, the SPR mode becomes the dominant mode only when the surrounding index increases to 1.35 and the mode gets isolated from the top. After this, this mode does not shift in wavelength with increase in the surrounding refractive index.

For the cubic array with 220 nm side length in **Figure 4.6d**, the quality factors of the modes are enhanced, compared to the smaller size arrays, suggesting that the Fano resonance conditions have improved. The resonance wavelength of mode 1 is red shifting with the surrounding index increment, which shows the dominance of the LSPR mode. For mode 2, once the surrounding refractive index reaches 1.35, the mode is perfectly isolated from the top and does not change with refractive index which implies on the complete dominance of the SPR modes. For the cubic array with 250 nm side length in **Figure 4.6e**, the resonance of mode 1 is qualitatively stronger as compared to mode 1 in the array with 220 nm side length. Further, mode 1 is red shifting with the increase of the surrounding index which shows the dominance of the LSPR mode. On the other hand, mode 2 has lower Q compared to mode 2 in the array with 220 nm side length when the surrounding refractive index is 1.33. As the refractive index is increased, a stronger resonance is achieved. However, it is still less than that of the array with 220 nm side length. Due to this reason, even for a surrounding index of 1.35, the mode is not perfectly isolated from the top and shifts slightly in wavelength as the surrounding refractive index is increased. These results suggest that side lengths of 220 nm provide the best design for our goals where we have a sensitive LSPR dominant mode and an isolated SPR dominant mode when the surrounding refractive index is 1.35 or higher.

For quantitatively measuring the sensitivity of the sensors, we only consider those arrays with high Q resonance features and strong Fano resonances, which in this case are cubic arrays with 200, 220 and 250 nm side lengths, shown in **Figure 4.6c-e**, respectively. As the experimental data is very noisy, firstly we used Savitzky-Golay algorithm to smooth the data [96]. The Savitzky-Golay algorithm is a digital signal processing technique used for smoothing and differentiation of noisy data. This method aims to enhance the quality of data by removing high-frequency noise while preserving the essential features of the signal. It operates by fitting a polynomial function to a small window of neighboring data points and then using this polynomial to estimate the smoothed value at the center point of the window [96]. While it has never been used in plasmonics characterization before to our knowledge, it

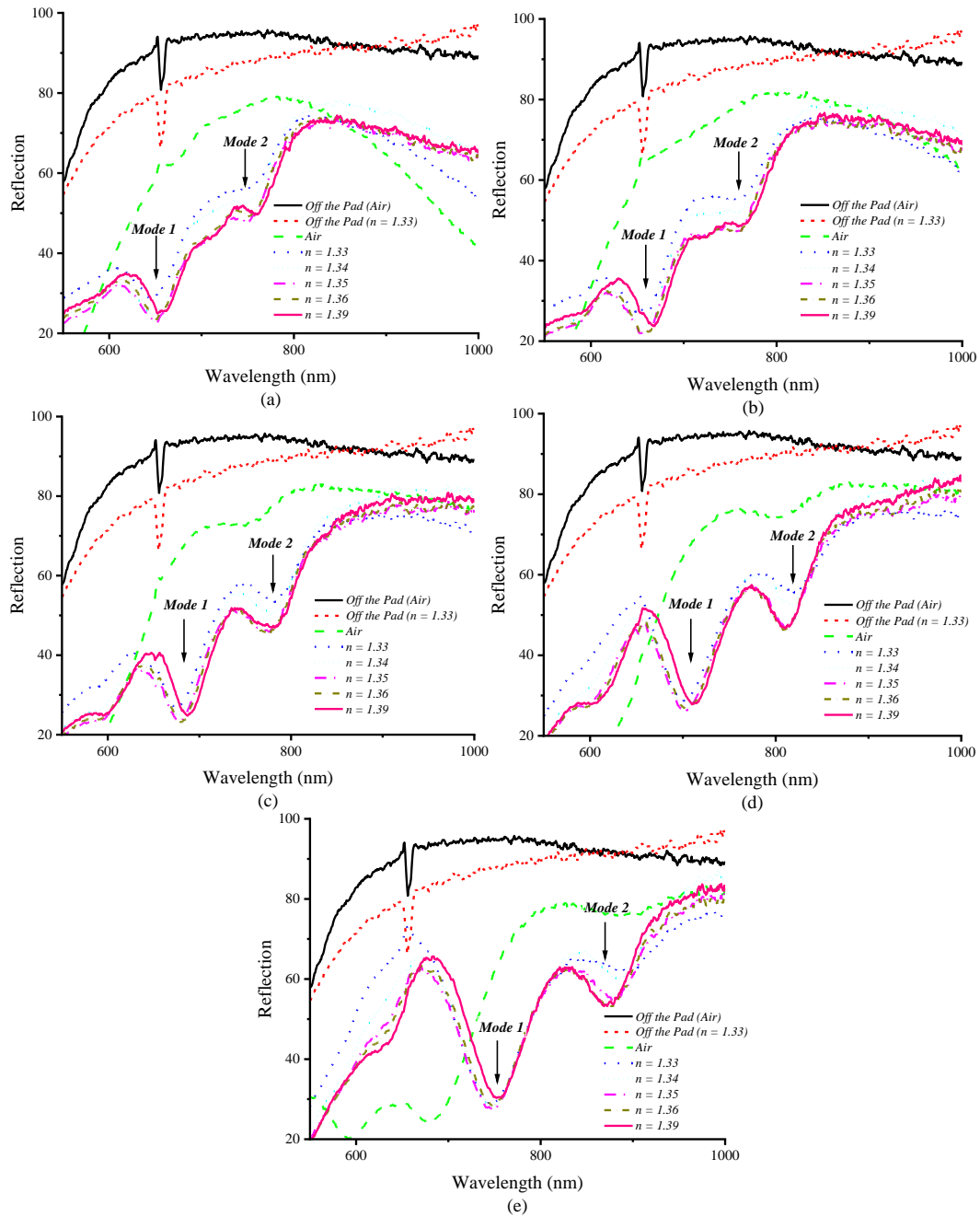


Figure 4.6. Reflection spectra of the cubic arrays with different surrounding refractive index and side lengths of (a) 170 nm, (b) 180 nm, (c) 200 nm, (d) 220 nm, and (e) 250 nm, respectively. for the sample with SiON spacer layer and 400 nm pitch.

has been successfully applied to spectroscopy data for machine learning especially in food analysis [97]. After smoothing the data, we calculated the first derivative of the reflection spectra for each array with different surrounding indices. Any local minimum and maximum in the reflection spectra will

appear in the first derivative as zero. In this way, we can calculate the sensitivity accurately. **Figure 4.7a-e** shows the first derivatives of the reflection spectra with different surrounding indices and corresponding changes in the resonance wavelengths of mode 1 and mode 2, for the cubic arrays with side lengths of 200, 220 and 250 nm. Mode 1 and Mode 2 are labelled in the first derivative curves and the wavelengths at which the derivative goes to zero. We notice the features become more apparent in the first derivative curves and this shows that this method can be powerful in analyzing sensors.

For the cubic array with 200 nm side length in **Figure 4.7a, b**, by fitting a line to the mode 1 resonance wavelengths, the sensitivity is found to be 223 nm/RIU. Further, mode 2 is isolated from the top when the surrounding index is 1.35 and 1.36, but it moves again when the surrounding index increases to 1.39. However, it moves much slower compared to mode 1, because of its strong dependency on the SPR modes. As we discussed earlier, when the surrounding refractive index increases higher than 1.35, mode 1 becomes an LSPR dominant Fano resonance and thus its resonance wavelength red shifts with the surrounding index increment. This also can be seen in **Figure 4.7b** in which after a refractive index of 1.35, the resonance wavelengths of mode 1 are almost perfectly located on a line. This suggests that mode 1 is stabilized as an LSPR dominant mode. If we calculated the sensitivity of mode 1 by only considering the surrounding indices of 1.35 and higher, the sensitivity enhances to 285 nm/RIU. For the cubic array with 220 nm side length in **Figure 4.7c, d**, the sensitivity of mode 1 is estimated to be 161 nm/RIU, which is lower than the array with 200 nm side length. Further, mode 2 is completely isolated from the top once the surrounding index passes 1.35. If we measure the sensitivity of mode 1 for refractive indices higher than 1.35, the sensitivity increases to 226 nm/RIU. For the cubic array with 250 nm side length in **Figure 4.7e, f**, the sensitivity of the mode 1 is found to be 117 nm/RIU. Further, mode 2 is blue shifting slowly with the surrounding index increment and seems to be almost isolated from the top when the surrounding index passes 1.36. These results suggest that the bulk sensitivity of mode 1 is higher when the side length is smaller, opposite to what would be expected if only near-field coupling was dominant.

During the design and simulations of the nano-cubes, we were able to achieve a sensitivity of 429 nm/RIU. Looking at the sensitivity values we achieved in the experiments, it seems that the sensors are not performing as expected. We were expecting to achieve a lower sensitivity compared to the simulations, due to the reduction in Q and changes in the refractive index of the spacer layer and thickness of deposited layers. However, because our simulations were able to predict many details correctly, we believed the sensors must be able to achieve a sensitivity value close to the simulations.

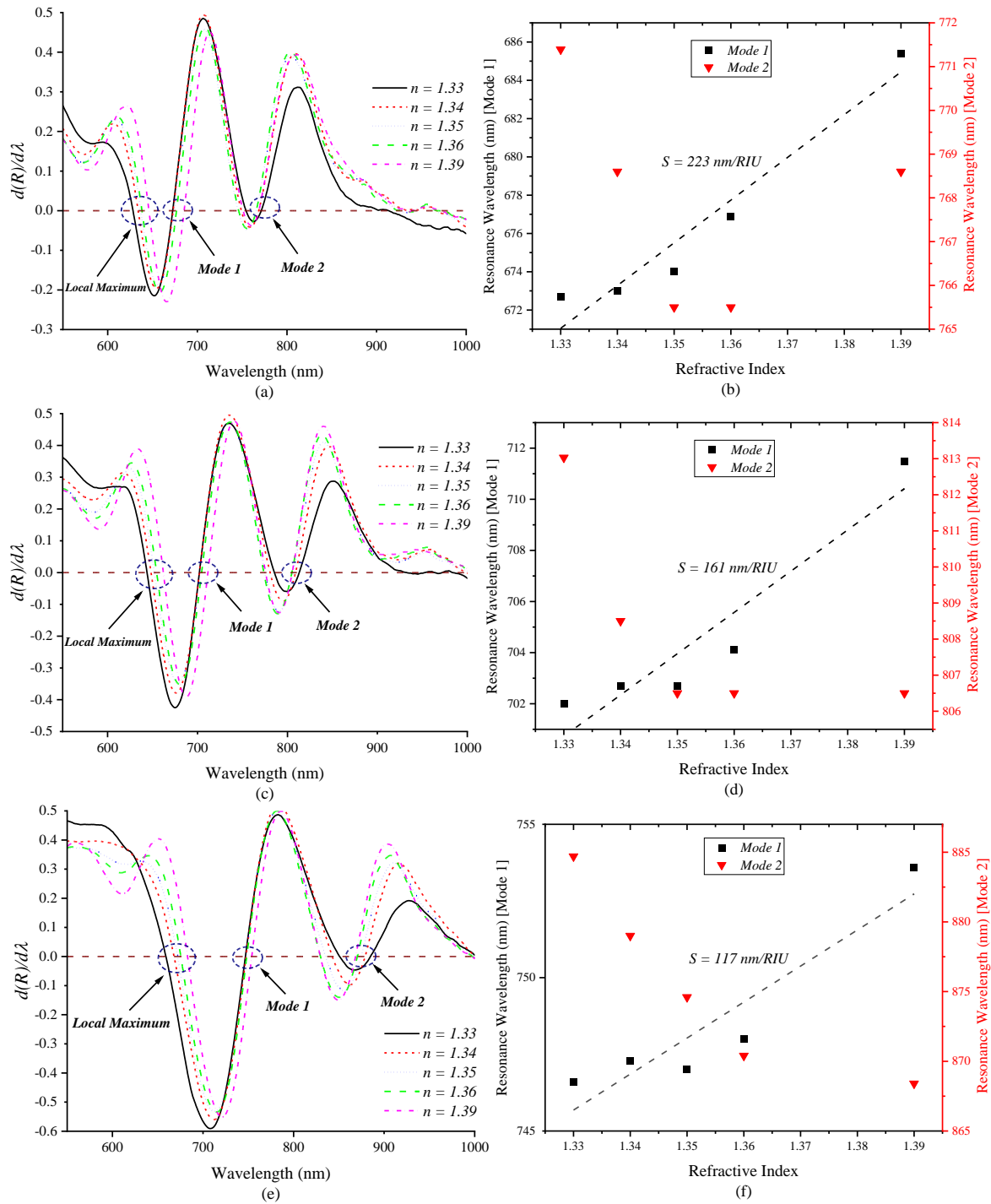


Figure 4.7. (a, c, e) First derivatives of the reflection spectra of the cubic arrays with 200, 220 and 250 nm side length respectively, for different surrounding indices and, (b, e, f) changes in the resonance wavelengths of mode 1 and 2 corresponding to **Figure 4.7a, c, e** respectively.

By taking a better look at **Figure 4.6**, we realize that some parts of the reflection spectra are moving faster than the other parts. For example, the left side of mode 1 is moving faster than the right side of it. It seems that, as we go to the longer wavelengths, the dependency of mode 1 on the LSPR modes of the grating layer gets weaker. Thus, as we go to the longer wavelengths, the sensitivity decreases until we reach mode 2 and the mode gets completely isolated from the LSPR modes of the top layer. Thus, to reveal the full sensing potential of the sensors, we need to select a point on the left side of mode 1, where the LSPR mode is dominant. There is a local maximum between 600 nm to 700 nm wavelengths for all of the arrays in **Figure 4.6**. This local maximum is created due to the existence of two dips on its both sides. One dip on its left side, around 600 nm wavelength, due to the excitation of an FP-LSPR coupled mode and the other dip on its right side, due to the excitation of an LSPR-SPR mode (mode 1). Looking at the shape of this local maximum, the quality factor of the peak is very similar to the quality factor of mode 1, and thus its resonance frequency seems to be an appropriate measurement point for sensor. These local maximums are also labelled on the first derivative curves in **Figure 4.7a, c, e**. It is clear from the first derivative curves that the local maximum is moving faster than mode 1. Further, the change of wavelength with refractive index is more linear than if the resonance of mode 1 is considered. **Figure 4.8a-c** shows the resonance wavelengths of the local maximum for different surrounding refractive indices, for the cubic arrays with 200, 220 and 250 nm, respectively. For each figure, a line is fitted to the points for measuring the sensitivity of the arrays. As seen in this figure, sensitivity values of 227, 291 and 367 nm/RIU are achieved for the cubic arrays with 200, 220 and 250 nm side length, respectively. These values are much higher than the sensitivity of mode 1. For the cubic array with 250 nm side length, a sensitivity of 367 nm/RIU is achieved which is close to the one we predicted during the simulations. The sensitivity of mode 1 can be increased by further optimizing the structure in a way that the LSPR mode is pushed to the center of mode 1.

Figure 4.9 shows the reflected colors from the cubic arrays with SiON spacer layer and 400 nm pitch, with different surrounding refractive indices. When moving to the right side of the figure, the surrounding refractive index increases, while moving from top to bottom the cube side length increases. The colors were captured from the center of the arrays while the sample was being tested under F40 camera. As seen in **Figure 4.9**, changing the surrounding from air to $n = 1.33$ causes a perceptible change in the reflected colors, for all the arrays. This is due to the excitation of the strong plasmonic modes while the surrounding index is 1.33, which manipulates the intensity of the reflection spectra. When the surrounding index changes in the range of 1.33 to 1.39, different arrays reflect different colors

which shows the dependency of these plasmonic modes on the size of the nanostructures and also surrounding medium.

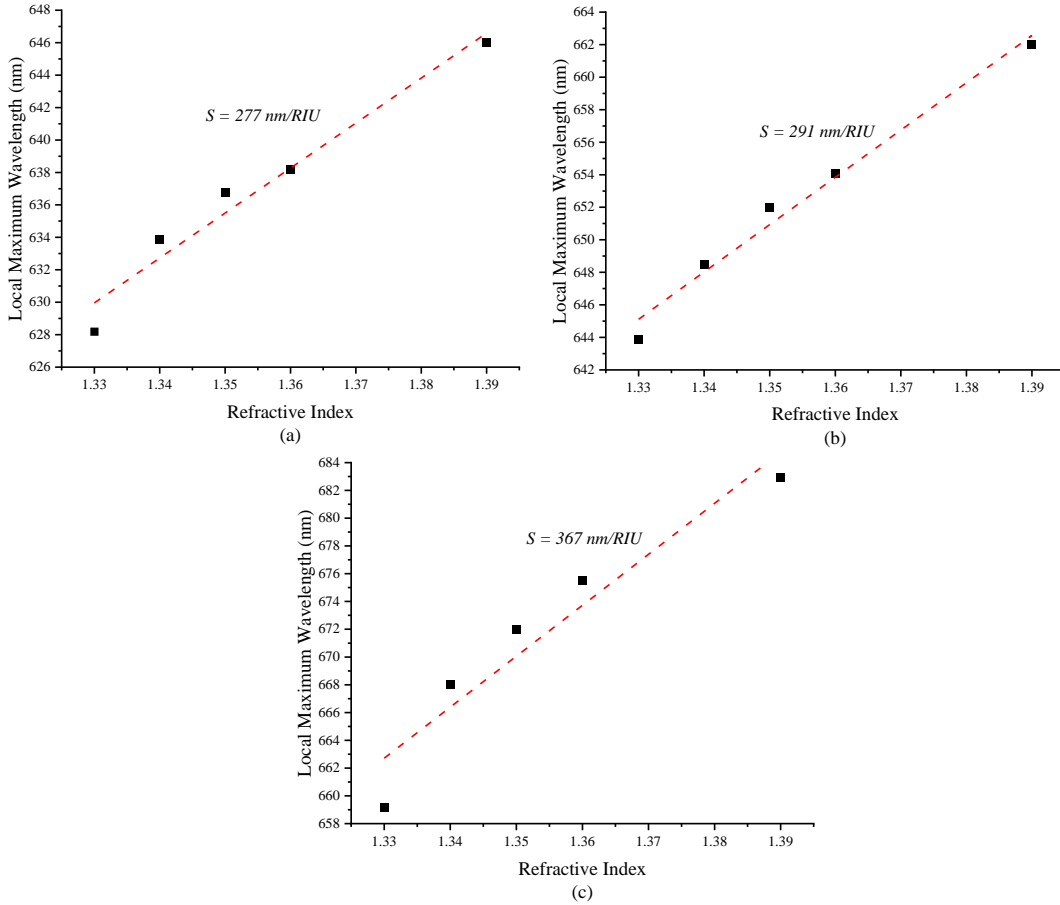


Figure 4.8a-c. Resonance wavelengths of the local maximum for different surrounding refractive indices, for the cubic arrays with 200, 220 and 250 nm, respectively.

4.7.2 Cubic Nano-gratings, SiON Spacer Layer, Pitch 450 nm

Figure 4.10a-e shows the reflection spectra of the sample with SiON spacer layer, and cubic arrays with 450 nm pitch and side lengths of 170, 180, 200, 220 and 250 nm, respectively. The reflection spectra were measured while the surrounding refractive index was changed. When the cube side length is smaller than 220 nm, a third mode is excited in between mode 1 and mode 2. As the side length increases, the third mode moves to the longer wavelengths and gets coupled with mode 2 and creates a

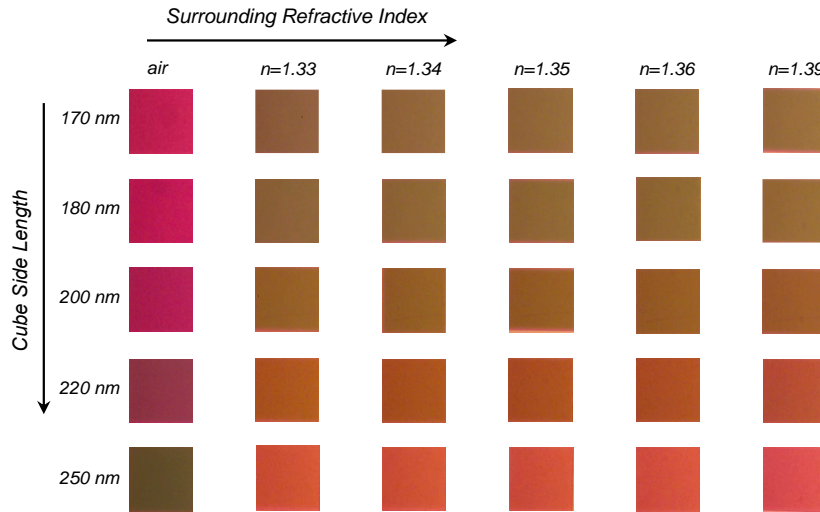


Figure 4.9. Reflected colors from the cubic arrays with SiON spacer layer and 400 nm pitch. Moving from top to bottom, the cube side length increases, and from left to right, the surrounding refractive index increases.

stronger mode with higher Q. This transition can be clearly seen in **Figure 4.10a-e**. Further, after a side length of 200 nm, the FP-LSPR mode around 600 nm wavelength, gets stronger and its quality factor increases. In regard to the Q of the modes, the cubic array with 250 nm side length in **Figure 4.10e** is performing better than other arrays. When the surrounding refractive index changes, different parts of the reflection spectra start to shift with different speeds. In shorter wavelengths, the dependency of the curves on the LSPR mode of the grating layer is higher and thus the reflection curves move faster. In longer wavelengths, the SPR modes of the underneath layers get stronger and thus the modes move slower with the change in surrounding refractive index. Once the side length reaches 250 nm and the surrounding refractive index goes higher than 1.35, the self-referencing mode is completely isolated from the surrounding environment, as seen in **Figure 4.10e**. It can be seen that the local maximum on the left side of the mode 1 is moving faster than the mode 1 and thus is a suitable feature for examining the sensing performance.

Figure 4.11a-f shows the first derivatives of the reflection spectra for different refractive indices and the changes in the resonance wavelengths of mode 1 and 2 and the local maximum, for the cubic array with 200, 220 and 250 nm side length, 450 nm pitch and SiON spacer layer. Mode 1 and 2 and the local maximum are labelled in **Figure 4.11a, c, f**. For the cubic array with 200 nm side length in **Figure 4.11a, b**, the sensitivity values of the mode 1 and the local maximum are very close together and are 223 and 224 nm/RIU, respectively. Mode 2 is shifting slowly and is not isolated from the top yet.

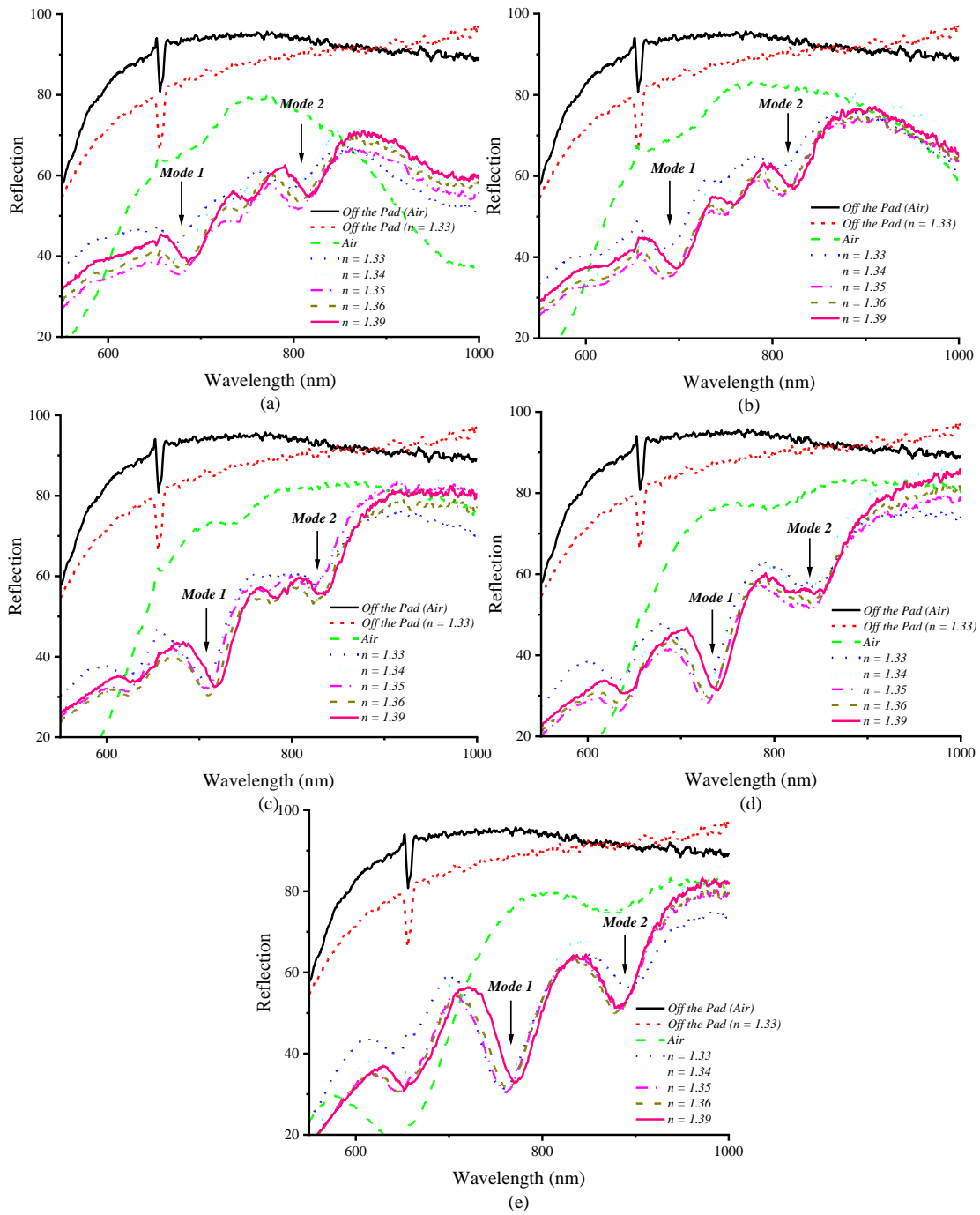


Figure 4.10a-e. Reflection spectra of the cubic arrays with different surrounding refractive index and side lengths of 170, 180, 200, 220 and 250 nm, respectively. The dielectric spacer layer is SiON and the lattice spacing is 450 nm.

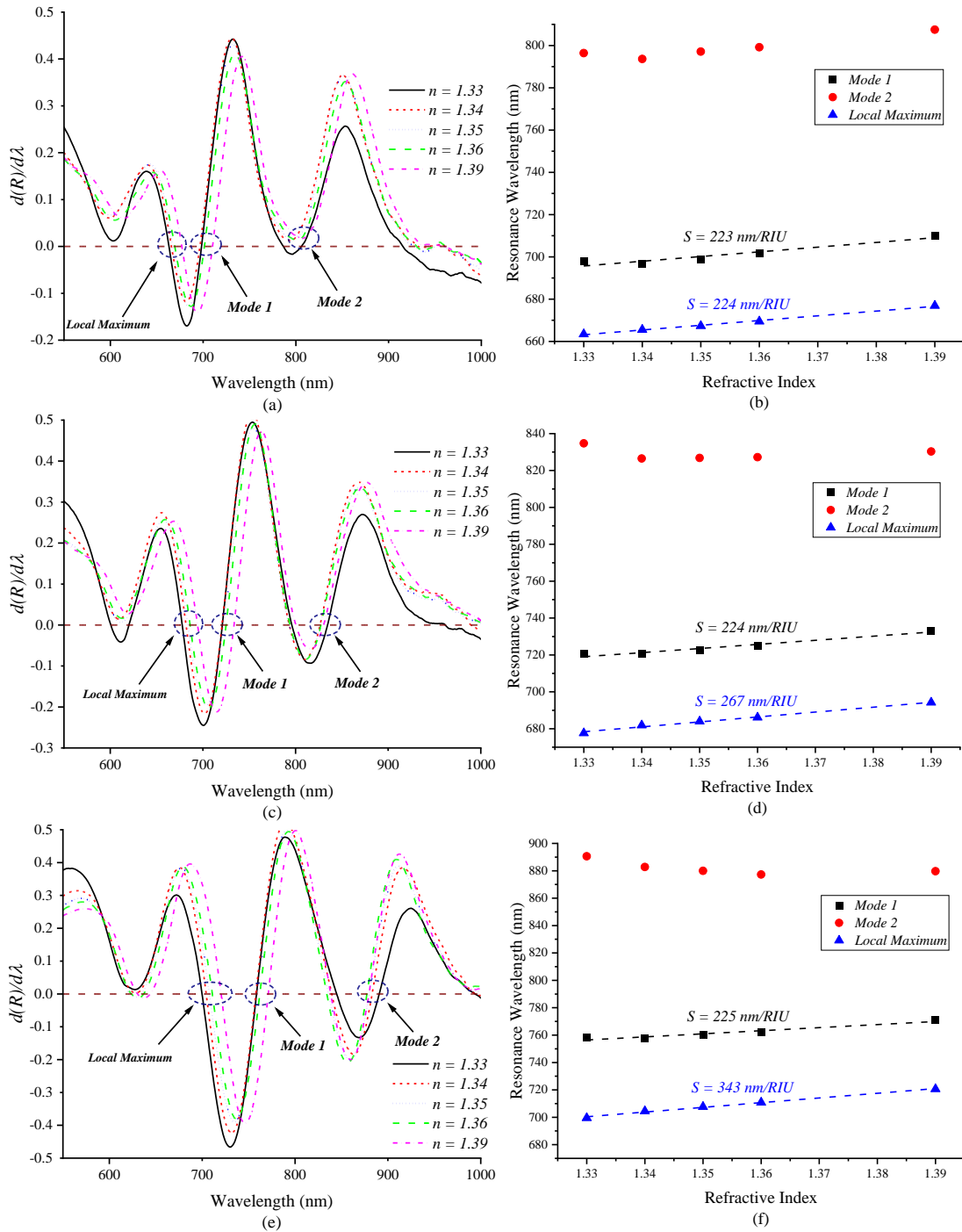


Figure 4.11. (a, c, e) First derivatives of the reflection spectra of the cubic arrays with 200, 220 and 250 nm side length respectively, for different surrounding indices and, (b, e, f) changes in the resonance wavelengths of mode 1 and 2 and the local maximum, corresponding to **Figure 11, a, c, e** respectively. The dielectric spacer layer is SiON and the lattice spacing is 450 nm.

For the 220 nm side length in **Figure 4.11c, d**, the sensitivity of mode 1 is approximately the same as the cubic array with 200 nm side length, however, the sensitivity of the local maximum is increased to 267 nm/RIU. Mode 2 also seems to be getting isolated from the top, when the surrounding index increases to 1.35 and higher. For the cubic array with 250 nm side length in **Figure 4.11e, f**, the sensitivity of mode 1 is slightly increased to 225 nm/RIU, compared to other arrays. The local maximum is shifting much faster and a sensitivity of 343 nm/RIU is achieved. Mode 2 seems to be slowly moving when the refractive index increases but for refractive indices in the range of 1.36 and 1.39, the location of the mode remains constant which suggests the complete isolation of the mode from the surrounding environment.

Reflected colors from the cubic arrays while the surrounding index was changing, is shown in **Figure 4.12**. When the cube side length increases, change in the reflected color is sensible for all the surrounding indices. However, when the surrounding index changes in the range of 1.33 to 1.39, the change in the color is not much, since some parts of the reflection curves slowly red shift and there is not much change in the intensity of the reflection curves.

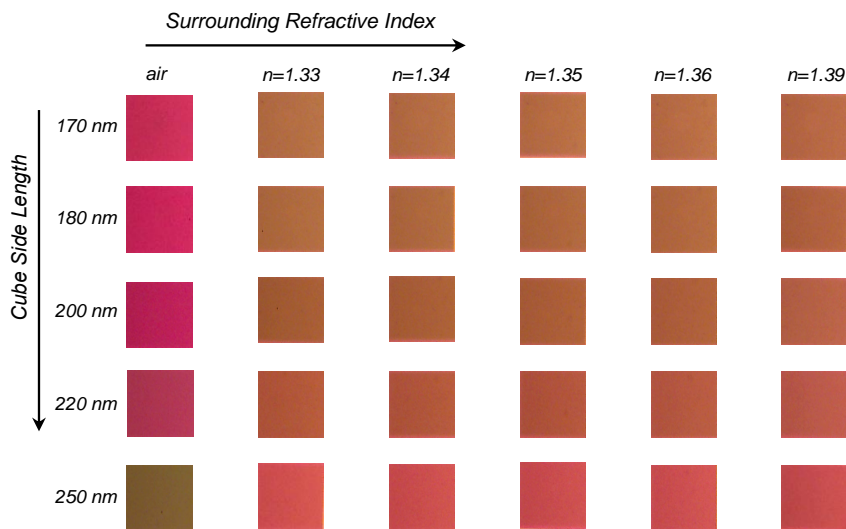


Figure 4.12. Reflected colors from the cubic arrays with SiON spacer layer and 450 nm pitch. Moving from top to bottom, the cube side length increases, and from left to right, the surrounding refractive index increases.

4.7.3 Cubic Nano-gratings, SiON Spacer Layer, Pitch 500 nm

In the sample with SiON dielectric spacer layer, those cubic arrays with lattice spacing values higher than 450 nm were showing plasmonic modes with lower Q, compared to the arrays with 400 and 450

nm pitch values. The only array with decent resonance features was the cubic array with 250 nm side length and 500 nm pitch. **Figure 4.13a-c** shows the reflection spectra with different surrounding indices, first derivatives of the reflection spectra and changes in the resonance wavelengths of the modes, respectively, for the cubic arrays with 250 nm side length and 500 nm pitch. As seen in **Figure 4.13a**, three major resonance features are excited in the reflection spectra and are labelled as mode 1 to 3. Referring to the simulation results in chapter 2, mode 1 is attributed to an FP-LSPR coupled mode which is now much stronger compared to the ones we observed in the cubic arrays with 400 and 450 nm pitch values. Mode 2 is an LSPR dominant mode and mode 3 is an SPR dominant mode. As can be seen in the reflection spectra, by changing the surrounding refractive index, the modes start to shift to

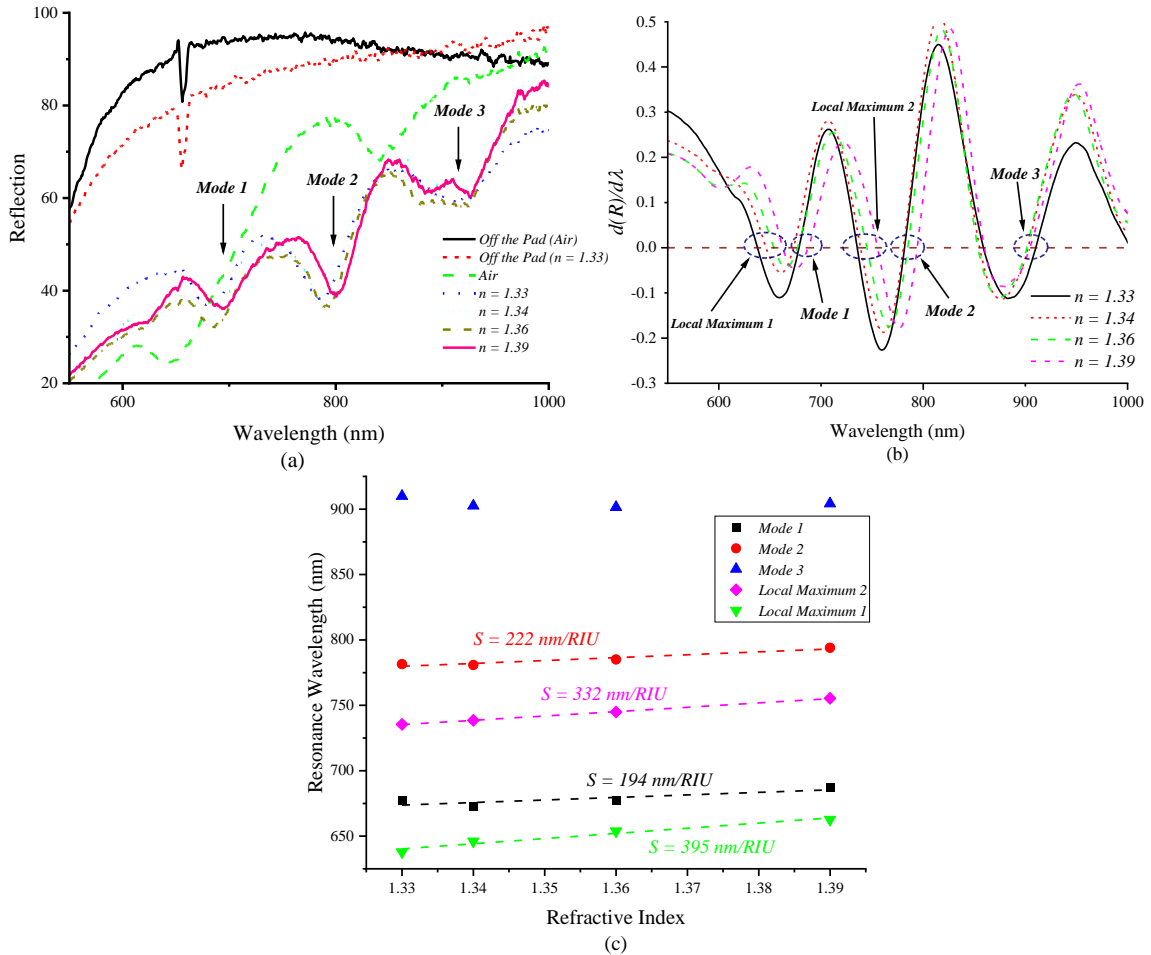


Figure 4.13. Reflection spectra with different surrounding indices, first derivatives of the reflection spectra and changes in the resonance wavelengths of the modes, for the cubic arrays with 250 nm side length and 500 nm pitch, respectively. The spacer layer is SiON.

longer wavelengths with different speeds. Further, it seems the local maximum on the left side of mode 1 and the local maximum between mode 1 and 2 are moving faster than the three modes and can be used as the measurement points for the sensitivity. The higher sensitivity of the local maximums compared to the modes can be seen in the first derivative curve in **Figure 4.13b**, where the local maximums and modes are labelled. Finally, the sensitivity of the modes and local maximums are calculated in **Figure 4.13c**. Mode 1 and 2 are showing 194 nm/RIU and 222 nm/RIU sensitivity values. Local maximum 1 and 2 are also showing 395 nm/RIU and 332 nm/RIU sensitivity values. The sensitivity of the local maximum 1 is very close to the value we achieved in the simulations for the cubic arrays with 200 nm side length and 400 nm pitch. This higher sensitivity compared to the optimized design in simulations shows that the existence of the adhesion layers and difference in the refractive index and thickness of different layers, has changed the optimized design during the experiment and now the highest sensitivity is achieved for a different side length and pitch value. The self-referencing mode, mode 3, is also moving slowly when the surrounding refractive index changes and seems to be almost isolated from the top when the surrounding index is higher than 1.35. Reflected colors from the array while the surrounding refractive index was changing, is shown in **Figure 4.14**.

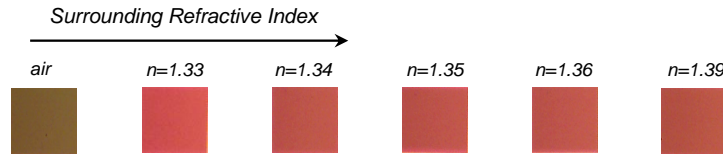


Figure 4.14. Reflected colors from the cubic array with 250 nm side length and 500 nm pitch, for different surrounding refractive indices. The spacer layer is SiON.

In summary, the cubic arrays in the sample with the SiON spacer layer are exhibiting acceptable performance compared to the simulation results. The quality factor values of the LSPR dominant modes are very close to the ones we achieved during the simulations, however, the quality factor values of the SPR modes are lower compared to the simulations. Further, some of the cubic arrays of this sample are showing comparable sensitivity values to the simulation results. However, since the LSPR dominant modes were showing uneven sensitivity on both sides of the Fano resonance, the highest sensitivity values were achieved by choosing the resonance wavelength of a local maximum adjacent to the LSPR dominant mode.

4.7.4 Cylindrical Nano-gratings, SiON Spacer Layer, Pitch 400 nm

As mentioned in chapter 3, during the lithography of the grating layers, rectangular and circular patterns were designed on the same sample with the SiON spacer layer. **Figure 4.15a-e** shows the reflection spectra with different surrounding refractive indices, for the cylindrical arrays with 170, 180, 200, 220 and 250 nm diameter, respectively. The pitch is 400 nm, and the spacer layer is SiON. For cylindrical arrays with 170 and 180 nm diameter, two modes are excited in the reflection spectra. However, the Q of the modes are not very high, and it seems the structure needs further optimization to enhance the Q. Also, mode 1&2 both are shifting as the surrounding refractive index changes. As the diameter increases to 200 nm in **Figure 4.15c**, Q of both modes increases and the Fano resonances are very well matched. Mode 1 is red shifting as the surrounding index increases. However, mode 2 is moving slower compared to mode 1 and complete isolation from the top has not been achieved yet. For the array with 220 nm diameter in **Figure 4.15d**, compared to the 200 nm diameter array, the Q of mode 1 is increased and Q of mode 2 is decreased. Also, the resonance wavelength of mode 2 seems to be isolated from the top as the surrounding refractive index changes. For the array with 250 nm diameter, the Fano resonances in mode 1 and 2 are separating and thus Q is decreased. Mode 1 is now divided into two different modes as we observed the same phenomenon in the simulations for the 200 nm diameter. Although the Q of mode 2 is decreased, the mode seems to be isolated from the top as the surrounding refractive index goes higher than 1.35.

To further investigate the sensing performance of the sensors, the first derivatives of the reflection spectra for different refractive indices and the changes in the resonance wavelengths of the modes as a function of the surrounding refractive index are shown in **Figure 4.16a-f**, respectively. Again, we are only measuring the sensitivity of those arrays which are showing higher Q, which are cylindrical arrays with diameters of 200, 220 and 250 nm. For the cylindrical array with 200 nm diameter in **Figure 4.16a, b**, mode 1 and mode 2 are labelled in the first derivative curves. For this array, we are not using the local maximum for the sensitivity measurement since the Q of the local maximum is lower than mode 1, and the resonance wavelength of mode 1 seems to be moving faster than the local maximum. Mode 1 shows 407 nm/RIU sensitivity to the changes in the surrounding refractive index. During the simulations, we achieved 400 nm/RIU sensitivity for the cylindrical arrays with 200 nm diameter. Thus, for the cylindrical arrays, it seems that the resonance conditions of the LSPR dominant Fano resonance is changed in such a way that the dependency of mode 1 on the LSPR modes of the top layers is increased, compared to the simulations. Thus, despite the cubic arrays with 200 nm side length showing

much better performance in simulations, surprisingly the cylindrical array with 200 nm diameter has higher sensitivity compared to the one we achieved in simulations. It seems that the chromatic dispersion of the spacer layer along with the Ti adhesion layers improved the dominance of mode 1 to

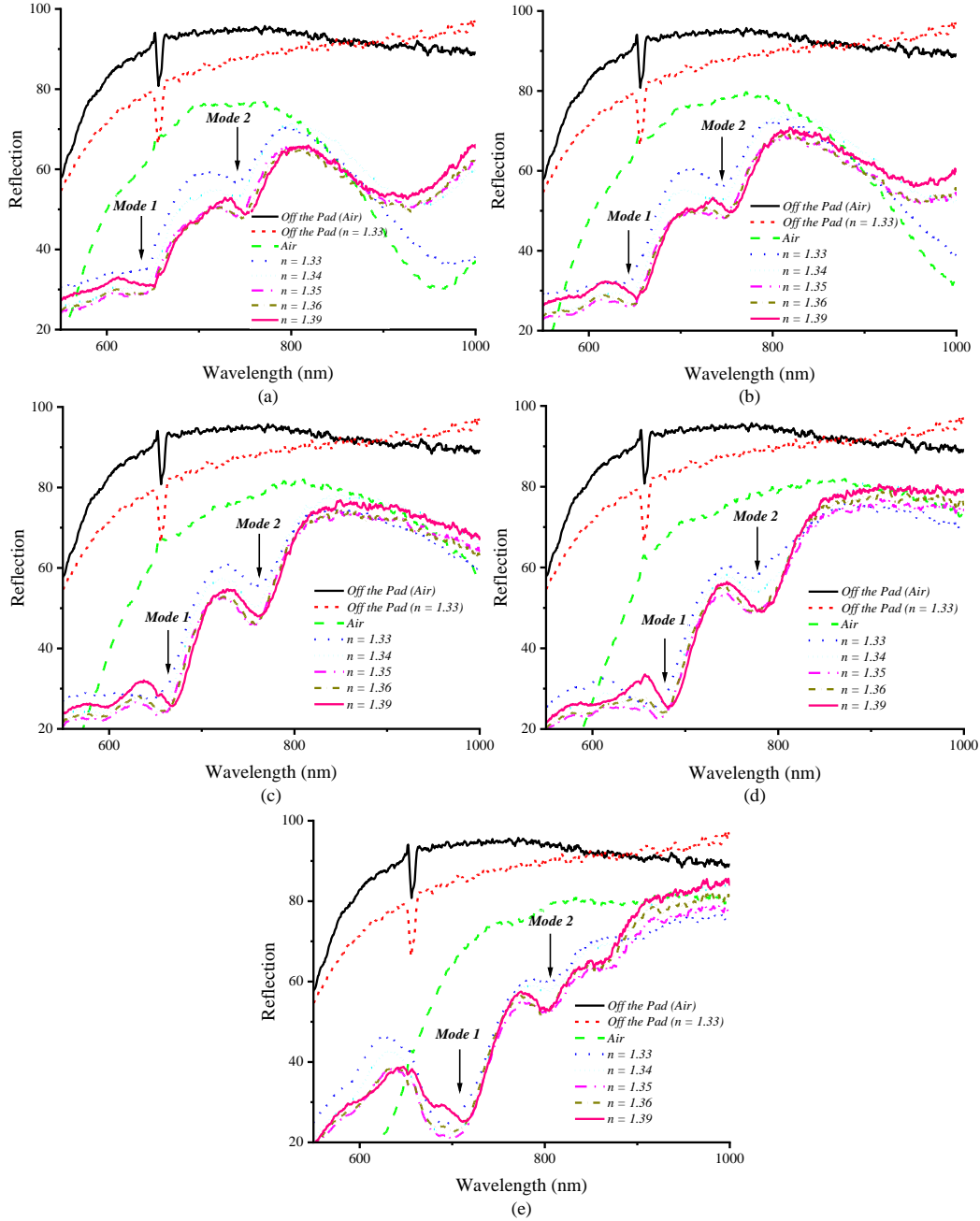


Figure 4.15a-e. Reflection spectra of the cylindrical arrays with different surrounding refractive indices and diameters of 170, 180, 200, 220 and 250 nm, respectively. The dielectric spacer layer is SiON and the lattice spacing is 400 nm.

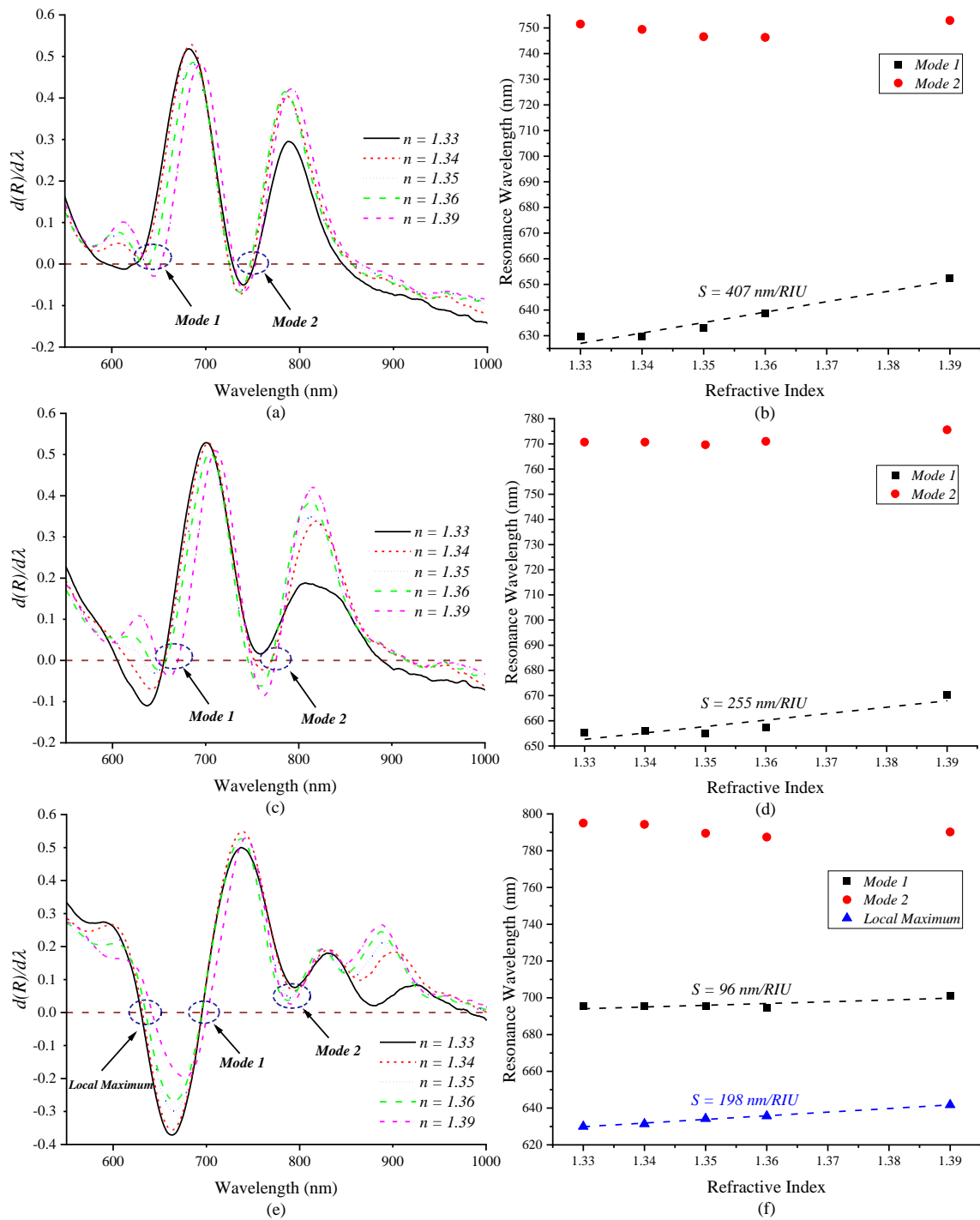


Figure 4.16. (a, c, e) First derivatives of the reflection spectra of the cylindrical arrays with 200, 220 and 250 nm diameter respectively, for different surrounding indices and, (b, e, f) changes in the resonance wavelengths of the modes, corresponding to **Figure 4.16 a, c, e** respectively. The dielectric spacer layer is SiON and the lattice spacing is 400 nm.

the LSPRs of the top layer and led to an enhancement of the sensitivity. We also achieved very decent cylindrical patterns due to the lack of sharp features and thus, the mode evolution experimentally is closer to that predicted by the simulations. . Mode 2 is also slowly moving with the change of refractive index which means it is not completely isolated from the top. For the cylindrical arrays with 220 nm diameter in Figure 4.16c, d, the sensitivity of the mode 1 is decreased to 255 nm/RIU compared to the 200 nm cylinders. However, mode 2 is almost isolated from the top and is moving very slowly as the refractive index changes. For the cylindrical arrays with 250 nm diameter in Figure 4.16e, f, again the sensitivity of the mode 1 is reduced to 96 nm/RIU. Again, smaller nanostructures are giving higher sensitivity, which demonstrates that just the proximity effect is not sufficient to explain the modes within the structure. However, as the local maximum happening on the left side of mode 1 has a very similar quality factor to mode 1, we can now use it as a measurement point for the sensitivity. As a result, the sensitivity of the local maximum is measured to be 198 nm/RIU which is higher than the sensitivity of the mode 1 for the same array. Also, the isolation of the self-referencing mode (mode 2) is improved compared to the arrays with smaller diameter, however, the Q of the mode is decreased. Figure 17 shows the reflected colors from the cylindrical arrays as the refractive index changes.

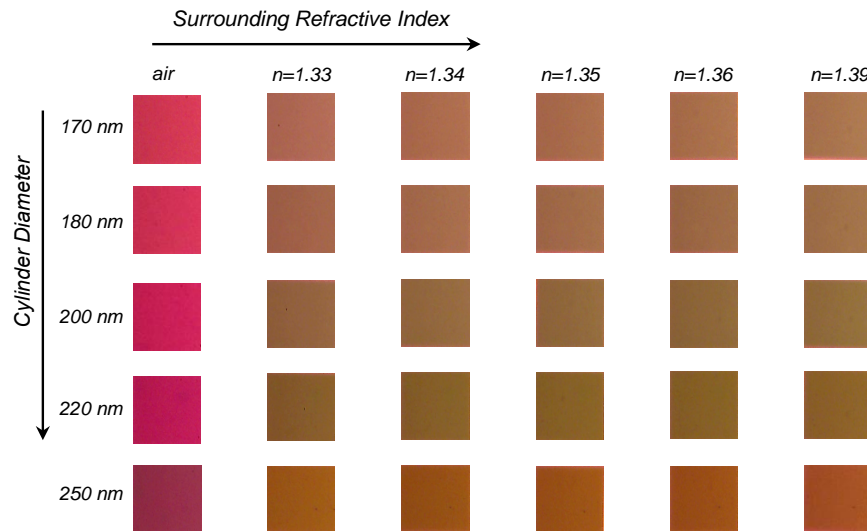


Figure 4.17. Reflected colors from the cylindrical arrays with SiON spacer layer and 400 nm pitch. Moving from top to bottom, the cylinder diameter increases, and from left to right, the surrounding refractive index increases.

4.7.5 Cylindrical Nano-gratings, SiON Spacer Layer, Pitch 450 nm

Figure 4.18a-e shows the reflection spectra with different surrounding refractive indices, for the cylindrical arrays with 170, 180, 200, 220 and 250 nm diameter, respectively. The pitch is 450 nm, and the spacer layer is SiON. For the cylindrical arrays with 170 and 180 nm diameters in **Figure 4.18a, b**, three modes are excited in the reflection spectra. However, the quality factors of all the modes are very low and further optimization is needed to achieve decent resonance features. As the diameter increases to 200 nm in **Figure 4.18c**, the Q of mode 1 increases and Q of modes 2 and 3 remains the same. For the cylindrical array with 220 nm diameter in **Figure 4.18d**, the Q of mode 1 further increases and mode 2 and 3 get combined together and create a strong Fano resonance. Further, a 4th mode is excited within the structure which is a Fabry-Perot mode combined with LSPR. As the diameter increases to 250 nm in **Figure 4.18e**, the quality factor of the modes is further improved.

Corresponding first derivatives of the reflection spectra and changes in the resonance features versus the surrounding refractive index are shown in **Figure 4.19a-f**, for the cylindrical arrays with 200, 220 and 250 nm diameter. For the cylindrical array with 200 nm diameter in **Figure 4.19a, b**, the sensitivity of mode 1 is 108 nm/RIU. Further, mode 3 is also sensitive to the changes in the surrounding index with a sensitivity of 177 nm/RIU. This high sensitivity of mode 3 proves that this mode is an LSPR dominant mode and thus mode 2 should be an SPR dominant mode. Due to the low Q of mode 2, the sensitivity of this mode is not calculated. For the cylindrical array with 220 nm diameter in **Figure 4.19c, d**, the sensitivity of mode 1 is increased to 151 nm/RIU. Further, mode 2 and 3 are combined and create a Fano resonance which its resonance wavelength shifts slowly with the change of surrounding index. This proves that mode 2 is a SPR dominant mode and once it is combined with mode 3, creates a Fano resonance that is also an SPR dominant mode. As the diameter increases to 450 nm, as seen in **Figure 4.19e, f**, the sensitivity of mode 1 increases to 430 nm/RIU. This value is higher than the value we achieved for both cylindrical and cubic arrays during the simulations. This high sensitivity again proves that the chromatic dispersion of the dielectric spacer layer has improved the sensitivity performance of the cylindrical arrays. However, the quality factor of mode 1 is not very high which suggests that the figure of merit is not very high. Mode 2 & 3 is shifting slowly with the change of the surrounding refractive index, however the complete isolation from the top is not achieved. Reflected colors from the array are also shown in **Figure 4.20** for different refractive indices. Once the surroundings are changed from air to 1.33, the change in the reflected colors is sensible for all the

arrays. However, as the refractive index increases from 1.33, the color change is not very sensible since there is not much change in the intensity of the reflection spectra, as seen in **Figure 4.18a-e**.

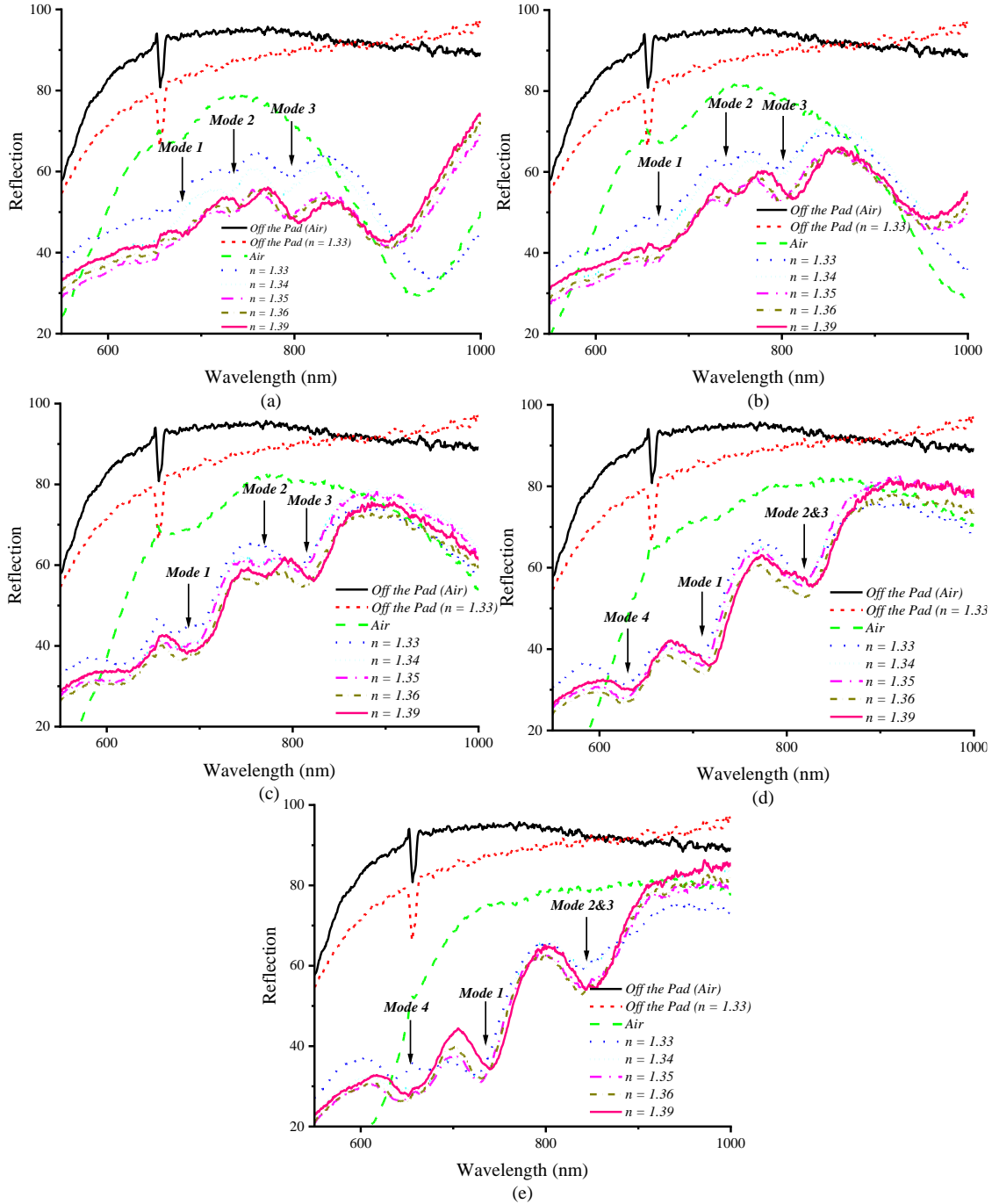


Figure 4.18a-e. Reflection spectra of the cylindrical arrays with different surrounding refractive indices and diameters of 170, 180, 200, 220 and 250 nm, respectively. The dielectric spacer layer is SiON and the lattice spacing is 450 nm.

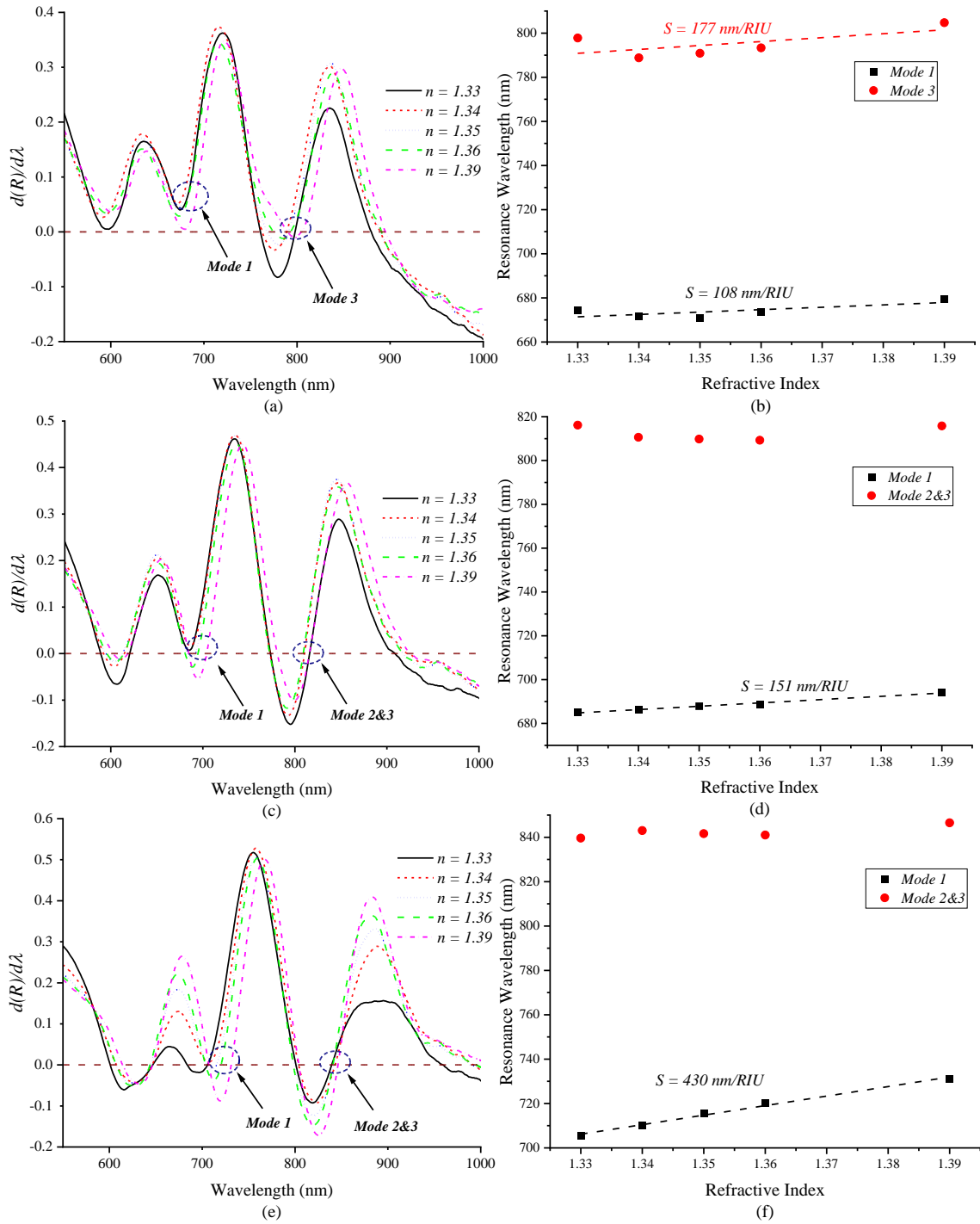


Figure 4.19. (a, c, e) First derivatives of the reflection spectra of the cylindrical arrays with 200, 220 and 250 nm diameter respectively, for different surrounding indices and, (b, e, f) changes in the resonance wavelengths of the modes, corresponding to **Figure 4.19a, c, e** respectively. The dielectric spacer layer is SiON and the lattice spacing is 450 nm.

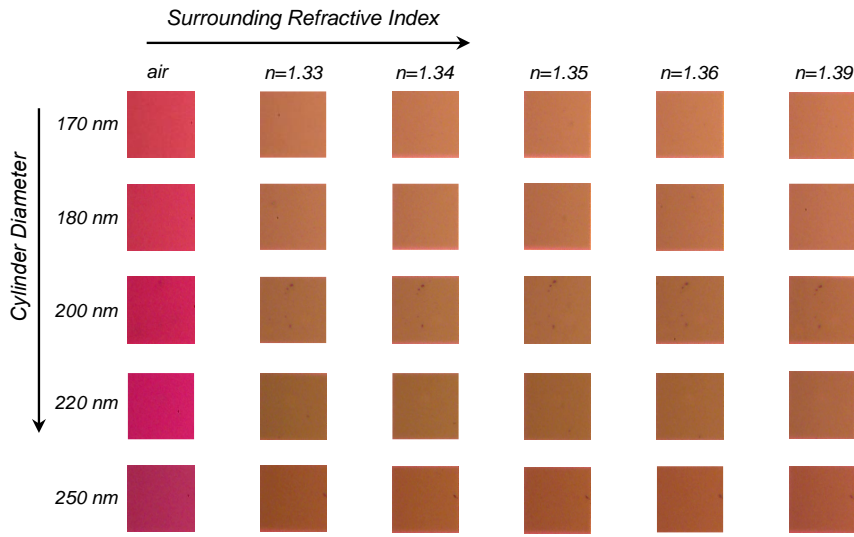


Figure 4.20. Reflected colors from the cylindrical arrays with SiON spacer layer and 450 nm pitch. Moving from top to bottom, the cylinder diameter increases, and from left to right, the surrounding refractive index increases.

To summarize the performance of the sample with SiON spacer layer, based on the results, we can claim that the cubic arrays are showing resonance features with higher quality factors which is a result of stronger field confinement in the corners of the cubes. On the other hand, cylindrical arrays show higher sensitivity compared to the cubic arrays, due to the decent circular patterns that were achieved during the lithography. Further, the chromatic dispersion of the dielectric layer has improved the sensitivity performance of the cylindrical arrays, while the cubic arrays were showing lower performance compared to the simulations, due to the chromatic dispersion.

4.7.6 Cubic Nano-gratings, SiN Spacer Layer, Pitch 400 nm

Figure 4.21a-e shows the reflection spectra of the cubic arrays with the SiN spacer layer, with side lengths of 170, 180, 200, 220 and 250 nm, respectively, for different surrounding refractive indices. The pitch is 400 nm. For the cubic array with 170 nm side length in **Figure 4.21a**, two major modes are excited which are labelled as mode 1 and 2. Further, another weak mode is excited between mode 1 and 2 which gets combined with mode 2 as the side length of the cubes increases to 180 nm, as seen in **Figure 4.21b**. Also, the local maximum which is located on the left side of mode 1 is moving faster than mode 1 for both arrays and thus its resonance wavelength can be a measurement point for the sensitivity. For the cubic arrays with 200 nm side length in **Figure 4.21c**, the quality factors of both modes are enhanced. Mode 1 is red shifting with increasing the surrounding refractive index while

mode 2 is isolated from the top as the surrounding index is higher than 1.34. It is also clear that the local maximum on the left side of mode 1 is moving faster than mode 1. For the cubic array with 220 nm side length in **Figure 4.21d**, the strength and the quality factors of both modes are slightly improved

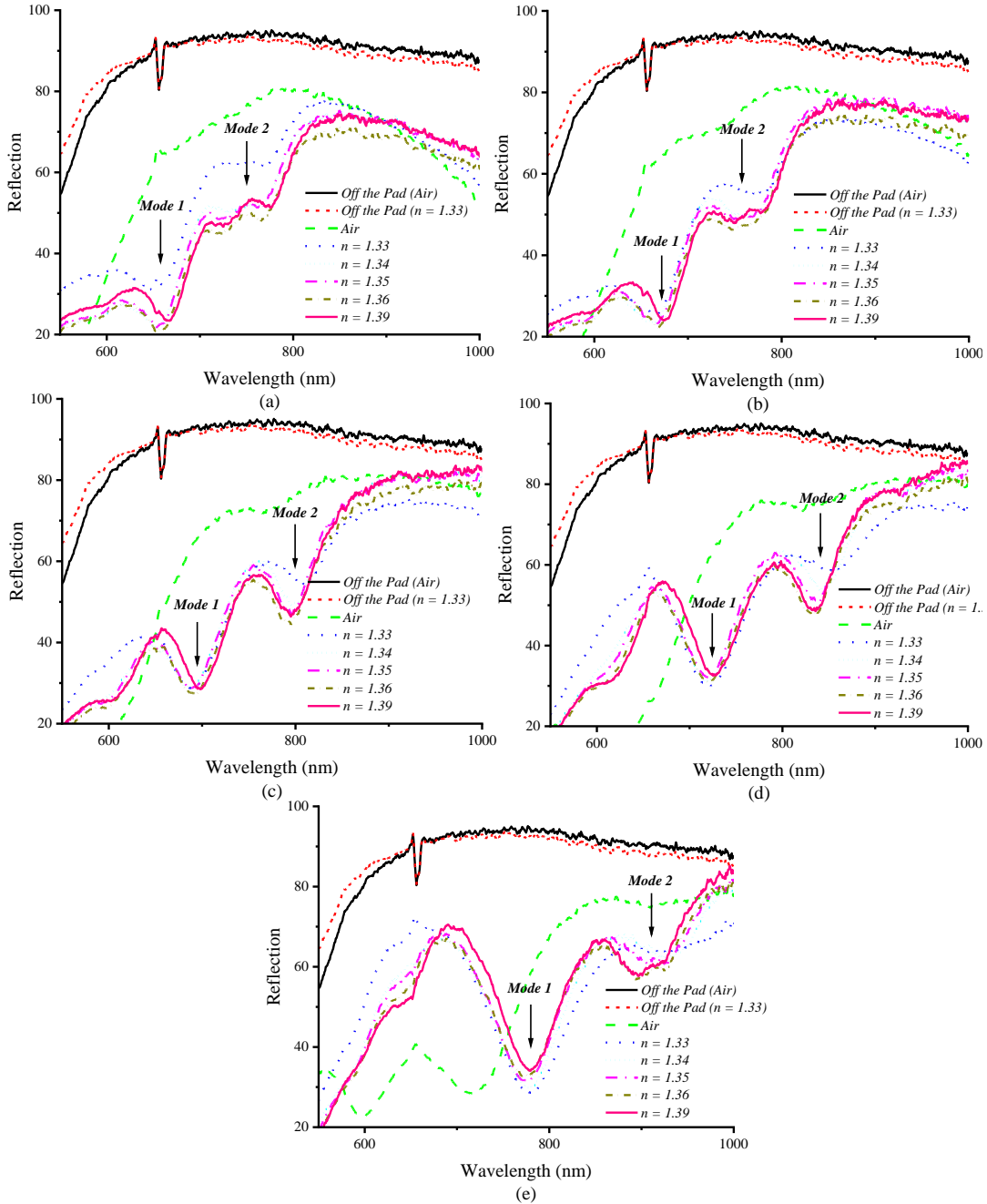


Figure 4.21a-e. Reflection spectra of the cubic arrays with different surrounding refractive index and side lengths of 170, 180, 200, 220 and 250 nm, respectively. The dielectric spacer layer is SiN and the lattice spacing is 400 nm.

compared to the array with 200 nm side length. However, the isolation of mode 2 happens when the surrounding index is above 1.35. For 250 nm side length in **Figure 4.21d**, mode 1 is much stronger than the ones in smaller length arrays. However, mode 2 Fano resonance is separated to two modes and the Q is decreased.

Figure 4.22a-f shows the first derivatives of the reflection spectra and changes in the resonance wavelengths of the modes versus surrounding refractive index, for the cubic arrays with 200, 220 and 250 nm side lengths. For the cubic array with 200 nm side length in **Figure 4.22a, b**, sensitivity of mode 1 is 169 nm/RIU. However, the local maximum on the left side of mode 1 is showing a higher sensitivity of 293 nm/RIU, which suggests that the LSPR mode of the top layer is stronger around the resonance wavelength of the local maximum. Further, the resonance wavelength of mode 2 seems to be completely isolated from the surroundings when the refractive index is 1.35 and higher. This array is showing slightly higher sensitivity compared to the cubic array with 200 nm side length in the SiON spacer sample which had a sensitivity of 277 nm/RIU. This shows that the higher refractive index of SiN compared to SiON has improved the dominance of the LSPR modes of the top layer in the reflection spectra. For the 220 nm side length in **Figure 4.22c, d**, the sensitivities of mode 1 and the local maximum are 108 and 317 nm/RIU, respectively. Increasing the cubes' side lengths to 220 nm, reduced the sensitivity of the mode 1 and enhanced the sensitivity of the local maximum. Also, mode 2 is almost isolated from the top for surrounding refractive index of 1.35 and higher. Compared to the sample with SiON spacer layer and identical cube length which had a sensitivity of 291 nm/RIU, the sensitivity is slightly increased which is similar to the trend we observed in 200 nm side length array. For the cubic array with 250 nm side length in **Figure 4.22e, f**, the sensitivity of the mode 1 is almost zero which suggests that mode 1 is now an SPR dominant mode and is almost isolated from the surrounding environment. However, the sensitivity of the local maximum is further increased compared to the smaller size arrays and is 422 nm/RIU. This is the highest sensitivity that we achieved for the cubic arrays in both samples so far and is slightly lower than the sensitivity value we achieved in simulations for the cubic array with 200 nm side length and 400 nm pitch. This suggests that firstly, the higher refractive index of SiN layer, compared to the SiON layer, has improved the separation of the modes, and thus led to an enhancement of the sensitivity to a value very close to the simulations. Secondly, the existence of the adhesion layers and chromatic dispersion of the spacer layer has changed the plasmonic excitation conditions and the maximum sensitivity is happening for the cubic array with

250 nm side length, while the highest sensitivity was achieved in 200 nm side length during the simulations.

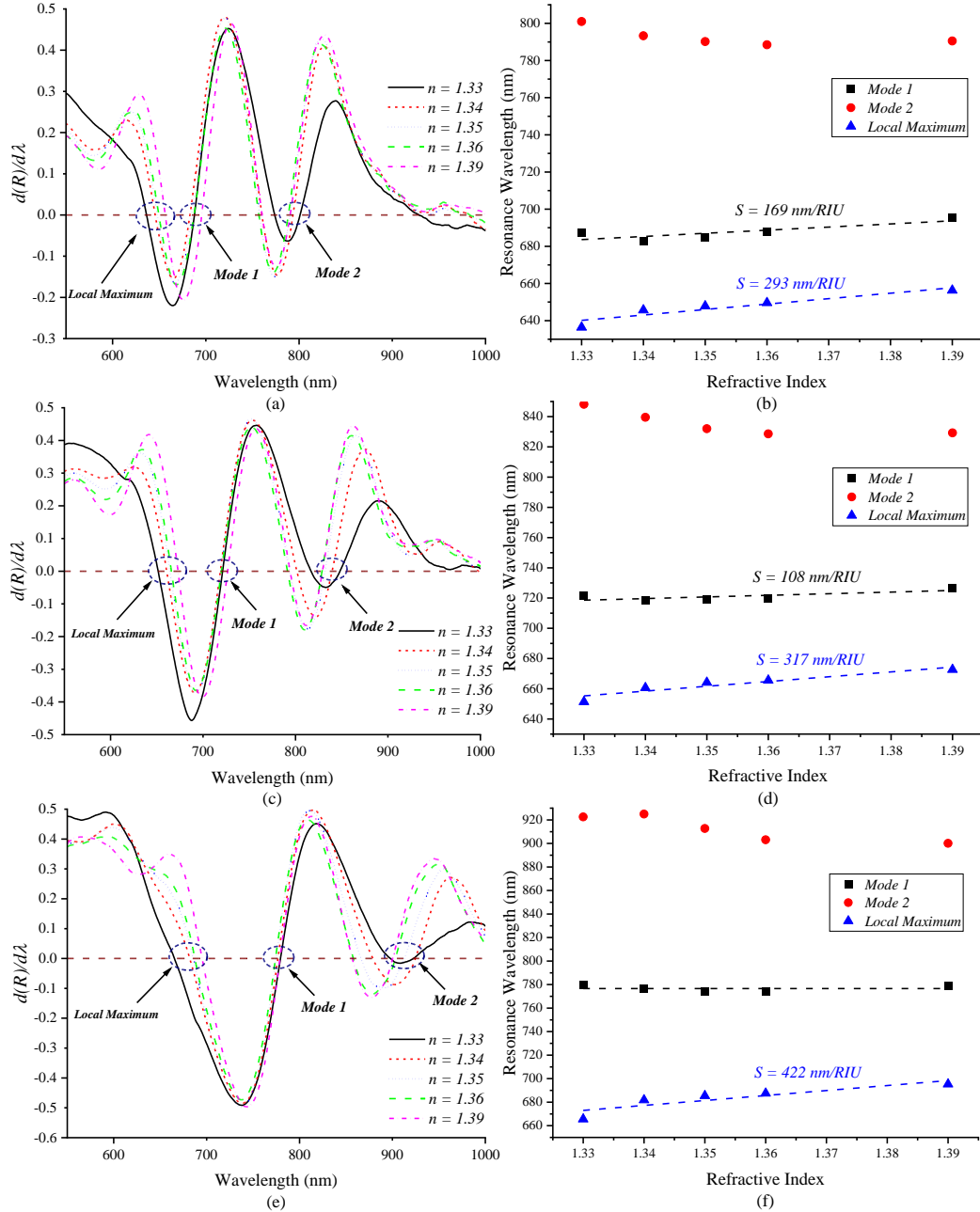


Figure 4.22. (a, c, e) - First derivatives of the reflection spectra of the cubic arrays with 200, 220 and 250 nm side length respectively, for different surrounding indices and, (b, e, f) changes in the resonance wavelengths of mode 1 and 2 and the local maximum, corresponding to **Figure 4.22a, c, e** respectively. The dielectric spacer layer is SiN and the lattice spacing is 400 nm.

Figure 4.23 shows the reflected colors from the cubic arrays with the SiN spacer and 400 nm pitch, for different refractive indices. Different colors are reflected from the arrays which show the manipulation of the reflection spectra due to the plasmonic mode excitement.

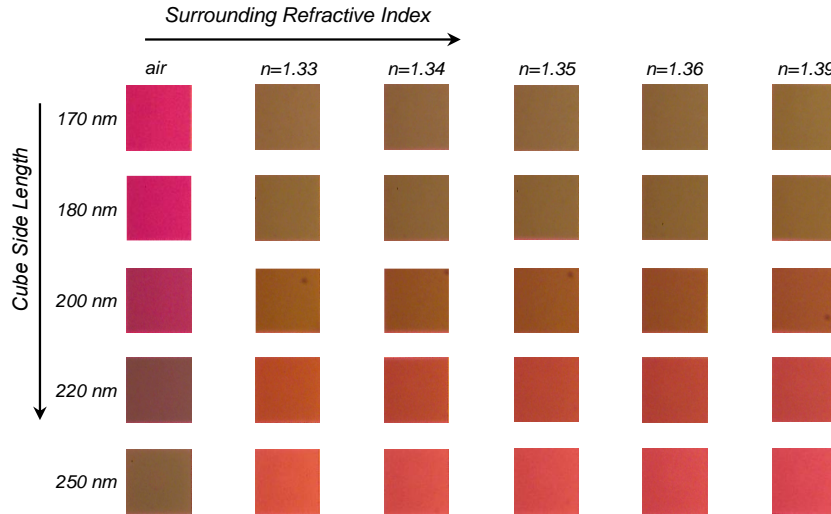


Figure 4.23. Reflected colors from the cubic arrays with SiN spacer layer and 400 nm pitch. Moving from top to the bottom, the cube side length increases, and from left to right, the surrounding refractive index increases.

4.7.7 Cubic Nano-gratings, SiN Spacer Layer, Pitch 450 nm

Figure 4.24a-e shows the reflection spectra of the cubic arrays with the SiN spacer layer, with side lengths of 170, 180, 200, 220 and 250 nm, respectively, for different surrounding refractive indices. The pitch is increased to 450 nm. Three major modes are excited for the cubic array with 170 nm side length, as shown in **Figure 4.24a**. However, the quality factor of the modes is low, and the structure needs further optimization to improve the Q. By increasing the side length to 180 nm in **Figure 4.24b**, the Q of mode 1 is slightly increased and mode 2 is shifted toward longer wavelengths and is getting close to mode 3. Once the side length is increased to 200 nm in **Figure 4.24c**, a fourth mode is excited in shorter wavelengths which is an FP-LSPR mode. The Q of mode 1 is also increased and mode 2 & 3 are almost combined and creating a Fano resonance. Further enhancement of the cube side length to 220 nm has improved the strength and quality factors of mode 1 and mode 4, as shown in **Figure 4.24d**. Also, the Fano resonance, resulting from the combination of mode 2 & 3, is completely formed and the resulting mode is almost isolated from the top as the refractive index is 1.34 and higher. Also, it can be seen that the local maximum between mode 1 and mode 4 is moving faster than other parts of the curves. For the cubic array with 250 nm side length in **Figure 4.24e**, the quality factors of all the three

modes are enhanced. For this array, the self-referencing mode is fully isolated when the refractive index is 1.36 and higher. First derivatives of the reflection spectra and changes in the resonance wavelengths versus the surrounding refractive index, are shown in **Figure 4.25a-f**.

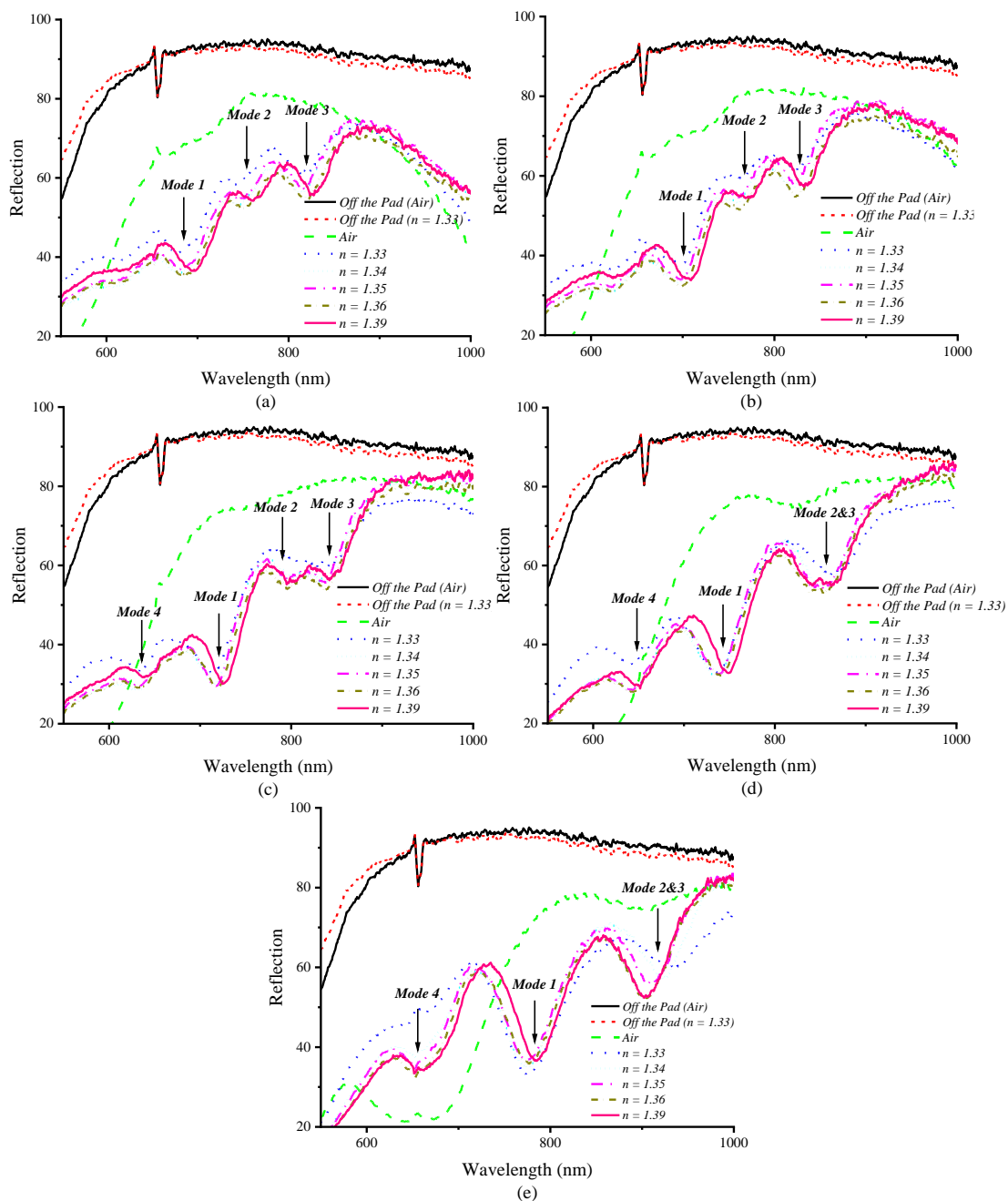


Figure 4.24a-e. Reflection spectra of the cubic arrays with different surrounding refractive index and side lengths of 170, 180, 200, 220 and 250 nm, respectively. The dielectric spacer layer is SiN and the lattice spacing is 450 nm.

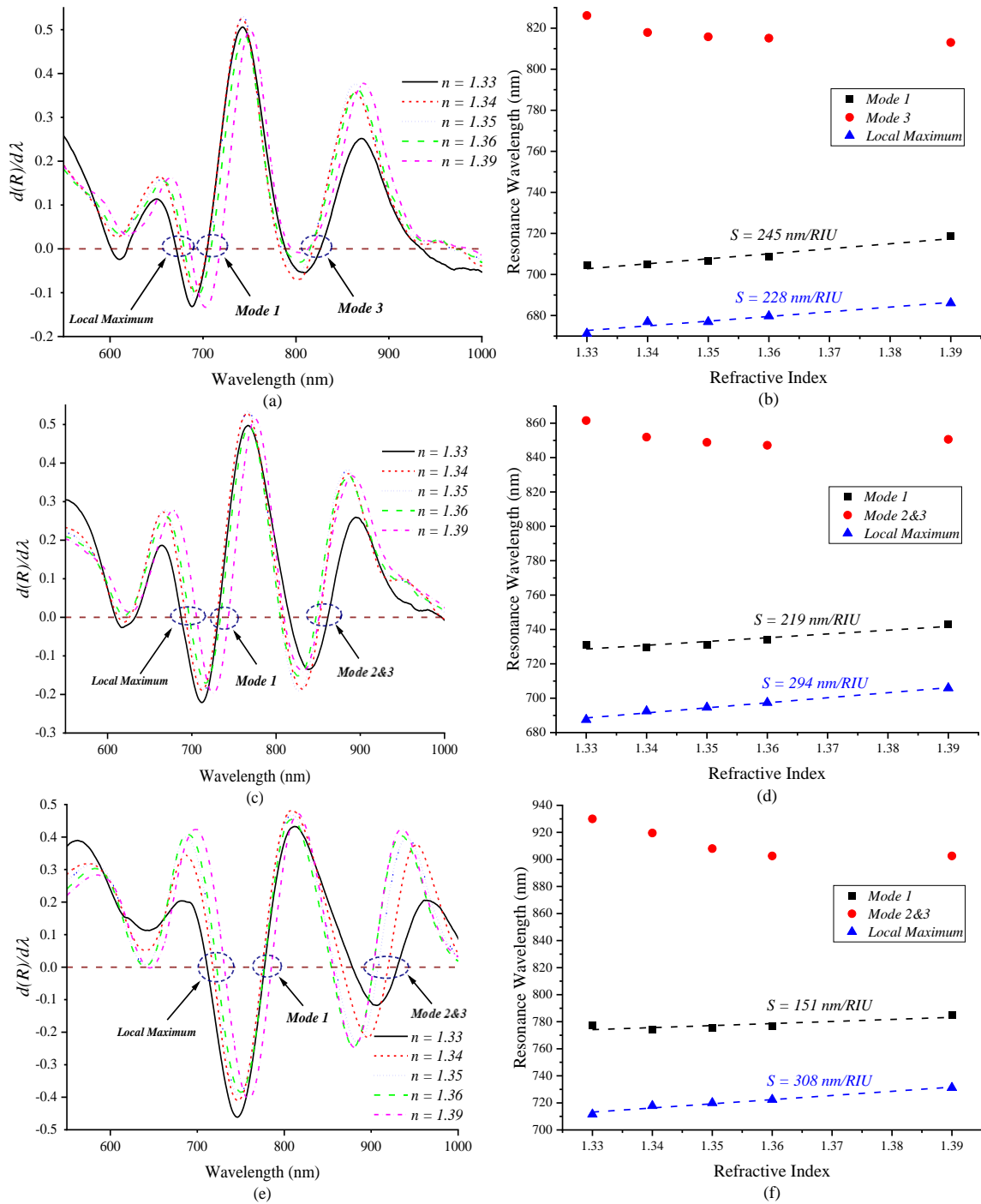


Figure 4.25. (a, c, e) - First derivatives of the reflection spectra of the cubic arrays with 200, 220 and 250 nm side length respectively, for different surrounding indices and, (b, e, f) changes in the resonance wavelengths of mode 1 and 2 and the local maximum, corresponding to **Figure 25a, c, e** respectively. The dielectric spacer layer is SiN and the lattice spacing is 450 nm.

Again, the sensitivity is measured only for those arrays that have high Q resonance features, which are cubic arrays with 200, 220 and 250 nm side lengths. Cubic array with 200 nm side length shows 245 nm/RIU sensitivity for mode 1, as seen in **Figure 4.25a, b**. Further, the local maximum happening on the left side of the mode 1 is showing a sensitivity of 228 nm/RIU. Both sensitivity values are higher than the sensitivity values of the similar array in SiON sample, which shows that SiN spacer layer is doing a better job than the SiON spacer layer in case of separation of the modes. Mode 3 is also moving very slowly and gets isolated from the top as the refractive index increases. For 220 nm side length in **Figure 4.25c, d**, the sensitivity of the mode 1 is decreased to 219 nm and the sensitivity of the local maximum is increased 294 nm/RIU. This suggests that enhancing the cube side length has changed the Fano resonance conditions of the mode 1 and this mode is now more dependent on the SPR resonances of the underneath layers. Further, the LSPR modes are now pushed toward shorter wavelengths which caused the enhancement of the sensitivity of the local maximum. The Fano resonance of the Mode 2&3 is moving very slowly and is getting isolated as the refractive index increases. As the cube side length increases to 250 nm in **Figure 4.25e, f**, the LSPR modes are pushed further towards the shorter wavelengths and as a result the sensitivity of the mode 1 is reduced to 151 nm/RIU and the sensitivity of the local maximum increases to 308 nm/RIU. The self-referencing mode blue shifts with the enhancement of the surrounding refractive index and finally gets isolated from the surroundings. Reflected colors from these arrays are shown in **Figure 4.26**, for different surrounding refractive indices.

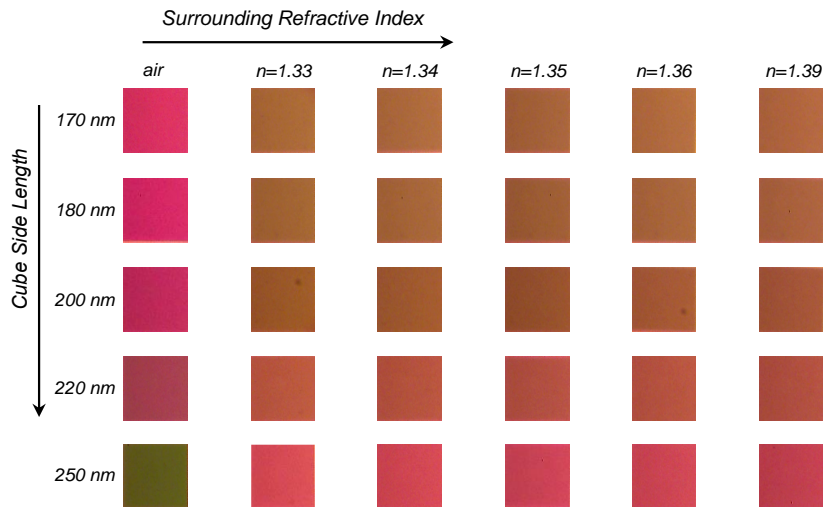


Figure 4.26. Reflected colors from the cubic arrays with SiN spacer layer and 450 nm pitch. Moving from top to the bottom, the cube side length increases, and from left to right, the surrounding refractive index increases.

4.7.8 Cubic Nano-gratings, SiN Spacer Layer, Pitch 500 nm

For lattice spacing values higher than 450 nm, there was only one array that showed high Q resonance features. This was the cubic array with 500 nm pitch and 250 nm side length. For this array, **Figure 4.27a-c** shows the reflection spectra with different surrounding indices, first derivatives of the reflection spectra and changes in the resonance wavelengths of the modes, respectively. As seen in **Figure 4.27a**, three major modes are excited within the array. Mode 1 is attributed to an FP-LSPR mode. Mode 2 is an LSPR dominant mode, and mode 3 is an SPR dominant mode.

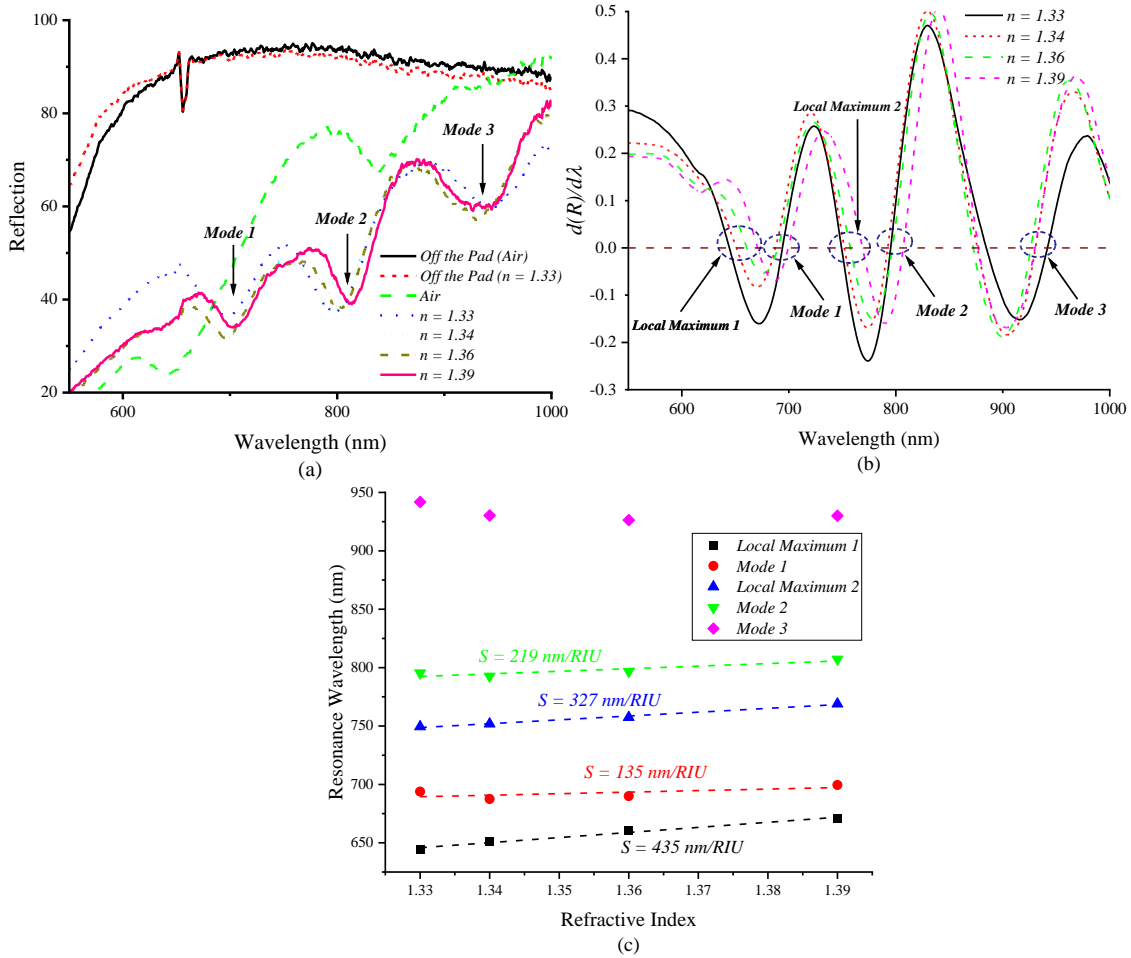


Figure 4.27. Reflection spectra with different surrounding indices, first derivatives of the reflection spectra and changes in the resonance wavelengths of the modes, for the cubic arrays with 250 nm side length and 500 nm pitch, respectively. The spacer layer is SiN.

Further, there are three maximums happening in the reflection curve, on the left side of mode 1 (local maximum 1), one between mode 1 and 2 (local maximum 2), and one between mode 2 and 3. We will

only use the first two maximums for the sensitivity measurement as the third maximum between mode 2 and 3 is very similar to mode 3 and it is not very sensitive. These modes and local maximums are labelled in **Figure 4.27b**. It is clear from the first derivative curves that local maximums are moving faster than the modes when the surrounding refractive index changes. The changes in the resonance wavelengths of the modes and local maximums versus the surrounding refractive index are plotted in **Figure 4.27c**. Mode 1 and 2 show 135 and 219 nm/RIU sensitivity, respectively. Further, Local maximum 1 and 2 show 435 and 327 nm/RIU sensitivity, respectively. Although the quality factor of the local maximum 1 is not very high, this resonance feature shows the highest sensitivity we achieved so far. Mode 3 as a self-referencing mode is almost isolated from the surrounding environment and its resonance wavelength does not change much when the refractive index changes. This array shows higher sensitivity compared to the similar array with SiON spacer layer which again confirms that SiN is doing a better job in separating the modes, compared to the SiON. **Figure 4.28** shows the reflected colors from the array while the surrounding refractive index was changing.

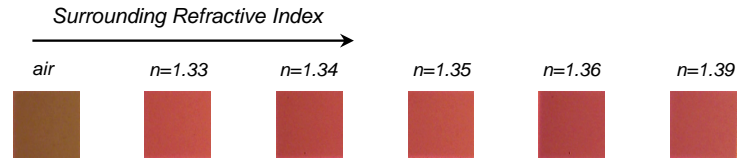


Figure 4.28. Reflected colors from the cubic array with 250 nm side length and 500 nm pitch, for different surrounding refractive indices. The spacer layer is SiN.

4.7.9 Cylindrical Nano-gratings, SiN Spacer Layer, Pitch 400 nm

Nano-gratings with cylindrical shape were also created on the sample with SiN spacer layer. **Figure 4.29a-e** shows the reflection spectra with different surrounding refractive indices, for the cylindrical arrays with 170, 180, 200, 220 and 250 nm diameter, respectively. The pitch is 400 nm for all the arrays and spacer layer is SiN. For the cylindrical arrays with 170 and 180 nm diameters in **Figure 4.29a, b**, two major modes are excited within the arrays. However, the Q of the modes are low. A very weak mode is also excited between the two major modes which is moving toward mode 2 as the diameter increases. Eventually, this mode combines with the mode as the diameter increases to 200 nm, as seen in **Figure 4.29c**. Further enhancement of the diameter to 220 nm led to an increase in the quality factors of mode 1 and 2 in **Figure 4.29d**. However, as the diameter increases to 250 nm, the Fano resonances of both modes start to separate. This can be clearly seen in **Figure 4.29e**. To examine the sensing performance of the cylindrical arrays, after smoothing the data, the first derivatives of the reflection

spectra were calculated. Again, only cylindrical arrays with high Q features were included, which are arrays with 200, 220 and 250 nm side lengths. The first derivative curves along with the changes in the resonance wavelengths of the modes versus the refractive index of the surroundings, are shown in **Figure 4.30a-f**.

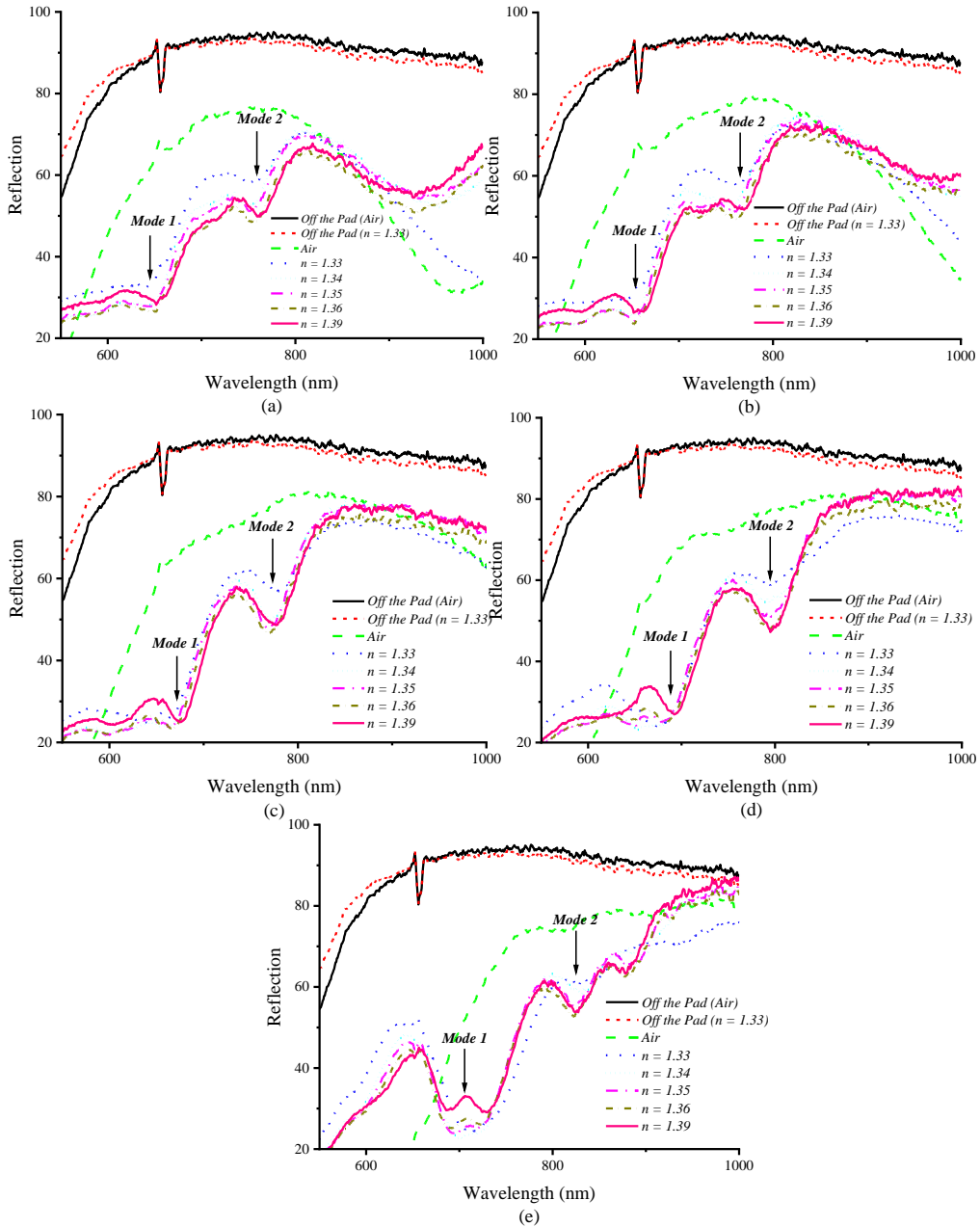


Figure 4.29a-e. Reflection spectra of the cylindrical arrays with different surrounding refractive indices and diameters of 170, 180, 200, 220 and 250 nm, respectively. The dielectric spacer layer is SiN and the lattice spacing is 400 nm.

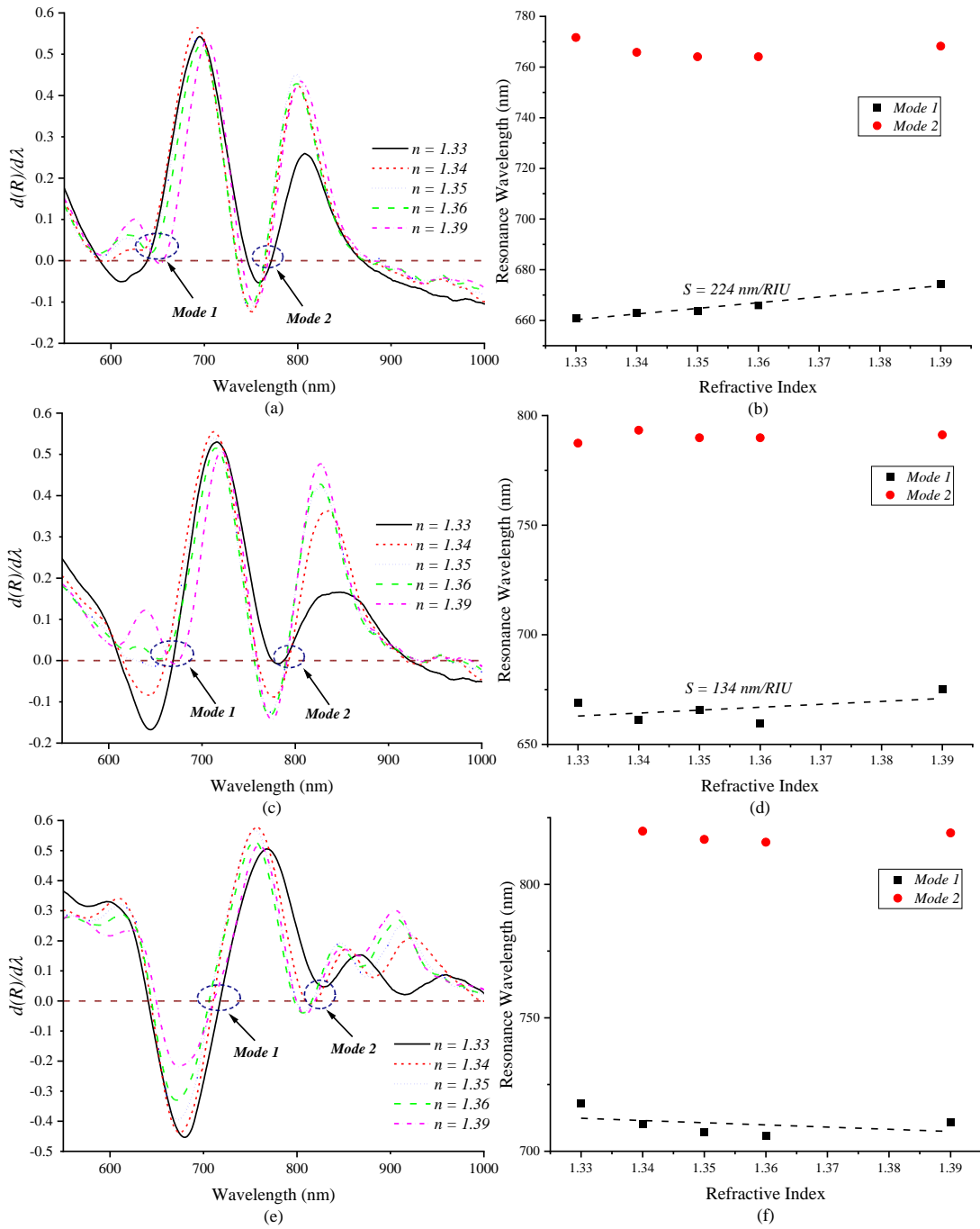


Figure 4.30. (a, c, e) First derivatives of the reflection spectra of the cylindrical arrays with 200, 220 and 250 nm diameter respectively, for different surrounding indices and, (b, e, f) changes in the resonance wavelengths of the modes, corresponding to **Figure 4.30a, c, e** respectively. The dielectric spacer layer is SiN and the lattice spacing is 400 nm.

The local maximums in the reflection curves are not moving any faster than the modes as thus we only used mode 1 for the sensitivity measurements, similar to the cylindrical arrays in the sample with SiON spacer layer. The sensitivity of mode 1 is measured to be 224 and 134 nm/RIU for the cylindrical arrays with 200 and 220 nm diameters. These values are lower than the sensitivity value of the similar arrays with the SiON spacer layer. This means that for the cylindrical arrays, the SiON spacer layer is performing better in case of mode separation. For the cylindrical array with 250 nm diameter in **Figure 4.30e, f**, the sensitivity is almost zero. However, it should be mentioned that after smoothing the data and taking the first derivative of the reflection spectra, only one minimum appears in the reflection curve. However, as can be seen in **Figure 4.30e**, mode 1 is separated into two different modes and the mode in longer wavelengths is moving faster than the other one. Thus, the sensitivity is not zero. For all the three arrays, the self-referencing mode is moving slowly with the change of the surrounding refractive index. However, complete isolation from the top is achieved in cylindrical array with 220 nm diameter, for the refractive indices higher than 1.35. **Figure 4.31** also shows the reflected colors from the cylindrical arrays with 400 nm pitch, while the surrounding refractive index was changing.

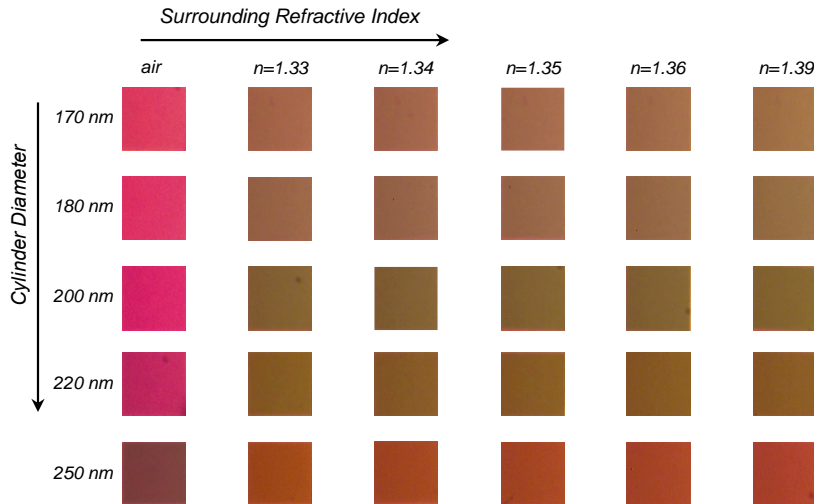


Figure 4.31. Reflected colors from the cylindrical arrays with SiN spacer layer and 400 nm pitch. Moving from top to the bottom, the cylinder diameter increases, and from left to right, the surrounding refractive index increases.

4.7.10 Cylindrical Nano-gratings, SiN Spacer Layer, Pitch 450 nm

Figure 4.32a-e shows the reflection spectra with different surrounding refractive indices, for the cylindrical arrays with 170, 180, 200, 220 and 250 nm diameter, respectively. The pitch is increased to 450 nm and spacer layer is SiN.

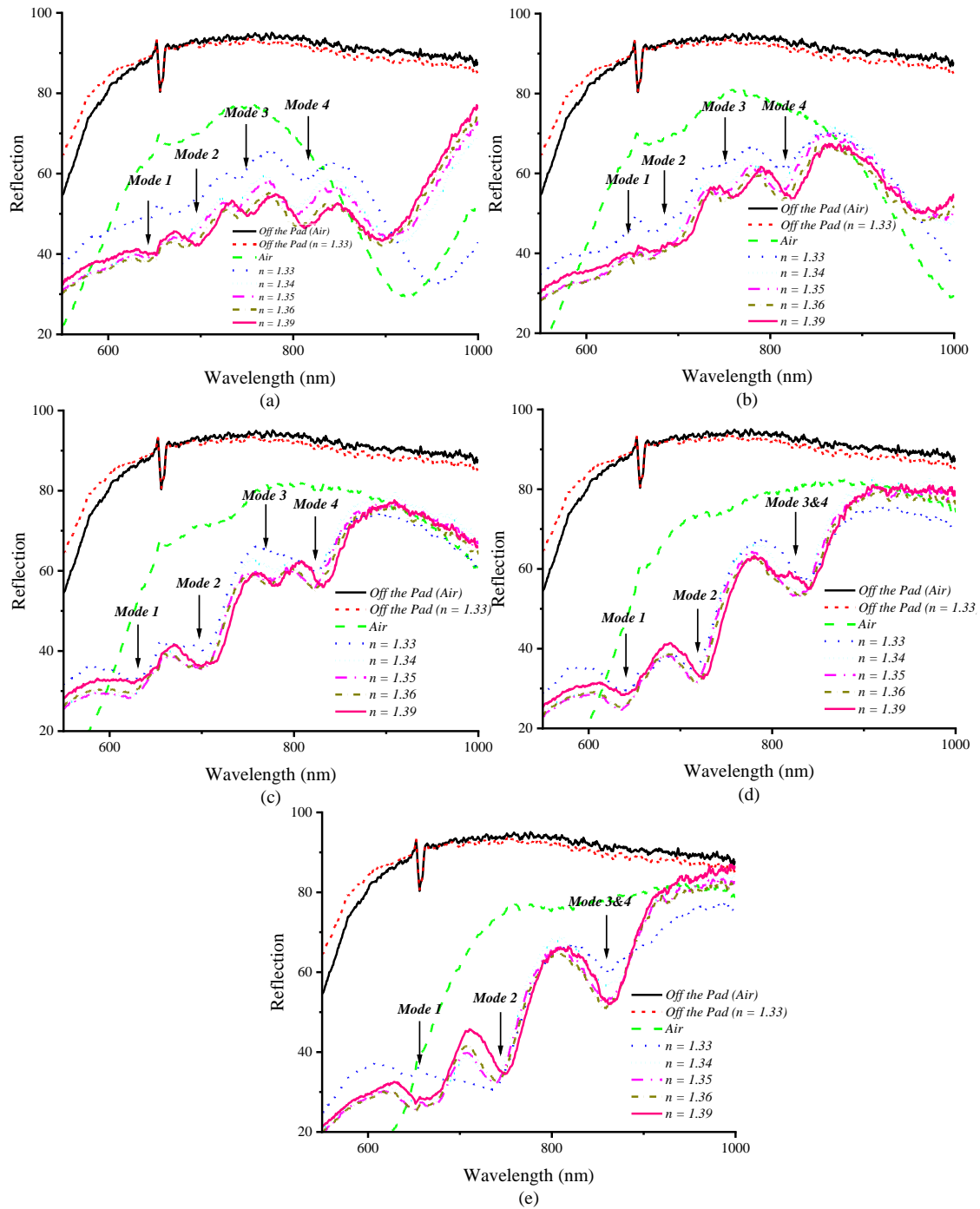


Figure 4.32a-e. Reflection spectra of the cylindrical arrays with different surrounding refractive indices and diameters of 170, 180, 200, 220 and 250 nm, respectively. The dielectric spacer layer is SiN and the lattice spacing is 450 nm.

As seen in this figure, four modes are excited for the arrays with 170, 180 and 200 nm diameters. These modes are getting stronger as the cylinder diameter increases. Once the diameter reaches 220 nm in **Figure 4.32d**, mode 3 and 4 combine and create a Fano resonance with higher Q. The highest Q for the modes is achieved when the diameter reaches 250 nm, as seen in **Figure 4.32e**. To measure the sensitivity of the arrays, the first derivatives of the reflection spectra were calculated for the cylindrical arrays with 200, 220 and 250 nm. Further, the changes in the resonance wavelengths of the modes versus the surrounding refractive index were calculated. These results are shown in **Figure 4.33a-f**. For the 200 nm diameter in **Figure 4.33a, b**, the sensitivity of mode 2 is calculated to be 240 nm. Also, the self-referencing mode is moving very slowly as the refractive index changes and is almost isolated from the top as the refractive index is higher than 1.36. For the 220 nm diameter in **Figure 4.33c, d**, the sensitivity is 325 nm/RIU for the mode 2. For this diameter, mode 3&4 is isolated from the surrounding environment when the refractive index is 1.34 and higher. For 250 nm diameter in **Figure 4.33e, f**, the sensitivity is enhanced to 422 nm/RIU and the isolation of the self-referencing mode from the top is improved. Compared to the similar arrays with SiON spacer layer, all the arrays here are showing higher sensitivity, except the cylindrical array with 250 nm diameter, which is showing slightly less sensitivity of 422 nm/RIU compared to the similar array with SiON spacer layer with a sensitivity of 430 nm/RIU. Reflected colors from the array with different surrounding refractive indices are shown in **Figure 4.34**.

To better compare the sensitivity results of the two samples, summary of the results is presented in **Figure 4.35a-d**. **Figure 4.35a, b**, shows the sensitivity results of the sample with the SiON spacer layer for the cubic and cylindrical arrays, respectively. The maximum sensitivity achieved from arrays are plotted versus the cube side length and cylinder diameter, while the pitch is also changing. For the cubic arrays in **Figure 4.35a**, the maximum sensitivity is achieved for the array with 500 nm pitch and 250 nm side length. For both 400 nm and 450 nm pitch values, as the side length increases, the sensitivity also increases. This means, for the cubic arrays with a constant pitch, as the distance between the cubes decreases, the mode separation is improved and thus the sensitivity increases. However, along with the sensitivity, the quality factor of the resonance features is important and must be considered when choosing an array. Also, when the side length is constant, arrays with 400 nm pitch show higher sensitivity compared to the arrays with 450 nm pitch. This also confirms that for 400 nm and 450 nm pitch values, as the distance between two cubes is decreased, the sensitivity is improved.

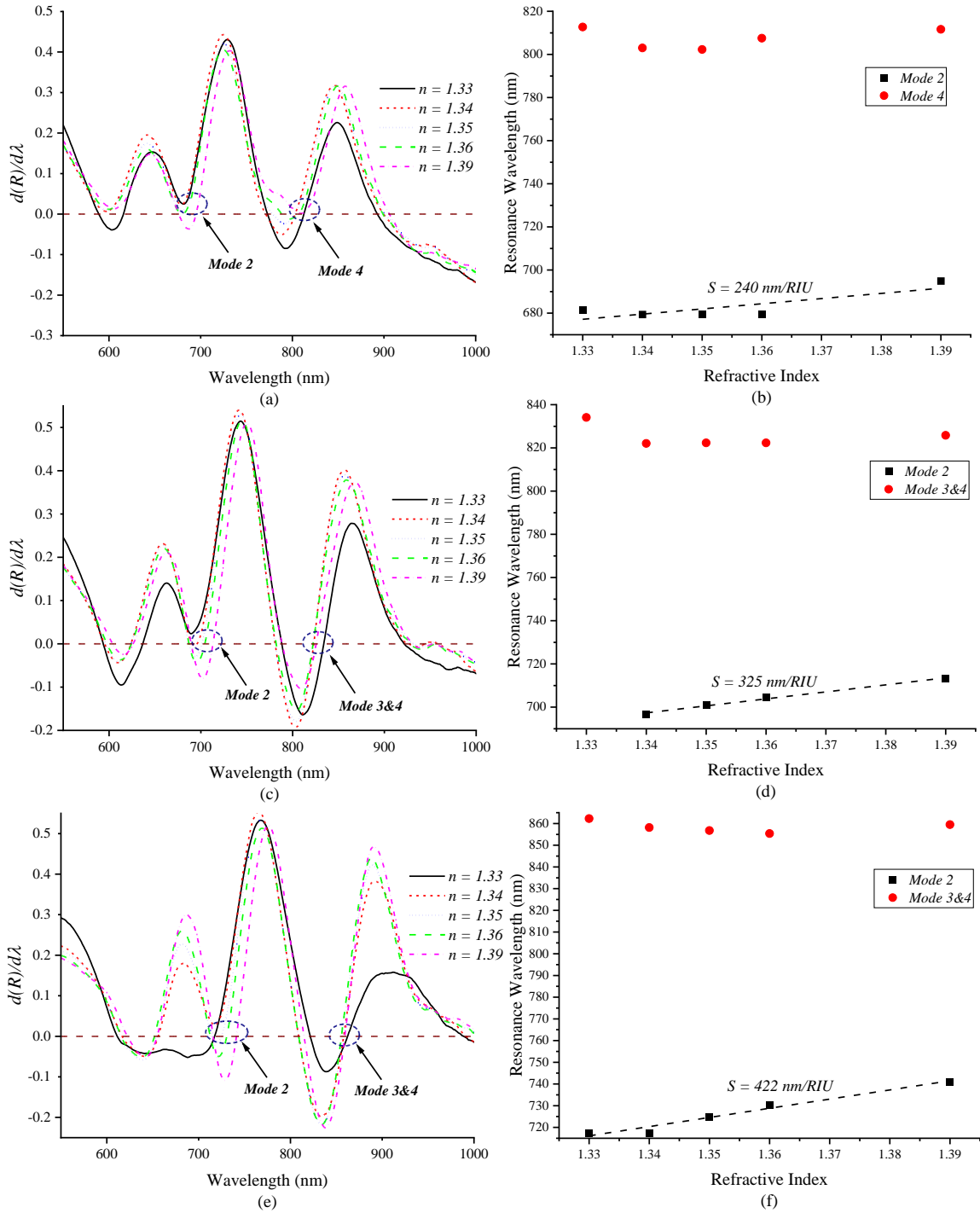


Figure 4.33. (a, c, e) First derivatives of the reflection spectra of the cylindrical arrays with 200, 220 and 250 nm diameter respectively, for different surrounding indices and, (b, e, f) changes in the resonance wavelengths of the modes, corresponding to **Figure 4.33a, c, e** respectively. The dielectric spacer layer is SiN and the lattice spacing is 450 nm.

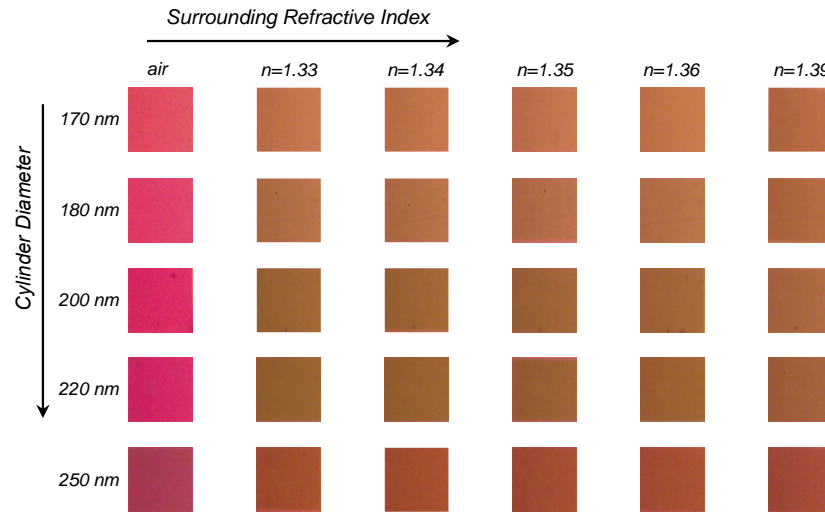


Figure 4.34. Reflected colors from the cylindrical arrays with SiN spacer layer and 450 nm pitch. Moving from top to bottom, the cylinder diameter increases, and from left to right, the surrounding refractive index increases.

As the pitch enhances to 500 nm, the array with 250 nm side length shows higher sensitivity compared to the arrays with similar side length and lower pitch values. This is due to the addition of a strong FP-LSPR mode to the system which increased the sensitivity. For the cylindrical arrays in **Figure 4.35b**, when the pitch is 400 nm, the sensitivity decreases by increasing the diameter. This shows that plasmonic mode excitement is highly dependent on the shape of the nanostructures. However, for 450 nm pitch, the sensitivity increases as the diameter increases, and the highest sensitivity is achieved when the diameter is 250 nm. Further, arrays with 400 nm pitch and 200 and 220 nm diameters show higher sensitivity compared to the arrays with similar diameters and 450 nm pitch. However, when the diameter is increased to 250 nm, the cylindrical array with 450 nm pitch shows higher sensitivity compared to the cylindrical array with 400 nm pitch. This suggests that excitement and separation of the modes is highly dependent on the size and spacing between the cylinders. **Figure 4.35c, d** shows the sensitivity results of the sample with SiN spacer layer for the cubic arrays and cylindrical arrays, respectively. For the cubic arrays in **Figure 4.35c**, similar to the SiON sample, when the pitch is constant, the sensitivity increases by enhancing the cube side length. Also, arrays with 400 nm pitch show higher sensitivity compared to arrays with similar size and 450 nm pitch. The highest sensitivity is achieved in the cubic arrays with 500 nm pitch and 250 nm side length. For the cylindrical arrays in **Figure 4.35d**, for 400 nm pitch, the sensitivity decreases as the diameter is increased. For 450 nm pitch however, the sensitivity is enhanced when the diameter is increased, and the highest sensitivity is achieved for the arrays with 450 nm pitch and 250 nm diameter.

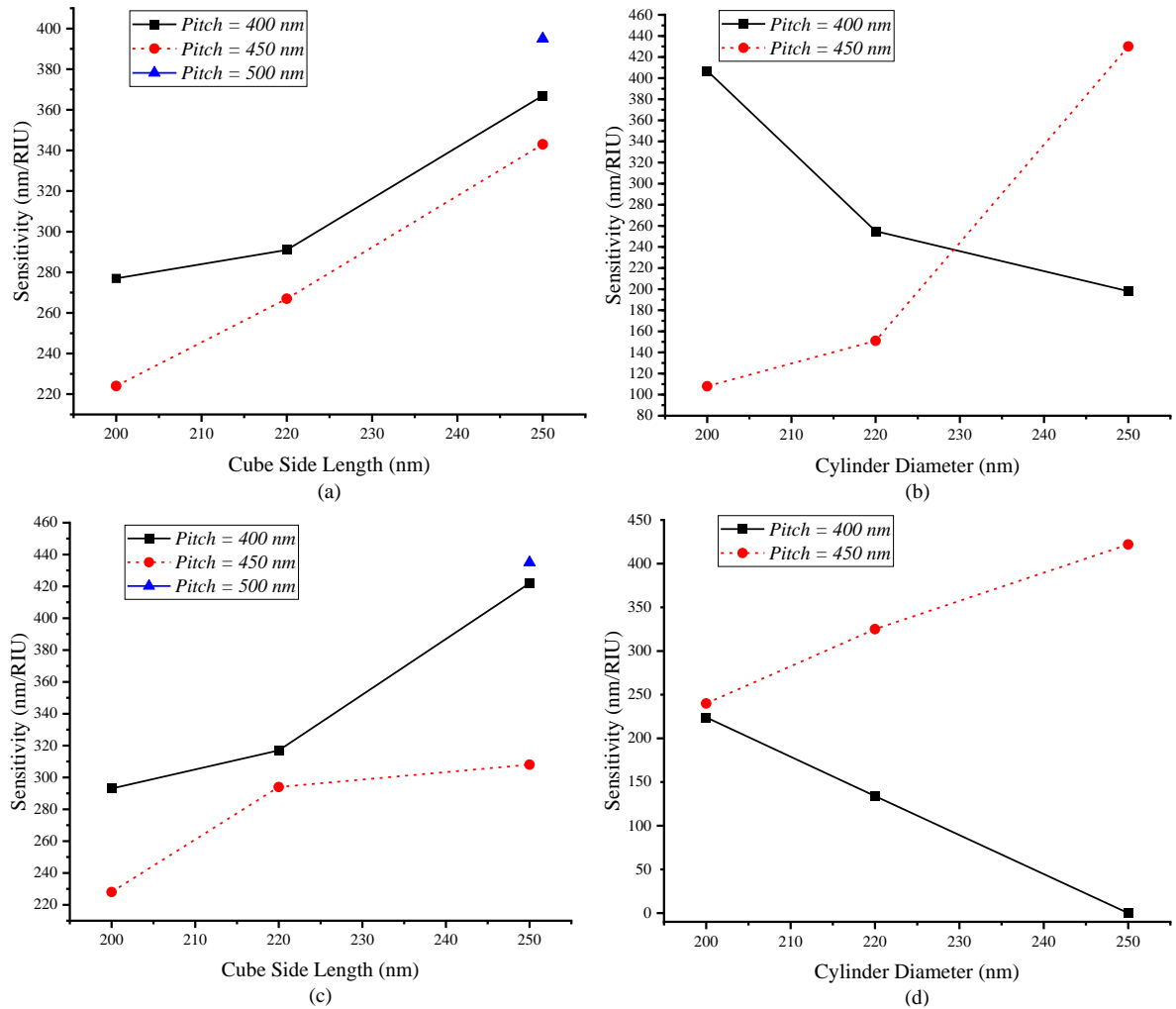


Figure 4.35. (a) and (b), The sensitivity results of the sample with the SiON spacer layer for the cubic and cylindrical arrays, respectively. (c) and (d), the sensitivity results of the sample with SiN spacer layer for the cubic arrays and cylindrical arrays, respectively.

Comparing the performance of the cubic arrays in SiON and SiN samples, the highest sensitivity in both samples is achieved in the array with SiN spacer layer, 250 nm side length and 500 nm pitch. The only cubic array in the sample with SiON spacer layer which is showing higher sensitivity compared to the similar array with SiN spacer layer, is the array with 450 nm pitch and 250 nm side length, which is showing 343 nm/RIU bulk sensitivity. A similar array in the SiN sample shows 308 nm/RIU sensitivity to the changes in the surrounding refractive index. Based on these results, for the cubic arrays, we can claim that SiN spacer layer is performing better in case of mode separation and thus sensitivity. For the cylindrical arrays, the highest sensitivity of the two samples is achieved for the array

with SiON spacer layer which has a diameter of 250 nm and a lattice spacing of 450 nm. When the pitch is 400 nm, all the arrays in the SiON sample show higher sensitivity values compared to the similar arrays in the sample with SiN spacer layer. However, when the pitch is 450 nm, except the array with 250 nm diameter, all the other arrays in SiN sample are showing higher sensitivity values versus the similar arrays with SiON spacer layer. For the arrays with 250 nm diameter and 450 nm pitch, the sensitivity values in the two samples are very close to each other and are 430 nm/RIU and 422 nm/RIU for SiON and SiN samples, respectively. These results show that for the cylindrical arrays, when the lattice spacing is 400 nm, the SiON spacer layer is performing better than the SiN layer, in case of mode separation. However, when the pitch is 450 nm, the SiN layer is performing better than the SiON, in case of mode separation.

Another crucial factor which needs to be considered is the sensitivity of the samples to the physical variations of the cubes. This is where the cubic nanostructures outperform the cylindrical ones for the SiON dielectric layer. A 30 nm change in the side lengths from the highest sensitivity achieved reduces the sensitivity to ~80 % of the maximum for the cubic designs. On the other hand for the cylindrical nanostructures, a similar change in the diameter reduces the sensitivity to less than 50% of the peak sensitivity. With the SiN layer, the change is similar for both cylindrical and cubic shapes for the pitch of 400 nm. Thus, the higher refractive index of the SiN layer is helping not only in defining the Fano resonances better but also making the structures more fabrication tolerant.

Table 4.1 summarizes the highest sensitivity values achieved for the different designs. For the sample with SiON spacer layer, the cylindrical arrays are showing higher sensitivity values compared to the cubic arrays. This is the opposite of what we observed in the simulations. As mentioned, this is because we achieved almost perfect patterns for the cylindrical arrays due to the lack of sharp features. Further, the addition of the adhesion layers and chromatic dispersion of the dielectric layer changed the domination situation of the LSPR modes in the Fano resonances which led to an alteration of the sensitivity. For the sample with SiN spacer layer, the cubic arrays are performing better than the cylindrical arrays, however, the difference between the highest sensitivity value achieved in the cubic arrays and that one of the cylindrical arrays is only 13 nm/RIU. This shows that even in this sample, the cylindrical arrays are performing almost as good as the cubic arrays.

Table 4.1. Summary of the highest sensitivity values achieved for different designs.

Spacer Layer	Pitch (nm)	Shape	Cube Length / Cylinder Diameter (nm)	Sensitivity (nm/RIU)	Mode 2 Stability Range
SiON	400	Cube	250	367	1.36-1.39
SiON	500	Cube	250	395	1.34-1.39
SiON	400	Cylinder	200	407	1.35-1.39
SiON	450	Cylinder	250	430	1.34-1.39
SiN	400	Cube	250	422	1.35-1.39
SiN	500	Cube	250	435	1.34-1.39
SiN	450	Cylinder	250	422	1.35-1.39

Thus, the optimized structures when we also include the fabrication tolerance are a cylindrical nanoparticle array with diameter of 250 nm and pitch of 450 nm and a cube nanoparticle array with side lengths of 250 nm and pitch of 400 nm. For these designs, mode 2 has been measured to be stable and does not vary with surrounding refractive index in the range of 1.35-1.39. In a bio-chemical sensor, the refractive index of the surrounding medium changes in the range of 0.01-0.0001. These results show that a photonic designer can optimize the structure to the specific needs of the background refractive index range.

To show the advantages of this work, we need to compare our results with the previously fabricated self-referenced sensors. Further, significant features of a low-cost self-referenced plasmonic sensor needs to be compared. There are few theoretical works related to the self-referenced plasmonic sensors which have been proposed contemporary to this work, however, we will only consider the experimental works for comparison. **Table 4.2** compares the important features of two self-referenced plasmonic sensors with this work. The fabricated sensor in reference [34] is based on one dimensional rectangular gold gratings. The problem with the one-dimensional grating is the fabrication variations that happen along the slit and thus make it harder to fabricate compared to our two-dimensional gratings. Further, achieving sharp corners in rectangular grating is hard which again suggests that our cylindrical gratings are easier to fabricate. The plasmonic sensor in reference [34] is working in visible to NIR range, however, as we seen, some of our designs are completely working in the visible range which makes the readout of our sensors easier. This sensor shows a sensitivity of 470 nm/RIU which is only slightly higher than the sensitivity values we achieved here. This sensor has resonance features with moderate

Q comparable to the resonance features of our work. The plasmonic sensor in reference [34] is taking advantage of the LSPR resonances of the top of the grating layer for sensitivity measurements and uses the LSPR resonances of the bottom of the gratings for self-referencing measurement. Although the self-referencing feature was isolated from the surrounding medium, the LSPR modes of the bottom of the slits are very close to the surrounding medium and thus this isolation is not very strong. The wavelength does shift when the surrounding refractive index changes. In our structure, the thin gold film is contributing to the excitation of the self-referencing point and the optical mode is guided within the layer and is thus, away from the surrounding medium. Another self-referenced plasmonic sensor was fabricated in reference [98] using multilayered cubic gratings. Basically, the structure is two cubic gratings layers which are separated by a nitride layer, in which the top grating layer is used for sensitivity and the underneath grating layer is used for self-referencing measurement. The structure has several extra fabrication steps compared to our structure. Further, the sensitivity of this sensor is significantly lower than what we achieved with a much simpler structure.

Table 4.2 Comparison of the previously fabricated self-referenced plasmonic sensors with this work

Reference	Structure	Ease of Fabrication	Operating Band	Sensitivity (nm/RIU)	Q	Complete Isolation
[34]	1-D Rectangular Grating	No	Vis-NIR	470	Moderate	No
[98]	Multilayered 2-D Cubic Grating	No	Vis-NIR	122	low	Yes
This Work	2-D Cubic and Cylindrical Grating	Yes	Vis and Vis-NIR	435	Moderate	Yes

4.8 Advantage of Self- Referencing

An experiment was designed to show one of the advantages of the self-referencing structure proposed in the thesis. A cubic array with 250 nm cube side length and 400 nm pitch, from the sample with the SiN spacer layer was tested in two different days using F40-UV and the reflection spectra were collected. The surrounding refractive index was set at 1.35. Each day the temperature of the environment was slightly different. Further, initial settings of F40-UV such as focusing and baseline measurements were different for each day, as they were done by a human. Due to these changes in the measurement conditions, the reflection spectrum for each day were a little different and resonance wavelengths of LSPR and SPR modes were shifted by a few nanometers. The reflection spectra are

shown in **Figure 4.36**. Also **Table 4.3** shows the resonance wavelengths of SPR, LSPR and local maximum for day 1 and 2. Further, the difference between the resonance wavelengths of the local maximums and the SPR modes, $D\lambda$, is shown for both days. As can be seen in this table, the resonance wavelengths are slightly different for each day.

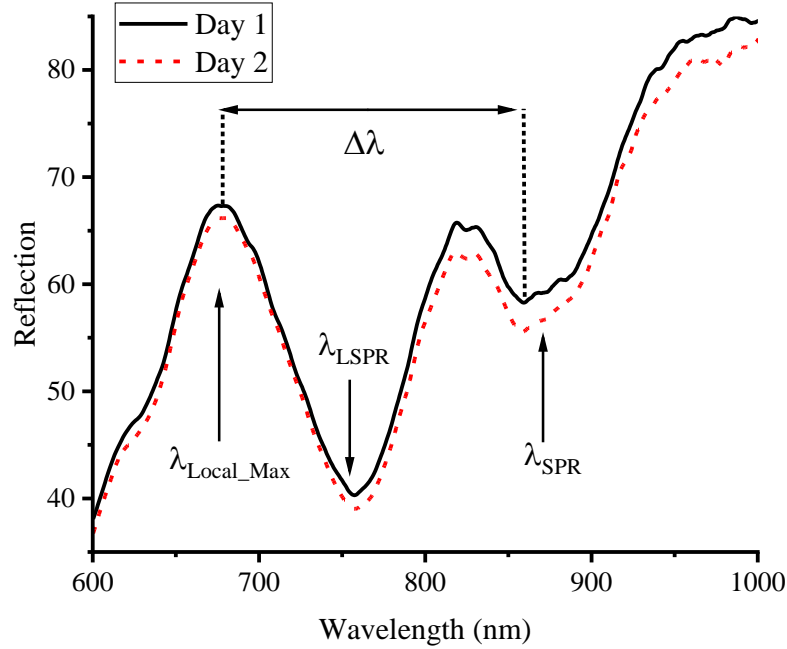


Figure 4.36 Reflection spectra of the cubic array with 250 nm side length and 400 nm pitch from the sample with SiN spacer layer for two different days.

Table 4.3 Resonance wavelengths of SPR, LSPR and local maximum for day 1 and 2.

	$\lambda_{\text{Local_Max}}$ (nm)	λ_{LSPR} (nm)	λ_{SPR} (nm)	$\Delta\lambda = (\lambda_{\text{SPR}} - \lambda_{\text{Local_Max}})$
Day 1	675.85	757.44	859.16	183.31
Day 2	676.91	758.14	859.84	182.93

The sensitivity of the local maximum to the changes of the surrounding refractive index is 422 nm/RIU for this array. If we use the local maximum for the sensitivity measurements, the minimum amount of change in the surrounding refractive index which is detectable by the sensor can be calculated as follows:

$$Minimum \Delta n = \frac{|\lambda_{Local_max}(Day\ 1) - \lambda_{Local_max}(Day\ 2)|}{Sensitivity} = \frac{|675.85 - 676.91|}{422} = 2.5 \times 10^{-3}$$

Thus, if we use the local maximum for the sensitivity measurements, the minimum amount of change in the surrounding index needs to be 2.5×10^{-3} so the sensor can detect it. If the change in the surrounding refractive index is below this number, it would be considered as noise and the sensor cannot detect it. Instead of using the resonance wavelength of the local maximum, we can use $\Delta\lambda$ for the sensitivity measurements. If we use $\Delta\lambda$, the minimum change in the surrounding refractive index detectable by the sensor, can be calculated as follows:

$$Minimum \Delta n = \frac{|\Delta\lambda(Day\ 1) - \Delta\lambda(Day\ 2)|}{Sensitivity} = \frac{|183.31 - 182.93|}{422} = 9 \times 10^{-4}$$

Thus the minimum detectable Δn is improved by a factor of 3 when we use $\Delta\lambda$ for measuring the sensitivity. This means that self-referencing has improved the resolution of the sensor. Note that due to temperature change, there are refractive index changes not accounted for in this calculation. By measuring the sensitivity of the sensor to temperature, a matrix can be developed which can further improve the sensitivity measurements.

4.9 Summary and Conclusion

We have characterized different nano-grating arrays on two different samples with SiON and SiN dielectric spacer layers. All the arrays showed at least two resonance features in the visible to near IR range and confirmed the simulations. The quality factors of the resonance features were lower than the one we achieved in the simulations, however, cubic arrays with side lengths of 200 nm and cylindrical arrays with diameters of 200 nm and higher, were still showing resonance features with decent quality factors. Sensitivity performance of the arrays were close to the simulation results and for some arrays we achieved higher sensitivity values compared to the simulations. The self-referencing mode was isolated from the surrounding environment for most of the arrays. However, this isolation happens in different surrounding refractive indices due to the chromatic dispersion of the spacer layer.

Chapter 5

High Quality-Factor Hybrid Plasmonic-Nanowire Structural Color Generation

There are numerous benefits in integration of plasmonics with nanowires for sensing applications. Optical modes in nanowires can couple with plasmonic modes and create narrow high-Q resonance features. Accordingly, in this chapter a hybrid plasmonic-nanowire structure is proposed and investigated for generation of high Q resonance and structural colors. Multiple localized surface plasmon resonance (LSPR) modes and plasmonic surface lattice resonance (SLR) modes are excited within the structure by introducing a thin gold layer on top of a Titanium dioxide (TiO₂) nanowire array. Nanowire arrays support diameter dependent resonant optical modes and when the wavelength of the optical resonance coincides with the plasmonic resonance; high-Q SLR modes are generated. The LSPR modes create a resonance feature in the reflection in the visible range. Thus, a wide range of vivid colors can be generated by this easy-to-fabricate structure via tuning geometrical parameters like the length and diameter of the nanowires and thickness of the plasmonic layer. A high Q of 233 is achieved with a low linewidth of 2.65 nm in the visible range.

5.1 Introduction

Recently, there have been significant efforts in miniaturizing biomedical and optoelectronic devices. To this end, precisely engineered plasmonic nanostructures with multiple optical functionalities such as filtering, sensing, and surface-enhanced spectroscopy have been realized in a single chip [99, 100]. Arrays of plasmonic nanostructures with plasmon localization ability and surface intensity enhancement, can manipulate the optical response of surface plasmons and form the miniaturized multifunctional optoelectronic devices of the future [101, 102]. To sufficiently make use of the multi functionalities of such devices, multi-resonance transmission and reflection spectra with high-quality factor (Q-factor) are required [103]. Although, Q-factor as a figure of merit for the design and performance of plasmonic nanostructures can be limited by plasmon loss channels, tuning geometrical parameters, shape, and arrangement of materials provide degrees of freedom to achieve high Q-factors [103]. High Q factor resonance features can be achieved from periodically arranged plasmonic nanostructures that can support collective resonances called plasmonic surface lattice resonances

(SLRs) [104-106]. Plasmonic SLRs are the result of coupling between the collective response of individual LSPR modes and in-plane diffraction orders of the periodic nanostructures [104-106].

Plasmonic nanostructures have gained a considerable amount of attention due to their capability in producing a wide range of colors which makes them quite desirable for ultrathin imaging and display technologies [107]. Using nanostructure metallic arrays of gold, silver, and aluminum; absorption, and scattering of lightwave can be manipulated using plasmonic resonances to generate different structural colors [107]. The strong dependency of optical resonances on geometry, periodicity, and constituent materials of metallic grating structures, makes them desirable candidates for generating color filters with arbitrary colors [107].

Localized surface plasmon resonance (LSPR) sensors are promising candidates for portable sensor technologies with low-cost, lightweight, and simple to use features [108]. Plasmonic sensors exhibit an enhancement in their absorption profile due to the localized surface plasmon resonance phenomenon. This absorption peak happens in the UV-vis-NIR range, and its position depends on the sensor's composition, shape, and local refractive index [109]. Changes in the local refractive index, which is induced by the variation of the surrounding analyte, change the position of the absorption peak. Reading out the sensor is being done by spectroscopically monitoring the changes in the position of the absorption peak [109]. However, the spectroscopic laboratory instruments are usually costly and bulky. When the LSPR phenomenon leads to an absorption enhancement in the visible range, it is possible to read out the sensor colorimetrically, avoiding the cost-effective laboratory instrumentation [109].

Kumar et al. [110], fabricated structural colors from nanodiscs arrays on top of a backreflector to obtain pitch pixels that reflect individual colors. However, the structure is not able to generate high Q resonance in the visible range. In another work [111], silver tandem nanodiscs were used for full color generation. Although a high Q resonance feature was realized, the structure is not easy to fabricate. Another work [112] exploited plasmonic SLR modes to generate high Q resonance features from rectangular gold arrays. Nevertheless, the resonance feature is in the telecommunication band and is not suitable for low-cost sensing applications. Yang et al. [113], have proposed metal-insulator-metal nanopillar arrays that support SLR modes and can generate a decent resonance feature with a high Q of 147 under the oblique incident. However, the structure is again difficult to fabricate, requiring multiple high resolution lithography steps. Two easy-to-fabricate plasmonic sensors were demonstrated

in previous works [45, 108]. Although they operate in visible range and are suitable for low-cost colorimetric sensing applications, they are not able to generate high Q resonances.

In this chapter, we propose and numerically investigate a hybrid plasmonic-nanowire structure. A thin gold layer is introduced on top of a periodic TiO_2 nanowire array and the entire structure can be fabricated on top of a TiO_2 thin film and a glass substrate. The structure requires one lithography and one etching step. The periodic TiO_2 nanowire array can support guided optical modes in the visible range. Further, the thin gold layer on top can support LSPR modes in the interfaces of gold and air and interfaces of gold and TiO_2 . The proposed structure is designed in a way that the resonance of at least one of the LSPR modes matches in wavelength with the resonance of the nanowire optical mode. Thus, strong SLR and LSPR modes can be excited in the visible range, resulting in high Q resonances and vivid structural colors. Tuning geometrical parameters provides degrees of freedom to design the structure for different applications. We optimize the structure to have two resonance features in the visible range with the highest possible Q factor for both peaks, while the surrounding medium is air. For the optimized structure, we achieved Q factors of 178 and 6.6 for SLR and LSPR modes, respectively. Further, a wide range of vivid colors is simulated. The LSPR-dominant peak is expected to be extremely sensitive to the changes in the local refractive index while the SLR mode depends less on the surrounding medium. As these modes are excited in the visible range, any change in the local refractive index can result in changing the reflected color from the structure. Such a structure can be used to fabricate low-cost colorimetric sensors with the self-referencing ability [108]. This chapter is organized as follows. In the next section, we analyze the proposed design and discuss the supported modes within the structure. Then we will evaluate the response of the structure to the changes in the geometrical parameters such as NW diameters, the thickness of the gold layer, and effective length.

5.2 Proposed Design

The schematic diagram of the periodic nanowire array is shown in **Figure 5.1**. TiO_2 nanowires with a layer of gold on the top, are separated by a lattice spacing of 400 nm and are placed on top of a thin TiO_2 film. The nanowires are capped with a thin layer of gold to support plasmonic modes. The proposed structure can be fabricated by first growing a thin film of TiO_2 on a glass substrate, and then create gold nanodiscs using lithography and lift-off followed by etching the nanowires into the TiO_2 . The gold layer on the top can support LSPR modes. Various parameters are important in the design including nanowires diameter, nanowires length, gold layer thickness, and TiO_2 film thickness. By

altering mentioned parameters, the excitation and coupling of LSPR and SLR modes can be controlled with respect to the specific application.

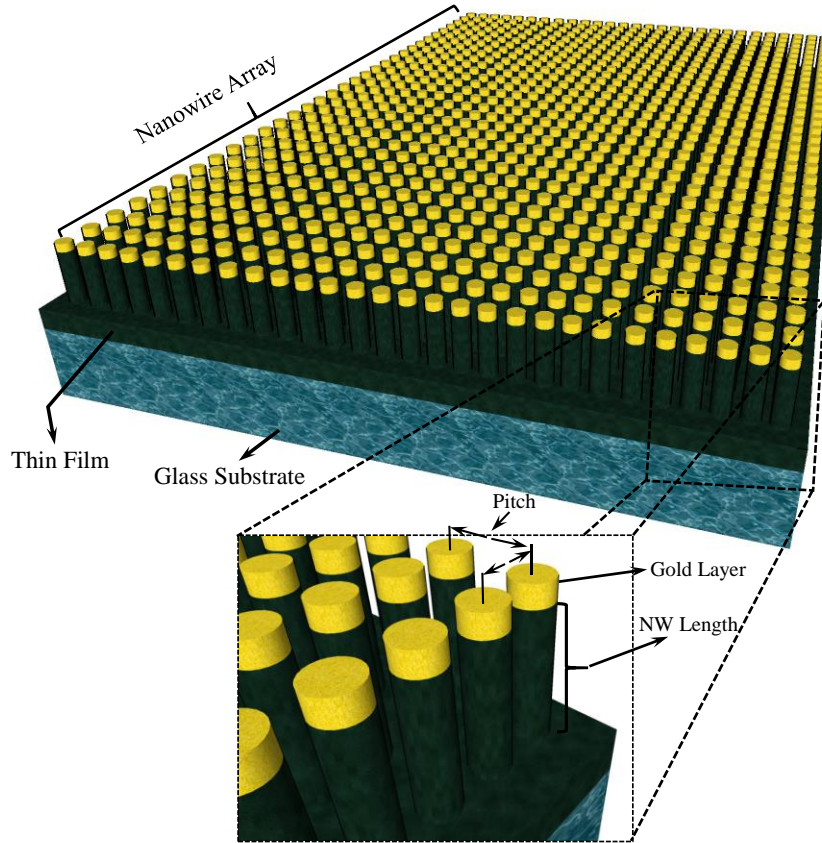


Figure 5.1. Schematic diagram of the proposed nanowires array

The proposed structure was simulated by a commercial software (Rsoft) using rigorous coupled wave analysis (RCWA) to understand the various resonances which are created. Dielectric properties of gold and TiO_2 were extracted from experimental data in [67] and [113], respectively. Periodic boundary conditions in transverse plane were utilized to account for the periodic nature of the system and a cell containing a nanowire structure was simulated in three dimensions. The incident light is assumed to be a plane wave incident normally on the structure. Based on the convergence studies, 12 harmonics were chosen for simulation. In addition, for accuracy, results were verified using simulation of some sample structures with finite difference time domain method.

The nanostructure was designed to achieve the highest quality factor when the surrounding medium is air. Once the structure was optimized, very well-defined resonance peaks with a high Q factor were

created. Accordingly, the NW diameter and NW length are set to 150 nm and 120 nm, respectively. The height of the gold layer on the top is set to 50 nm and the thickness of TiO₂ film is equal to 40 nm. Further, the surrounding medium is assumed to be air (n=1). The absorption, reflection, and transmission spectra of the optimized structure are shown in **Figure 5.2a**.

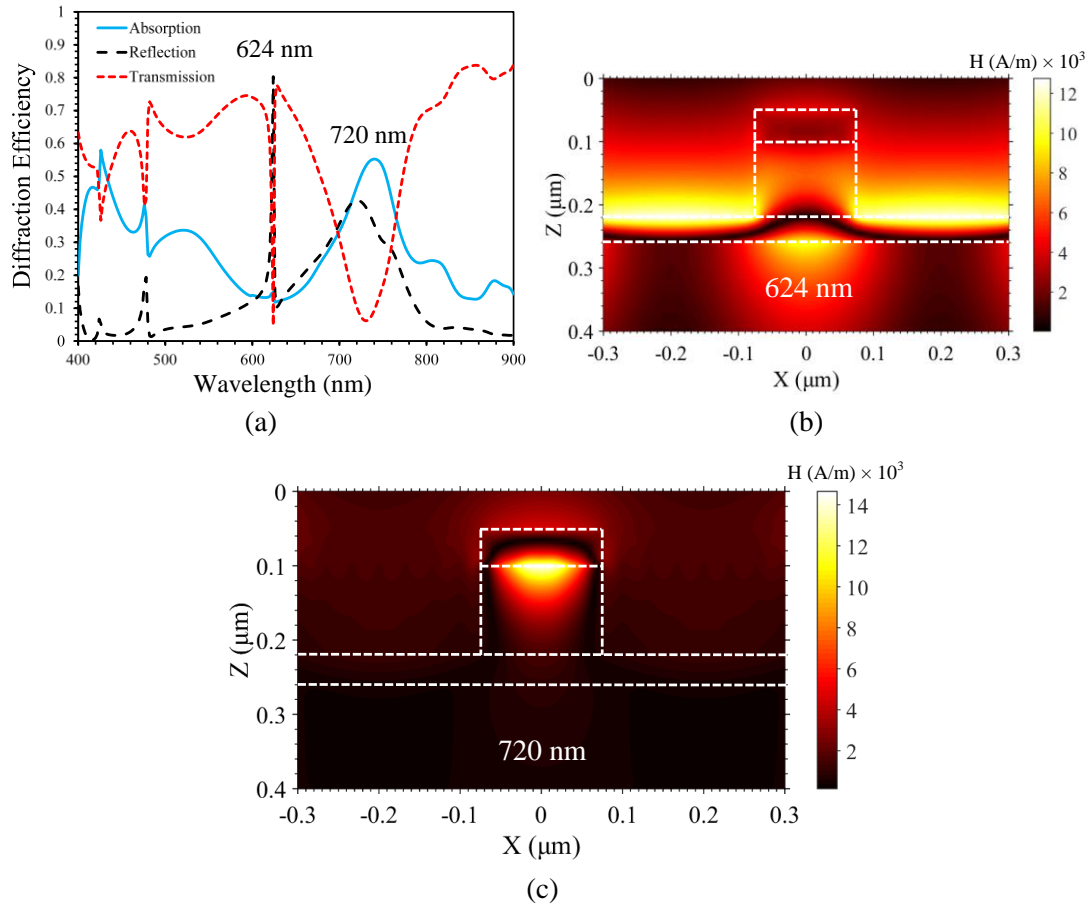


Figure 5.2. (a) Absorption, reflection, and transmission spectra of the proposed nanowire array, (b) and (c) distribution of H_y for two resonance features of optimized structure at 624 nm and 720 nm wavelengths respectively.

There are two major peaks in the reflection spectrum of the structure at wavelengths of 624 nm and 720 nm. Corresponding to the mentioned peaks in the reflection spectrum, there are two dips in the transmission spectrum and one peak in the absorption spectrum at a wavelength of 720 nm. In order to understand the reason for reflection enhancement in these wavelengths, the magnetic field distributions, $|H|$, are calculated and shown in **Figure 5.2b, c**. At a wavelength of 624 nm, as seen in **Figure 5.2b**, LSPR modes are excited on the top of the gold layer and the interface of the gold layer and TiO₂

nanowire. However, the majority of the field is concentrated on the TiO₂ film surface due to the in-plane diffraction. Coupling of the diffraction modes in the plane of the array and collective LSPR modes create a strong SLR mode that results in a very narrow peak with a high quality factor in the reflection spectrum. As seen in **Figure 5.2c**, at the wavelength of 720 nm, strong LSPR modes are excited on top of the gold layer and interface of the gold and NW, while the majority of localized surface plasmons are excited in between gold and TiO₂ nanowire. Further, a portion of the field is reflected from the surface of TiO₂ film and within the structure. This can also be seen from the absorption and reflection spectra in **Figure 5.2a**.

Figure 5.3 provides a more informative view of the reflection spectrum of the optimized structure. As seen in this figure, SLR and LSPR peaks are very well-defined with quality factors of 178 and 6.6, respectively. As mentioned, the structure was optimized to achieve two resonance peaks in the visible range with the highest possible Q. However, if only one resonance feature is needed, the quality factor of SLR mode can be enhanced to 233 by tuning the geometrical parameter, as we will see in the next section. This gives degrees of freedom to design the structure for different applications. For instance, as the refractive index of the surrounding medium changes, it is expected that the resonance frequencies of SLR and LSPR modes shift, and thus the reflected color changes. However, as the SLR mode is the result of the coupling of LSPR modes and in-plane diffractions, it is expected that the SLR resonance feature would be less sensitive to the changes in the local refractive index compared to the LSPR resonance feature. Thus, for sensing applications, the SLR peak can be used as a self-referencing feature while the LSPR peak is being used for sensing the changes in the surrounding medium [108]. Also, the sensor can be read out colorimetrically which is another advantage of the structure.

5.3 Effect of NW Diameter

SLR and LSPR modes are highly dependent on the shape and dimensions of the nanostructures. This gives degrees of freedom to design the structure with respect to the application. In order to understand how the wavelength, strength, and Q of the resonance peaks change, the proposed structure was simulated while the geometrical parameters were being changed. **Figure 5.4a** shows the reflection spectra of the proposed nanostructure for different NW diameters. Further, a three-dimensional curve of reflection spectra for various NW diameters and magnetic field distributions of the resonance features at corresponding diameters are shown in **Figure 5.4b, c**, respectively. As seen in **Figures 5.4a, b**, the SLR and LSPR modes are not excited while NW diameter is less than 70 nm.

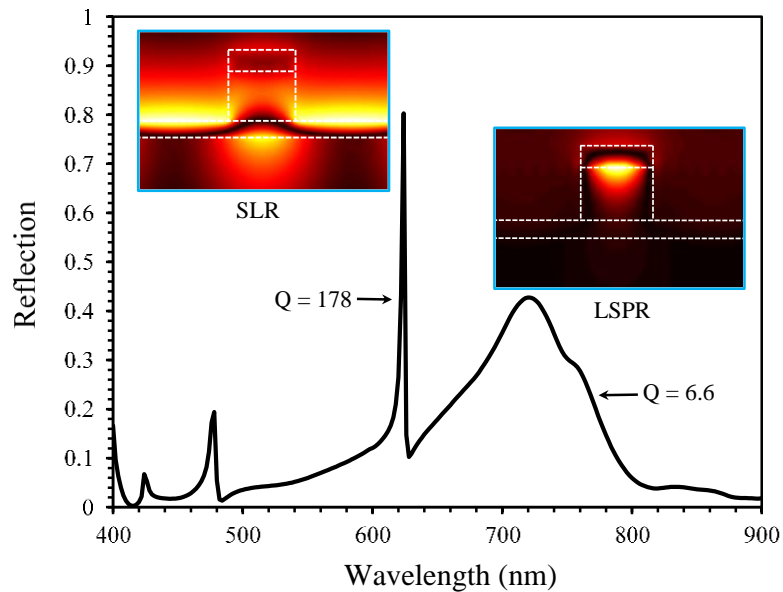


Figure 5.3. Reflection spectrum of the optimized structure and magnetic field distributions of corresponding resonance features

As the NW diameter reaches 70 nm, the SLR mode gets excited, and as the diameter increases more, the SLR mode gets stronger, and its resonance wavelength shifts slightly to the higher wavelengths. However, for NW diameters higher than 170 nm, the linewidth of the SLR resonance peak increases which leads to a reduction in Q . As can be seen from **Figure 5.4c**, although the intensity of the magnetic field of SLR modes reduces at higher diameters, the amount of confined field within the structure increases which leads to a resonance with a higher line width.

The LSPR mode in the structure is cavity enhanced. Nanowire allow for resonant excitation of the optical mode where the resonance wavelength is diameter dependent [114]. When the resonant wavelength of the nanowire and LSPR resonance within the gold are at the same wavelength, a strong resonance is observed. For the structure under study, this appears for NW diameters of approximately 130 nm, as seen in **Figure 5.4b**. The peak gets stronger as NW diameter increases, and its central wavelength shifts to higher wavelengths. Further, as seen in **Figure 5.4c**, LSPR modes on top of the gold layer and the interface of gold and TiO_2 get much stronger at higher NW diameters. It is expected that the resonance wavelength of LSPR modes is sensitive to the changes in the local refractive index. Thus, if the sensing application is required, one can design the structure with an NW diameter of more than 130 nm to get the LSPR resonance feature.

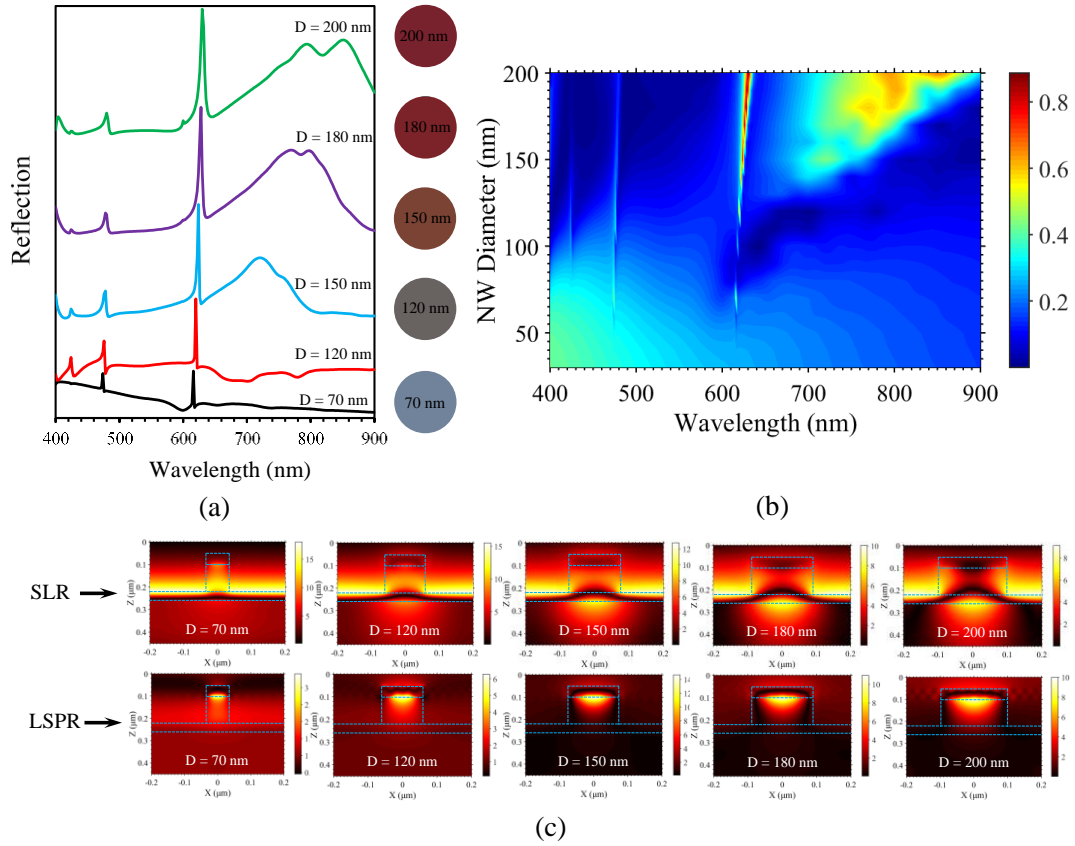


Figure 5.4. (a) Reflection spectra of the proposed design with different NW diameter and the reflected color from each spectrum, (b) a three-dimensional view of the reflection spectra as functions of NW diameter and wavelength, and (c) magnetic field distributions of SLR and LSPR resonance features with a unit of $A/m \times 10^3$

The simulated color from each spectrum is shown on the right side of **Figure 5.4a**. To simulate the reflected colors, color-matching function with CIE 1931 2° standard observer under illumination D65 from the American Society for Testing and Materials E308-01 (ASTM, 2001) were used [115]. The CIE 1931 chromaticity space can be used to show the trend of reflected colors from the nanostructure while NW diameters are changed. The nanowire diameters were changed from 30 nm to 200 nm by a step size of 10 nm and the reflected color from each array was simulated using a CIE 1931 color-matching function. The simulation colors are shown in **Figure 5.5** for 18 samples with different NW diameters. The black dashed line with the arrow shows the evolution trend for the colors when the NW diameters are increased. As seen in this figure, the reflected colors vary from light blue to red by enhancing the NW diameters. This is reasonable since LSPR modes are excited at higher NW diameters and add red color to the reflected spectrum.

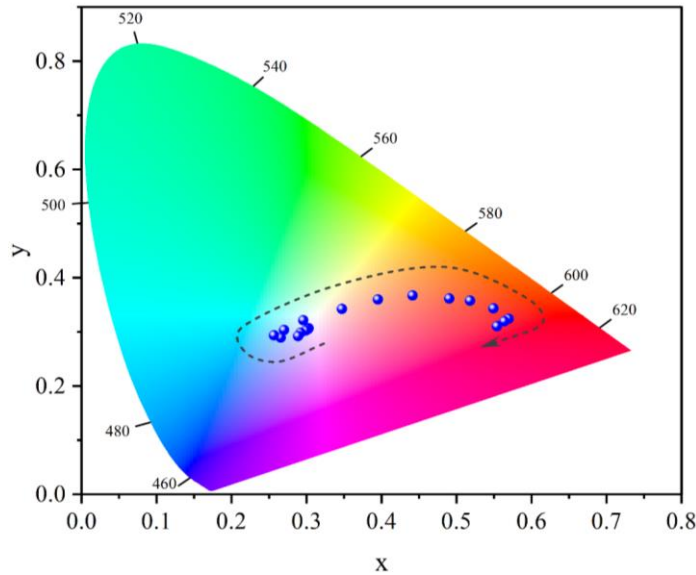


Figure 5.5. Reflected colors from 18 samples with different NW diameters. The dashed line with arrow shows the evolution trend of colors when the size of NW diameters is increased.

Table 5.1 provides quantitative information about the SLR resonance feature for different NW diameters. One can see from **Table 5.1** that resonance wavelength shifts slightly to the higher wavelengths as the NW diameter increases. A high Q of 233 has been achieved at an NW diameter of 100 nm with a linewidth of 2.65 nm.

Table 5.1. Quantitative information of SLR resonance feature

NW Diameter (nm)	70	100	120	130	140	150	160	170	180	190	200
Resonance wavelength (nm)	616	618	620	621	622	624	625	626	628	629	630
Linewidth (nm)	3.6	2.65	2.7	7.2	2.8	3.5	5.1	5	5.5	6.6	7.6
Q	171	233	229	86	222	178	122	125.2	114	95	82

5.4 Gold Layer Thickness

Figure 5.6a shows the reflection spectra of the proposed structure for different thicknesses of the top gold layer. Reflected color from each spectrum is also shown on the right side. Further, a three-dimensional curve of reflection spectra and magnetic field distributions of SLR and LSPR resonance features are shown in **Figures 5.6b, c**, respectively. As seen in **Figures 5.6a, b**, when the gold thickness is less than 60 nm, the SLR resonance feature is very well defined with a high quality-factor. Once the gold height goes above 60 nm, the SLR resonance feature gets weaker, and its shape is deformed. It can

be seen from fields distributions in **Figure 5.6c** that as the gold thickness goes higher than 60 nm, the field strength decreases. Further, the LSPR resonance feature is not strong enough for a gold thickness less than 30 nm and gets much stronger when gold height goes above 50 nm. Also, as seen in **Figure 5.6c**, the field distributions of LSPR modes get much stronger when gold height is increased. Thus, one can design the top gold layer between 30 nm and 60 nm to get two resonance features in the reflection spectrum with high Q.

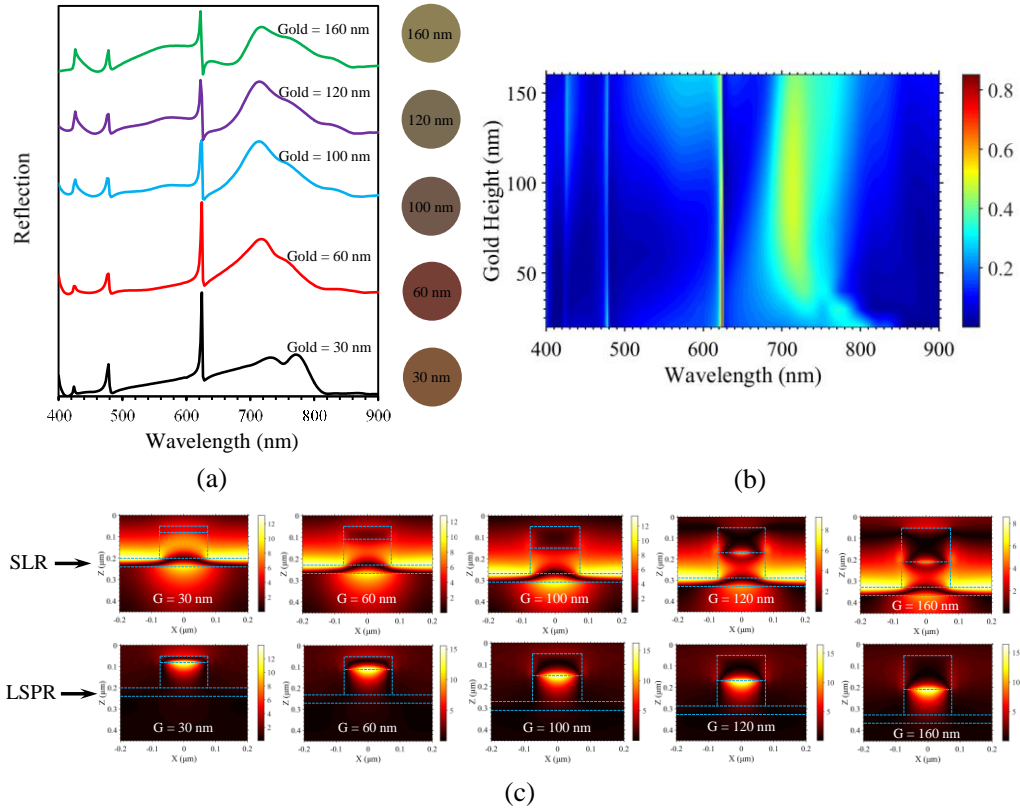


Figure 5.6. (a) Reflection spectra of the proposed design with different thicknesses of the top gold layer and the reflected color from each spectrum, (b) a three-dimensional view of the reflection spectra as functions of gold thickness and wavelength, and (c) magnetic field distributions of SLR and LSPR resonance features with a unit of $A/m \times 10^3$

Figure 5.7 shows the simulated color using CIE 1931 color-matching function for different gold thicknesses. Gold thickness was changed from 20 nm to 160 nm with a step size of 10 nm (15 samples) and reflected color from each sample was simulated using the color-matching function. The black dashed line with the arrow shows the evolution trend for the colors when the gold thickness is increased. As can be seen in **Figure 5.7**, reflected color does not change a lot with increasing the gold thickness.

As the LSPR peak shifts to the lower wavelengths, once the gold thickness is increased, the reflected color varies from brown to light brown and yellow.

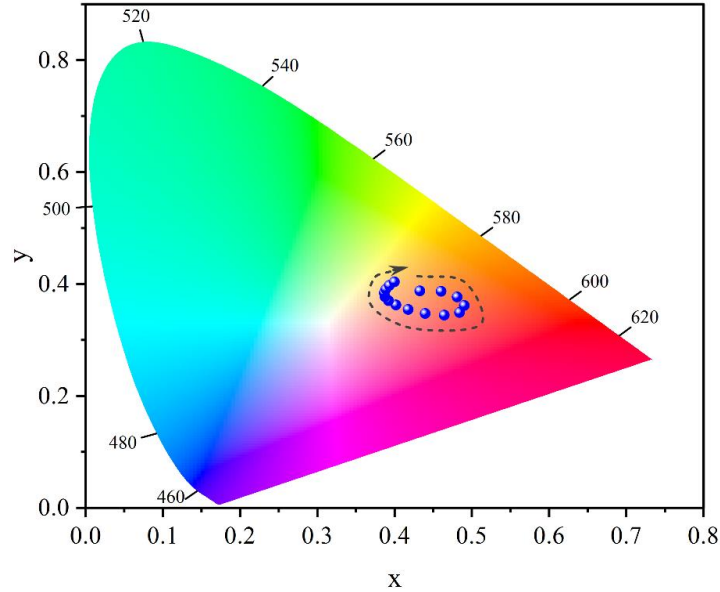


Figure 5.7. Reflected colors from 15 samples with different gold thicknesses. The dashed line with arrow shows the evolution trend of colors when the gold thickness is increased.

5.5 Total TiO₂ Thickness Variations

Total TiO₂ thickness is defined as the total length of TiO₂ nanowire plus the length of TiO₂ thin film. The plasmonic nanowire structure was simulated while the total TiO₂ thickness was set to 80, 100, 130, 160, 200, and 250 nm. While the total TiO₂ thickness was kept constant, the length of nanowires (etch) was increased from 20 nm by a step size of 10 nm, till the TiO₂ film reaches a minimum length of 20 nm. Under these circumstances, the structures were simulated to see how the resonance features will change. In this section, we are mainly looking for designs that can excite SLR modes within the structure. Thus, for most of the designs, the NW diameters were set to 100 nm. However, as seen before, LSPR modes can be easily excited by the proposed structure by setting the NWs diameter to 130 nm or more.

Figure 5.8 shows the reflection spectra of the proposed structure with total TiO₂ thickness of 130, 160, 200, 250 nm. Only those designs are shown that can support SLR modes. As seen in **Figures 5.8a, b**, total TiO₂ thicknesses of 130 nm and 160 nm can support four SLR modes with different NW lengths. Each resonance feature has a different strength and resonance wavelength. Further, as seen in **Figures**

5.8c, d, total TiO₂ thickness of 200 nm and 250 nm can only support two SLR modes with different strength and resonance wavelengths. As a result, the strength and resonance wavelength of the SLR resonance feature can be tuned by changing the total TiO₂ thickness and etch, based on the application.

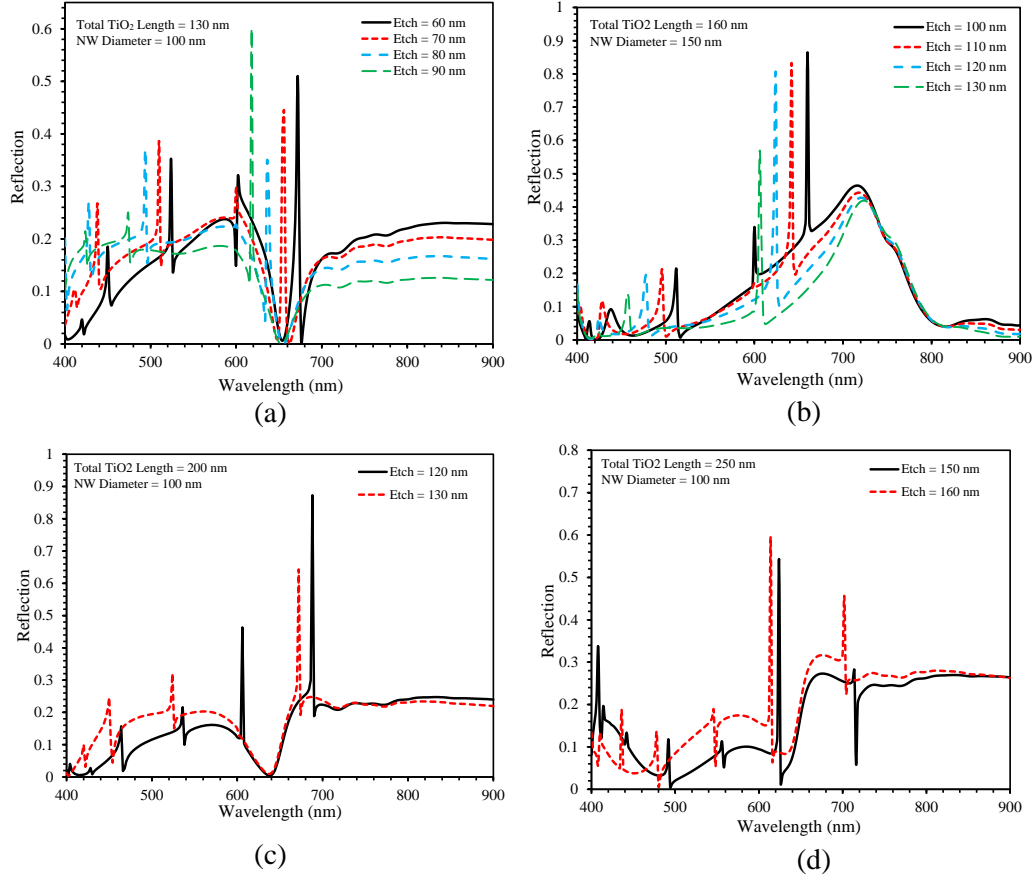


Figure 5.8. Reflection spectra of proposed nanowire structure for different etch values, (a) total TiO₂ thickness of 130 nm and NW diameter of 100 nm, (b) total TiO₂ thickness of 160 nm and NW diameter of 150 nm, (c) total TiO₂ thickness of 200 nm and NW diameter of 100 nm, and (d) total TiO₂ thickness of 250 nm and NW diameter of 100 nm.

Figure 5.9a-d shows the simulated colors for total TiO₂ thickness of 130 nm, 160 nm, 200 nm, and 250 nm, respectively. For each TiO₂ thickness, the NWs length was increased from 20 nm by a step size of 10 nm till the thickness of TiO₂ film reached 20 nm. Then, reflected color from each sample was simulated using the color-matching function. The black dashed line with the arrow shows the evolution of the color trend when the etch is increased. For **Figure 5.9c, d**, the evolution of simulated colors starts with dashed line 1 and then continues with dashed line 2. As can be seen in **Figure 5.9**, a wide range of color-matching functions can be covered by adjusting the total TiO₂ thickness.

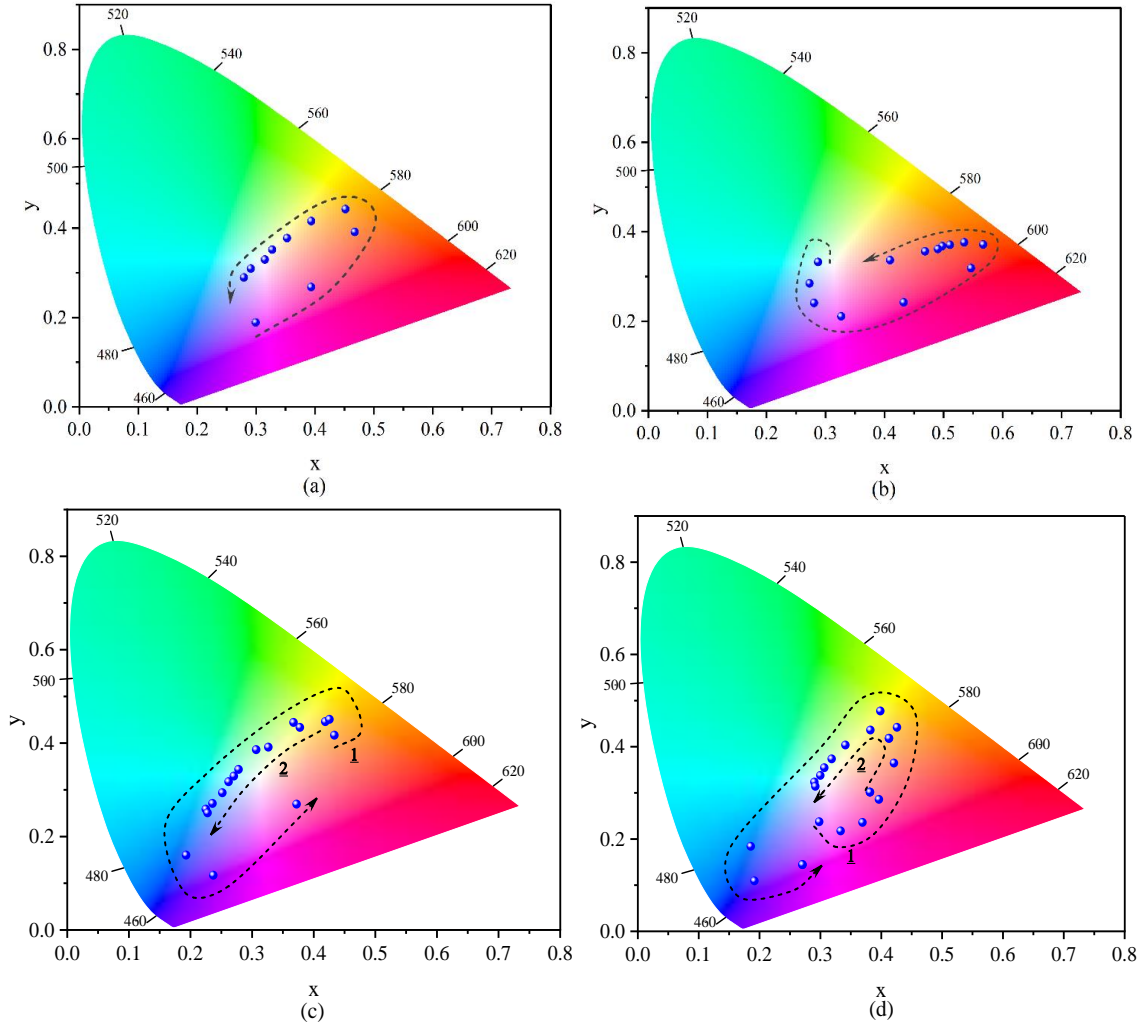























Figure 5.9. Reflected colors from the proposed nanostructure with total TiO₂ thicknesses of (a) 130 nm, (b) 160 nm, (c) 200 nm, and (d) 250 nm. The black dashed line shows the color evolution as etch increases.

Table 5.2 provides a list of simulated colors from different designs. A wide range of colors has been simulated by changing the total TiO₂ thickness and the etch. As the structure supports SLR and LSPR modes, it is expected that by changing the local refractive index, the properties of these modes change and result in reflecting a different color. This can be used in fabricating low-cost colorimetric sensors.

Table 5.2. Simulated colors from different designs.

Effective Length (nm)	NW Diameter (nm)	Etch (nm)	Color
130	100	20	
130	100	40	
130	100	60	
130	100	110	
160	150	20	
160	150	40	
160	150	60	
160	150	80	
160	150	140	
200	100	20	
200	100	40	
200	100	60	
200	100	80	
200	100	90	
200	100	110	
200	100	120	
200	100	170	
250	100	40	
250	100	80	
250	100	110	
250	100	130	

5.6 Conclusion

In this chapter, we propose and numerically evaluate a plasmonic-nanowire hybrid device which generates vivid structural color. By placing a thin gold layer on top of a TiO₂ nanowire array, the structure can support SLR and LSPR modes. These modes produce resonance features in the visible range of the reflection spectra and thus generate vivid colors. The SLR mode which is the result of the

coupling of in-plane diffraction and collective response of individual LSPR modes creates a peak in the reflection spectrum with a high Q of 233. The structure was analyzed for different geometrical parameters. Through tuning the diameter of the nanowires, gold thickness, and total TiO₂ thickness of nanowires, a wide range of colors were simulated ; encouraging us to experimentally fabricate and demonstrate the device.

Chapter 6

Fabrication and Characterization of the Plasmonic-Nanowire Hybrid Structure

In this chapter, we describe the fabrication and characterization details of the hybrid plasmonic-nanowire structure proposed in Chapter 5. Integration of nanowires with noble metals can provide an opportunity for coupling of optical modes in nanowires with plasmonic modes and, thus generation of resonance features with high Q. Such a structure can be used for sensing and structural color generation.

6.1 Fabrication of the TiO₂ Nanowires Capped with Gold

6.1.1 Lithography and Mask Definition

The proposed hybrid structure in Chapter 5 contains highly ordered TiO₂ nanowires capped with a thin layer of gold. Further, there is also a TiO₂ thin film. The entire structure is fabricated on top of a glass substrate. The fabrication steps of the hybrid plasmonic-nanowire structure are summarized in **Figure 6.1**. The structure was fabricated on a Corning EAGLE GX glass substrate, the same as the plasmonic structures demonstrated in Chapter 4. For the first sample, we aimed for the optimized structure that was simulated in Chapter 5. In the optimized structure, the thickness of the TiO₂ thin film was 40 nm and the length of the TiO₂ nanowires was 120 nm. We intended to use top-down approach for the fabrication of TiO₂ nanowires, as this method was successfully used in our group for the fabrication of highly ordered semiconductor nanowires. In the top-down approach, the surface is patterned with a hard mask, and nanowires are etched into the substrate. Thus, a 160 nm thick TiO₂ film was deposited on the substrate using an AJA magnetron sputtering system [116]. The deposition was done at room temperature, at 300 W power, and with a deposition rate of approximately 1 nm per minute. Then, the sample was spin-coated with PMMA A4 at a speed of 4000 rpm. Due to the presence of the TiO₂ film under the e-beam resist, to avoid the charge build-up during the lithography, PMMA Electra92 was also spin-coated on the sample at a speed of 5000 rpm. E-beam lithography was done at 20 kV using the RAITH150^{two} lithography system with a step size of 10 nm. Different arrays with 100 μm × 100 μm dimensions, including circular patterns, were designed using Raith CAD software with lattice spacings of 400 and 450 nm, while the diameters of the circles were changing from 110 nm to 230 nm with 20 nm increments. The minimum e-beam dose required for developing such a pattern on PMMA

was found to be $400 \mu\text{C}/\text{cm}^2$ through a series of dose test experiments. After lithography, the sample was soaked in DI water for two minutes to remove the PMMA Electra92 and then dried again with nitrogen. Then, the sample was developed in MIBK: IPA (1:3) for 30 seconds, cleaned in IPA for another 30 seconds, and finally dried with nitrogen. Subsequently, the sample was mounted in the Intlvac e-beam deposition system, and a 3 nm thick Ti as an adhesion layer, followed by a 50 nm thick gold layer, was deposited on the sample. In order to fabricate the nanowires using the top-down approach, a 100 nm Aluminum (Al) layer was deposited on the sample to act as a hard mask during the dry etching. Finally, the sample was soaked overnight in PG remover bath, and lift-off was done to create the circular patterns, which are nano-discs made of the three mentioned metallic layers.

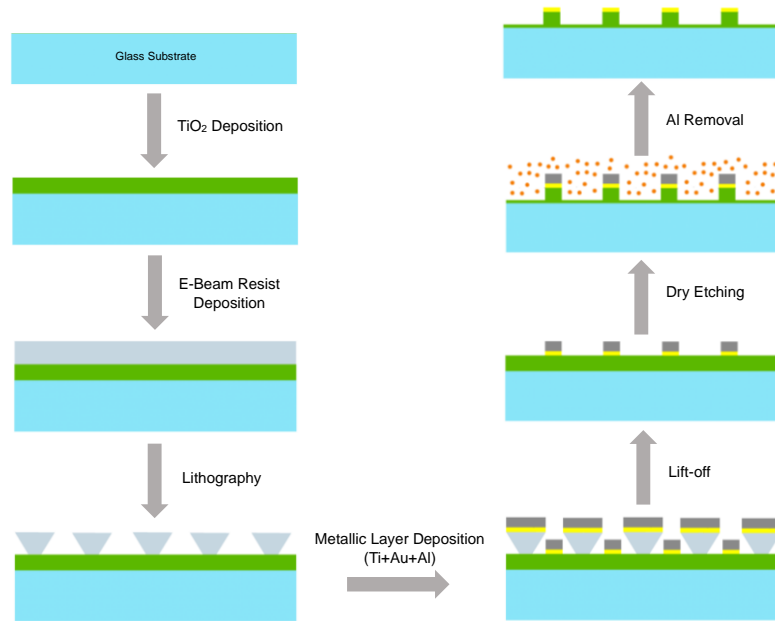


Figure 6.1. Summary of the fabrication steps for the TiO_2 nanowires capped with a layer of gold.

6.1.2 Dry Etching

We've used dry etching for the fabrication of the TiO_2 nanowires. In dry etching, isotropic etching maintains a consistent etching rate in all directions, indicating that a material's characteristics remain direction-independent. In contrast, anisotropic etching selectively removes material along specific directions, exhibiting direction-dependent behavior. Selectivity refers to the comparison of etching rates between a masking material (utilized for patterning) and the etching rate of the target material. Dry etching technology can be categorized into three distinct categories known as vapor phase etching, sputter etching, and reactive ion etching (RIE).

Reactive Ion Etching (RIE) is a technique for anisotropic etching that offers precise control over the morphologies of nanostructures, including sidewall smoothness, diameter, length, and shape, while also enabling the maintenance of high aspect ratios and the preservation of axial heterostructures, doping, and the crystal orientation of the bulk material. However, achieving all these features requires the use of inductively coupled plasma (ICP) in conjunction with RIE, typically applied to a wafer covered with hard masks that have been patterned using optical or electron beam lithography. In an RIE system, a single RF plasma source is responsible for controlling both the density and energy of ions. This reduces independent control on the density and energy of ions and makes it challenging to achieve a balanced combination of etch rate, anisotropy, and damage control for nanowires. Conversely, when an ICP source is introduced, it can generate plasma density that is 10-100 times greater while operating at pressures 5-100 times lower than RIE systems. ICP-RIE separates the control of incident ion energy from the generation of plasma density by applying RF power independently to a coil wrapped around the plasma chamber. This decoupling allows for independent management of both features. As a result, it enables a higher etch rate due to the increased plasma density, precise morphology control through the independent adjustment of ion energy using forward power, and minimizes physical damage caused by ion bombardment to achieve the desired outcomes [117].

The masked sample was installed in an OXFORD PlasmaTherm ICP-RIE for the dry etching process. A recipe was already available in the QNFCF for the dry etching of the TiO₂ and was directly used without optimization. **Table 6.1** presents the details of this recipe for the dry etching of TiO₂ in the ICP-RIE system.

Table 6.1. Details of the recipe for the dry etching process of TiO₂

<i>C₄F₈ flow rate</i>	10 sccm
<i>O₂ flow rate</i>	10 sccm
<i>Ar flow rate</i>	80 sccm
<i>Pressure</i>	5 mTorr
<i>ICP Power</i>	1500 Watts @ 2MHz
<i>RF Power</i>	150 Watts @ 13.56MHz
<i>Temperature</i>	60 °C
<i>Selectivity TiO₂: Al mask</i>	13:1

The chemistry of the dry etching process of the TiO_2 can be briefly explained as described below [118, 119]. Octafluorocyclobutane (C_4F_8) plasma manipulates the surface of the TiO_2 and forms titanium fluorides (TiF_x) and C-F polymer. Subsequently, the C-F polymer and TiF_x will be removed by Oxygen (O_2) plasma. Further, the presence of the Argon (Ar) enhances the plasma density of the C_4F_8 . The etch rate of the recipe was unknown. For the successful demonstration of the proposed structure, we needed to control the etch depth precisely. Thus, experiments were first done to study the etch rate. A thin layer of TiO_2 was deposited on a Si substrate, and the sample was placed inside the ICP-RIE system several times, and each time, the thickness of the TiO_2 layer was measured using an ellipsometer. Three built-in optical models for TiO_2 existed in the ellipsometer. The sample was tested using an ellipsometer, and all three optical models were fitted to the experimental data. **Figure 6.2** shows the fit results from the ellipsometer for the Tauc-Lorentz model [120] (experimental curves are in solid lines, while the fit curves are dotted lines for different incident angles). For the Tauc-Lorentz model in **Figure 6.2**, the mean square error (MSE) of the fit was 8.5. MSE is defined by determining the error from the measured reflection spectra and that predicted by the model. As a result, the Tauc-Lorentz model was selected for the thickness measurement of the TiO_2 film, as it provides the lowest MSE. Through multiple tests, the etch rate of the TiO_2 was found to be approximately 90 nm/min.

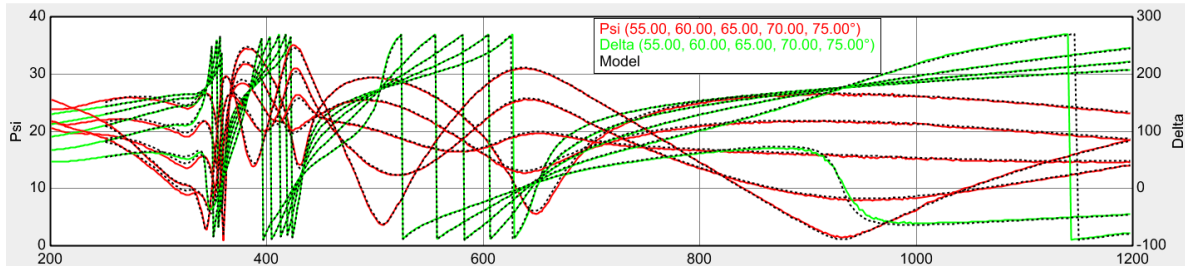


Figure 6.2. The fit result from the ellipsometer for the Tauc-Lorentz model for TiO_2 film.

Further, the refractive index of the TiO_2 film was extracted from the ellipsometer and is shown in **Figure 6.3**. As seen in this figure, the refractive index value is 2.7 at 400 nm wavelength and decreases exponentially as the wavelength increases. During the simulations in Chapter 5, we have set the refractive index of the TiO_2 to be 2.7. However, the actual refractive index of the TiO_2 is lower than the 2.7 and is changing due to the chromatic dispersion. The difference in the refractive index is expected to affect the quality factors of the modes and their resonance wavelengths compared to the ones in simulations.

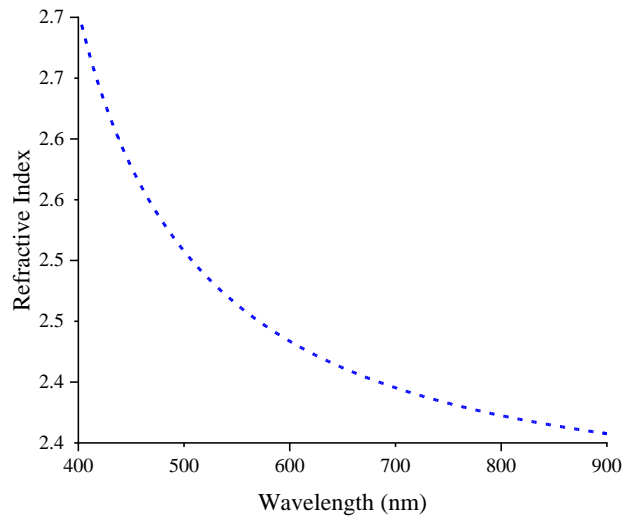


Figure 6.3. The refractive index of the deposited TiO₂ extracted using the ellipsometer.

After finding the etch rate of the TiO₂, the main sample with the Al mask was placed in the ICP-RIE system, and TiO₂ was etched till a 40 nm TiO₂ film remained on the sample, and the length of nanowires was approximately equal to 120 nm.

6.1.3 Al Mask Removal

For Al mask removal, we used Al etchant type D. The etch rate of the Al etchant was 3 nm per second at room temperature. The sample was dipped into the Al etchant for 2 minutes to ensure no Al remained on the sample, then immersed in water as a stopper. In the compatibility table of the Al etchant type D [121], it was mentioned that the Al etchant would not etch Ti and gold. However, there was no information about the possibility of etching of TiO₂. To make sure the Al etchant will not attack the TiO₂, a separate sample with a TiO₂ film was dipped into the Al etchant for 2 min. The thickness of TiO₂ film was measured with an ellipsometer before and after the test, and no change in the thickness was observed.

6.1.4 Fabricated Structure

Figure 6.4a-d shows the SEM images of the fabricated TiO₂ nanowires capped with a layer of gold. In **Figure 6.4a, b**, the pitch is 400 nm, and the diameter of the nanowires is 130 nm and 150 nm respectively. In **Figure 6.4c, d**, the pitch is 450 nm, and the diameters are 170 nm and 230 nm, respectively. Before taking the SEM images, a 3 nm thick Ti layer and 10 nm thick gold layer were deposited on the sample due to the non-conductivity of the sample. As seen in the SEM images, the

nanowires are tapered with the top of the nanowires being a bit narrower than the bottom of the nanowires. This suggests that the etching recipe needs further optimizations to achieve vertical sidewalls. However, as different variations of the structure were fabricated with different diameters and pitch values, the chance of exciting optical modes in nanowires and plasmonic modes in the gold layer is still high, and the current structures should be able to provide desirable results. As seen in **Figure 6.4**, increasing the diameter reduces the aspect ratio of the nanowires, and the nanowires look like nano-discs.

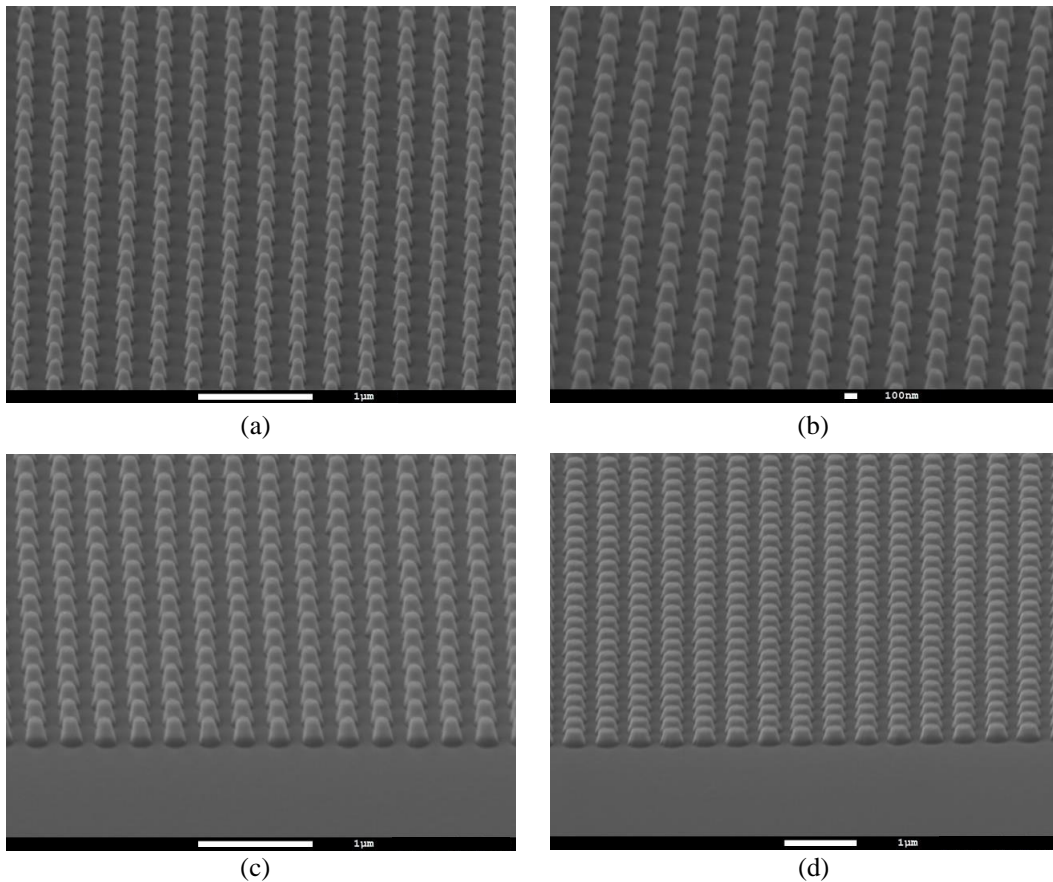


Figure 6.4. SEM images of the fabricated nanowires with (a) 400 nm pitch and 130 nm diameter, (b) 400 nm pitch and 150 nm diameter, (c) 450 nm pitch and 170 nm diameter, and (d) 450 nm pitch and 230 nm diameter.

6.2 Characterization of the TiO₂ Nanowires

Characterization of the nanowires was done using F40, and the reflection spectra and reflected color from each array were recorded. F40 is a similar system to F40-UV, however, it only measures the

reflection in the visible range. Firstly, we used the 10X magnification lens in the F40, which gives a spot size of $25\ \mu\text{m}$, and thus, we can measure the reflection from the center of each array. **Figure 6.5a, b**, shows the reflection spectra collected from the nanowire arrays with different diameters for lattice spacings of 400 nm and 450 nm, respectively. For the 400 nm pitch in **Figure 6.5a**, no major peak is observed for 110 and 130 nm diameters. As the diameter increases to 150 nm, a peak is observed at approximately 650 nm. This peak was observed at 720 nm during the simulations and is attributed to the coupling of the LSPR modes in the gold layer and optical modes of nanowires. This mode is blue-shifted compared to the simulations due to the Ti adhesion layers and chromatic dispersion of the TiO_2 . As the diameter increases further, this peak is red-shifted, and for 230 and 250 nm diameters, the mode is moved to the near IR region. For the 450 nm pitch in **Figure 6.5b**, a similar peak is observed in the reflection spectra for the diameters higher than 150 nm. However, the shape and the resonance wavelengths of the peaks are slightly different from the 400 nm pitch nanowires. It seems the nanowire arrays excite only one of the modes achieved in simulations, and the high Q mode resulting from the surface lattice resonance (SLR) did not get excited within the arrays.

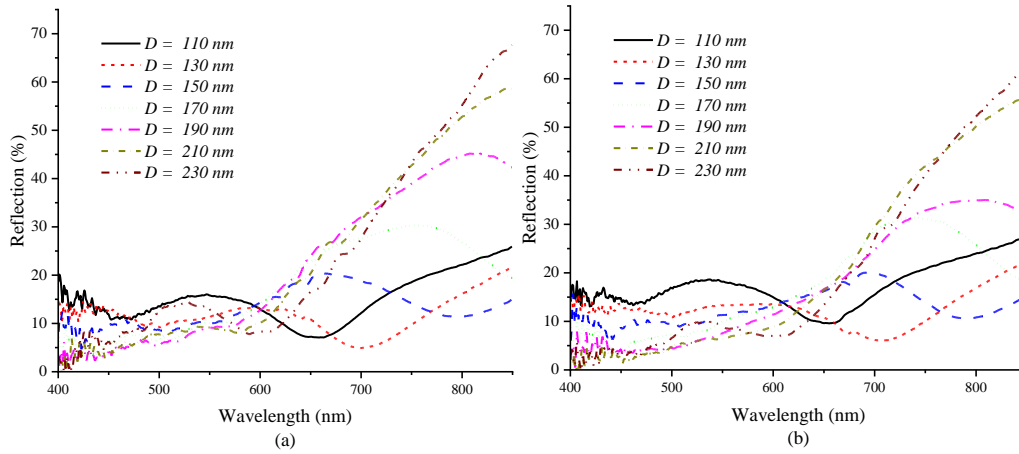


Figure 6.5a, b. Reflection spectra collected from the nanowire arrays with different diameters for lattice spacings of 400 nm and 450 nm, respectively.

However, as the SLR mode is a result of coupling between the collective response of individual LSPR modes and in-plane diffraction orders of the nanowires, it is possible that the spot size of $25\ \mu\text{m}$ is not large enough to excite such a mode and a larger area of the arrays need to be tested. Thus, the magnification was changed to 4X, and a larger spot size of $62.5\ \mu\text{m}$ was used to measure the reflection from the center of the arrays. **Figure 6.6a, b** shows the reflection spectra of the nanowire arrays with

different diameters for 400 nm and 450 nm lattice spacing, respectively. For the 400 nm pitch in **Figure 6.6a**, the high Q SLR peak starts to appear in the reflection curve when the nanowire diameter is 130 nm. As the nanowire diameter increases, the peak shifts slightly red, and its strength and quality factor increases. The highest Q is achieved for the 210 nm diameter. Compared to the simulation results from Chapter 5, the quality factor of the SLR mode is decreased. There are several reasons for this reduction in Q, including the chromatic dispersion of the TiO₂, the Ti adhesion layers, surface roughness, and the changes in the thickness of different layers. For 450 nm pitch in **Figure 6.6b**, the Q of the SLR mode is decreased, and the highest Q is achieved for 210 nm diameter.

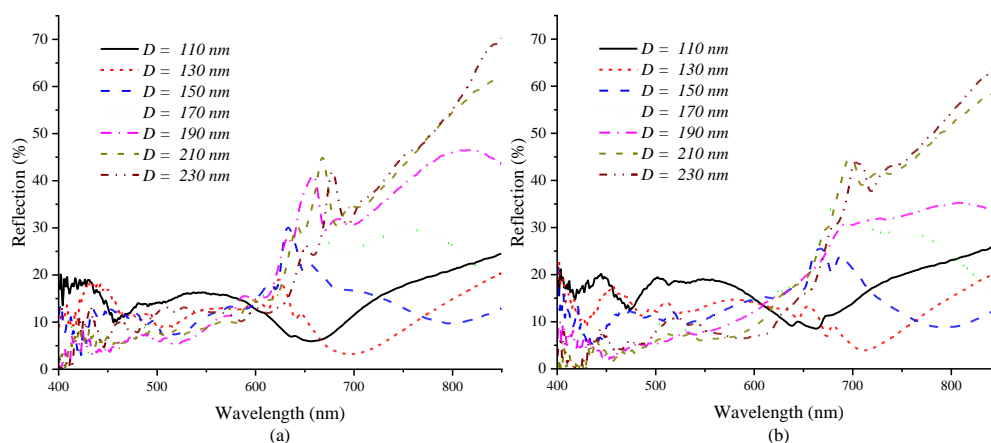


Figure 6.6a, b. The reflection spectra of the nanowire arrays with different diameters for 400 nm and 450 nm lattice spacing, respectively. The spot size is 62.5 μm .

Reflected colors from the arrays are also shown in **Figure 6.7**. As seen in this figure, arrays mainly reflect red colors, and for these lattice spacings and nanowire lengths, the plasmonic mode gets excited in the red region. This was also the case in the simulations.

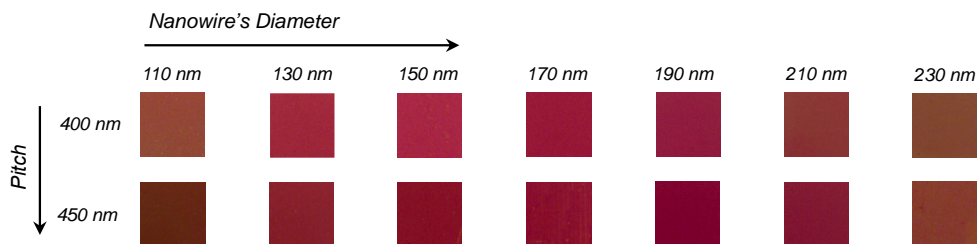


Figure 6.7. Reflected colors from the nanowire arrays.

6.3 Color Generation and Sensitivity

The TiO₂ nanowire arrays, which are capped with a layer of gold, showed lots of potential for generating different colors during the simulations. In order to show the structural color properties of the nanowires, several arrays with different nanowire diameters, lattice spacings, and nanowire lengths were fabricated. Firstly, a 300 nm thick TiO₂ layer was deposited on a glass substrate using sputtering. Then, PMMA A4 and Electra92 were spin-coated on the sample, and circular arrays were designed using the Raith CAD software. Each array has 100 μm × 100 μm dimensions and is separated from the adjacent arrays by 100 μm distance. The diameter ranged from 110 nm to 250 nm with a 20 nm increment, and pitch values were 350 nm, 400 nm, and 450 nm. After lithography and development, 3 nm Ti and 50 nm gold were deposited on the sample. Further, a 100 nm thick Al layer was deposited on the gold as a hard mask for the dry etching. The lift-off was done using PG remover to achieve metallic nano-discs. **Figure 6.8** shows the nano-disc arrays on top of 300 nm TiO₂ film under an optical microscope. As seen in this figure, each metallic array reflects a different color, which shows the excitation of the plasmonic modes within each array, even with the presence of the Al layer.

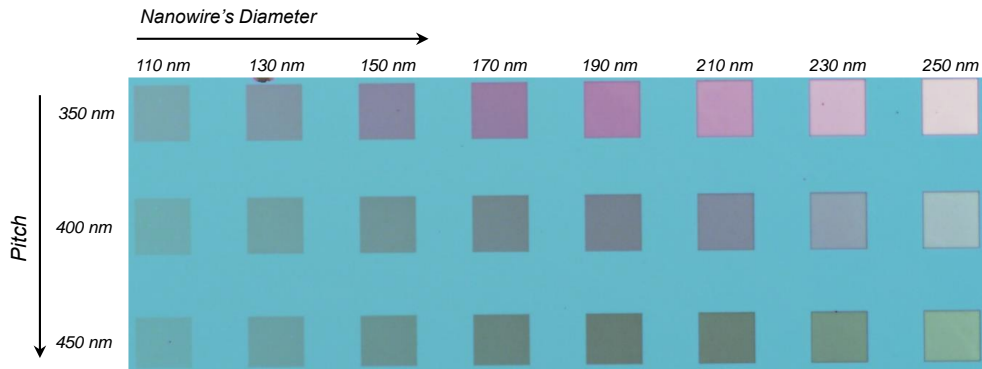


Figure 6.8. Reflected colors from the metallic nano-discs, including Ti, gold and Al. Nanowires were not etched yet. Each array is 100 μm × 100 μm, and there is a 300 nm TiO₂ film underneath.

The masked patterns were then placed inside the ICP-RIE system, and nanowires were etched into the TiO₂ film to achieve nanowire arrays with 100 nm length. Thus, the thickness of the TiO₂ film underneath the arrays was 200 nm. **Figure 6.9a-c** shows the 100 nm long nanowire arrays under an optical microscope for surrounding index of 1 (air), 1.33, and 1.39, respectively. For the air surrounding in **Figure 6.9a**, each array reflects a different color, which shows the different mode excitation within each array. Although the arrays were optimized to support resonance modes with the air surrounding, still some arrays should be able to generate resonance modes with n=1.33 as the surrounding index. As

seen in **Figure 6.9b**, changing the surrounding index to 1.33 caused changes in the reflecting colors from all the arrays. Reflecting different colors from each array shows that even with a surrounding index of 1.33, nanowire arrays are supporting resonance features. Changing the surrounding index to 1.39 in **Figure 6.9c**, slightly changes the reflected colors compared to the 1.33 surrounding index, and this suggests that the arrays are sensitive to the changes in the surrounding index.

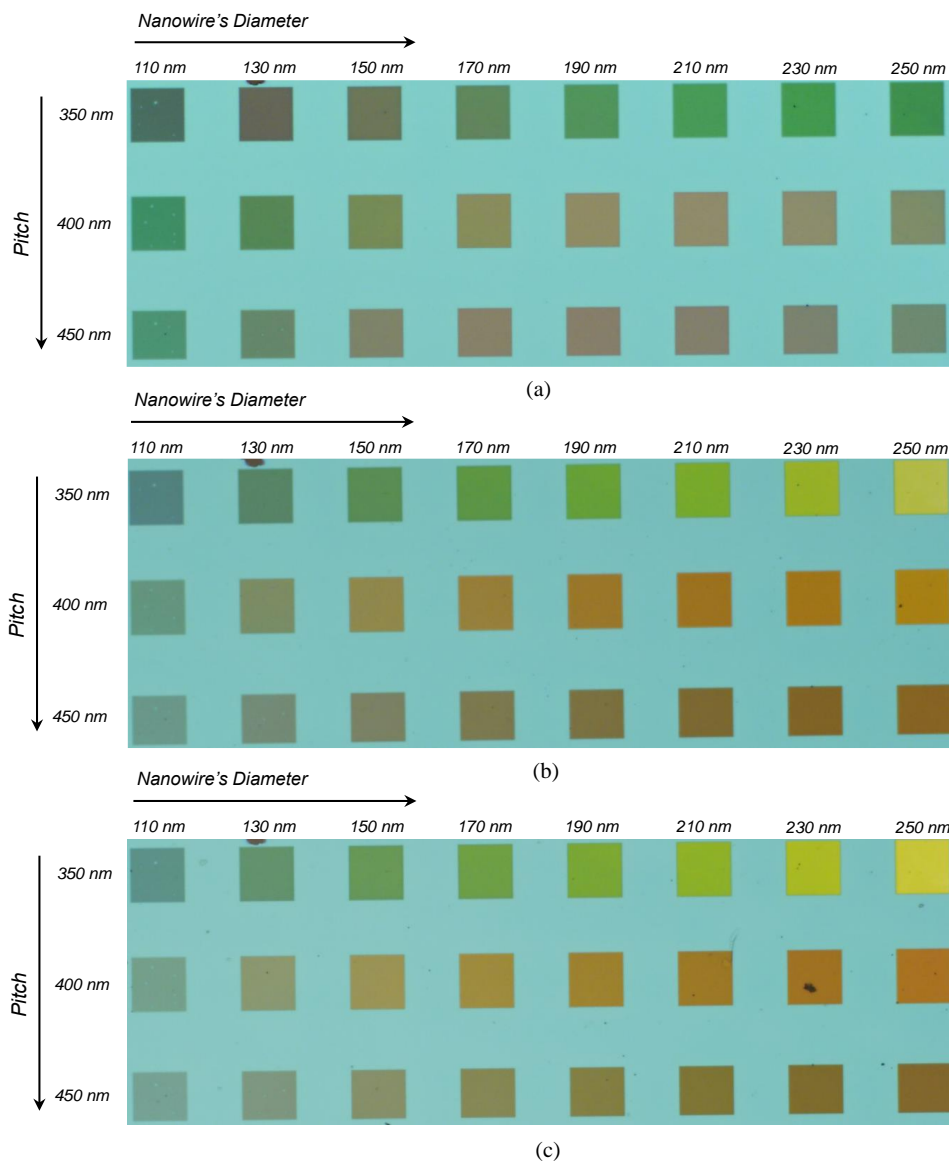


Figure 6.9. Reflected colors from the TiO_2 arrays with a 100 nm length capped with 50 nm gold and 100 nm Al with (a) air surrounding, (b) surrounding index of 1.33 and (c) surrounding index of 1.39.

However, as the quality factor of the resonance features was not very high at this nanowire length, we did not measure the sensitivity.

The sample was again placed in the ICP-RIE system, and nanowires were etched into the TiO₂ layer to 260 nm nanowires length. At this point, a 40 nm thick TiO₂ film was presented underneath the arrays, and nanowires were capped with 50 nm gold and 100 nm Al. **Figure 6.10** shows the nanowire arrays with 260 nm length with the air surrounding under an optical microscope. Nanowire arrays reflect different colors, and as the nanowire's diameter increases, the arrays generate very vivid colors, which shows the presence of high Q modes in the reflection spectra. To our knowledge, this is the first time such vivid colors have been demonstrated in bright field reflections. Previously, our group had demonstrated similar vivid colors using diffraction. However, those were very sensitive to the incident angle. These colors are being generated due to guided optical modes.

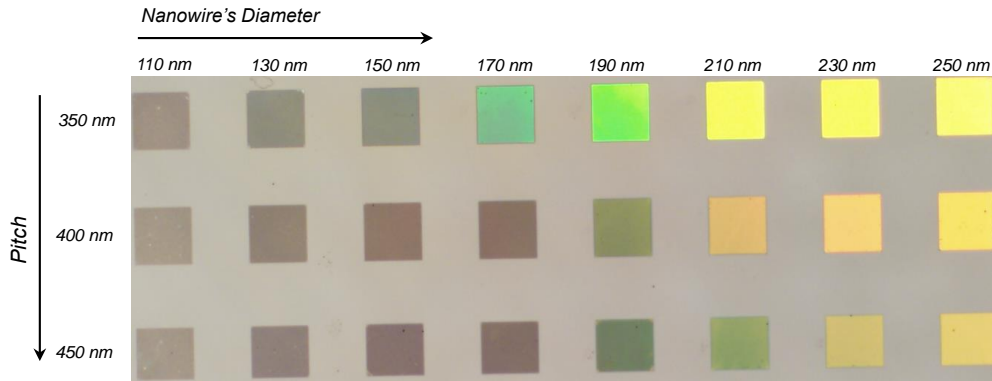


Figure 6.10. Reflected colors from the TiO₂ arrays with a 260 nm length capped with 50 nm gold and 100 nm Al with the air surrounding.

Figure 6.11a-c shows the reflection spectra of the nanowire arrays with 350, 400, and 450 nm lattice spacings, respectively. The TiO₂ film is 40 nm, the nanowire length is 260 nm and nanowires are capped with 50 nm gold and 100 nm Al, with air as the surrounding. For the nanowire arrays with 350 nm pitch in **Figure 6.11a**, when the nanowire's diameter is less than 170 nm, no peak is observed in the reflection spectra. A peak in the reflection spectra is achieved when the diameter is 170 nm and more. For these nanowire's diameters, an optical mode is excited within the nanowire arrays which causes a peak in the reflection spectra. Further, this optical mode is coupled with the LSPR modes happening in the interface of gold and TiO₂, and also on top of the Al layer, leading to a high Q mode. The highest Q is achieved for 190 nm diameter, which means the coupling between the optical modes in nanowires and LSPR modes is very efficient. However, as the diameter increases, the resonance wavelength is red shifting,

and nanowires are guiding for a wider wavelength range, which causes a reduction in Q . Further, the highest reflection intensity is achieved for 210 nm, in which the nanowires reflect about 85% of the light. For the 400 nm pitch in **Figure 6.11b**, the peak in reflection spectra is achieved for 210 nm diameter and higher. Nanowire arrays for this pitch are reflecting less light compared to the 350 nm pitch since the distance between each nanowire is now higher. For the 450 nm pitch in **Figure 6.11c**, the peaks in reflection spectra are only achieved for nanowire arrays with 230 nm and 250 nm diameters. Further, these modes are separated into two different peaks, which shows that the mode coupling for this pitch is not happening very efficiently. Again to our knowledge, such high Q single peak reflections have been first time observed in nanostructures without using diffraction.

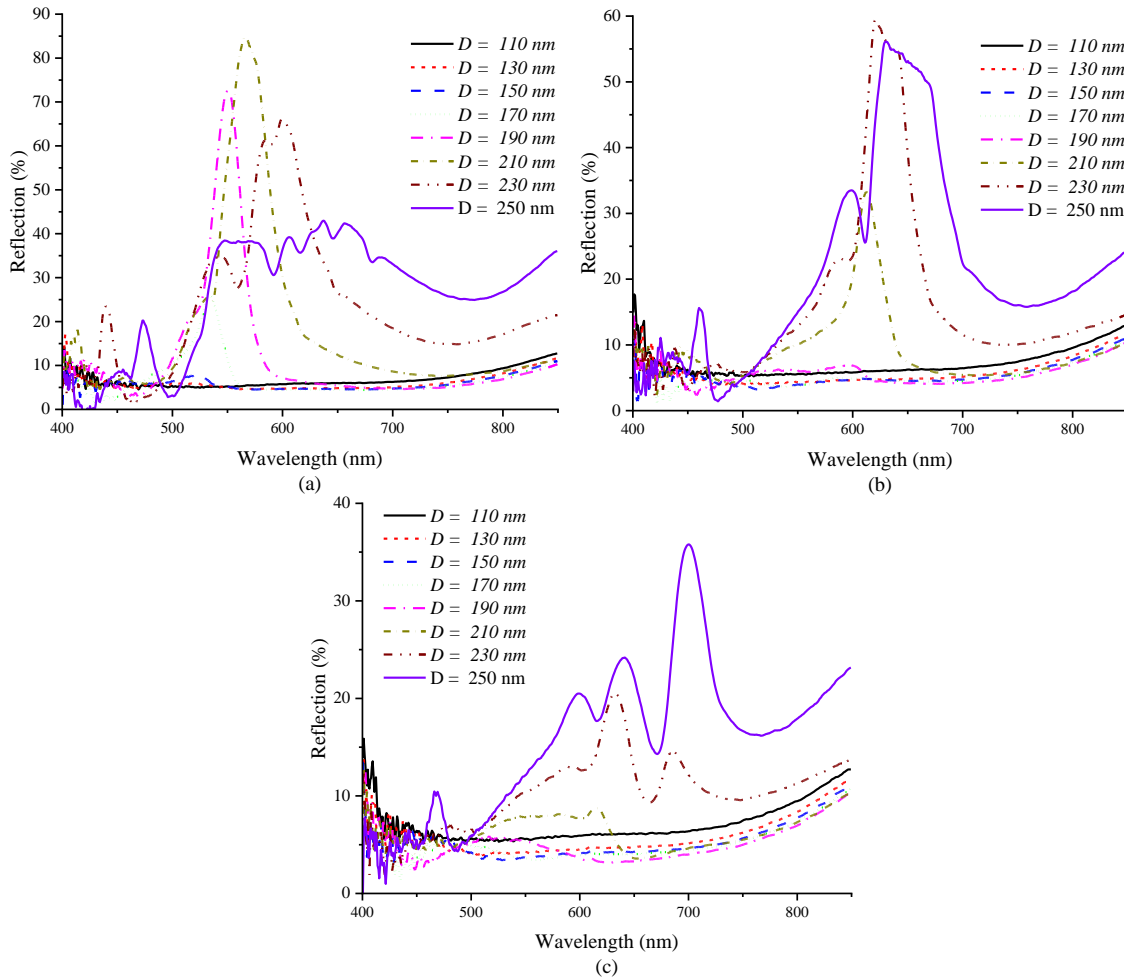


Figure 6.11a-c. Reflection spectra of the nanowire arrays with 350, 400, and 450 nm lattice spacings, respectively. The TiO_2 film is 40 nm, the nanowire length is 260 nm and nanowires are capped with 50 nm gold and 100 nm Al, with air as the surrounding.

The fabricated nanowire arrays were tested with a surrounding refractive index of 1.33 to see if the arrays could produce high Q modes for this surrounding index. **Figure 6.12a-c** shows the reflection spectra of the nanowire arrays with surrounding refractive index of 1.33, with 350, 400, and 450 nm lattice spacing, respectively. The length of the nanowires was 260 nm with 50 nm gold and 100 nm Al on top. For the 350 nm pitch value in **Figure 6.12a**, nanowire arrays with diameters as small as 130 nm show a peak in the reflection spectra. The Q of the peak increases with the diameter enhancement and the resonance wavelength redshifts. Further, the highest Q is achieved for a diameter of 170 nm. For diameters higher than 170 nm, the Fano resonance is separated into two different modes, which reduces the Q.

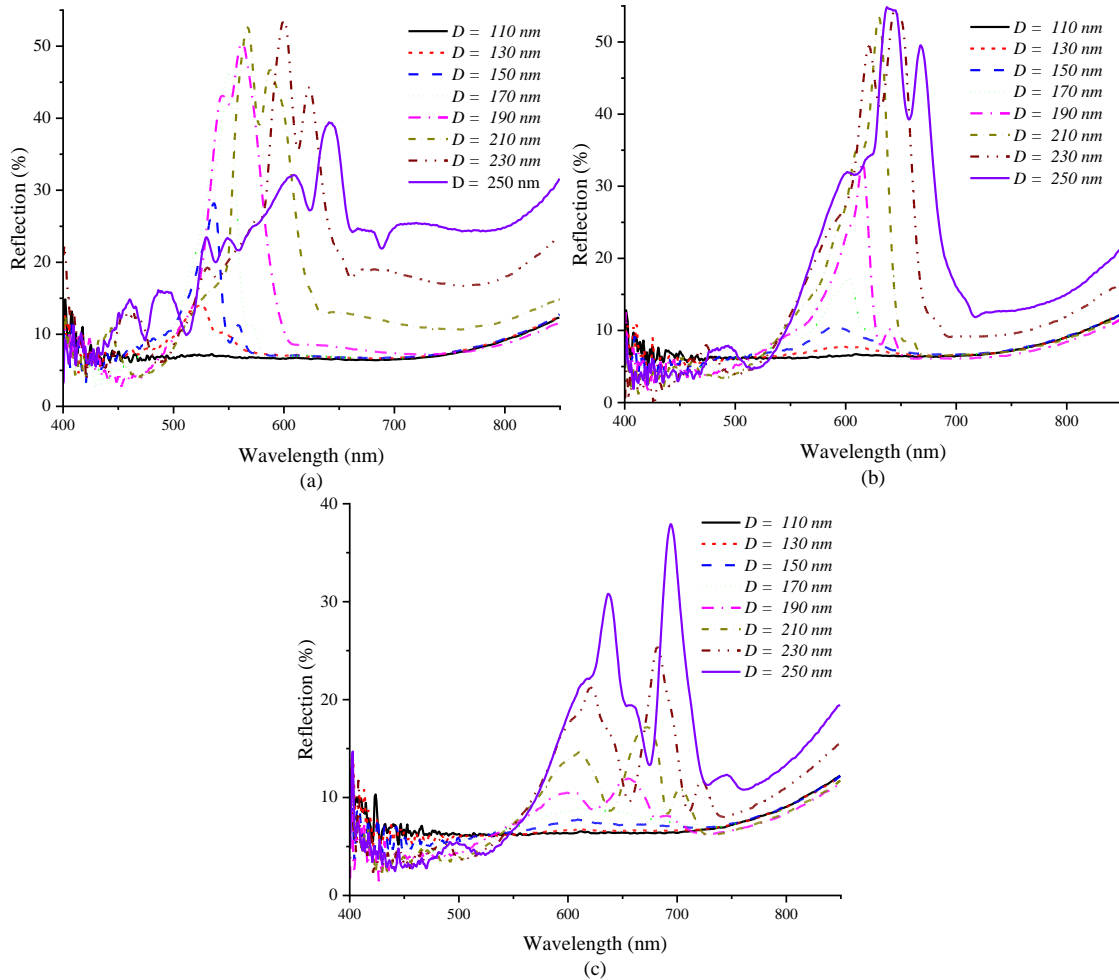


Figure 6.12a-c. Reflection spectra of the nanowire arrays with 350, 400, and 450 nm lattice spacings, respectively. The TiO_2 film is 40 nm, the nanowire length is 260 nm, and nanowires are capped with 50 nm gold and 100 nm Al, with 1.33 as the surrounding refractive index.

For 400 nm pitch in **Figure 6.12b**, the highest Q is achieved for a diameter of 210 nm, and for higher diameters, the peak is separated into two modes. Compared to the air surrounding, more nanowire arrays are showing a peak in the reflection spectra. For the 450 nm pitch in **Figure 6.12c**, the mode separation starts for a diameter of 190 nm and the quality factor and strength of the modes are increased as the diameter enhances. However, these arrays reflect less light compared to the arrays with lower pitch values.

Since the nanowire arrays show high Q features with a surrounding index of 1.33, the sensitivity of the arrays was tested by changing the surrounding refractive index. **Figure 6.13a-d** shows the reflection spectra of the nanowire arrays with 350 nm pitch for nanowire diameters 170, 190, 210, and 230 nm, respectively. The surrounding refractive index changed from 1.33 to 1.39. Further, the changes in the resonance wavelength versus the surrounding refractive index and the calculated sensitivity are shown within each figure. We only measured the sensitivity of those arrays that offer high Q modes. We again smoothed the experimental data and calculated the first derivatives of the reflection spectra for measuring the sensitivity. However, the first derivative curves are not shown here, and only the sensitivity results are presented. For the nanowire arrays with 170 nm diameter in **Figure 6.13a**, the sensitivity is 122 nm/RIU. Although this sensitivity value is lower than that of the sensitivity range we achieved for the nano-grating structures in Chapter 4, the mode has a higher Q here, which improves the figure of merit. Also, the structure promises to make sensors by just using color without the need for a spectrometer. The reason for the lower sensitivity of the nanowires is that here, the mode is a result of the coupling of optical modes in nanowires and LSPR modes of the metallic layers and the dependency of the mode on the LSPR resonances of the interface of the Al and surrounding index is not very high. Thus, the mode is less sensitive to the changes in the surrounding refractive index; however, it offers a higher Q due to the efficient coupling of plasmonic and optical modes. For nanowire arrays with 190 nm diameter in **Figure 6.13b**, the peak is separated into two modes, and the peak in the longer wavelengths is having a high Q; thus, it was used for measuring the sensitivity. The sensitivity of this array is slightly increased and is 183 nm/RIU. For the nanowire arrays with 210 nm diameter in **Figure 6.13c**, the peak is separated into two modes, labeled as mode 1 and mode 2. The sensitivity of modes 1 and 2 is 134 and 170 nm, respectively. This suggests that the dependency of mode 2 on the LSPR resonances of the top layer is higher for this nanowire diameter. For the nanowire array with 230 nm diameter, as seen in **Figure 6.13d**, the sensitivity of modes 1 and 2 is decreased to 97 and 60 nm/RIU, respectively. At this diameter, mode 1 is more dependent on the LSPR modes of

the top layer compared to mode 2, which shows that the mode coupling is highly dependent on the diameter of the nanowires.

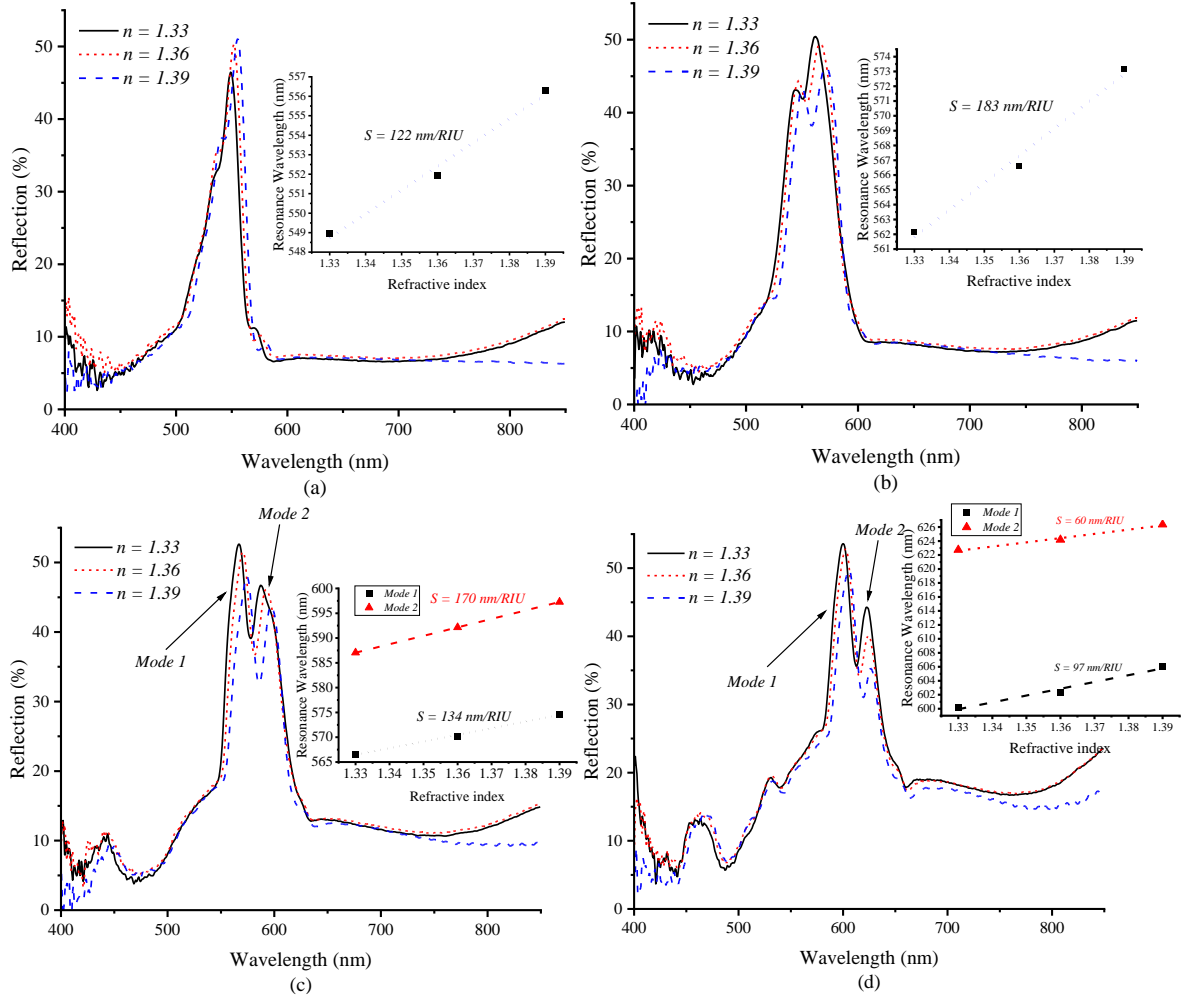


Figure 6.13a-d. Reflection spectra of the nanowire arrays with 350 nm pitch for nanowire diameters of 170, 190, 210, and 230 nm, respectively. The surrounding refractive index was changing from 1.33 to 1.39. Further, the changes in the resonance wavelength versus the surrounding refractive index and the calculated sensitivity are shown within each figure.

Figure 6.14a-c shows the reflection spectra of the nanowire arrays with 400 nm pitch and 210, 230, and 250 nm diameters, respectively. The surrounding refractive index is changing, and the changes in the resonance wavelengths versus the refractive index are shown within each figure. For nanowire arrays with 210 nm diameter in **Figure 6.14a**, the sensitivity to the changes in the surrounding refractive index is 97 nm/RIU. However, due to the efficient optical and plasmonic mode matching, this array offers a high Q resonance feature. For the 230 nm diameter nanowire array in **Figure 6.14b**, the peak

is separated into two modes which are labelled as mode 1 and 2. Mode 1 and 2 are showing 145 and 157 nm/RIU sensitivity, respectively. This suggests that the dependency of mode 2 on the LSPR modes of the top layer is slightly higher. Similar to this array, nanowire arrays with 250 nm diameter in **Figure 6.14c** show two separate modes, in which modes 1 and 2 show 133 and 144 nm/RIU sensitivity to the changes of surrounding refractive index.

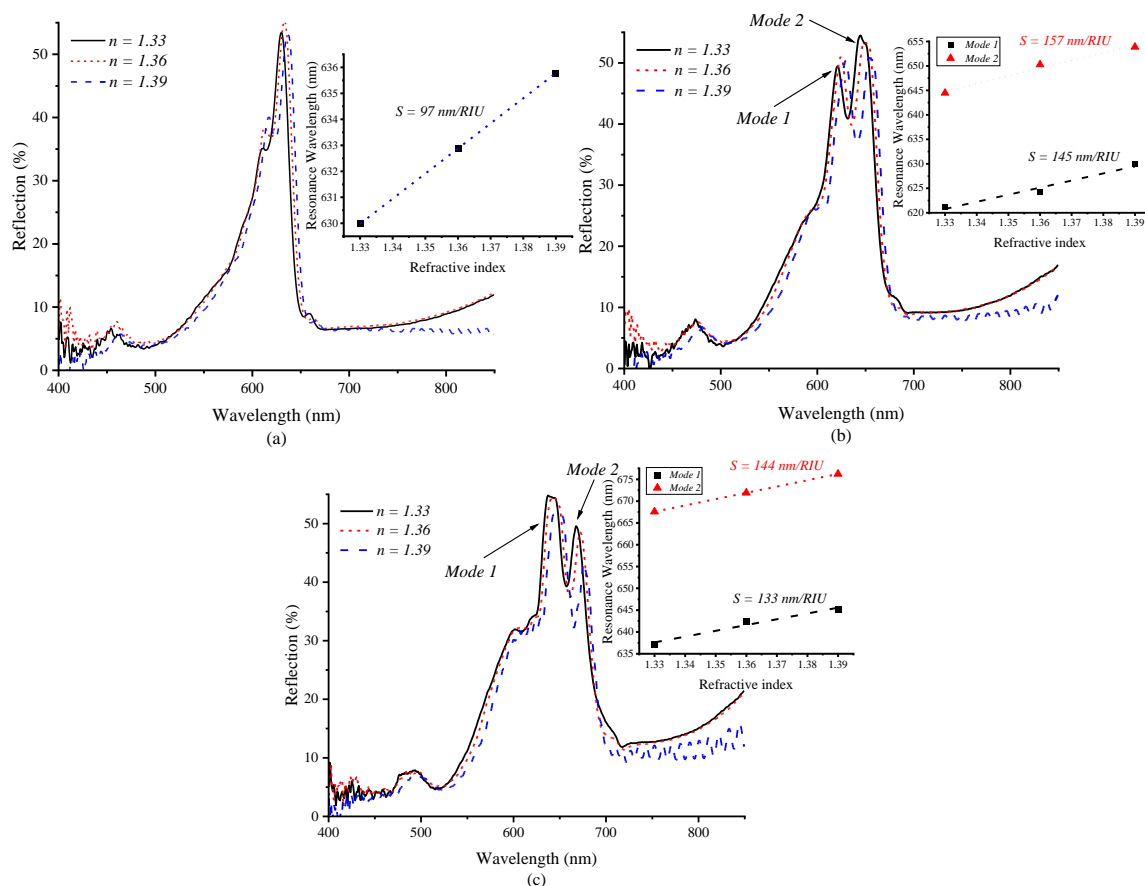


Figure 6.14a-c. Reflection spectra of the nanowire arrays with 400 nm pitch for nanowire diameters of 210, 230, and 250 nm, respectively. The surrounding refractive index was changing from 1.33 to 1.39. Further, the changes in the resonance wavelength versus the surrounding refractive index and the calculated sensitivity are shown within each figure.

For 450 nm pitch, only the nanowire array with 250 nm diameter is showing high Q modes. **Figure 6.15** shows the reflection spectra of this array with different surrounding indices, along with the changes in the resonance wavelengths versus the refractive index. Although the two separate modes in this array have high quality factors, the sensitivity of mode 1 and 2 are 108 and 107 nm/RIU, respectively. Among

all the nanowire arrays, those arrays with 350 nm pitch are showing the best sensitivity results; however, the sensitivity values are lower than 200 nm/RIU.

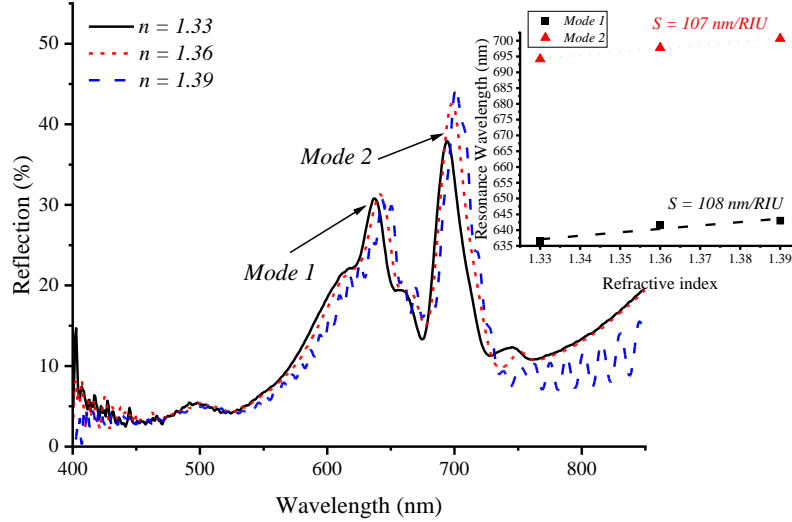


Figure 6.15. Reflection spectra of the nanowire array with 450 nm pitch and 250 nm diameter, with different surrounding indices. Changes in the resonance wavelengths versus the refractive index are also shown.

Figure 6.16a-c shows the nanowire arrays under an optical microscope with surrounding indices of 1.33, 1.36, and 1.39, respectively. As seen in this figure, arrays are reflecting different colors compared to **Figure 6.10** in which the surrounding was air. Changes in the reflected colors are not very sensitive when the surrounding index changes from 1.33 to 1.36 and 1.39 since the sensitivity of the arrays is not very high, and there are very few changes in the intensity of the reflection spectra as the surrounding index changes.

The Al mask was removed using Al etchant, and the nanowire arrays were tested again using F40 for color generation and sensitivity. **Figure 6.17a-d** shows the nanowire arrays under an optical microscope after removing the Al mask for surrounding indices of air, 1.33, 1.36, and 1.39, respectively. Comparing the reflected colors from these arrays with the ones with the Al mask, we realize that reflected colors are very similar and only for some arrays are slightly different. Further, the reflection spectra of the unmasked arrays, with various surrounding refractive indices, were similar to the masked arrays in the case of shape and resonance wavelengths. However, the masked arrays were showing slightly higher reflections. The sensitivity values of the arrays were also very similar to the masked arrays. Because of the similarity of the results, they are not shown here. The reason for this similar behavior is the fact that the contribution of the LSPR modes, which are happening at the

interface of the top metallic layer with the surrounding environment, is very small compared to the strong optical modes in nanowires and the LSPR modes at the interface of the gold and TiO₂. Thus, removing the top Al layer does not affect the Fano resonances, and thus, the reflection spectra and sensitivity remain almost the same.

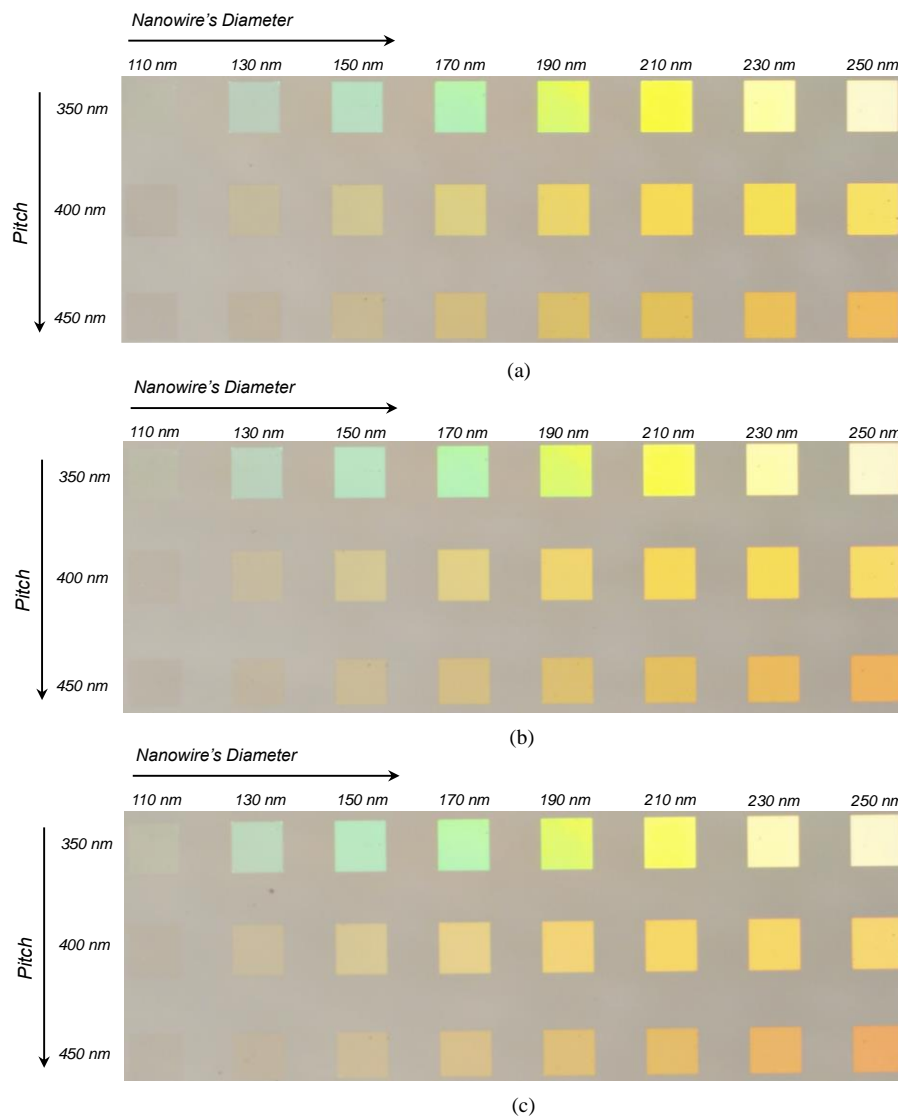


Figure 6.16a-c. Reflected colors from the nanowire arrays under an optical microscope with surrounding refractive indices of 1.33, 1.36 and 1.39, respectively.

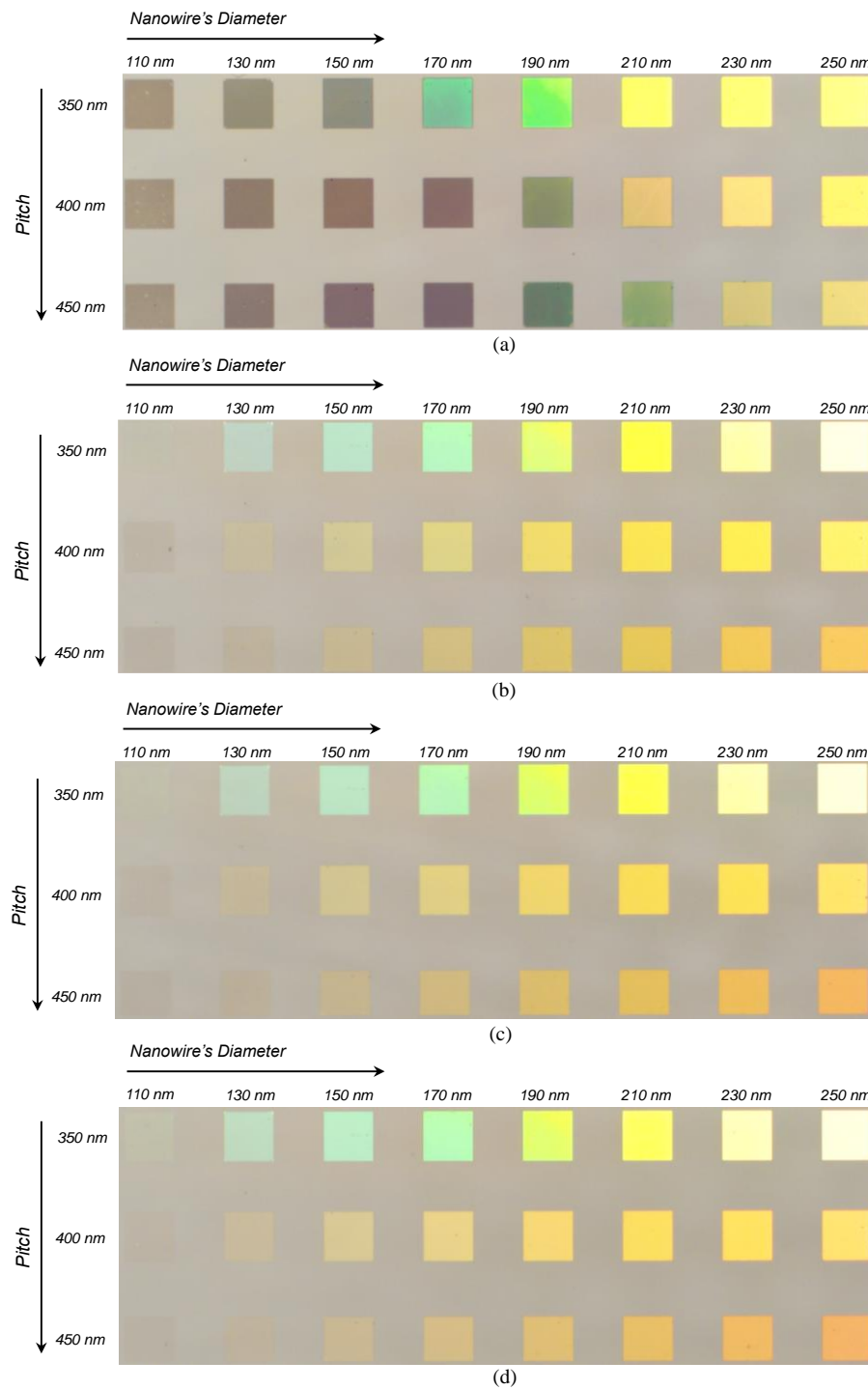


Figure 6.17a-d. Reflected colors from the nanowire arrays without the Al mask, under an optical microscope with surrounding refractive indices of 1 (air), 1.33, 1.36 and 1.39, respectively.

6.4 Summary and Conclusion

Fabrication and characterization details of the plasmonic-nanowire hybrid structure were presented in this chapter. TiO₂ nanowires, which are capped with a layer of gold, were fabricated using dry etching, where precise control over the length of the nanowires was possible. The optimized structure showed two resonance features due to the matching of optical modes and plasmonic modes, which confirms the simulation results of Chapter 5. Further, by tuning the nanowire's length, a wide range of vivid colors was achieved, along with high quality resonance features in the reflection spectra.

Chapter 7

Summary and Future Works

The purpose of this work was to introduce several low-cost platforms for realization of high-performance plasmonic sensors with self-referencing capability. These sensors are based on metallic nano-gratings which can support multiple Fano resonances and are sensitive to the changes in the surrounding refractive index. This work was motivated by the fact that current plasmonic sensors are suffering from the high cost associated with the fabrication of complex geometries, costly readout technologies and poor performance under unstable environmental conditions. We believe that the fabricated sensors in this work provide a direction to overcome these challenges.

In chapter 2, two self-referenced plasmonic sensors were designed and evaluated using FDTD and both sensors were optimized to generate high quality factor resonance features in visible and near IR range. Both sensors were based on gold nano-gratings with cubic and cylindrical shapes, which can support several modes. In both sensors, the resonance feature which is dominated by the LSPR modes of the top grating layers was showing high sensing performance, while another resonance feature was isolated from the surrounding refractive index and can be used as a self-referencing mode. Further, both sensors were easy-to-fabricate and were operating in visible to near IR region which makes the readout easy. Both designs were fabricated in chapter 3 and several variations of the structures were fabricated to validate the simulation results and optimize the sensors experimentally. Highly ordered cubic and cylindrical shapes were realized through e-beam lithography and lift-off. A series of dose test experiments were designed to find the right e-beam dose for each structure. Further, two separate samples were fabricated with two different dielectric spacer layers to make sure sufficient refractive index is provided to separate the modes. In chapter 4 the sensors were characterized and examined for sensing while the surrounding refractive index was subjected to change. The fabricated sensors were able to generate several resonance features in the visible to near IR range, as was predicted in simulations. However, the location of the modes and the quality factors were different compared to the simulation results. These changes were due to the presence of the adhesion layers and also chromatic dispersion of the dielectric spacer layers. The fabricated sensors showed high performance in case of sensitivity to the changes of the surrounding and for some designs, surprisingly, the sensitivity values were higher than the ones predicted in the simulations. Further, the sensors were generating a resonance

feature that was isolated from the surrounding environment and can be used as a self-referencing feature during the measurements.

In chapter 5, another easy-to-fabricate structure was designed and numerically evaluated using FDTD simulations. The structure was based on highly ordered TiO₂ nanowires which were capped with a layer of gold, and they are placed in a periodic lattice with sub-wavelength spacing. The structure generated high-quality resonance features through matching the top layer's plasmonic modes with the optical modes of nanowires and the lattice modes. Further, the structure was able to reflect a wide range of vivid colors and showed lots of potential for realizing low-cost colorimetric plasmonic sensors. In chapter 6, details of fabrication and characterization of the TiO₂ nanowires were described. Highly ordered nanowire arrays were fabricated using e-beam lithography and dry etching and were tested for structural color generation and sensitivity. The fabricated structures reflected vivid colors and generated high Q features in the reflection spectra. Further, the structures were sensitive to the changes in the surrounding refractive index and thus they were reflecting different colors when the surrounding index was changing, which make them suitable for realization of colorimetric sensors.

This work proposed new structures and experimentally confirmed different spectral features which arise from it. It gives a photonic designer guidelines on how to optimize the structure for different applications. Based on the results achieved in this work, there are several works that can be accomplished in the future:

- The self-referencing sensors which were fabricated in chapter 3 can be used to build an actual self-referenced sensor for food safety applications, water safety applications, etc.
- The nanowire arrays fabricated in chapter 6 can be used for building colorimetric sensors for a wide range of applications including gas sensing.
- As the fabricated structures in this work are able to excite several plasmonic modes, they should be able to enhance the intensity of the Raman signal and can be used for surface enhanced Raman spectroscopy (SERS)
- Optical or ultraviolet (UV) lithography can be used to fabricate the cubic nano-gratings in chapter 3, in order to achieve sharper corners and thus enhancing the Q of the modes. Despite the e-beam lithography, optical and UV lithography will not face the charge build-up issue and achieving sharper corners is possible.

- As observed in chapter 6, a larger spot size has led to an increase in the Q of the SLR modes. In order to achieve much higher Q, nanowire arrays with $500 \mu\text{m} \times 500 \mu\text{m}$ dimensions can be fabricated. Then the array can be characterized using an optical setup that can produce a large spot size and thus the Q can be further increased.

In conclusion, this work provides a clear path toward the realization of the low-cost self-referencing plasmonic sensors. All the details from initial conceptualization to design, simulation, fabrication and characterization of the nanostructure-based sensors are presented and discussed. The structures are first optimized using simulations and all the different variations are considered and explained. Then, all the structures are optimized experimentally and in every step, the experimental results are compared with simulations and in case of any difference, the reasons behind it are explained. We believe this work provides a comprehensive guideline to a photonic designer towards the implementation of nanostructure-based devices for different applications.

References

- [1] Freestone I., Meeks N., Sax M. and, Higgitt C, (2008) “The Lycurgus Cup - A Roman nanotechnology”, *Gold Bulletin*, Volume 40, Issue 4, 270 – 277
- [2] Wood R.W., (1902) “On a remarkable case of uneven distribution of light in a diffraction grating spectrum”, *Phil. Mag.* 4, 396–402
- [3] Li D., Zhou H., Hui X., He X., and Mu X., (2021) “Plasmonic Biosensor Augmented by a Genetic Algorithm for Ultra-Rapid, Label-Free, and Multi-Functional Detection of COVID-19”, *Anal. Chem.* 93, 27, 9437–9444
- [4] Li E., and Chu H., (2014) “Plasmonic Nanoelectronics and Sensing”, Cambridge: Cambridge University Press., doi:10.1017/CBO9781139208802
- [5] Maier S. A., (2007) “Plasmonics: Fundamentals and Applications”, Springer, doi:10.1007/0-387-37825-1
- [6] Szunerits S., Boukherroub R., (2015) “Introduction to Plasmonics Advances and Applications”, CRC Press
- [7] Iwanaga M., (2016) “Plasmonic Resonators Fundamentals, Advances, and Applications”, Pan Stanford Publishing Pte. Ltd.
- [8] Richardson N.V., Holloway S., (2014) “Handbook of Surface Science: Modern Plasmonics”, Elsevier Volume 4, Pages 1-428
- [9] Ruthemann G., (1942) “Elektronenbremsung an Röntgenniveaus”. *Naturwiss* 30, 145
- [10] Kristensen A., Yang J. K. W., Bozhevolnyi S. I., Link S., Nordlander P., Halas N. J. and Mortensen N. A., (2017) “Plasmonic colour generation”, 2, 16088
- [11] Gu Y., Zhang L., Yang J. K. W., Yeo S. P. and Qiu C., (2015) “Color generation via subwavelength plasmonic nanostructures”, *Nanoscale*, 7, 6409
- [12] Jovanov V., Stiebig H., and Knipp D., (2018) “Tunable Multispectral Color Sensor with Plasmonic Reflector”, *ACS Photonics*, 5, 378–383
- [13] Walia, J., Dhindsa, N., Khorasaninejad, M., & Saini, S. S. (2014). Color generation and refractive index sensing using diffraction from 2D silicon nanowire arrays. *Small*, 10(1), 144-151.

- [14] Quan L. N., Kang J., Ning C-Z, and Yang P., (2019) “Nanowires for Photonics”, *Chem. Rev.* 119, 9153–9169
- [15] Barrigon E., Heurlin M., Bi Z., Monemar B., and Samuelson L. (2019) “Synthesis and Applications of III–V Nanowires”, *Chem. Rev.* 119, 9170–9220
- [16] Pescaglini A. and Iacopino D., (2015) “Metal nanoparticle–semiconductor nanowire hybrid nanostructures for plasmon-enhanced optoelectronics and sensing”, *J. Mater. Chem. C*, 3, 11785–11800
- [17] Snyder, A. & Love, J., (1983) “Optical Waveguide Theory”, Springer.
- [18] Sturmberg, B. C. P. et al., (2011) “Modal analysis of enhanced absorption in silicon nanowire arrays” *Optics express* 19, A1067-A1081
- [19] Nooke A., Beck U., Hertwig A., Krause A., Krüger H., Lohse V., (2010) “On the application of gold based SPR sensors for the detection of hazardous gases”, *Sens. Actuators B*, 149, pp. 194-198
- [20] Homola J., Dostalek J., Chen S., Rasooly A., Jiang S., Yee S.S., (2002) “Spectral surface plasmon resonance biosensor for detection of staphylococcal enterotoxin B in milk”, *Int. J. Food Microbiol.*, 75, pp. 61-69
- [21] Goodrich T.T., Lee H.J., Corn R.M., (2004) “Direct detection of genomic DNA by enzymatically amplified SPR imaging measurements of RNA microarrays”, *J. Am. Chem. Soc.*, 126, pp. 4086-4087
- [22] Berger C.E., Greve J., (2000) “Differential SPR immunosensing”, *Sens. Actuators B*, 63, pp. 103-108
- [23] Wang P., Liang O., Zhang W., Schroeder T., Xie Y., (2013) “Ultra-Sensitive Graphene-Plasmonic Hybrid Platform for Label-Free Detection”, *Adv.Mater.*, 25, 4918–4924
- [24] Duan Q., Liu Y., Chang S., Chen H., and Chen J., (2021) “Surface Plasmonic Sensors: Sensing Mechanism and Recent Applications”, *Sensors*, 21, 5262
- [25] Feng J., Siu V.S., Roelke A., Mehta V., Rhieu S.Y., Palmore G. T. R., Pacifici D. (2012) “Nanoscale plasmonic interferometers for multispectral, high-throughput biochemical sensing”. *Nano letters* 12 (2):602-609

- [26] Masson J.F. (2017) "Surface plasmon resonance clinical biosensors for medical diagnostics", *ACS sensors* 2 (1):16-30
- [27] Wei H., Abtahi S. M. H., Vikesland P.J. (2015) "Plasmonic colorimetric and SERS sensors for environmental analysis" *Environmental Science: Nano* 2 (2):120-135
- [28] Tseng S-Y, Li S-Y, Yi S-Y, Sun AY, Gao D-Y, Wan D (2017) "Food quality monitor: paper-based plasmonic sensors prepared through reversal nanoimprinting for rapid detection of biogenic amine odorants", *ACS applied materials & interfaces* 9 (20):17306-17316
- [29] Wang C, Yu C (2013) "Detection of chemical pollutants in water using gold nanoparticles as sensors: a review", *Reviews in Analytical Chemistry* 32 (1):1-14
- [30] Golightly RS, Doering WE, Natan MJ (2009) "Surface-enhanced Raman spectroscopy and homeland security: a perfect match?", ACS Publications
- [31] Valsecchi C, Brolo AG (2013) "Periodic metallic nanostructures as plasmonic chemical sensors", *Langmuir* 29 (19):5638-5649
- [32] Alleyne CJ, Kirk AG, McPhedran RC, Nicorovici N-AP, Maystre D (2007) "Enhanced SPR sensitivity using periodic metallic structures" *Optics express* 15 (13):8163-8169
- [33] Luk'yanchuk B, Zheludev NI, Maier SA, Halas NJ, Nordlander P, Giessen H, Chong CT (2010) "The Fano resonance in plasmonic nanostructures and metamaterials" *Nature materials* 9 (9):707
- [34] Wang Y, Sun C, Li H, Gong Q, Chen J (2017) "Self-reference plasmonic sensors based on double Fano resonances", *Nanoscale* 9 (31):11085-11092
- [35] Wu L, Chu H, Koh W, Li E (2010) "Highly sensitive graphene biosensors based on surface plasmon resonance", *Optics express* 18 (14):14395-14400
- [36] Jakab A, Rosman C, Khalavka Y, Becker J, Trügler A, Hohenester U, Sönnichsen C (2011) "Highly sensitive plasmonic silver nanorods", *ACS nano* 5 (9):6880-6885
- [37] PC W, Sun G, Chen WT, Yang K-Y, Huang Y-W, Chen Y-H, Huang HL, Hsu W-L, Chiang HP, Tsai DP (2014) "Vertical split-ring resonator based nanoplasmonic sensor", *Applied Physics Letters* 105 (3):033105

- [38] Sonnefraud Y, Verellen N, Sobhani H, Vandenbosch GA, Moshchalkov VV, Van Dorpe P, Nordlander P, Maier SA (2010) “Experimental realization of subradiant, superradiant, and Fano resonances in ring/disk plasmonic nanocavities”, *ACS nano* 4 (3):1664-1670
- [39] Cetin AE, Altug H (2012) “Fano resonant ring/disk plasmonic nanocavities on conducting substrates for advanced biosensing” *ACS nano* 6 (11):9989-9995
- [40] King NS, Liu L, Yang X, Cerjan B, Everitt HO, Nordlander P, Halas NJ (2015) “Fano resonant aluminum nanoclusters for plasmonic colorimetric sensing” *ACS nano* 9 (11):10628-10636
- [41] Zhang Z, Zhou B, Huang Y, Liao Z, Li Z, Li S, Wang S, Wen W (2014) “Gold crescent nanodisk array for nanoantenna-enhanced sensing in subwavelength areas” *Applied optics* 53 (31):7236-7240
- [42] Liu N, Weiss T, Mesch M, Langguth L, Eigenthaler U, Hirscher M, Sonnichsen C, Giessen H (2009) “Planar metamaterial analogue of electromagnetically induced transparency for plasmonic sensing” *Nano letters* 10 (4):1103-1107
- [43] Yanik AA, Cetin AE, Huang M, Artar A, Mousavi SH, Khanikaev A, Connor JH, Shvets G, Altug H (2011) “Seeing protein monolayers with naked eye through plasmonic Fano resonances” *Proceedings of the National Academy of Sciences* 108 (29):11784-11789
- [44] Sherry LJ, Chang S-H, Schatz GC, Van Duyne RP, Wiley BJ, Xia Y (2005) “Localized surface plasmon resonance spectroscopy of single silver nanocubes” *Nano letters* 5 (10):2034-2038
- [45] Khorasaninejad M, Raeis-Zadeh SM, Amarloo H, Abedzadeh N, Safavi-Naeini S, Saini SS (2013) “Colorimetric sensors using nano-patch surface plasmon resonators” *Nanotechnology* 24 (35):355501
- [46] Gartia MR, Hsiao A, Pokhriyal A, Seo S, Kulsharova G, Cunningham BT, Bond TC, Liu GL (2013) “Colorimetric plasmon resonance imaging using nano lycurgus cup arrays” *Advanced Optical Materials* 1 (1):68-76
- [47] Ma R-M, Ota S, Li Y, Yang S, Zhang X (2014) “Explosives detection in a lasing plasmon nanocavity” *Nature nanotechnology* 9 (8):600
- [48] Rose A, Zhu Z, Madigan CF, Swager TM, Bulović V (2005) “Sensitivity gains in chemosensing by lasing action in organic polymers” *Nature* 434 (7035):876
- [49] Hueber DM (2000) “Self referencing photosensor” Google Patents,

- [50] Lee S-M, Saini SS, Jeong M-Y (2010) “Simultaneous measurement of refractive index, temperature, and strain using etched-core fiber Bragg grating sensors” *IEEE Photonics Technology Letters* 22 (19):1431-1433
- [51] Montero D, Vázquez C, Möllers I, Arrúe J, Jäger D (2009) “A self-referencing intensity based polymer optical fiber sensor for liquid detection” *Sensors* 9 (8):6446-6455
- [52] Chan LL, Cunningham BT, Li PY, Puff D (2007) “Self-referenced assay method for photonic crystal biosensors: Application to small molecule analytes”, *Sens. Actuators B* 120 (2): 392–398.
- [53] Zu-Yin Z, Li-Na W, Hai-Feng H, Kang-Wen L, Xun-Peng M, Guo-Feng S (2013) “A high figure of merit localized surface plasmon sensor based on a gold nanograting on the top of a gold planar film”, *Chinese Physics B* 22 (10):104213
- [54] Chen J, Sun C, Gong Q (2014) “Fano resonances in a single defect nanocavity coupled with a plasmonic waveguide”, *Optics letters* 39 (1):52-55
- [55] Srivastava SK, Abdulhalim I (2015) “Self-referenced sensor utilizing extra-ordinary optical transmission from metal nanoslits array”, *Optics letters* 40 (10): 2425-2428.
- [56] Abutoama M, Abdulhalim I (2015) “Self-referenced biosensor based on thin dielectric grating combined with thin metal film”, *Optics Express* 23 (22): 28667- 28682.
- [57] Wang X, Zhu J, Wen W, Wu X, Wu Y, Su Y, Tong H, Qi Y, Yang H (2019) “Wide range refractive index sensor based on a coupled structure of Au nanocubes and Au film”, *Opt. Mater. Express* 9(7): 3079-3088
- [58] Kumar S, Shukla MK, Maji PS, Das R (2017) “Self-referenced refractive index sensing with hybrid-Tamm-plasmon-polariton modes in sub-wavelength analyte layers”, *Journal of Physics D: Applied Physics* 50 (37):375106
- [59] McMahon JM, Henzie J, Odom TW, Schatz GC, Gray SK (2007) “Tailoring the sensing capabilities of nanohole arrays in gold films with Rayleigh anomaly-surface plasmon polaritons”, *Optics express* 15 (26):18119-18129
- [60] Mock JJ, Hill RT, Degiron A, Zauscher S, Chilkoti A, Smith DR (2008) “Distance-dependent plasmon resonant coupling between a gold nanoparticle and gold film”, *Nano letters* 8 (8):2245-2252

- [61] Liu S, Leech D, Ju H (2003) "Application of colloidal gold in protein immobilization, electron transfer, and biosensing" *Analytical letters* 36 (1):1-19
- [62] Kawata H, Carter JM, Yen A, Smith HI (1989) "Optical projection lithography using lenses with numerical apertures greater than unity", *Microelectronic Engineering* 9 (1-4):31-36
- [63] Wu B, Kumar A (2007) "Extreme ultraviolet lithography: A review", *Journal of Vacuum Science & Technology B: Microelectronics and Nanometer Structures Processing, Measurement, and Phenomena* 25 (6):1743-1761
- [64] Vieu C, Carcenac F, Pepin A, Chen Y, Mejias M, Lebib A, Manin-Ferlazzo L, Couraud L, Launois H (2000) "Electron beam lithography: resolution limits and applications", *Applied surface science* 164 (1-4):111-117
- [65] Moharam M, Gaylord T (1981) "Rigorous coupled-wave analysis of planar-grating diffraction", *JOSA* 71 (7):811-818
- [66] Synopsys's Rsoft. Available online: <https://www.synopsys.com>.
- [67] Yakubovsky DI, Arsenin AV, Stebunov YV, Fedyanin DY, Volkov VS (2017) "Optical constants and structural properties of thin gold films", *Opt. Express* 25(21): 25574-25587
- [68] Eriksson T, Granqvist C (1986) "Infrared optical properties of silicon oxynitride films: experimental data and theoretical interpretation", *Journal of applied physics* 60 (6):2081-2091
- [69] Denisse C, Troost K, Oude Elferink J, Habraken F, Van der Weg W, Hendriks M (1986) "Plasma-enhanced growth and composition of silicon oxynitride films", *Journal of applied physics* 60 (7):2536-2542
- [70] Kuiper A, Koo S, Habraken F, Tamminga Y (1983) "Deposition and composition of silicon oxynitride films", *Journal of Vacuum Science & Technology B: Microelectronics Processing and Phenomena* 1 (1):62-66
- [71] Hao F, Sonnefraud Y, Dorpe PV, Maier SA, Halas NJ, Nordlander P (2008) "Symmetry breaking in plasmonic nanocavities: subradiant LSPR sensing and a tunable Fano resonance", *Nano letters* 8 (11):3983-3988

- [72] Lassiter JB, Sobhani H, Fan JA, Kundu J, Capasso F, Nordlander P, Halas NJ (2010) “Fano resonances in plasmonic nanoclusters: geometrical and chemical tunability”, *Nano letters* 10 (8):3184-3189
- [73] Ren J, Wang G, Qiu W, Lin Z, Chen H, Qiu P, Wang J-X, Kan Q, Pan J-Q (2017) “Optimization of the Fano resonance lineshape based on graphene plasmonic hexamer in mid-infrared frequencies”, *Nanomaterials* 7 (9):238
- [74] Cubukcu E, Zhang S, Park Y-S, Bartal G, Zhang X (2009) “Split ring resonator sensors for infrared detection of single molecular monolayers”, *Applied Physics Letters* 95 (4):043113
- [75] Sepúlveda B, Calle A, Lechuga LM, Armettes G (2006) “Highly sensitive detection of biomolecules with the magneto-optic surface-plasmon-resonance sensor”, *Optics letters* 31 (8):1085-1087
- [76] Elhadj S, Singh G, Saraf RF (2004) “Optical properties of an immobilized DNA monolayer from 255 to 700 nm”, *Langmuir* 20(13): 5539-5543
- [77] Oldham N. C. and Hill C. J., (2002), “Deposition of $\text{Ga}_2\text{O}_{3-x}$ ultrathin films on GaAs by e-beam evaporation”, *Journal of Vacuum Science & Technology A* 20, 809
- [78] Podlucky L., Vincze A., Kováčová S., Chlupík J., Kováč J., and Uherek F., (2021), “Optimization of Fabrication Process for SiON/SiO_x Films Applicable as Optical Waveguides”, *Coatings* 2021, 11, 574
- [79] Zhang J. , Fouad M., Yavuz M., Cui B., (2011), “Charging effect reduction in electron beam lithography with nA beam current”, *Microelectronic Engineering*, Volume 88, Issue 8, 2196-2199
- [80] <https://www.edmundoptics.ca>
- [81] Bansal N. P., (2018) "Advances in EB-PVD thermal barrier coatings," *Surface and Coatings Technology*, vol. 349, pp. 624-641
- [82] <https://intlvac.com/Systems/Thin-Film-Deposition/Nanochrome-II>
- [83] Todeschini M., Bastos da Silva Fanta A., Jensen F., Wagner J. B., and Han A., (2017) “Influence of Ti and Cr Adhesion Layers on Ultrathin Au Films”, *ACS Appl. Mater. Interfaces*, 9, 42, 37374–37385

- [84] Cuomo J. J., and Gottscho R. A., (1997) "Handbook of Plasma Processing Technology: Fundamentals, Etching, Deposition, and Surface Interactions," Noyes Publications.
- [85] Rossnagel S. M., Coburn J. W., and Boxman R. L., (2010) "Handbook of Plasma Processing Technology: Fundamental, Etching, Deposition, and Surface Interactions," William Andrew Inc.
- [86] Chu P. K., Li L. C., (2002) "Plasma-surface modification of biomaterials," *Materials Science and Engineering: R: Reports*, vol. 36, issues 5-6, pp. 143-206.
- [87] <https://www.jawoollam.com/resources/ellipsometry-tutorial/optical-constants>
- [88] Wörhoff K., Driessen A., Lambeck P.V., Hilderink L.T.H., Linders P.W.C., Popma Th.J.A. , (1999) "Plasma enhanced chemical vapor deposition silicon oxynitride optimized for application in integrated optics", *Sensors and Actuators*, 74, 9–12
- [89] Wörhoff K., Hilderink L. T. H., Driessen A., and Lambeck P. V., (2002) "Silicon Oxynitride; A Versatile Material for Integrated Optics Applications", *J. Electrochem. Soc.* 149 (8), F85-F91.
- [90] <https://www.filmetrics.com/thickness-measurement/f40>
- [91] Mansuripur M., (1986) "Distribution of light at and near the focus of high-numerical-aperture objectives," *J. Opt. Soc. Am. A* 3, 2086-2093.
- [92] <https://www.cargille.com/>
- [93] Chryssis A. N., Saini S. S., Lee S. M., Yi H., Bentley W. E. and Dagenais M., (2005) "Detecting hybridization of DNA by highly sensitive evanescent field etched core fiber Bragg grating sensors," *IEEE Journal of Selected Topics in Quantum Electronics*, vol. 11, no. 4, pp. 864-872.
- [94] Debu D. T., Ghosh P. K., French D., and Herzog J. B., (2017) "Surface plasmon damping effects due to Ti adhesion layer in individual gold nanodisks," *Opt. Mater. Express* 7, 73-84.
- [95] Lahiri B., Dylewicz R., De La Rue R. M., and Johnson N. P., (2010) "Impact of titanium adhesion layers on the response of arrays of metallic split-ring resonators (SRRs)," *Opt. Express* 18, 11202-11208.
- [96] https://en.wikipedia.org/wiki/Savitzky%E2%80%93Golay_filter
- [97] Sohn S.-I., Oh Y.-J., Pandian S., Lee, Y.-H., Zaukuu J.-L. Z., Kang H.-J., Ryu T.-H., Cho W.-S., Cho Y.-S., Shin E.-K, (2021) "Identification of Amaranthus Species Using Visible-Near-Infrared (Vis-NIR) Spectroscopy and Machine Learning Methods", *Remote Sens.*, 13, 4149.

- [98] Sperling, J. R., Macias, G., Neale, S. L., & Clark, A. W. (2018) “Multilayered nanoplasmonic arrays for self-referenced biosensing” *ACS applied materials & interfaces*, 10(40), 34774-34780.
- [99] Li K., Wang Y., Jiang K., Ren Y., Dai Y., Lu Y. and Wang P., (2016) “reproducible and sensitive plasmonic MIM substrates for surface-enhanced Raman scattering”, *Nanotechnology* 27, 495402
- [100] Lin V. K., Teo S. L., Marty R., Arbouet A., Girard C., Alarcon-Llado E., Liu S. H., Han M. Y., Tripathy S., Mlayah A., (2010) “Dual wavelength sensing based on interacting gold nanodisk trimers”, *Nanotechnology* 21, 305501
- [101] Tabakman S. M., Lau L., Robinson J. T., Price J., Sherlock S. P., Wang H., Zhang B., Chen Z., Tangsombatvisit S., Jarrell J. A., Utz P. J. & Dai H., (2011) “Plasmonic substrates for multiplexed protein microarrays with femtomolar sensitivity and broad dynamic range”, *Nature Communications* 2, 466
- [102] Chu Y., Banaee M. G., and Crozier K. B., (2010) “Double-Resonance Plasmon Substrates for Surface-Enhanced Raman Scattering with Enhancement at Excitation and Stokes Frequencies”, *ACS Nano* 4, 2804–2810
- [103] Chorsi H. T., Lee Y., Alù A. and Zhang J. X. J., (2017) “Tunable plasmonic substrates with ultrahigh Q-factor resonances”, *Scientific Reports* 7, 15985
- [104] Bin-Alam M. S., Reshef O., Mamchur Y., Alam M. Z., Carlow G., Upham J., Sullivan B. T., Ménard J. M., Huttunen M. J., Boyd R. W. and Dolgaleva K., (2021) “Ultra-high-Q resonances in plasmonic metasurfaces”, *Nature Communications* 12, 974
- [105] Yang X., Xiao G., Lu Y., and Li G., (2019) “Narrow plasmonic surface lattice resonances with preference to asymmetric dielectric environment”, *Optics Express*, 27 (18), 25384-25394
- [106] Wang W., Ramezani M., Väkeväinen A. I., Törmä P., Rivas J. G., and Odom T. W., (2018) “The rich photonic world of plasmonic nanoparticle arrays,” *Mater. Today* 21, 303–314
- [107] Hedayati M. K., and Elbahri M., (2016) “Review of Metasurface Plasmonic Structural Color”, *Plasmonics*, 1–17
- [108] Kohandani R., and Saini S. S., (2020) “Self-Referencing Plasmonic Array Sensors”, *Plasmonics*, 15:1359–1368

- [109] Reinhard I., Miller K., Diepenheim G., Cantrell K., and Hall W. P., (2020) “Nanoparticle Design Rules for Colorimetric Plasmonic Sensors”, *ACS Appl. Nano Mater.*, 3, 4342–4350
- [110] Kumar K., Duan H., Hegde R., Koh S. C. W., Wei J. N., and Yang J. K. W., (2012) “Printing colour at the optical diffraction limit”, *Nature Nanotechnology*, 7, 557–561
- [111] Wang H., Wang X., Yan C., Zhao H., Zhang J., Santschi C., and Martin O. J. F., (2017) “Full Color Generation Using Silver Tandem Nanodisks”, *ACS Nano*, 11, 4419–4427
- [112] Yang X., Xiao G., Lu Y., and Li G., (2019) “Narrow plasmonic surface lattice resonances with preference to asymmetric dielectric environment”, *Optics Express*, 27 (18) 25384–25394.
- [113] Sarkar S., Gupta V., Kumar M., Schubert J., Probst P. T., Joseph J., and König T.A.F., (2019) “Hybridized guided-mode resonances via colloidal plasmonic self-assembled grating”, *ACS Appl. Mater. Interfaces*, 11, 13752–13760
- [114] Seo K., Wober M., Steinvurzel P., Schonbrun E., Dan Y., Ellenbogen T., and Crozier K. B., (2011) “Multicolored Vertical Si Nanowires”, *Nano Lett.*, 11, 4, 1851–1856
- [115] ASTM. E308-01, (2001) “Standard Practice for Computing the Colors of Objects by Using the CIE System”, pp 1–32
- [116] <https://www.ajaint.com/sputtering-systems.html>
- [117] Racka-Szmidt K., Stonio B., Żelazko J., Filipiak M., Sochacki M. (2021) “A Review: Inductively Coupled Plasma Reactive Ion Etching of Silicon Carbide” *Materials (Basel)* 24;15(1):123.
- [118] Imamura T. et al, (2021) “Cyclic C₄F₈ and O₂ plasma etching of TiO₂ for high-aspect-ratio three-dimensional devices” *Jpn. J. Appl. Phys.* 60 036001.
- [119] Li X., Ling L., Hua X., Fukasawa M., Oehrlein G., Barela M. J., Anderson H., (2003) “Effects of Ar and O₂ additives on SiO₂ etching in C₄F₈-based plasmas”, *J. Vac. Sci. Technol. A* 21, 284–293.
- [120] https://en.wikipedia.org/wiki/Tauc%E2%80%93Lorentz_model
- [121] <https://transene.com/aluminum/>